From analytical to fully numerical predictions of the broadband noise radiated by a full fan-OGV stage

Danny Lewis

To cite this version:

Danny Lewis. From analytical to fully numerical predictions of the broadband noise radiated by a full fan-OGV stage. Other. Université de Lyon, 2020. English. NNT : 2020LYSEC032 . tel-03258046

HAL Id: tel-03258046
https://theses.hal.science/tel-03258046v1

Submitted on 11 Jun 2021

N° d’ordre NNT: 2020LYSEC32

THÈSE de DOCTORAT DE L’UNIVERSITÉ DE LYON
opérée au sein de l’École Centrale de Lyon

École Doctorale N° 162
Mécanique, Énergétique, Génie Civil, Acoustique

Spécialité de doctorat : Mécanique des fluides et Acoustique

Soutenue publiquement le 16/11/2020, par
Danny Lewis

From analytical to fully numerical predictions of the broadband noise radiated by a full fan-OGV stage.

Devant le jury composé de:

Cinnella, Paola	Professeur	Art & Métiers ParisTech	Rapporteure
Duchaine, Florent	Directeur de recherche	CERFACS	Rapporteur
François, Benjamin	Docteur	ONERA	Examinateur
Gea Aguilera, Fernando	Docteur	Safran Aircraft Engines	Invité
Grace, Sheryl	Professeur	Boston University	Examinatrice
Jacob, Marc	Professeur	École Centrale de Lyon	Directeur de thèse
Moreau, Stéphane	Professeur	École Centrale de Lyon	Directeur de thèse
Roger, Michel	Professeur	École Centrale de Lyon	Président du jury
Sanjosé, Marlène	Professeur	ÉTS Montréal	Examinatrice

No one I think is in my tree
I mean it must be high or low

The Beatles

L'aerodinamica è il risarcimento per chi non sa spremere cavalli dal motore.

diceva **Enzo Ferrari**, a torto.

Remerciements

Cette thèse a été réalisée au sein du groupe Acoustique du Laboratoire de Mécanique des Fluides et d'Acoustique (LMFA) de l'École Centrale de Lyon. Elle fait partie intégrante du projet TurbonoiseBB, financé par le programme européen de recherche et d'innovation Horizon 2020 (projet No. 690714). Une extension de contrat a également été financée par la chaire industrielle ARENA liant le centre Acoustique et Safran Aircraft Engines. L'ensemble des simulations numériques a été réalisé grâce aux ressources de calcul fournies par le réseau GENCI (CINES-OCCIGEN, projet No. A0062A06074), le CERFACS, et par PMCS2I-FLMSN.

Je souhaite tout d'abord remercier les membres du jury d'avoir accepté d'évaluer mon travail de thèse dans ces conditions si particulières. Je tiens tout particulièrement à remercier chaleureusement mes deux directeurs de thèse Marc Jacob et Stéphane Moreau, pour la qualité de leur encadrement et leur disponibilité malgré la distance qui nous séparait. Ce travail est le résultat d'un réel travail d'équipe, qui a été nourri par votre expérience et vos conseils. Nombre de surprises ont rythmé ce doctorat, certaines beaucoup plus appréciées que d'autres, et je suis heureux d'avoir développé avec vous une relation qui va bien au-delà du travail de recherche.

Je souhaite exprimer toute ma gratitude à l'équipe CFD du CERFACS, qui m'a accueilli pendant ma première année de thèse et m'a fourni un cadre idéal pour débuter ce doctorat que ce soit au niveau humain, scientifique ou des moyens de calcul. Cela a notamment été possible grâce à la bonne humeur et à l'efficacité du personnel administratif (Chantal) et du secrétariat (Marie et Nicole) mais aussi grâce à la disponibilité de l'équipe informatique. Je tiens à remercier Florent Duchaine de m'avoir accueilli au CERFACS et d'avoir mené à bien toutes les démarches pour l'obtention des heures de calcul sur les calculateurs nationaux. Je tiens également à exprimer toute ma reconnaissance à Nicolas Odier pour ses nombreux conseils et sa disponibilité tout au long de ce doctorat. Cette expérience au CERFACS n'aurait pas été aussi enrichissante sans les formidables rencontres que j'y ai faites. Je pense tout d'abord à la fameuse team LBM : mon premier co-bureau Florian, beatboxer à ses heures perdues et avec qui j'ai définitivement développé mon odorat, Thomas pour nos nombreuses compositions symphoniques et pour sa capacité à lier si harmonieusement maçonnerie et tennis, Christophe pour m'avoir fait découvrir que le tennis peut se jouer uniquement avec des slices (pour mon plus grand malheur) et pour nos échanges sur la culture nipponne, Gauthier, pour son sens de la recherche inégalé et ses vannes pleines de nuances, Bastien pour les découvertes musicales et son expertise du houblon, et JF pour sa pédagogie et son concept de goûter ininterrompu. Je pense également aux personnes hors du CERFACS qu'il m'a été possible de rencontrer grâce à eux : Mai, Adélie, Laura, Octavie et Viviane. Merci à Maxime, le plus grand pâtissier que le CERFACS ait connu, d'avoir supporté le bruit et mes aller-retours incessants dans son bureau pour lui demander conseil. Enfin, merci à Laurent d'avoir accepté de parler aussi fort que moi lors de nos discussions de groupe, et à Adèle pour son autodérision et sa capacité à capter le soleil avec l'angle parfait.

La suite de ce doctorat s'est déroulée au sein de l'équipe acoustique du LMFA. Je tiens à remercier tous les permanents avec qui j'ai pu interagir au quotidien sur de nombreux sujets. J'ai une pensée particulière pour Michel Roger qui m'a initié à l'acoustique, à l'art de jouer avec les mots et pour qui une espièglerie n'est jamais de trop au détour d'un couloir. Merci également à Fred pour les bons moments passés ensemble, ainsi qu'à Vincent et Alexis pour nos échanges. J'adresse tous mes remerciements à Marie-Gabrielle Perriaux pour sa disponibilité, à Laurent Pouilloux pour son efficacité, son implication sans faille dans la vie du laboratoire et surtout pour sa bonne humeur lors de chacune de ses visites. J'ai également apprécié l'aide de Christophe Bailly qui a su être à l'écoute dans les moments plus difficiles. Ces années aux LMFA ont évidemment été marquées par des rencontres fantastiques. Tout d'abord mes co-bureaux qui ont dû me supporter pendant ces longues années : Miguel avec qui j'ai parfait mon frantugais (nivou internaschiounal, c'est ça qu'ça donne) et développer ma précision (à tous les niveaux), Léo pour ses cascades improbables et ses pourboires généreux, Helmut toujours bien habillé en soirée, Gabriele pour sa gourmandise et son soutien inconditionnel pour défendre la culture italienne, et enfin Jean, pour sa bienveillance et sa bonne humeur au quotidien. Nombre d'autres doctorants et post-doctorants ont contribué à rendre cette expérience mémorable et je les en remercie : Yann et son expertise (limitée) en langue des signes, Elina la plus grande skateuse sur tapis volant au monde, David l'admirateur de marinières et de predators (crochet à gauche, crochet à droite, schlack), Marion pour son autodérision et Mary Cooper pour sa confiance en mes goûts musicaux, Paul et son déhanché ensorcelé par Céline, Rafael toujours partant pour de nouvelles ~~fractures~~ aventures, Vianney qui vole vers de nouveaux horizons, Simon le grand percussionniste, Pierre le Flamboyant toujours friand d'une représentation du Muppet Show, Ariane et sa démarche aux allures de fée qui toise le second degré comme si ce n'était qu'une température, Mohcène futur champion de MMA, le caporal Mathieu, Arthur l'homme qui murmure à l'oreille des oiseaux, Damien qui n'aura finalement pas réussi à abattre un mur avec le babyfoot, Georgios le magka mou, Etienne le Proust de la madeleine, Bertrand et sa vision du monde, Yuanyuan et son sourire permanent, Jérôme et ses vaches à lait qui trainent sur le terrain de tennis, Thomas notre artiste du cirque, Igor qui a fait de la sieste un art à part entière, Courtney, Daher, Alexis et Hugo pour la bonne ambiance au quotidien.

Cette thèse n'aurait pu arriver à son terme sans les échanges avec l'équipe acoustique de Sherbrooke. Je tiens à exprimer toute ma reconnaissance envers Marlène, véritable couteau suisse de la CFD qui m'aura soutenu et aidé tout au long de la thèse malgré un contexte difficile. J'ai également apprécié les échanges avec Pavel et Régis, et les moments passés ensemble à l'AIAA.

Collaborer avec l'ensemble des membres du projet TurbonoiseBB a également été un réel plaisir, tant pour l'aspect scientifique que pour l'expérience humaine que le projet m'a apportée.

Je tiens à remercier les amis qui me suivent depuis de nombreuses années, du lycée jusqu'à l'ENSICA en passant par les classes préparatoires, ainsi que celle qui m'accompagne maintenant au quotidien, de rendre ma vie toujours plus drôle et agréable.

Je remercie finalement ma famille, pour son soutien sans faille depuis toujours et pour la force qu'elle me donne chaque jour pour avancer.

Abstract

The fan-Outlet Guide Vane (OGV) stage of aircraft engines is currently being considered as one of the major contributors to the total noise radiated by an aircraft, particularly at approach and take-off operating conditions. This trend will intensify with the future Ultra High Bypass Ratio engine architecture, which will be characterized by an increased bypass ratio resulting from a larger diameter. To meet the increasingly stringent noise regulation requirements, significant progress has already been achieved by aircraft manufacturers. Most of these improvements are related to the tonal component of the fan-OGV stage noise, while less progress has been made in reducing the broadband component. The latter originates from stochastic phenomena involving the interaction of turbulent structures with solid surfaces such as walls, blades and vanes. At subsonic operating points, the main mechanism responsible for both broadband and tonal noise generation is the Rotor-Stator Interaction (RSI), which results from the impingement of the turbulent rotor wakes onto the stator, generating unsteady loading on the vanes. The present study focuses on the latter mechanism and aims at assessing the capacity of two state of the art methods, with different levels of computational cost and accuracy, to provide reliable broadband noise predictions. The first one couples a simulation solving the Reynolds Averaged Navier-Stokes (RANS) equations with analytical models. It provides broadband RSI noise estimates at moderate computational costs and is particularly well suited for pre-design studies. The second method, more accurate but significantly more demanding in terms of computational resources, is a hybrid numerical approach. It couples a Large Eddy Simulation (LES), for the computation of the noise sources, with an acoustic analogy, dedicated to the propagation of the sound in the far-field. It is currently considered as one of the most advanced method to carry out comprehensive acoustic analyses on a fan-OGV stage. These two approaches are applied to a realistic fan-OGV stage geometry operating at approach conditions, and are directly compared to each other through comprehensive aerodynamic and acoustic analyses. The capacity of both approaches to provide reliable noise predictions is demonstrated, with a significant increase in accuracy observed with the second approach, which is obtained as a trade-off with a higher computational cost. The impact of the modeling hypotheses of each method on the reliability of their respective noise predictions is assessed, and an overall better understanding of the complex flow features characterizing the approach operating condition is provided. Furthermore, additional noise sources on both the OGV and the fan are brought to light. Their relative contribution to the total noise is directly compared to that of the RSI noise, showing that the RSI mechanism is not necessarily the only dominant noise source at approach conditions.

Keywords: aeroacoustics, turbomachinery, rotor-stator interaction, broadband noise, fan noise, analytical modeling, large eddy simulation, unsteady simulation.

Résumé

L'étage de soufflante des turboréacteurs est actuellement considéré comme l'une des principales sources de bruit d'un avion, en particulier en phase d'approche et de décollage. Face à une règlementation de plus en plus contraignante vis à vis de la pollution sonore, et par anticipation de l'intensification du bruit de soufflante induite par les futures configurations à très fort taux de dilution, un certain nombre d'initiatives ont été prises dans le but de limiter l'émission de bruit par les moteurs. Elles portent cependant majoritairement sur la composante tonale du bruit, tandis que le bruit à large bande n'a été réduit que de manière marginale. Ce dernier provient de l'interaction de structures turbulentes avec les surfaces solides du moteur telles que son carénage, les pales du rotor ou les aubes du stator. Cette composante du bruit est majoritairement produite par le mécanisme d'interaction rotor-stator, également responsable d'une partie du bruit tonal, notamment en phase d'approche et de décollage. Ce dernier résulte de l'impact des sillages turbulents du rotor sur le stator de l'étage de soufflante (OGV), générant ainsi des fluctuations de charge sur les aubes du stator. Le présente thèse propose une étude de ce mécanisme et plus particulièrement de sa composante à large bande. Elle a notamment pour but d'évaluer la capacité de deux méthodes à fournir des prédictions de bruit à large bande fiables. Ces deux méthodes définissent l'état de l'art actuel et proposent deux niveaux différents de coût et de précision. La première couple une simulation d'écoulement par la méthode des équations de Navier-Stokes moyennées (RANS) avec des modèles analytiques de prédiction de bruit. Cette méthode permet d'estimer le bruit à large bande d'interaction rotor-stator et est particulièrement adaptée aux étapes de pré-conception dans le contexte industriel grâce à son faible coût. La seconde est une méthode numérique hybride couplant une simulation aux grandes échelles (LES), permettant de calculer les sources acoustiques au sein de l'étage de soufflante, avec une analogie acoustique, en charge de la propagation en champ lointain du bruit émis par ces dernières. Cette méthode, qui est l'une des plus avancées pour ce type de problématique, fournit des prédictions de bruit à large bande plus précises mais requiert l'utilisation d'importantes ressources de calcul. Les deux approches sont appliquées à une géométrie représentative d'un étage de soufflante en phase d'approche, et directement confrontées à travers une étude aérodynamique et acoustique complète. La capacité des deux approches à fournir des prédictions de bruit fiables est démontrée, en particulier pour la seconde méthode un gain substantiel de précision est observé, mais requiert un coût de calcul supplémentaire important. L'impact des hypothèses de modélisation de chaque méthode sur la fiabilité de leurs prédictions acoustiques respectives est évalué, et les particularités de l'écoulement caractérisant la phase d'approche sont mises en évidence. Par ailleurs, des sources de bruit à large bande supplémentaires sont identifiées sur le rotor et le stator, et leurs contributions respectives au bruit à large bande total sont estimées et comparées à celle du mécanisme d'interaction rotor-stator, révélant que ce dernier n'est pas nécessairement l'unique source de bruit prépondérante en phase d'approche.

Mots-clés: aéroacoustique, turbomachine, interaction rotor-stator, bruit à large bande, bruit de soufflante, modèle analytique, simulation aux grandes échelles, simulation instationnaire.

Contents

List of Symbols and Acronyms

Latin characters

(m, μ)	Duct mode order: azimuthal order m, radial order μ
$\dot{Q}$	Volume heat source
$\mathbf{F}$	Net force vector
$\mathbf{q}$	Heat flux vector
$\mathbf{u}$	Velocity vector
c	Vane or blade chord
c_0	Speed of sound
C_f	Friction coefficient
C_p	Pressure coefficient
d	Non-overlapping area
E	Total energy
G_0	Free-field Green's function in a medium at rest
G_{duct}	Green's function for annular ducts with a uniform flow
G_{mov}	Free-field Green's function in a uniformly moving medium
h	Intervane channel height
J_m	Bessel function of first kind of order m
$k_0 = \frac{\omega}{c_0}$	Acoustic wave number
$k^{\pm}_{x,m\mu}$	Axial wave number of the duct mode (m, μ)
L_{r,u_i}	Radial coherence length scale of the velocity component u_i
Lr_p	Coherence length scale of the pressure on the vane surface
M	Mach number
P	Static pressure
p	Acoustic pressure
P_t	Total pressure
T	Temperature
T_t	Total temperature
T_{ij}	Lighthill's tensor
V_r	Radial velocity component
V_x	Axial velocity component
V_θ	Circumferential velocity component
w	Upwash velocity fluctuation
Y_m	Bessel function of second kind of order m

Greek characters

α	Flow angle $\alpha = \arctan(V_\theta/V_x)$
$\beta = \sqrt{1-M^2}$	Compressibility parameter
χ_s	Stagger angle
$\chi_{m,\mu}$	Duct eigenvalues of the mode (m,μ)
δ	Boundary layer thickness
γ_p	Coherence function of the pressure on the vane surface
γ_{u_i}	Coherence function of the velocity component u_i
$\kappa_{m,\mu}$	Cut-off parameter of the duct mode (m,μ)
Λ	Integral length scale
μ	Dynamic viscosity
μ_t	Turbulent viscosity
Ω	Rotational speed
ω	Angular frequency
$\Psi_{m,\mu}$	Duct eigenfunctions of the mode (m,μ)
ρ	Density
Σ	Solidity of the stator row
σ	Interblade phase angle
τ	Viscous stress tensor

Subscripts

c	Auto-correlation based estimate (int. length scale).
$casing, T$	Related to the outer casing of the annular duct
hub, H	Related to the hub of the annular duct
j	Jurdic estimate (int. length scale).
p	Pope estimate (int. length scale).
rms	Root mean square of the variable

Superscripts

$+$	Upstream value
$-$	Downstream value
$'$	Fluctuating values

Acronyms

2D	Two dimensional
3D	Three dimensional
ACAT1	TurbonoiseBB fan rig
BPF	Blade Passing Frequency
CAA	Computational Aero-Acoustics
CD	Controlled Diffusion
CFD	Computational Fluid Dynamics
CPU	Computational
DES	Detached Eddy Simulation
DNS	Direct Numerical Simulation
FW-H	Ffowcs Williams and Hawkings
HBR	High Bypass Ratio
HW	Hot-Wire
IGV	Inlet Guide Vane

LBM	Lattice-Boltzmann Method
LBR	Low Bypass Ratio
LE	Leading Edge
LEE	Linearized Euler Equations
LES	Large Eddy Simulation
MPT	Multiple Pure Tones
OGV	Outlet Guide Vane
PSD	Power Spectral Density
RANS	Reynolds Averaged Navier-Stokes
RMS	Root Mean Square
RSI	Rotor-Stator Interaction
SDT	Source Diagnostic Test
SWL	Sound poWer Level
TE	Trailing Edge
TI	Turbulence Intensity
TKE	Turbulence Kinetic Energy
TLS	Turbulence integral Length Scale
TLV	Tip Leakage Vortex
TSV	Tip Separation Vortex
UHBR	Ultra-High Bypass Ratio
URANS	Unsteady Reynolds Averaged Navier-Stokes
WALE	Wall-Adapting Local Eddy-viscosity
WMLES	Wall-Modeled LES
WMLES-FWH	Approach coupling a Wall-Modeled LES with the FW-H analogy
WND	Wave Number Decomposition

List of Figures

List of Tables

Introduction

General context

According to ICAO[1]'s 2018 annual report, a 4.5% to 8.7% increase in the number of passengers transported by airplanes was observed every year since 2010. This almost constant growth in air transport, coupled with an increased urbanization of areas in the vicinity of airports, have inevitably led to a more significant exposure of the population to pollutant and noise emissions. This phenomenon has turned into a major environmental concern urging the establishment of more constraining pollutant and noise emission regulations. To do so, the ICAO has identified three major axis of action: the reduction of pollutant emitted by aircraft engines on a local scale, the reduction of the emission of greenhouse gas on a global scale, and the reduction of the noise pollution. The present work deals with the latter axis.

In Europe, the ACARE [2] has set several objectives for the upcoming years to reduce noise pollution: noise emissions from airplanes produced in 2020 should be reduced by 50% and by 65% for those delivered in 2050, with respect to airplanes from the 2000's. These objectives must be reached for the three certification points identified by ICAO: at approach, sideline and fly-over operating points (see fig. 1).

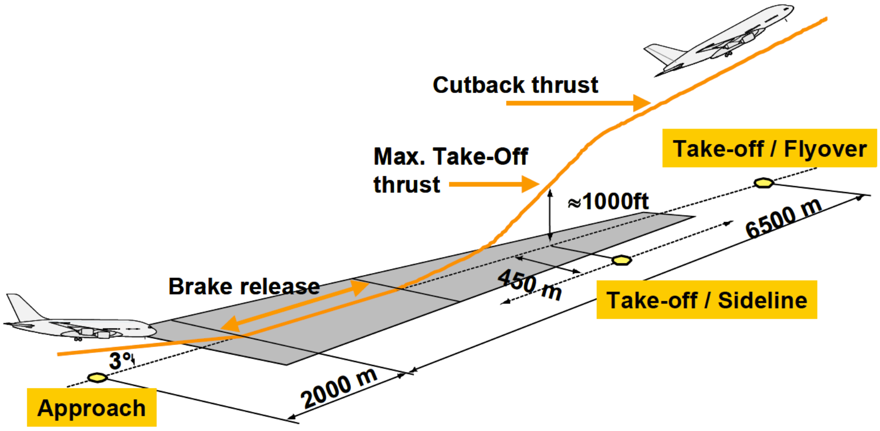

Figure 1: Noise certification flight paths and control points. (adapted from [1])

---

[1] International Civil Aviation Organization

[2] Advisory Council for Aviation Research and Innovation in Europe

In order to comply with these constraints, companies involved in aircraft manufacturing have come together to address the question of noise pollution. Significant noise reductions have already been achieved by engine manufacturers mainly by modifying the architecture of the engines. Indeed, the first single-flux engines that were released in the 1940's, also called turbojets, exclusively relied on the speed of the exhaust hot gas to produce thrust. Since the acoustic power resulting from a jet flow evolves as the eighth power of the flow velocity [16, 17], the turbojet acoustic footprint was quite substantial. With the aim of reducing the fuel consumption of the engines, the turbojet was later upgraded to a double-flux engine architecture, also called turbofan, depicted in fig. 2. This type of engine mainly relies on the increased mass-flow rate of the bypass flow to generate the required thrust and simultaneously reduces the velocity of the exhaust hot gas of the core flow. Consequently, the overall exhaust velocity of the engine was significantly reduced, resulting in a decreased fuel consumption but also in a reduced radiated noise.

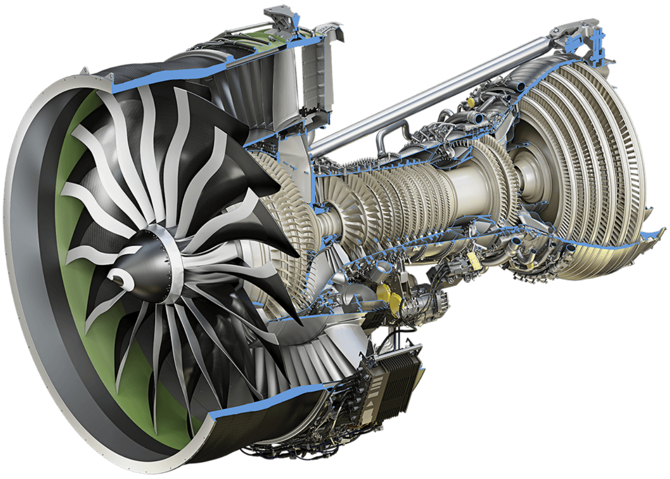

Figure 2: High Bypass Ratio (HBR) engine. (GE9X engine [2])

Turbofans are currently the most widely used type of engines. They have been extensively upgraded from Low Bypass Ratio[3] engines (LBR), to High Bypass Ratio engines (HBR), which positively impacted the fuel consumption and modified the relative contribution of the different noise sources. Figure 3 shows how the increase in the bypass ratio has redistributed the contribution of the noise sources in a turbofan architecture. For LBR engines, which are relatively similar to turbojets, the jet is the dominant noise source whereas the fan noise is very limited. The noise is mainly radiated downstream of the engine. With the increase in the bypass ratio, the jet noise has been significantly reduced. In parallel, the fan contribution has been increased both upstream and downstream of the engine, turning the fan stage into the major contributor to the noise production especially at approach and take-off operating points [18] (see fig. 4). These modifications of the relative noise levels of the different noise sources have eventually led to a radiated noise that is more balanced between the upstream and downstream components.

However, in order to sustain the foreseen increase in air transport, further improvements need to be made. One candidate to further decrease noise pollution, while maintaining the fuel burn reduction trend, is the Ultra-High Bypass Ratio engine (UHBR). This solution is basically an extension of current turbofan engine architectures: it displays a larger diameter, resulting in an increased bypass ratio, and a shorter nacelle to compensate the weight and drag penalties that would arise from the engine widening. In such architectures, the fan stage is expected to become a major contributor to the total radiated noise at all certification points. Additonally, as

---

[3] Ratio between the mass-flow rate of the bypass flow and the mass-flow rate of the core flow.

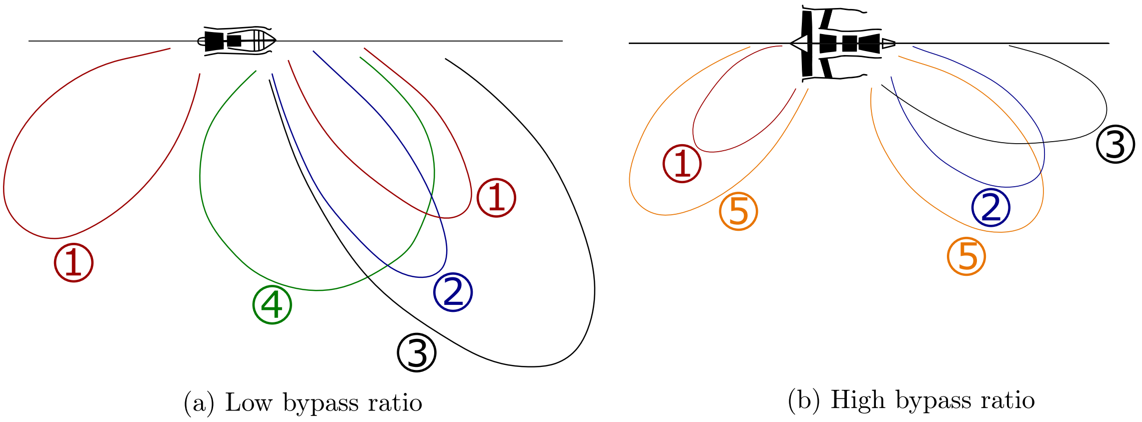

(a) Low bypass ratio (b) High bypass ratio

Figure 3: Evolution of the directivity and relative noise levels of the different noise sources with respect to the bypass ratio. Color code: 1: compressor, 2: turbine, 3: jet, 4: shock, 5: fan. (adapted from [3])

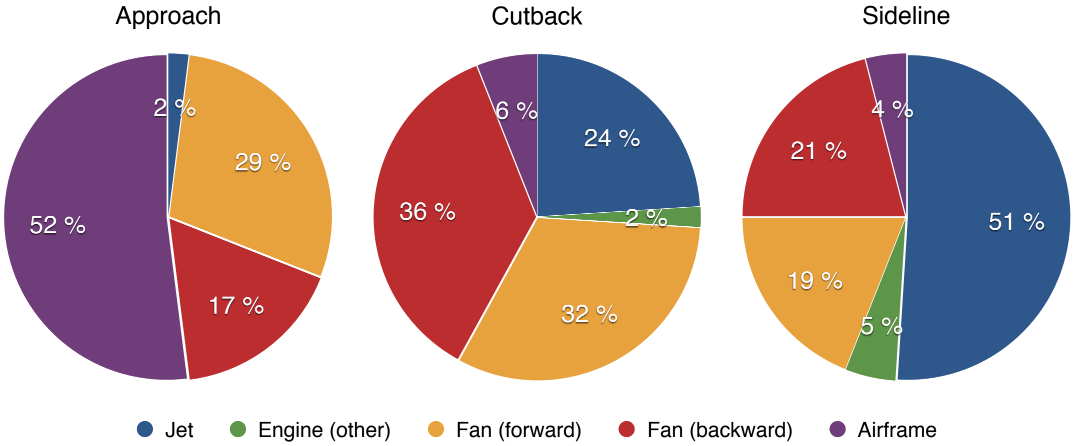

Figure 4: Example of noise source sensitivity on a typical long range aircraft, at the three certification points [4].

with current engines, a clever selection of the number of blades and vanes in the engine, as well as the use of passive noise control technologies such as acoustic liners, have made it possible to significantly reduce the tonal component of the noise, leading to an expected dominant broadband component. This component of the noise originates from random fluctuating mechanisms in the engine. More precisely, in fan-Outlet Guide Vane (OGV) stages, it results from the interaction of turbulent structures with solid walls involved in inlet turbulence ingestion, turbulent boundary layers, tip gap vortex and in the impingement of the fan wakes onto the OGVs. The latter mechanism is referred to as the Rotor-Stator Interaction (RSI) mechanism and has been identified as the dominant mechanism responsible for both broadband and tonal noise generation within a fan stage [5, 19, 20].

Overview of the thesis

This brief introduction has revealed that the fan stage of aircraft engines is actually responsible for a major part of the noise radiated by an aircraft, whether tonal or broadband, at both approach and take-off operating points. In particular, the rotor-stator interaction noise has been identified as one of the most significant noise sources in current and future engine architectures. Reducing the impact of this mechanism then appears to be a direct way to tackle the problem of aircraft noise pollution. The present thesis focuses on the study of the broadband component of the rotor-stator interaction noise, exclusively at approach conditions. It aims at improving the understanding of the physics lying within this complex mechanism in order to improve, assess, and develop two of the most used approaches to perform noise predictions: an analytical approach, which provides fairly accurate predictions at a very low computational cost, and a more advanced approach based on numerical simulation, which requires substantial computational resources but provides more accurate results. Another goal is also to clearly identify and understand the noise sources resulting from this mechanism in order to lead the way to innovative low-noise OGV design processes.

In that perspective, the present manuscript is structured as follows. Chapter 1 is dedicated to the literature review. The main objectives of this chapter are to provide the fundamental knowledge to be able to carry out broadband noise predictions on the RSI mechanism, as well as to clearly define the scope of this study. The principle of axial turbomachines, the main noise sources within a fan stage, as well as the numerous methods to estimate the noise resulting from them are thoroughly presented. This chapter eventually leads to the precise definition of the objectives of the present study and of the associated research strategy.

Chapters 2-4 present the work that has been performed on the ACAT1 fan-stage, which has been experimentally assessed in the framework of the European project TurbonoiseBB. This configuration is representative of a scaled modern turbofan engine, making it a good candidate for in-depth studies on broadband noise predictions within a fan-stage (see section 2.1 for more details on this configuration). A complete analytical and numerical study is carried out on the ACAT1 fan-stage at approach conditions. Chapter 2 first presents the benchmark configuration. The set-ups of the three numerical simulations are then detailed (computational domains, meshes and solvers). The proofs of convergence of the computations are eventually provided along with the flow extractions that have been performed on the simulations. Chapter 3 presents an in-depth aerodynamic analysis of the flow within the ACAT1 fan-stage. The three simulations are directly compared to the experimental data and between each other. The particularities of each simulation are shown and the main flow features are emphasized. Chapter 4 finally presents the noise estimates obtained using both analytical and numerical approaches on the three performed simulations.

Chapter 5 is a comparative study of three of the most advanced analytical models for broadband RSI noise predictions. The main objective is to assess the impact of the multiple assumptions made in the models and quantify their responsiveness to different input parameter modifications. This study has been performed on the Source Diagnostic Test (SDT) case, which is a 22-in fan rig that was experimentally assessed in the framework of the NASA advanced Subsonic Technology Noise Reduction Program.

CHAPTER 1

State of the art

Introduction

As emphasized in the introduction of this study, aircraft engines are responsible for a major part of the noise radiated by an aircraft. It is then of paramount interest to study the multiple sources responsible for this noise production, and especially the rotor-stator interaction noise, which is the dominant noise mechanism. This chapter aims at giving the fundamentals and the theoretical background to understand the aeroacoustic phenomena involved in a complete fan-OGV stage. Its goal is also to identify the available tools to carry out broadband interaction noise studies and to justify the choices made for the present work. This chapter eventually leads to the presentation of the main objectives of the present study and of the research strategy that has been adopted to achieve them.

Contents

1.1 Axial turbomachines

The term turbomachines refers to any device in which an energy transfer either from, or to, a flow of fluid occurs through the action of one or more rotating blade rows [21]. Two main categories of turbomachines can be identified. On the one hand turbines extract the energy from the fluid to produce power by expanding the fluid to a lower pressure. On the other hand compressors or impellers transfer this power to the fluid to increase its pressure. Based on the turbomachine architecture, three subcategories can be identified. When the flow is mainly parallel to the axis of rotation of the turbomachine, the device is categorized as an axial flow turbomachine. When the flow is mainly in a plane perpendicular to the rotation axis, the device is categorized as a radial flow turbomachine. The third category, which is referred to as mixed flow turbomachine, is a hybrid architecture displaying non-negligible components of the through-flow in both radial and axial directions.

Modern turbofan engines are a great example of axial flow architectures that couple compressors and turbines to produce thrust. A generic turbofan architecture is presented in fig. 1.1. In turbofan engines, the inlet flow is first driven by a ducted fan that uses the mechanical energy absorbed by the turbine to accelerate the flow rearwards. Unlike in turbojet engines, the flow is then split into two parts. One part is the core flow (in red), which is first compressed successively in the low-pressure and high-pressure compressors. It then reaches the combustion chamber where it is burnt along with fuel. The resulting high temperature gas mixture then feeds successively the high-pressure and low-pressure turbines where part of the energy produced by the compression and the combustion is recovered to drive the compressor stages. The core flow is finally ejected through the turbine exhaust duct as a hot jet. The second part of the flow is the bypass flow. It is first compressed by the fan, then straightened by the downstream OGV and finally ejected through the exhaust nozzle as a cold jet that surrounds the hot core jet. This part of the flow represents more than 80% of the total mass-flow rate and is the major contributor to the production of thrust.

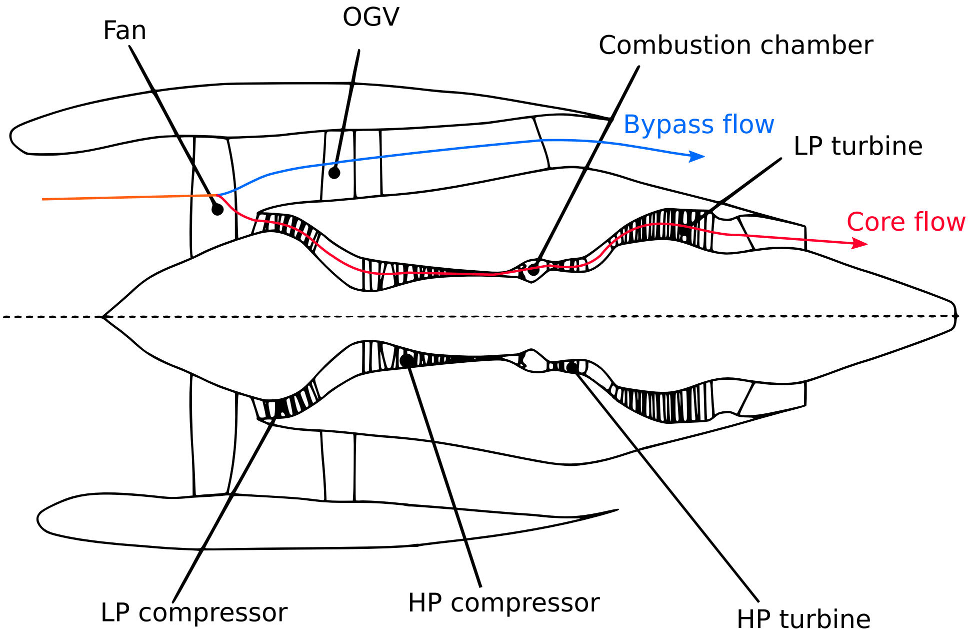

Figure 1.1: Schematic view of a High Bypass Ratio engine.

1.2 Fan noise sources

As highlighted by Lighthill's [16, 17] and Ffowcs Williams and Hawkings' [22] analogies, the fan noise sources can be classified into three categories:

- Monopole sources: they are directly linked to the kinematics of the surfaces. The noise resulting from these sources is usually referred to as thickness noise because it originates from the volume displacement of fluid during the motion of the surfaces.

- Dipole sources: they are due to the interaction of the flow with the solid surfaces. They are mainly attributed to aerodynamic force fluctuations.

- Quadrupole sources: they are due to the flow in the outer region of the surfaces. It characterizes the flow self-turbulence and is often referred to as shear noise in the context of jet flows.

Depending on the Mach number at which the fan is operating, some of these sources can be considered as dominant or negligible. Indeed, monopole and quadrupole sources are significant compared to dipole sources only for rotor tip Mach numbers higher than 0.5 and 0.9, respectively. Additionally, even though dipole sources are always responsible for most of the radiated noise regardless of the operating point, their number can vary with respect to the Mach number as well.

Figure 1.2 shows typical sound power spectra resulting from the previously mentioned sources at approach and take-off operating points. The most salient feature these spectra reveal, is that the noise radiated by a fan stage can be split into two distinct components with different acoustic signatures. One component is the tonal noise, which results from periodic fluctuations of the flow and appears at multiple discrete frequencies. The other component is the broadband noise produced by random fluctuating mechanisms, and more precisely by the interaction of turbulent structures with solid walls. Contrary to the tonal noise, the broadband noise extends continuously over a large range of frequencies. Depending on the operating point, these two components display significantly different behaviors. At approach conditions (fig. 1.2a), the flow is subsonic. The tonal noise is mainly produced by the periodic interaction of the fan wakes with the OGV, creating tones at the Blade Passing Frequency (BPF) and its harmonics. These tones can also be produced on the fan blades by inlet flow distortions that are either due to a non-axisymetric geomety such as a scarfed inlet, or to ingested distortions of the upstream flow such as long coherent structures or side wind effects. At take-off condition, the flow is in transsonic regime at the rotor tip, leading to the creation of shock waves and of the associated tones as seen in fig. 1.2b. Due to small blade-to-blade geometric variations (angles, thickness etc.), the blade-to-blade periodicity of the shocks is broken, which leads to tones at multiples of the rotational shaft frequency instead of the BPF and its harmonics. These tones are named Multiple Pure Tones (MPT) and constitute the so-called *buzz saw noise*, which contributes to the quadrupole noise in transsonic regimes.

The present study focuses on HBR configurations at approach conditions, which implies that all non dipole sources can be neglected (as explained in section 1.4.3). These subsonic dipole sources, summarized in fig. 1.3, are presented in detail in the following sections.

1.2.1 Broadband noise sources

The broadband noise sources for a subsonic operating point are highlighted in blue in fig. 1.3.

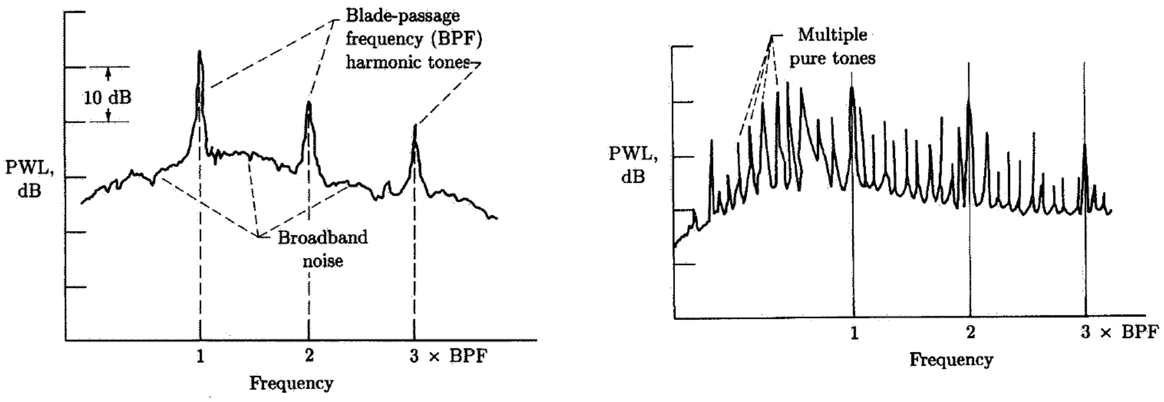

(a) Subsonic case, approach condition.

(b) Supersonic case, take-off condition.

Figure 1.2: Typical sound power spectra of a fan-OGV stage, extracted from [5].

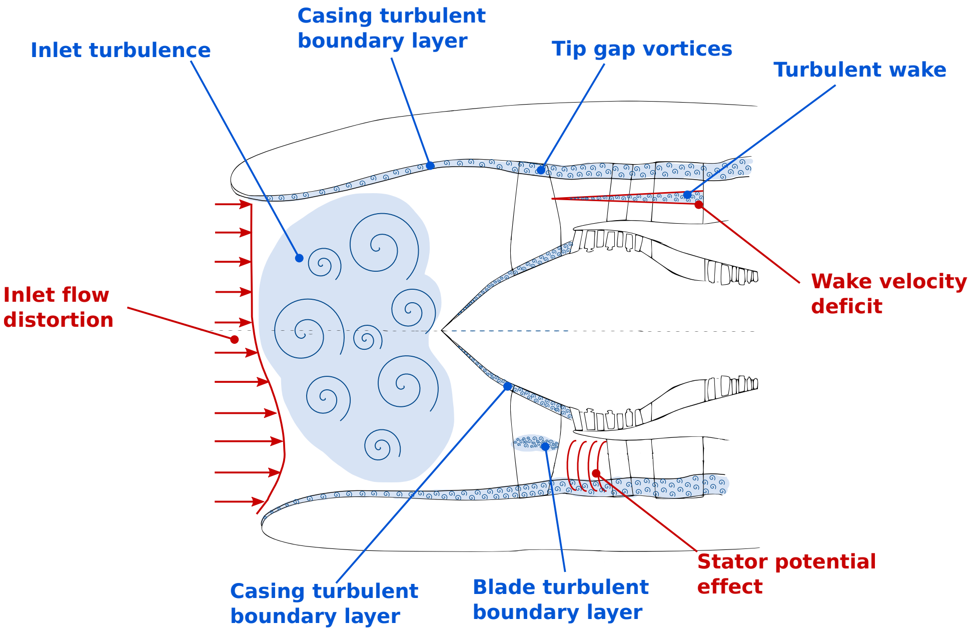

Figure 1.3: Broadband (in blue) and tonal (in red) noise sources of a High Bypass Ratio engine at subsonic flow conditions.

1.2.1.1 Blade/Vane self-noise

The self-noise is mostly linked to the topology and state of turbulence of the boundary layers on the blade pressure and suction sides. For a turbulent boundary layer, the velocity fluctuations are convected down to the trailing edge, which acts like a scattering point where the turbulent kinetic energy encompassed in the boundary layer is converted into acoustic energy. This mechanism is referred to as trailing edge noise [23–30]. In addition to this phenomenon, for off-design operating points, the blades/vanes are operating at higher angles of attack, which sometimes leads to flow separations or recirculation bubbles on the blade suction sides. This mechanism tends to create large turbulent structures that produce broadband noise when they reach the trailing edge, mainly at lower frequencies [31].

1.2.1.2 Wake interaction noise

The rotor wakes, created by the mixing of both the suction and pressure side boundary layers at the trailing edge, are a zone of intense turbulent flows. The turbulent structures within the wakes are then convected by the mean flow down to the stator, impinging onto the vane leading edges and producing random load fluctuations, which creates broadband noise. This noise source has been identified as one of the major contributors to the broadband noise radiated by modern aircraft engines [20], and has been extensively studied both experimentally [32–42] and numerically [12, 13, 43–61] over the past decades. The present study focuses on this mechanism.

1.2.1.3 Turbulence ingestion noise

Atmospheric turbulence can also be responsible for broadband noise production [62, 63]. The turbulent structures in the inlet flow interact with the rotor, inducing load fluctuations with sources mainly located at the rotor blade leading edge.

1.2.1.4 Duct boundary layer noise

At the Reynolds number at which aircraft engines are operating, thick and highly turbulent boundary layers develop on hub and shroud walls. These boundary layers inevitably interact with the fan and the stator and create broadband noise. They also contributes to the tip noise as they interact with the rotor blades in the vicinity of their tip. Duct boundary layer noise has notably been studied by Stephens and Morris [64]. Even though this source is of second order with respect to other mechanism, it is expected to become more important in engines featuring boundary layer turbulence ingestion devices.

1.2.1.5 Tip gap noise

The rotor tip clearance flow results from the pressure gradient between the pressure and suction side at the blade tip. In this region of the flow, a high speed flow exits the gap as a cross-flow jet that is deflected by the surrounding flow and rolls up into one or two vortices: the Tip Leakage Vortex (TLV), created at the rotor leading edge, and the Tip Separation Vortex (TSV), created at mid-chord (see fig. 1.4). The tip vorticies then interact with the outer flow or the near airfoil wall region, creating two highly turbulent shear-layers identified as major mechanisms for broadband self-noise production [65–69]:

- a jet-like flow, which supposedly generates sound when leaving the clearance region either directly or by interacting with the blade tip edge(s). The sound mechanism related to this source is quadrupolar as evidenced in [65]
- the tip vortices, which produce broadband noise through two different mechanisms. On the one hand, the TLV, which induces a scrapping of the tip surface and a diffraction on the pressure side. On the other hand, the TSV, which generates fluctuations that are convected to the blade wall pressure field down to the trailing edge where they are converted into noise following the same mechanism as the trailing edge noise, thus forming a local dipole source that is much more coherent than distributed trailing edge noise.

These two sources are notably responsible for a broadband self-noise production in the form of large broadband humps. These humps correspond to periodic quasi-tonal spectral features that occur at frequencies below the BPF and its harmonics [70, 71]. This quasi-tonal characteristic is mainly due to the mixing of coherent flow structures (the tip gap vortex) with uncorrelated flow structures (the turbulent flow). Depending on the operating point, the tip vortex may interact with the rotor it originated from, the neigboring rotor blades [69], or with the downstream stator with a noise signature at the blade passing frequency harmonics, thus contributing to the RSI noise.

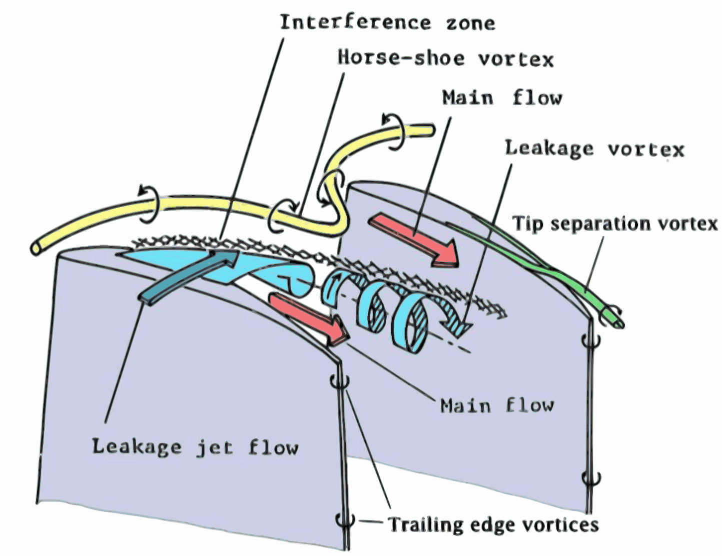

Figure 1.4: Schematic view of the rotor tip clearance flow (extracted from Leitner *et al.* [6]).

1.2.2 Tonal noise sources

The mechanisms responsible for tonal noise production at subsonic flow conditions are highlighted in red in fig. 1.3.

1.2.2.1 Wake interaction noise

The periodic part of the wake interaction noise consists in the impact of the periodical mean velocity deficit induced by the wake structure, onto the the stator row. The velocity deficit can be seen as a virtual envelope separating the wake flow from the background flow. This envelope is considered identical from one blade to another, which implies that the stator vanes are periodically impacted by these envelopes at the BPF and its harmonics. Due to its periodic nature, tonal noise results in narrow peaks in the far-field noise spectrum as seen in fig. 1.2. Similarly to its broadband noise counterpart, this mechanism has been identified as one of the main noise sources in fan-OGV configurations and has been extensively studied in the literature [72–80], and considerably reduced over the past decades.

1.2.2.2 Inflow distortion noise

Tonal noise can also arise from steady inlet flow distortions induced by installation or ground effects. Non axisymmetric inlet geometries can, for instance, create such distortions as evidenced by Daroukh *et al.* [81–83]. These steady distortions interact with the rotor leading edge, where they generate tonal noise at the BPF harmonics.

1.2.2.3 Potential interaction noise

The presence of the stator vane in the flow induces a bending of the streamlines that leads to local steady pressure field distortions. This field distortion is known to decrease quite rapidly in the upstream direction [84], preventing the rotor trailing edge from interacting with it in current engine architectures. However, for future UHBR architectures, the rotor-stator spacing will be significantly reduced to compensate the larger diameter of the engine, leading to an increase in the potential interaction mechanism. In this case, the rotor trailing edge would pass through a periodic potential field imposed by the stator, which would induce load fluctuations on the rotor blade surface that would eventually be converted into tonal noise at the BPF harmonics. Additionally, this mechanism could be even more intensified by the introduction of an heterogeneity in the stator row for structural matters [82, 85].

Fan noise sources — **Summary**

In this section, the main sources of both broadband and tonal noises have been presented. In the case of a fan equipped with thin blades and operating at approach condition, the Mach number is below 0.5, which makes it possible to neglect the monopole and the quadrupole sources. At such low Mach numbers, steady loading noise is also expected to be negligible. The numerous dipole sources, mainly corresponding to aerodynamic force fluctuations on solid walls, have been briefly presented in the case of a subsonic configuration and for both the tonal and the broadband components of the noise. The rotor-stator interaction mechanism has appeared as the dominant broadband and tonal noise source, justifying the need to further study this mechanism.

1.3 Numerical simulation

"Computational Fluid Dynamics" (CFD) is a branch of fluid mechanics that aims at numerically solving the spatially and temporally discretized equations of fluid dynamics. Its reduced costs with respect to experimental investigations, its ability to extract data anywhere in a flow field, as well as the increase in the available computational resources have turned it into a first-hand tool to carry-out fluid dynamics studies on complex flow configurations. Due to the numerous assumptions/approximations that are made within a CFD approach, CFD studies still need to be validated against experimental data, which prevents them from being a stand-alone tool. Indeed, a wide range of CFD methods, with different types of assumptions and modeling choices, exists. This section aims at giving an overview of the state of the art of CFD methods, by putting into perspective the level of flow description of each of them along with their respective computational cost.

1.3.1 Equation of fluid dynamics

Before presenting the different numerical approaches, let us recall the equations they are based on. A compressible fluid is considered. If t, ρ, $\mathbf{u}$, p, τ, E and $\mathbf{q}$ stand for the time, density, velocity vector, pressure, viscous stress tensor, total energy and heat flux vector, respectively, and if the fluid is subject to a net force vector $\mathbf{F}$, and to a volume heat source $\dot{Q}$, the entire motion and thermodynamic behavior of the fluid can be described by the Navier-Stokes equations:

$$\frac{\partial \rho}{\partial t} + \frac{\partial}{\partial x_j}(\rho u_j) = 0 \tag{1.1}$$

$$\frac{\partial (\rho u_i)}{\partial t} + \frac{\partial}{\partial x_j}(\rho u_i u_j + p\delta_{ij} - \tau_{ij}) = \rho F_i \quad i = 1, 2, 3 \tag{1.2}$$

$$\frac{\partial (\rho E)}{\partial t} + \frac{\partial}{\partial x_j}(\rho E u_j + p u_j - \tau_{ij} u_j + q_j) = \rho F_j u_j + \dot{Q} \tag{1.3}$$

Equations (1.1)-(1.3) are the mass conservation equation (or continuity equation), the momentum equation and the total energy equation, respectively. Since the system is composed of fifteen unknowns for five equations, ten closure equations are required to completely describe the fluid. If a perfect gas is considered, its thermodynamic properties can be described through the perfect gas state law:

$$\frac{p}{\rho} = rT, \tag{1.4}$$

where $r = R/M = c_p - c_v$ is the specific mixture gas constant (r = 287.058 m^2.s^{-2}.K^{-1} for air mixture). R is the universal gas constant (R = 8.3145 kg.m^2.s^{-2}.K^{-1}.mol^{-1}) and M the molecular weight of the gas. c_p and c_v are the constant pressure and volume specific heat capacity respectively. They can be considered as constant for calorifically perfect gases such as air. The second closure equation is the Fourier law, which describes the thermal transfer by relating the heat flux $\mathbf{q}$ with the temperature gradient:

$$q_i = -\lambda \frac{\partial T}{\partial x_i} \tag{1.5}$$

where λ is the thermal conductivity of the considered fluid. Finally the Newtonian fluid assumption is usually made and considers that the viscous stresses τ_{ij} are linearly proportional to the local strain rate at each point:

$$\tau_{ij} = \mu \left(\frac{\partial u_i}{\partial x_j} + \frac{\partial u_j}{\partial x_i} \right) - \frac{2}{3}\mu \left(\frac{\partial u_i}{\partial x_i} \right) \tag{1.6}$$

where μ is the dynamic viscosity of the fluid that can be computed thanks to Sutherland's law:

$$\mu(T) = \mu_{ref} \left(\frac{T}{T_{ref}} \right)^{\frac{3}{2}} \frac{T_{ref} + S}{T + S} \tag{1.7}$$

where $\mu_{ref} = 1.711.10^{-5}$ kg.m^2.s^{-1} is the dynamic viscosity at reference temperature T_{ref} = 273.15 K and the constant for air S = 110.4 K is obtained experimentally. The Navier-Stokes equation along with these three state/behavior laws is eventually a complete system, which fully describes the behavior of a compressible Newtonian perfect gas.

1.3.2 Review of the available numerical approaches

The Navier-Stokes equations presented in the previous section are then discretized in time and space. These equations can be solved using multiple numerical approaches, which mainly differ by the way they treat turbulence. Indeed, above a critical Reynolds number, all flows shift from a laminar state to a turbulent state that is characterized by the appearance of non-deterministic fluctuations around mean values for all the flow variables. This chaotic behavior, which is a direct consequence of the nonlinearity of the Navier-Stokes equations, creates a wide range of turbulent scales as shown by the typical isotropic turbulence spectrum depicted in fig. 1.5. Three characteristic length scales can be identified:

- The integral length scale l_I corresponds to the size of the largest and most energetic turbulent structures. These flow structures are those contributing the most to the turbulent kinetic energy. This length scale slowly varies with the Reynolds number, except in the boundary layer.
- The Taylor length scale l_T, also called the Taylor microscale, is the intermediate length scale at which the fluid viscosity starts to significantly affect the dynamics of turbulent eddies in the flow. Eddies with a lower length scale than l_T take part in the dissipation of the kinetic energy into heat.
- The Kolmogorov length scale l_K, which characterizes the size of the smallest turbulent eddies.

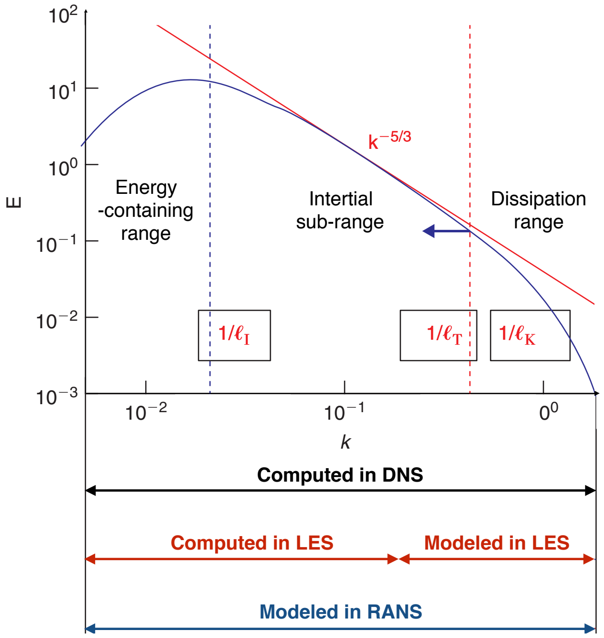

Figure 1.5: Energy spectrum of turbulence in function of wave number k, with indication of the range of application of the DNS, LES and RANS models (adapted from Hirsch [7]).

Based on these three length scales, the turbulence spectrum can be divided into three main zones that follow the energy cascade principle initiated by Richardson, and completed by Kolmogorov's hypotheses (see Pope [86] for more details):

- The energy-containing range: the energy is produced and is contained in large eddies. In this zone, both isotropic and anisotropic eddies can be found since they are influenced by the boundary conditions of the flow.
- In the inertial sub-range, the energy resulting from the breaking-up of the larger structures is transferred successively down to smaller structures. The associated energy spectrum decreases following Kolmogorov's law ($E \sim k^{-5/3}$).
- The dissipation range, closes the cascade process: the energy transferred from the energy-containing range is eventually dissipated into heat by the smallest structure

The two latter ranges form the "universal equilibrium range" because, as argued by Kolmogorov, in this region the main information about the mean flow and the boundary conditions, which are embedded in the large structures, is lost. This leads to a sort of statistical universality in this range, which only contains isotropic eddies. These properties of turbulence make it possible to discriminate the different numerical approaches by sorting them with respect to the range of turbulent eddies they actually capture.

1.3.2.1 Direct Numerical Simulation

The highest level of description of the flow is obtained by using Direct Numerical Simulation (DNS), which directly solves the Navier-Stokes equations. The DNS approach computes all the turbulent scales, from the largest ones in the energy containing zone, down to the smallest dissipation scales (Kolmogorov scale). No modeling of any kind is involved in this method, which means that the only approximations that are made are inherent to the numerical implementation and related to the discretization schemes, the boundary condition implementations or to the structure of the numerical code itself. For such a method, high-order discretization schemes are compulsory to minimize the dissipation and dispersion of the flow structures/waves that are induced by the discretization of the equations. Moreover, it requires dense meshes in which the smallest cells must be at least of the order of magnitude of the Kolmogorov length scale. These two constraints inevitably induce high-computational costs, which can be prohibitive depending on the considered flow configuration. Choi and Moin [87], for instance, have estimated that the required number of grid points for a DNS on a flat-plate would scale as $Re_{L_x}^{37/14}$, where Re_{L_x} is the Reynolds number based on the streamwise extent of the flat plate L_x. For typical Reynolds numbers encountered in fan-OGV stages (see fig. 1.6), this would lead to almost 10^{16} grid points, which is largely out of reach considering the current available computational power. As a consequence, DNS is not suitable for the simulation of a complete fan-OGV stage. It has however been successfully used for canonical cases such as for the simulation of low Reynolds channel flows [88] or for low-pressure turbines [89–93] in which the Reynolds number is significantly lower than in any other engine stages.

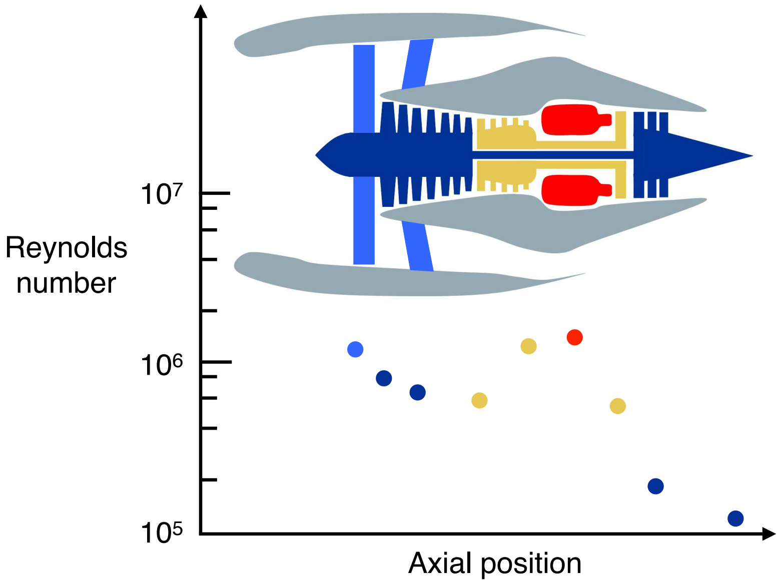

Figure 1.6: Reynolds number variation through an HBR engine (adapted from Tucker *et al.* [8]).

1.3.2.2 Scale resolving approaches: Large Eddy Simulation

In order to be able to simulate turbulent flow configurations with higher Reynolds numbers, a coarser level of description than DNS has to be introduced. As emphasized in the previous section, turbulent flows exhibit a wide range of flow scales that do not equally contribute to the production/transport of the turbulent kinetic energy. The largest structures, both isotropic and anisotropic, produce the energy, whereas the smaller ones, all isotropic and homogeneous, transport this energy and dissipate it. Therefore, one way to simultaneously reduce the computational cost of a turbulence resolving method, and still recover most of the turbulent energy, is to resolve only the largest scales of turbulence while the smaller ones can be more easily modeled since they follow a universal behavior. This idea is at the root of the scale resolving methods, which are usually named Large Eddy Simulations (LES). In practice, large and small structures are splitted either through an explicit spatial filtering of the Navier-Stokes equations, or by an implicit filtering induced by the mesh resolution (see section 1.3.3 for more details on the filtering and the modeling involved in LES). As the small turbulent scales are responsible for such a prohibitive cost for DNS, their modeling (also called sub-grid scale modeling) directly reduces the density of the mesh required for an LES, which significantly reduces its cost with respect to DNS. Indeed, Choi and Moin have estimated that the number of grid points for a wall-resolved LES of a flat-plate scales as $Re_{L_x}^{13/7}$ [87]. For typical Reynolds numbers encountered in a fan-OGV stage (see fig. 1.6), this would lead to a mesh made of 10^{11} points. Even though the reduction of the cost of the simulation with respect to DNS is really substantial, wall-resolved LES remains quite expensive for the present study. One could suggest to coarsen the wall-mesh to increasingly reduce its size and obtain an affordable simulation. This would however produce significantly inaccurate results. Indeed, phenomena such as intense turbulence kinetic energy production, or backward energy transfer, take place in the boundary layer and totally escape the usual sub-grid modeling. Coarsening the mesh would then make the sub-grid modeling inoperative and would produce unreliable results [9]. To overcome this issue, two main robust cost reducing alternatives have been developed:

- Wall-modeled LES (WMLES): by imposing the velocity and velocity gradients values on the wall surface through a model, one can avoid resolving the full boundary layer down to the inner viscous layer. The first mesh point near the surface is usually localized in the logarithmic layer, leading to a drastic reduction of the density of the mesh. Indeed, Choi and Moin have estimated that the number of grid-points required for a wall-modeled LES on a flat-plate scales as Re_{L_x} [87]. Wall-modeled LES then appears as a worth considering tool to carry out turbulence resolving simulations on a fan-OGV stage. The main drawback of such approaches is that an important physical aspect of the flow dynamics is modeled, which adds a source of error to the simulation. This approach has been extensively used for compressors [94], turbines [95–97] and turbofans [43, 44, 98, 99].

- Hybrid RANS-LES approaches: these approaches offer an alternative to alleviate the issue of traditional LES by modeling the flow near the walls with a RANS approach. Many hybrid approaches have been developed such as the so-called Detached Eddy Simulation (DES) developed by Spalart *et al.* [100, 101], which models the flow near the walls with a RANS approach, as far as the flow remains attached to the solid wall. The remaining part of the computational domain is treated with a LES approach. A similar approach has been used by Bonneau *et al.* [102] in the context of a fan-OGV stage.

1.3.2.3 Statistical approaches: RANS-URANS simulations

Simulations using the Reynolds Averaged Navier-Stokes (RANS) equations are the most widely used in the industrial context. In the framework of this approximation, the turbulent equations are averaged over the whole spectrum of turbulent fluctuations, providing a statistically averaged solution to any specific flow configurations. This means that, contrary to DNS or LES, turbulence is completely modeled, from the largest scales to the smallest ones. RANS equations are thus based on a statistical treatment of turbulence that assumes that each flow variable can be decomposed into a mean part and a fluctuating part. The introduction of such a decomposition into the Navier-Stokes equations eventually results in the definition of the Reynolds stress tensor. This tensor is unknown and requires modeling to get a closed system of equations. Based on an analogy with the viscous stress tensor, Boussinesq proposed a closure method that links the Reynolds stress tensor to the strain. Its formulation displays the turbulent viscosity μ_t that constitutes the term on which the modeling focuses to close the RANS system of equation. Many models with different levels of complexity are available. The most widely used models are based on two transport equations to evaluate μ_t. This is the case of the k-ϵ [103], k-ω [104] and k-kl [105] models, which are among the most popular ones even though they resort to significantly stringent hypotheses (isotropic turbulence, equilibrium between turbulence production and dissipation, and the inclusion of constants that are calibrated on canonical configurations). Simpler models with only one transport equation, such as the Spalart-Allmaras model [106], have also been developed but rely on the same main hypotheses. A last category known as Reynolds Stress Models (RSM models) have been developed in order to provide a higher order closure of RANS equations. They aim at modeling each one of the tensor components, which implies an increased computational cost. This also introduces additional unknowns (closure), which are even more difficult to model and to measure. Despite their significant additional cost, the increase in accuracy with respect to simpler models is limited as they are also based on a statistical description of turbulence, which appears to be the most restrictive assumption of the RANS approach.

None of these models have shown to produce reliable flow simulations in all flow configurations. More specifically, in configurations in which the model hypotheses are questionable, such as for turbomachines, the choice of turbulence model may have a significant impact on the results, regarding for instance the potential flow separations or the prediction of the correct level of turbulent kinetic energy.

The classic steady RANS approach provides a time averaged solution of the RANS equations. This method is however not adapted to the simulation of flows exhibiting an intense unsteadiness (*e.g.* the vortex shedding behind a cylinder), as it will not provide a converged solution in such cases. The Unsteady-RANS (URANS) approach, which is basically an extension of the steady RANS approach to obtain a time dependent statistically averaged flow, removes this limitation and it accounts for these phenomena. The unsteadiness that is simulated is however limited to the periodic and deterministic phenomena that are characterized by a particular frequency of occurrence (vortex shedding, rotating blades, tonal noise etc.). The chaotic unsteadiness related to turbulence is still modeled statistically. This method has been extensively used in turbomachines [76, 78, 107–111].

1.3.3 Large Eddy Simulation

The above review of numerical methods has highlighted LES, in its wall-modeled and hybrid forms, as the most adapted approach to carry out turbulence resolving simulations on a fan-OGV stage. The present section is devoted to present in more detail the main principles of LES, with a particular focus on the equations that are solved and on how unresolved turbulent structures are modeled.

1.3.3.1 Main principles

As explained in section 1.3.2, the main principle of LES is to filter out the small dissipative turbulent scales from the flow, and to resolve the larger turbulent structures that contain most of the turbulent kinetic energy. In practice, the filtering step is performed either through an explicit spatial filtering of the Navier-Stokes equations or by the mesh itself that behaves as an implicit filter. The latter point of view will be adopted for the rest of the present study. More precisely, let Δ be the local characteristic length of a grid-cell of dimension $(\Delta_i, \Delta_j, \Delta_k)$ in the directions (i, j, k) such that:

$$\Delta = (\Delta_i \Delta_j \Delta_k)^{1/3} \tag{1.8}$$

The cut-off wavenumber induced by such a mesh is then of the order of:

$$\kappa_c = \frac{2\pi}{\lambda_c} = \frac{\pi}{\Delta}. \tag{1.9}$$

As a consequence, all the turbulent structures with a wavelength larger than λ_c are resolved whereas those with smaller wavelengths, referred to as sub-grid scales, are filtered-out. The mesh then behaves as a low-pass filter in the wave-number domain as illustrated in fig. 1.7. In practice, the cut-off wave-number κ_c must be ideally set between the integral length scale and the Taylor microscale in order to be in the universal equilibrium range. The closer κ_c is from the Taylor microscale, the more accurate the simulation is.

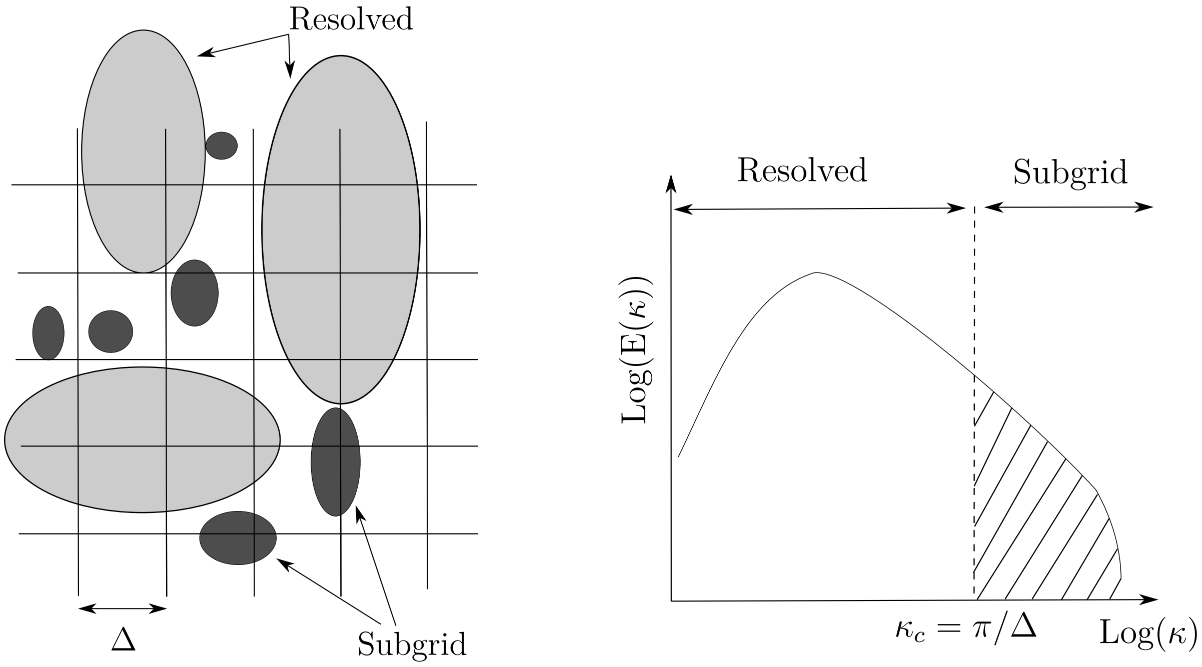

(a) Physical space.

(b) Fourier space.

Figure 1.7: Schematic view of the implicit filtering induced by the mesh : grid and theoretical filters are the same, yielding a sharp cutoff filtering in Fourier space between the resolved and sub-grid scales. [9].

Finally, the LES approach can be divided into two categories, depending on the way it deals with the sub-grid scales:

- Explicit LES approaches in which an extra term referred to as Sub-Grid Scale (SGS) model is introduced to compensate the resolution error induced by the filtering.
- Implicit LES approaches that do not rely on SGS models but compensate the resolution error through the numerical error induced by the chosen numerical method.

The former is further developed in the following sections.

1.3.3.2 Filtered Navier-Stokes equations

The previous section showed that, because of the filtering step, any flow variable ϕ can be split into two parts: a resolved part $\overline{\phi}$, and a modeled part ϕ' so that:

$$\phi = \overline{\phi} + \phi'. \tag{1.10}$$

The filtered compressible Navier-Stokes equations are then deduced by resorting to the Favre decomposition as follows:

$$\phi = \widetilde{\phi} + \phi'' \quad \text{with } \widetilde{\phi} = \frac{\overline{\rho\phi}}{\overline{\rho}} \text{ and } \overline{\rho\phi''} = 0, \tag{1.11}$$

which eventually yields:

$$\frac{\partial\bar{\rho}}{\partial t} + \frac{\partial}{\partial x_j}\left(\bar{\rho}\widetilde{u_j}\right) = 0, \tag{1.12}$$

$$\frac{\partial(\overline{\rho}\widetilde{u_i})}{\partial t} + \frac{\partial}{\partial x_j}\left(\overline{\rho}\widetilde{u_i}\widetilde{u_j} + \bar{p}\delta_{ij} - \overline{\tau_{ij}} - \tau_{ij}^{SGS}\right) = \bar{\rho}F_i, \quad i = 1, 2, 3 \tag{1.13}$$

$$\frac{\partial(\bar{\rho}\widetilde{E})}{\partial t} + \frac{\partial}{\partial x_j}\left(\bar{\rho}\widetilde{E}\widetilde{u_j} + \bar{p}\widetilde{u_j} + \overline{q_j} + q_j^{SGS} - \widetilde{u_i}\widetilde{\tau_{ij}} - \widetilde{u_i}\tau_{ij}^{SGS}\right) = \bar{\rho}F_j\widetilde{u_j}, \tag{1.14}$$

where τ_{ij}^{SGS} is the sub-grid scale stress tensor and $q_j^{SGS}$the sub-grid scale heat flux.

1.3.3.3 Sub-grid scale model

In order to have a solvable system of equations, closure equations need to be provided for τ_{ij}^{SGS} and q_j^{SGS}. These closure equations can be classified into two categories [9]:

- The structural models that compute the sub-grid flow through series expansions of the terms in the filtered equations,
- The functional models that mostly rely on physically based assumptions (energy transfer, local equilibrium).

The latter method is usually presented as the basic approach to deal with the LES equation system closure. In order to reduce the modeling effort, it usually resorts to the so-called turbulent viscosity μ_{SGS}, which is coherent with the fact that sub-grid structures are mostly related to dissipation phenomena [86]:

$$\tau_{ij}^{SGS} = 2\mu_{SGS}\left(\frac{\partial\widetilde{u_i}}{\partial x_j} + \frac{\partial\widetilde{u_j}}{\partial x_i} - \frac{2}{3}\frac{\partial\widetilde{u_k}}{\partial x_k}\delta_{ij}\right), \tag{1.15}$$

$$q_j^{SGS} = \frac{\bar{p}\mu_{SGS}c_p}{P_{rSGS}}\frac{\partial\tilde{T}}{\partial x_j}, \tag{1.16}$$

where the sub-grid Prandtl number is set to $P_{rSGS} = 0.9$ in the case of cold air [112]. The modeling then consists in providing a relationship for μ_{SGS} that faithfully transposes the behavior of the sub-grid scales.

Smagorinsky's model [113] is usually presented as the model that laid the foundation of sub-grid scale modeling. It directly links the turbulent viscosity to the size of the mesh and the resolved (or filtered) rate of strain $\widetilde{S}_{ij} = \frac{1}{2}\left(\frac{\partial \widetilde{U}_i}{\partial x_j} + \frac{\partial \widetilde{U}_j}{\partial x_i}\right)$:

$$\mu_{SGS} = l_s^2 \|\widetilde{S}\| = \bar{\rho}\left(C_s\Delta\right)^2 \|\widetilde{S}\|, \tag{1.17}$$

$$\|\tilde{S}\| = \sqrt{2\widetilde{S}_{ij}\widetilde{S}_{ij}}. \tag{1.18}$$

$l_s = C_s\Delta$ is the Smagorinsky length scale, which is taken to be proportional to the filter width Δ (which is the size of a mesh cell) through the Smagorinsky coefficient C_s. Under the assumption that the turbulence is homogeneous, isotropic and that an equilibrium is reached between the production and the dissipation of turbulence, this constant can be set to $C_s = 0.18$ [114]. It has however been shown that in the presence of shear-layers, this model is highly dissipative and tends to be inaccurate in predicting the transition to turbulence [115]. In near-wall region for intance, $\|\tilde{S}\|$ significantly increases because of the significant mean velocity gradient, inducing a non-zero turbulent viscosity in near-wall regions where turbulent fluctuations are actually damped for real flows. In order to force a zero μ_{SGS} in near-wall regions, the exponential damping function of Van Driest [116] has been widely used in early LES studies. However, it requires the use of a lower Smagorinsky constant and does not produce the proper near-wall scaling for the eddy-viscosity. More sophisticated models providing a new relationship for μ_{SGS} based on Smagorinsky's model have also been developed. This is the case of Lévêque *et al.* [117] who enhanced the Smagorinsky model by substracting the magnitude of the mean resolved rate of strain $\|\langle\bar{S}\rangle\|$ to Smagorinsky's ν_{SGS} relationship to build the shear-improved Smagorinsky model (SISM):

$$\nu_{SGS} = \left(C_s\Delta\right)^2 \left(\|\bar{S}\| - \|\langle\bar{S}\rangle\|\right). \tag{1.19}$$

This model has been successfully applied in several turbomachinery studies [11, 69, 118], proving its robustness in presence of wall bounded flows with respect to the classical Smagorinsky model. Other models based on a directional weighting of the strain-rate have also been found to appropriately model the SGS in regions of strong shear and or anisotropy [119]. Dynamic Smagorinsky models, which locally compute a Smagorinsky coefficient on each grid point depending on the the flow physics, have also been developed [120].

Another drawback of the Smagorinsky model is the fact that it only relies on the strain rate of the turbulent structures and not on their rotational rate. Indeed, as indicated by Hunt *et al.* [121, 122], turbulent flows can be decomposed into three types of zones that do not contribute to the same extent to the dissipation of the energy: the stream region (relatively fast, not very curved, not diverging or converging strongly) contains the energy, while the energy dissipation is concentrated in the eddy zones (strong swirling flow with vorticity) and the convergence zones (irrotational straining motion with strong convergence and divergence of streamlines). As a consequence, models based merely on the strain rate of the turbulent structures are a good measure of the dissipative activity only in the convergence zone. Taking into account the rotational rate would then enable to compute more precisely the dissipative behavior of the sub-grid scales. This is the main idea lying behind the Wall-Adapting Local Eddy-viscosity (WALE) sub-grid scale model from Nicoud and Ducros [123], who proposed a model that makes use of the deviatoric part of the square of the velocity gradient tensor S_{ij}^d, which also depends on the anti-symmetric part that is linked to vorticity:

$$\mu_{SGS} = (C_w \Delta)^2 \frac{\left(S^d_{ij} S^d_{ij}\right)^{\frac{3}{2}}}{\left(\tilde{S}_{ij}\tilde{S}_{ij}\right)^{\frac{5}{2}} + \left(S^d_{ij} S^d_{ij}\right)^{\frac{5}{4}}}, \tag{1.20}$$

$$S^d_{ij} = \frac{1}{2}\left(\widetilde{g_{ij}}^2 - \widetilde{g_{ji}}^2\right) - \frac{1}{3}\delta_{ij}\widetilde{g}^2_{kk} \text{ and } \widetilde{g}^2_{ij} = \frac{\partial \widetilde{u_i}}{\partial x_k}\frac{\partial \widetilde{u_k}}{\partial x_j}, \tag{1.21}$$

where the recommended value for the WALE constant is around $C_w = 0.5$. Using this approach, the model complies with the cubic decrease of the sub-grid scale viscosity μ_{SGS} with the wall distance, which was not the case of the Smagorinsky model. The main drawback of the WALE model is that the turbulent viscosity does not vanish in the particular case of solid rotation, as it should. The σ-model, developed by Nicoud *et al.* [124] as an extension of the WALE model, corrects this issue.

Numerical simulations ——— Summary

The main available numerical simulation approaches have been presented. They mainly differ by their level of description of the flow, which can be measured through the way they deal with turbulence:

- Direct Numerical Simulation : resolves all the turbulent structures from the largest turbulent structures (characterized by the integral length scale) producing the flow energy, to the smallest (characterized by the Kolmogorov length scale), which dissipate this energy.
- Large Eddy Simulation: only resolves the large turbulent structures of the flow and models the non-resolved ones through the use of a sub-grid scale model that reproduces their universal behavior. Three sub-categories of the LES approach have been presented: the wall-resolved LES (standard approach), the wall-modeled LES, the hybrid RANS-LES approach.
- (U)RANS: is the most widely used approach for flow computations. It provides a statistical average of the flow solution in which all the turbulent structures are modeled. The Unsteady RANS approach (URANS) enables to take into account additional deterministic phenomena. All the stochastic phenomena related to turbulence remain modeled.

The relative cost of each method has been estimated for the typical range of Reynolds numbers that can be encountered in a fan-OGV stage. This process has revealed that only the URANS, the hybrid RANS-LES and the wall-modeled LES are reasonable candidates for performing simulations on a complete fan-OGV stage. Moreover, only the two latter methods can be used in order to get unsteady information about the turbulent state of the flow, since the stochastic behavior of the turbulence is only partly modeled contrary to the URANS method. Finally the LES approach has been described in more details, with a particular emphasis on the filtering and sub-grid scale modeling steps. A non-exhaustive list of sub-grid scale models have been presented with their respective assets and drawbacks.

1.4 Fan broadband noise prediction methods

1.4.1 Introduction

As emphasized in section 1.2, the broadband RSI noise accounts for a major part of the noise radiated by an aircraft engine, at subsonic operating points.. As a consequence, it has been the subject of extensive research studies over the past decades with two concomitant objectives: to understand the underlying physics in the RSI mechanism and to develop new tools and approaches in order to predict the subsequent noise. This has led to a wide range of methods that can be gathered into two main categories:

- Analytical/Semi-analytical approach: each model endeavors to describe the noise resulting from the interaction of turbulent structures (wake and background turbulence) with a vane cascade. Some of these models are empirical [125, 126], but the present study exclusively focuses on physics based models, which basically aim at modeling the noise sources resulting from the RSI mechanism, and use them in the framework of some form of acoustic analogies. These models rely on a set of hypotheses on the fan-OGV stage geometry, the duct geometry and the flow conditions which aim at simplifying the problem, and which enable its solving through purely analytical methods[1], or numerical methods[2]. These assumptions inevitably affect the accuracy of the method but drastically reduce its computational cost, in comparison with fully numerical predictions, making it a first-hand tool to quickly provide noise estimates and carry out optimization studies, especially in the industrial context. Moreover, this approach is particularly adapted for studies that need to isolate the RSI mechanism in order to quantify its relative contribution to the total radiated noise, as will be discussed in the present dissertation.
- Numerical approach : only a limited number of assumptions, significantly less stringent than those made for analytical models, are made for fully numerical predictions. This makes it possible to take into account complex geometrical features and realistic flows when solving of acoustic generation and propagation equations. Nevertheless, this enhanced accuracy is counterbalanced by an increased computational cost that is variable depending on the type of numerical approach. Computational techniques for flow-generated sound[3] can be classified into two categories [128]:
  - Direct noise simulation: the direct approach computes the sound together with its fluid dynamic source field by solving the compressible flow equations. Depending on the desired level of description of turbulence, multiple simulation methods (DNS, LES, Hybrid RANS-LES) can be used to compute both the broadband noise sources and the acoustic field. The computational domain of such approach must be large enough to include the sources of interest and, at least, part of the acoustic near-field when computing the far-field is inconceivable in terms of computational resources. The computation of the acoustic field requires high-order low dissipative and low dispersive numerical schemes, associated with minimal reflections from the domain boundaries. When only the acoustic near-field is available, the extension to the acoustic far-field is then handled by analytical or numerical techniques (see section 1.4.5.1 for more details).
  - Hybrid noise simulation: hybrid approaches decouple the computation of the flow from the computation of sound. These methods are generally a two-step process

---

[1] Such as the the Wiener-Hopf method used by Glegg [127], Hanson [49] and Posson [12] (see section 1.4.4).

[2] Such as the collocation method used by Ventres *et al.* [45].

[3] Also regrouped under the label CAA, which stands for Computational Aero-Acoustics.

that separates the computation of the acoustic sources, performed through the use of a numerical simulation, from the propagation, achieved using an acoustic analogy. Because of the use of acoustic analogies, the hybrid approach assumes only a one-way coupling of the aerodynamic with the acoustic parts of the flow: the unsteady flow generates sound and modifies its propagation, whereas the sound does not affect the aerodynamic behavior of the flow. This assumption is fairly justified for low Mach number flows but is questionable for transsonic regimes for which compressible effects such as shock waves must be considered in a two-way coupling approach (see section 1.4.5.2 for more details on the hybrid approach).

The approaches mentioned in this section have different levels of description of the flow/sound, different computational costs and finally, different processes to compute the broadband noise generated by the RSI mechanism. The aim of the following sections is to present all these methods in more details, in order to have a better overview of their respective capability, and to be able to choose the best suited tools for the RSI broadband noise predictions of the present study.

1.4.2 Propagation in an annular duct

The numerous prediction methods presented in the following sections are based on different types of propagation techniques. This is especially the case for analytical models: some of them use a free-field radiation whereas others consider an in-duct propagation. The present section presents the specific features related to the propagation of acoustic waves in an annular duct with the aim of emphasizing the fundamental differences with free-field propagation conditions.

1.4.2.1 Solution of the wave equation in a duct with a mean axial flow

Let us consider an annular duct of axis x, an inner radius R_{hub} and an outer radius R_{casing}. Any point inside the duct can be described in the cylindrical coordinate system so that $\mathbf{x_d} = (x, r, \theta)$, where r and θ are the radial and azimuthal coordinates, respectively. The pressure field in a hard-walled annular duct in the presence of a uniform axial mean flow $\mathbf{U} = (U, 0, 0)$ follows the convected wave equation:

$$\left[\Delta - \frac{1}{c_0^2}\frac{\mathrm{D}^2}{\mathrm{D}t^2}\right] \quad p\left(\mathbf{x}_d, t\right) = 0, \tag{1.22}$$

where c_0 is the speed of sound of the medium, $\frac{D}{Dt} = \frac{\partial}{\partial t} + U\frac{\partial}{\partial x}$ and the Laplacian operator in cylindrical coordinate is:

$$\Delta = \frac{\partial^2}{\partial x^2} + \frac{\partial^2}{\partial r^2} + \frac{\partial}{r\partial r} + \frac{\partial^2}{r^2\partial\theta^2}. \tag{1.23}$$

Additionally, a slip boundary condition is considered at the inner (hub) and outer (casing) surfaces of the duct:

$$\frac{\partial}{\partial r}p\left(\mathbf{x}_d, t\right) = 0 \text{ for } r = R_{hub} \text{ and } r = R_{casing}. \tag{1.24}$$

Equation (1.22) can then be rewritten as follows:

$$\left[\beta^2\frac{\partial^2}{\partial x^2} + \frac{\partial^2}{\partial r^2} + \frac{\partial}{r\partial r} + \frac{\partial^2}{r^2\partial\theta^2} - \frac{2M}{c_0}\frac{\partial^2}{\partial x\partial t} - \frac{1}{c_0^2}\frac{\partial^2}{\partial t^2}\right] p(\mathbf{x}_d, t) = 0, \tag{1.25}$$

where $M = U/c_0$ corresponds to the Mach number and $\beta^2 = 1 - M^2$.

It can be shown (see appendix A for a complete derivation of the equations) that the solution of this equation can be expressed as follows:

$$p\left(x, r, \theta, t\right) = \sum_{m \in \mathbb{Z}} \sum_{\mu \in \mathbb{N}} E_{m,\mu}\left(r\right) \mathrm{e}^{-i\omega t + ik^{\pm}_{x,m\mu}x + im\theta}. \tag{1.26}$$

$E_{m,\mu}$ is defined as a linear combination of Bessel functions:

$$E_{m,\mu}(r) = A_{m,\mu} J_m\left(\chi_{m,\mu} r\right) + B_{m,\mu} Y_m\left(\chi_{m,\mu} r\right), \tag{1.27}$$

where J_m and Y_m are the Bessel functions of first and second kind respectively, and $\chi_{m,\mu}$ are the duct eigenvalues that verify the following boundary conditions:

$$\frac{\partial E_{m,\mu}}{\partial r} = 0, \quad \text{for } r = R_{hub} \text{ and } r = R_{casing}. \tag{1.28}$$

ω is the angular frequency, m and μ are the azimuthal and the radial order, respectively, of the duct mode (m, μ) and $k^{\pm}_{x,m\mu}$ are the axial wave number of the duct mode (m, μ) propagating upstream $(+)$ and downstream $(-)$, defined as:

$$k^{\pm}_{x,m\mu} = \frac{-Mk_0 \mp \kappa_{m,\mu}}{\beta^2}, \tag{1.29}$$

$$\kappa^2_{m,\mu} = k_0^2 - \beta^2 \chi^2_{m,\mu}, \tag{1.30}$$

$$k_0 = \frac{\omega}{c_0}. \tag{1.31}$$

1.4.2.2 Duct cut-off condition

The latter section has revealed that, depending on the sign of $\kappa^2_{m,\mu}$, not all the modes propagate in the duct:

- if $k_0^2 > \beta^2\chi^2_{m,\mu}$, $\kappa_{m,\mu}$ is real, and consequently the term $k^{\pm}_{x,m\mu}$ in the phase term $e^{ik^{\pm}_{x,m\mu}x}$ will be real as well. The mode is then propagating with no attenuation and is referred to as cut-on.

- if $k_0^2 < \beta^2\chi^2_{m,\mu}$, $\kappa_{m,\mu}$ is an imaginary number, and consequently the term $k^{\pm}_{x,m\mu}$ in the phase term $e^{ik^{\pm}_{x,m\mu}x}$ will be complex. This creates a real term $e^{-\|\mathrm{Im}(k^{\pm}_{x,m\mu})\|x}$, where Im() designates the imaginary part of the number in parentheses. This form implies that the wave is decaying in the direction of propagation. The corresponding mode is then classified as being cut-off and is often designated as an "evanescent wave".

The decay of cut-off modes is an important feature of duct acoustics because it limits the number of acoustic modes that will propagate from a source to a duct exit, where they can radiate to the acoustic far field. Indeed, the rate of decay of the cut-off modes is not the same for every couple of values (m, μ). It depends on the value of the cut-off ratio, which is defined as $\alpha_{m,\mu} = \beta\chi_{m,\mu}/k_0$. If $\alpha_{m,\mu} \gg 1$, $\|\mathrm{Im}(k^{\pm}_{x,m\mu})\|$ is large, which implies that the amplitude of the mode (m, μ) decays to zero over a distance that is a fraction of an acoustic wavelength. However if $\alpha_{m,\mu} \approx 1$ and $\alpha_{m,\mu} > 1$, then the modes are only close to cut-off and their rate of decay is much smaller. This implies that if the source that produces the latter mode is not far enough from the duct exit, it is expected to radiate into the far-field once it reaches the edge of the duct [10]. This means that the propagation properties of an acoustic mode are determined by the duct geometry, the source position in the duct and the flow convection velocity, indicating a radiation process that is radically different from the free-field propagation. This property of the duct has been extensively exploited in the engine design process to cut-off the first modes at the BPF, which significantly reduced the radiated tonal noise. For broadband noise however, these noise reduction concepts are not as easily applicable. Therefore, the noise sources have to be directly addressed.

1.4.3 Acoustic analogy

As mentioned in the introduction of this section, both analytical and numerical approaches rely on the use of acoustic analogies. The aim of the present section is to present the principles of the acoustic analogy, starting from the Navier-Stokes equations and then developing its main principles with a particular focus on specific analogies that are used in the present study.

1.4.3.1 Principle of acoustic analogies: Lighthill's acoustic analogy

Aeroacoustics, as the science describing the sound generated by flows, is an integral part of fluid dynamics, which means that it is fully described by the set of equations presented in section 1.3.1. In addition to the inherent complexity of this system of non-linear equations, acoustics accounts for only a small part of the energy embedded in a flow, with pressure fluctuations displaying Root-Mean-Square (RMS) values that are several orders of magnitude smaller than the hydrodynamic pressure fluctuations due to turbulence [129]. Aeroacoustic studies are therefore inevitably challenging, especially those using the direct numerical approach, and require sophisticated and adapted tools to be carried out.

In order to tackle the complexity related to aeroacoustic phenomena, Lighthill [16, 17] came up with the concept of acoustic analogy for the noise generated by turbulence. The idea is to restate the full equations of gas dynamics as an equivalent wave equation in a homogeneous medium at rest (or in uniform motion), by adopting the point of view of a distant observer, in order to take some benefits from the formal simplicity of classical linear acoustics.

More specifically, let us consider an unsteady flow field localized in a limited part of a large volume of fluid. Outside of this fluctuating region, the medium is assumed at rest and uniform with a speed of sound c_0 and a mean flow density ρ_0.
In the case of a medium at rest with no acoustic sources, nor external forces, and no heat sources, the propagation of sound is governed by the homogeneous wave equation:

$$\frac{\partial^2 \rho'}{\partial t^2} - c_0^2 \frac{\partial^2 \rho'}{\partial x_i^2} = 0, \tag{1.32}$$

where $\rho' = \rho - \rho_0$ is the density fluctuation. However, this equation is no longer valid when adding the localized fluctuating flow. The full Navier-Stokes equations should be used instead, without body forces ($\mathbf{F} = \vec{0}$) nor heat source ($\dot{\mathbf{Q}} = \vec{0}$). Taking the time derivative of the continuity equation (eq. (1.1)) and subtracting the divergence of the momentum equation (eq. (1.2)) yields:

$$\frac{\partial^2 \rho}{\partial t^2} - \frac{\partial^2 \left(\rho u_i u_j\right)}{\partial x_i \partial x_j} = -\frac{\partial^2 (-p\delta_{ij} + \tau_{ij})}{\partial x_i \partial x_j}. \tag{1.33}$$

By subtracting each side of the equation by $c_0^2 \frac{\partial^2 \rho}{\partial x_i \partial x_i}$, and after rearranging the equation to form a wave operator on the left-hand side of the equation, one finally obtains Lighthill's equation:

$$\frac{\partial^2 \rho}{\partial t^2} - c_0^2 \frac{\partial^2 \rho}{\partial x_i \partial x_i} = \frac{\partial^2 T_{ij}}{\partial x_i \partial x_j}, \tag{1.34}$$

where $T_{ij} = \rho u_i u_j + \left(p - c_0^2\rho\right)\delta_{ij} - \tau_{ij}$ is the so-called Lighthill's stress tensor. It should be noted that c_0 is the speed of sound of the medium at rest surrounding the unsteady flow region, and is different from the local speed sound. Additionally, when considering a pure acoustic problem, this equation reduces to the homogeneous wave equation at large distances from the flow since all the right-hand side terms are negligible for small amplitude acoustic wave and isentropic propagation.

It should be noted that this equation is exact and includes all the aeroacoustic phenomena. It can indeed be reinterpreted as a wave equation in which the double divergence of Lighthill's stress tensor appears as a quadrupole source term. There is thus an analogy between the density fluctuations that would arise from a real flow, and the ones that would result from a quadrupole source distribution of strength T_{ij} in a fictitious non-moving acoustic medium with sound speed c_0. This interpretation must however be done with care because the right-hand side term cannot be considered as a real source since it contains the acoustic field to be determined. To overcome this problem, one should consider the left-hand terms from the observer's point of view while the right-hand term is limited to the source region. This approach, in conjuction with some assumptions regarding Lighthill's stress tensor to turn this source term into an exploitable one[4], makes it possible to solve this equation explicitly. Once this step has been performed, the density fluctuations can be obtained using the Green's function technique to solve Lighthill's equation:

$$\rho'(\mathbf{x}, t) = \frac{1}{c_0^2} \int_{-\infty}^{+\infty} \iiint_{V(\tau)} \frac{\partial^2 T_{ij}}{\partial y_i \partial y_j}(\mathbf{y}, \tau) G_0(\mathbf{x}, t|\mathbf{y}, \tau) \mathrm{d}V(\mathbf{y}) \mathrm{d}\tau, \tag{1.35}$$

where $G_0(\mathbf{x}, t|\mathbf{y}, \tau)$ is the free-field Green's function in a medium at rest defined as

$$G_0(\mathbf{x}, t|\mathbf{y}, \tau) = \frac{\delta\left(t - |\mathbf{x} - \mathbf{y}|/c_0 - \tau\right)}{4\pi|\mathbf{x} - \mathbf{y}|}, \tag{1.36}$$

which is the solution of the inhomogeneous wave equation with an impulse point source located at position $\mathbf{y}$ and triggered at time τ:

$$\left[\frac{1}{c_0^2}\frac{\partial^2}{\partial \tau^2} - \frac{\partial^2}{\partial y_i^2}\right] G_0(\mathbf{x}, t|\mathbf{y}, \tau) = \delta(\mathbf{x} - \mathbf{y})\delta(t - \tau). \tag{1.37}$$

In eq. (1.35), $\mathbf{x}$ and $\mathbf{y}$ correspond to the coordinates of the observer and the sources respectively. The volume V is the volume that encloses the source region (see fig. 1.8)

1.4.3.2 Goldstein's acoustic analogy

Equation (1.35) is the final result of Lighthill's acoustic analogy. This analogy appears to be quite suited to modeling the noise radiated by free-field turbulence (*e.g.* jet mixing noise) under Lighthill's hypotheses but not to all free-field sources (*e.g.* noise radiated by shear-layer instabilities, Mach waves or jet screech feedback tones). Furthermore, this form of acoustic analogy does not address directly the problem of physical boundaries. This could be partly overcome by including a suitable Green's function to replace G_0. These Green's function are usually referred to as "Tailored Green's functions". They can be analytically obtained for some canonical cases such as the propagation in the presence of a thin half-plane [131], or in the

---

[4] One common assumption is to consider a high Reynolds, low Mach number flow, in which mechanical effects (*i.e.* mixing of fluid) dominate. These hypotheses make it possible to neglect the thermal mixing source term $\left(p - c_0^2\rho\right)\delta_{ij} = \left(p' - c_0^2\rho'\right)\delta_{ij}$ (as the flow can be considered isentropic), the viscous stress τ_{ij}, which reduces Lighthill's stress tensor to $T_{ij} = \rho_0 U_i U_j$, $\boldsymbol{U}$ being the velocity field $\boldsymbol{u}$ cleaned of its acoustic part. In this case, Lighthill's analogy recovers the classic result of Chu and Kovásznay [130] indicating that non-linear aerodynamic interactions induce density fluctuations at lower order of magnitude, which propagates as sound.

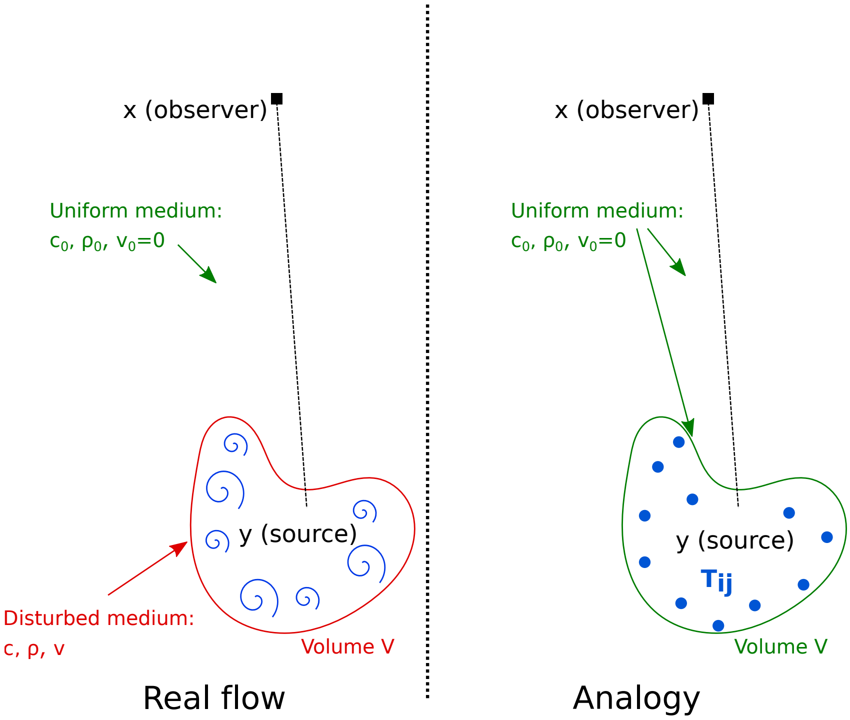

Figure 1.8: Illustration of the the principle of Lighthill's acoustic analogy (adapted from Daroukh [10]).

presence of a duct [132] (see section 1.4.3.2). However, for more complex cases such as the geometry of a complete ducted fan-OGV stage, with twisted rotating blades, the tailored Green's function can only be computed numerically, which considerably increases the CPU cost of such methods. Another possible track to investigate such complex cases is to replace the surfaces by additional equivalent sources. Such investigations have notably been carried out by Curle [133] and by Ffowcs Williams and Hawkings (FW-H) [22], who extended Lighthill's analogy [16, 17] to account for fixed solid boundaries, and moving boundaries with mean axial flow respectively. Goldstein [132] generalized FW-H's analogy to arbitrary Green's functions and applied it to take into account an annular duct geometry in the presence of moving boundaries. This latter analogy, also called Goldstein's analogy, is particularly adapted for fan noise studies. It has been extensively used by Ventres *et al.* [45] and by Posson *et al.* [12, 46, 48] for analytically based broadband noise predictions, and by Arroyo *et al.* [44] in the frame of an LES-hybrid numerical approach. However, the FW-H analogy has been so far even more used than Goldstein's analogy in this context [43, 44, 73, 98], but since it can be seen as a simpler case of Goldstein's analogy (no mean flow or duct walls), only Goldstein's analogy is presented in this section, which describes the main steps to obtain it. It is based on both Goldstein's [132] and Glegg and Devenport's books [134].

1.4.3.2.1 Acoustic analogy for a moving medium

The first step to obtain the relationship of Goldstein's analogy is to solve Lighthill's equation for a uniformly moving medium. Let us consider a ducted rotor-stator configuration of axis y_1, y_2 and y_3 being the two other coordinates. By introducing the following coordinate transformation:

$$\tilde{y}_i = y_i - \delta_{1i} U \tau, \qquad (1.38)$$

with U the axial constant velocity of the flow, the problem is transformed from a uniformly moving medium problem, to a stationary medium problem. Considering that the acoustic propagation is governed by a stationary-medium wave equation in the $\tilde{y}$ reference frame, it should be possible to use Lighthill's equation in this coordinate system to describe the sound radiated by a localized source region embedded in a uniform flow. Given that the momentum and continuity equations used to obtain Lighthill's equation are invariant under Galilean transformation, as given by eq. (1.38), Lighthill's equation can be rewritten in the moving reference frame as follows:

$$\frac{\partial^2 \rho'}{\partial \tau^2} - c_0^2 \frac{\partial^2 \rho'}{\partial \tilde{y}_i \partial \tilde{y}_i} = \frac{\partial^2 \tilde{T}_{ij}}{\partial \tilde{y}_i \partial \tilde{y}_j}, \tag{1.39}$$

where

$$\tilde{T}_{ij} = \rho \tilde{v}_i \tilde{v}_j + \delta_{ij}[(p - p_0) - c_0^2(\rho - \rho_0)] - \tau_{ij}, \tag{1.40}$$

τ_{ij} being the (i,j)th component of the viscous stress tensor, and the subscript 0 indicating the mean of the considered variable. $\tilde{T}_{ij}$ is Lighthill's tensor expressed in terms of the velocity

$$\tilde{v}_i = v_i - \delta_{1i} U, \tag{1.41}$$

measured in the $\tilde{y}$ reference frame. Here, $\rho' = \rho - \rho_0$.

As stated by Goldstein [132], it is more convenient to solve this equation in the fixed reference frame y_i while keeping the moving-frame velocities. This leads to the following equation:

$$\frac{D_0^2 \rho'}{D\tau^2} - c_0^2 \frac{\partial^2 \rho'}{\partial y_i \partial y_i} = \frac{\partial^2 \tilde{T}_{ij}}{\partial y_i \partial y_j} \tag{1.42}$$

where

$$\frac{D_0}{D\tau} \equiv \frac{\partial}{\partial \tau} + U \frac{\partial}{\partial y_1}. \tag{1.43}$$

This equation can be solved by introducing the convected Green's function G_{mov}:

$$G_{mov}(\mathbf{x}, t \mid \mathbf{y}, \tau) = \frac{\delta\left(\tau - t + R_e/c_0\right)}{4\pi R_s}, \tag{1.44}$$

where:

$$\begin{aligned} R_s^2 = (x_1 - y_1)^2 + \beta^2 \left[(x_2 - y_2)^2 + (x_3 - y_3)^2\right] \quad & \beta = 1 - M^2 \\ R_e = \tfrac{1}{\beta^2}\left[R_s - M\left(x_1 - y_1\right)\right] \quad & M = U/c_0, \end{aligned}$$

which is the solution of the uniformly moving-medium wave equation:

$$\left(\frac{1}{c_0^2}\frac{D_0^2}{D\tau^2} - \frac{\partial^2}{\partial y_i \partial y_i}\right) G_{mov}(\mathbf{x}, t|\mathbf{y}, \tau) = \delta(\mathbf{x} - \mathbf{y})\delta(t - \tau). \tag{1.45}$$

Let us assume that eqs. (1.42) and (1.45) are verified in a volume region of space $\nu(\tau)$ that is bounded by a set of solid surfaces $S(\tau)$ moving at speed $\mathbb{V}_s$ with a unit normal $\mathbf{n}$ (pointing outward from ν).

Following a different methodology than Ffowcs Williams and Hawkings [22], Goldstein solved this equation using the Green's function method considering a uniformly moving medium, which after some algebra detailed in [132] leads to the following solution for the density fluctuations:

$$\begin{aligned}\rho'(\mathbf{x},t) = \frac{1}{c_0^2}\int_{-T}^{T}\int_{\nu(\tau)} \tilde{T}_{ij}\frac{\partial^2 G_{mov}(\mathbf{x},t|\mathbf{y},\tau)}{\partial y_i \partial y_j} d\mathbf{y} d\tau \\ +\frac{1}{c_0^2}\int_{-T}^{T}\int_{S(\tau)} F_i \frac{\partial G_{mov}(\mathbf{x},t|\mathbf{y},\tau)}{\partial y_i} dS(\mathbf{y}) d\tau \\ +\frac{1}{c_0^2}\int_{-T}^{T}\int_{S(\tau)} \rho_0 \mathbb{V}_n' \frac{D_0 G_{mov}(\mathbf{x},t|\mathbf{y},\tau)}{D\tau} dS(\mathbf{y}) d\tau\end{aligned} \tag{1.46}$$

where T is a very large finite interval of time, and

$$\mathbb{V}_n' = (\mathbb{V}_s - \mathbf{i}U)\cdot\mathbf{n} = \mathbb{V}_n - n_1 U. \tag{1.47}$$

Equation (1.46) recovers the same three contributions as those already observed in Ffowcs Williams and Hawkings' equation:

- The first volume integral represents the generation of sound by a volume distribution of quadrupole sources in the limited area enclosing the sources.

- The second term can be seen as the loading noise, produced by the exertion of a net unsteady force F on the fluid, and can be assimilated to a surface dipole source distribution.

- The last term corresponds to the thickness noise resulting from the unsteady volume displacement effects of the surface. It is equivalent to a surface distribution of monopoles.

1.4.3.2.2 Green's function for annular ducts with a uniform flow

In the previous section, the extension of Lighthill's acoustic analogy to uniformly moving medium containing moving surfaces has been presented. This analogy is well adapted to propellers or open-rotors noise prediction but still needs some improvements to be used in the context of ducted fans. To do so, another Green's function G_{duct}, which takes into account both the annular duct hard walls and the convective effect, needs to be derived. This can be achieved by solving eq. (1.45) with the following boundary conditions:

$$\frac{\partial G_{duct}}{\partial n} = 0, \quad \text{for } r = R_{hub} \text{ and } r = R_{casing} \tag{1.48}$$

As detailed in [132], the solution can be obtained using the separation of variables technique, which leads to the following equation:

$$G_{duct}(\mathbf{x},t|\mathbf{y},\tau) = \frac{i}{4\pi}\sum_{m=-\infty}^{+\infty}\sum_{\mu=0}^{+\infty}\frac{\Psi_{m,\mu}(r_x,\theta_x)\overline{\Psi}_{m,\mu}(r_y,\theta_y)}{\Gamma_{m,\mu}} \times \int_{-\infty}^{+\infty}\frac{e^{-i\omega(t-\tau)+ik^{\pm}_{x,m\mu}(x-y)}}{\kappa_{m,\mu}} d\omega \tag{1.49}$$

the $\Psi_{m,\mu}$ being the annular duct eigenfunctions given by:

$$\Psi(r,\theta) = E_{m,\mu}(r)\mathrm{e}^{im\theta} \tag{1.50}$$

where $E_{m,\mu}(r)$ is defined as in eq. (1.27). A detailed derivation of G_{duct} is presented in appendix A.

Substituting eq. (1.49) in eq. (1.46) leads to the so-called Goldstein analogy:

$$\begin{aligned}\rho'(\mathbf{x},t) = \frac{1}{c_0^2}\int_{-T}^{T}\int_{\nu(\tau)} T'_{ij}\frac{\partial^2 G_{duct}(\mathbf{x},t|\mathbf{y},\tau)}{\partial y_i \partial y_j} d\mathbf{y}d\tau \\ +\frac{1}{c_0^2}\int_{-T}^{T}\int_{S(\tau)} F_i\frac{\partial G_{duct}(\mathbf{x},t|\mathbf{y},\tau)}{\partial y_i}dS(\mathbf{y})d\tau \\ +\frac{1}{c_0^2}\int_{-T}^{T}\int_{S(\tau)} \rho_0 \mathbb{V}'_n\frac{D_0 G_{duct}(\mathbf{x},t|\mathbf{y},\tau)}{D\tau}dS(\mathbf{y})d\tau\end{aligned} \tag{1.51}$$

This expression, which is formally the same as the free-field expression, takes the mean flow and the duct geometry into account *via* the Green's function. It can be applied to any source distribution in the duct by specifying the source terms accordingly. In the next paragraph,the nature of fan-OGV sources will be briefly discussed.

1.4.3.2.3 Direct application to the fan-OGV noise

As mentioned in section 1.4.3.1, eq. (1.51), some additional assumptions need to be made in order to directly use eq. (1.51) since the desired density field appears on both sides of the equation. In the specific case of subsonic fan configurations, the quadrupole and monopole sources can both be neglected since the Mach number does not exceed 0.5 at approach conditions [22, 132]. Moreover, the Reynolds number being of order of magnitude 10^5 or 10^6, the viscous stress can be neglected and the net force $\mathbf{F}$ reduces to pressure induced forces. This also implies that the surface integral of the second term in eq. (1.51) is reduced to the surface integral on the blades/vanes. [22]. Eventually, eq. (1.51) reduces to:

$$\rho'(\mathbf{x},t) = \frac{1}{c_0^2}\int_{-T}^{T}\int_{S_b(\tau)} F_i\frac{\partial G_{duct}(\mathbf{x},t|\mathbf{y},\tau)}{\partial y_i}dS(\mathbf{y})d\tau \tag{1.52}$$

where S_b is the surface of the blades and vanes.

This equation, whether used with G_{duct}, G_{move} or G_0, is one of the foundations of the present study. It indeed reduces the computation of the noise resulting from the the rotor self-noise and the RSI mechanism, to the computation of the load fluctuations on the blade/vane surfaces.

1.4.4 Analytical modeling

There are numerous analytical models that aim at predicting the fan broadband interaction noise [135, 136]. Each model endeavors to describe the noise resulting from the interaction of turbulent structures (wake and background turbulence) with a vane cascade. Some of them are empirical [125, 126], but the present study exclusively focuses on physics based models, which basically aim at modeling the noise sources resulting from the RSI mechanism, and combine them with some form of acoustic analogies.

The early models were focusing on the interaction of a perturbation impinging onto an isolated airfoil. In this type of model, an incident gust normal to the vane is convected until it reaches its leading edge, creating an unsteady loading responsible for the broadband noise production. Sears [137] first formulated an isolated airfoil model in the specific case of incompressible flows, only valid at low frequency. Amiet developed a compressible response function [138], extended by Paterson and Amiet [63], to take into account trailing-edge back-scattering, and then by Moreau *et al.* [139] and Roger *et al.* [140] to three-dimensional (3D) aerodynamic gusts with subcritical and supercritical gusts. In these models, the airfoil is modeled as an infinitely thin flat plate immersed in a uniform inviscid flow with zero incidence, neglecting camber and mean loading effects. The latter effect was then introduced by Myers and Kerschen [141] and Evers and Peake [142] using asymptotic theories. These models allow to accurately predict the broadband noise radiated by low solidity rotors without external casing such as helicopter rotors or propellers. However, modern ducted fan-OGV stages now display a significant number of vanes with substantial overlapping, questioning the isolated vane assumption. In such a configuration, the influence of the neighboring vanes on the acoustic propagation, which one can refer to as cascade effect, cannot be neglected anymore.

A new range of models have therefore been developed to take the cascade effect into account. They all aim at resolving the integral equation of the problem using different approaches and different levels of modeling. The first models solved this equation numerically considering only a two-dimensional (2D) rectilinear cascade configurations, using the lifting surface method (equally called "singularity method") that can be based, for instance, on the discontinuity of the acceleration potential (Kaji and Okazaki [143]), on the pressure jump across a vane (Whitehead [144]) or even on the chordwise axial velocity discontinuity through a vane cascade (Smith [145]). The latter model eventually led to the creation of the code LINSUB (LINearised SUBsonic unsteady flow in cascade), which has been extensively used by Cheong *et al.* [146], Jurdic *et al.* [147] and Lloyd and Peake [148] for instance. All previously mentioned approaches share important characteristics:

- The considered incident flow is two-dimensional.
- The cascade response is consequently two-dimensional and is obtained by numerically solving an integral equation. This implies, in most cases, to resort to a collocation method, which negatively impacts the computational cost of the model.
- The sound propagation does not account for the effect of the duct walls.

Considering this, Goldstein [132] developed a method to model three-dimensional gusts and to compute the subsequent three-dimensional cascade response. Goldstein also developed the formalism to account for duct wall effects on the acoustic propragation. These improvements were later used by Atassi and Hamad [149] to model the RSI mechanism. Their study notably revealed the importance of three-dimensional effects on the radiated acoustic power. In parallel of these rectilinear cascade models, Namba [150, 151], Kodama and Namba [152] and Schulten [153, 154] developed their own models based on a singularity method for a ducted three-dimensional annular cascade. However, these models assume a null stagger angle, which leads to a bias in the intake/exhaust acoustic propagation.

Another category of models numerically solve the integral equation of the problem to obtain the cascade response, that is then used as an equivalent dipole source in the framework of an acoustic analogy to propagate the produced noise. This is the case of Ventres' model [45], which uses a collocation method to compute this integral considering a 2D flow impinging onto an annular cascade. In this model, the real distribution of the acoustic sources over the vanes is computed and used within an acoustic analogy considering an infinite duct with a constant axial mean flow, also called Goldstein analogy (see section 1.4.3.2). This model has been successively enhanced by Meyer and Envia [155], Nallasamy and Envia [13], and Grace *et al.* [55, 156–158], resulting in a model called RSI that eventually takes into account three-dimensional gusts.

Another branch of models, which analytically solves this equation through the use of the Wiener-Hopf technique, also emerged. This method was initially introduced and extended by Mani and Hovray [159], Koch [160], Peake [161] and Glegg [127]. Glegg notably developed a three-dimensional cascade response that does not rely on the direct computation of the acoustic sources on the vanes to obtain the acoustic field outside of the cascade. Glegg's model was then extended by Hanson and Horan [162] and by Hanson [49], who developed a model that uses a new formalism to take complex geometry features into account and, as in Ventres' model, takes the spanwise variations of the flow and the blade into account through the use of the strip theory. Posson *et al.* [12, 48] also extended Glegg's cascade response to the computation of the unsteady loading on the vanes. They also included Hanson's enhancements regarding the handling of complex geometries and the use of the strip theory. As in Ventres's model, the computed unsteady loading is also used as a dipole source in Goldstein's analogy. Posson's model can then be seen as a analytical version of Ventres' model extended to three-dimensional gusts. Masson *et al.* [163] eventually extended Posson's model by accounting for swirl using the generalized Green's function proposed by Posson and Peake [164] for homentropic flows. Mathews and Peake also recently developed a Green's function accounting for swirl but for a more general isentropic flow with a lined duct [165]. Other studies have also addressed the case of more realistic airfoil geometries. For instance, Baddoo *et al.* [166] developed a model that takes into account both the camber and the thickness of the airfoil if they are small enough. By testing a variety of airfoil geometries, they have demonstrated that these parameters have a significant impact on the actual radiated noise both upstream and downstream of the cascade.

In parallel, some models resorting to the mode-matching approach have been developed. This technique is based on modal expansions in various subdomains of the stator row. Bouley *et al.* [167] proposed such a model and applied it to the impingement of rotor wakes onto a 2D rectilinear cascade, showing results identical to those obtained with the Wiener-Hopf technique from Posson *et al.* [12, 48]. François *et al.* [47] extended this model to the prediction of the noise resulting from the turbulence impingement onto a zero-stagger three-dimensional annular vane cascade in a uniform flow, with no spanwise variations of the turbulent quantities. This was achieved without the use of the strip theory, allowing to completely take the radial mode scattering into account as well as the non-parallelism of the vanes, which are neglected in the strip theory. Additional work is currently being carried out by Girier *et al.* [168] to consider the curvature of the vane in order to model the vane geometry more precisely.

1.4.4.1 Overview of analytical models of rotor-stator interaction noise predictions

As highlighted by Ffowcs Williams and Hawkings [22], and Goldstein [132], the dominant noise source in a subsonic ducted fan-OGV is the unsteady loading on the vanes. Consequently, the main aim of analytical models is to compute the unsteady loading on the vanes resulting from the turbulent rotor wake impingement and in order compute the far-field acoustic power at intake and exhaust using an acoustic analogy. A similar global approach consisting of four main steps is followed by these models as described in [135] and [136], and summarized below:

- The geometry definition: all the models consider a fan stage in an infinite annular duct (fig. 1.9) in which rotor blades and stator vanes are modeled as zero thickness flat plates with finite chord and span. The equivalent flat plate radial evolution matches the pitch and spanwise stackings of the real geometry and preserves some of the main geometrical parameters involved in the blade design, such as the stagger, lean and sweep angles, that have a significant effect on both tonal and broadband noise [72, 169]. Other parameters inherent to the cascade such as the chord length c, the intervane channel height h, the parameter $s = 2\pi r_m / V$ (with r_m the mean radius and V the number of vanes), the solidity $\Sigma = c/s$ and the non-overlapping area d as shown is fig. 1.10 are also replicated with this approach. The geometry is then split into cylindrical strips (strip theory) at radius r, which have a finite radial extent Δr over which the geometric parameters are considered homogeneous. Every strip is then unwrapped into a rectilinear cascade with an infinite number of vanes to ensure periodicity.

- The definition of the impinging flow (excitation): in this step, the input parameters of the models are defined. These parameters aim at replicating as closely as possible the main flow features that govern the broadband noise generation and propagation such as the mean flow in the duct, the mean velocity deficit within the wake or the incident turbulence. To do so, the radial evolution of the axial velocity, the absolute velocity, the wake half-width as well as the wake and background turbulence are used as inputs of the models. The turbulence is described by two parameters, the integral length scale and the turbulence intensity, either separately in the wake and in the background flow, or averaged over the azimuthal direction. Additionally, since random phenomena are the cause of broadband noise, a statistical treatment through the use of a turbulent spectrum is required to describe the turbulent behavior of the flow. Within each strip determined in the geometry definition, the previously identified flow parameters are considered constant. On each strip, the real incident flow is modeled as a gust convected by a mean flow in the form of a harmonic perturbation by time and spatial Fourier transforms, defined by the mean and turbulent characteristics of the flow at the considered radius. Depending on the model, the incident flow can be modeled using 2D gusts, taking the two components of the wave number in the cascade plane into account, or using 3D gusts by considering a third wave number component in the spanwise direction. This choice has a dramatic impact on the predicted noise as will be seen in chapter 5.

- The computation of the acoustic sources: the vane or cascade response is then computed, providing the unsteady loading distribution on the vanes. As detailed in [135], for configurations displaying large values of h/c and of overlap (c-d), and small solidity Σ, such as propellers or Counter Rotating Open Rotors (CRORs), the unsteady loading can be computed using an isolated airfoil model. However, for ducted propulsion systems on which the present study focuses, the solidity and the overlap are more substantial, especially for the Outlet Guide Vane (OGV), which requires the use of cascade responses that take the neighboring vanes into account to compute the unsteady loading. As for the definition of the impinging flow, this cascade response can either be 2D or 3D.

- The sound radiation : the computed unsteady lift is then used as an equivalent dipole source distribution in a chosen acoustic analogy to recover the acoustic power upstream and downstream of the studied cascade. Different types of acoustic analogies can be used to best suit the studied configuration taking its specific features into account, among which the presence of duct walls or of a swirled flow in the inter-stage can be mentioned. These constraints led to multiple acoustic analogies such as a free-field analogy with a uniform mean flow (as in Hanson's model in section 1.4.4.3.1), an in-duct analogy with a uniform mean axial flow (see Ventres' and Posson's models in section 1.4.4.2 and 1.4.4.3.2 respectively) or even an in-duct analogy with swirling flow as recently proposed by Masson *et al.* [163].

As mentioned above, the strip theory approach must be used along with these models to predict the noise of a 3D annular configuration. This approach is only valid for flows with a small radial velocity component, which is a fair assumption as stated by Meyer and Envia [155] who showed that, for an axial turbo-machine, the radial component of the flow becomes negligible only a half-chord downstream of the rotor. Additionally, the lack of parallelism between adjacent blades as well as the radial scattering cannot be accounted for with this type of approach.

Furthermore, the amplitude of the impinging perturbations as well as the one of the cascade response are considered small with respect to the mean flow, which enables to restrict the analysis to a linearized problem. The viscosity of the fluid is also neglected. Indeed, as detailed

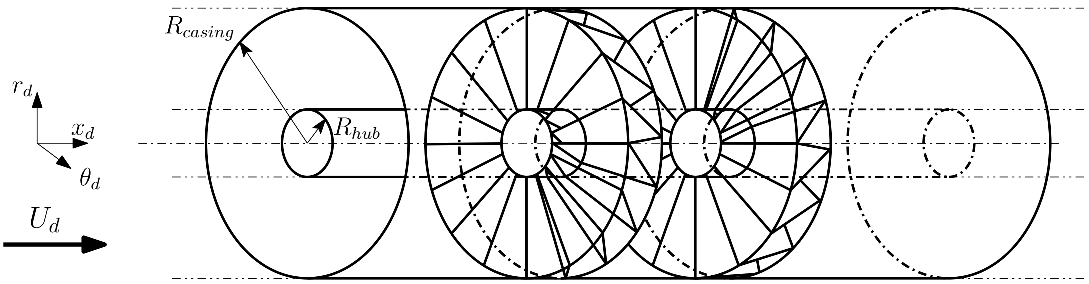

Figure 1.9: Fan stage configuration for the acoustic models (reproduced from de Laborderie [11]).

in [135], the radiated noise originates from the interactions between vortical perturbations and solid surfaces. These interactions are significantly faster than the characteristic lifetime of the perturbations, which leads to a negligible effect of the viscosity with respect to the inertial effects. As a consequence, viscosity is not considered in the interaction mechanisms, except at the trailing edge where the modeling of the wake is ensured through the use of a Kutta condition. These assumptions allow considering the convected Helmholtz equation as the main foundation of the models that are presented in the following sections.

The models discussed hereafter follow this global approach, in the scope of linear theory, with their own specific features. They particularly differ in the modeling of the incident flow, the method to compute the unsteady lift on each strip, and the type of acoustic analogy.

1.4.4.2 Model of Ventres

In the first version of the model of Ventres *et al.* [45], the impinging flow and the cascade response are both two-dimensional. A velocity fluctuation normal to the chord of the vane is considered. Let w be such a gust, of angular frequency ω and impinging on the vane number ν. w is written as follows:

$$w(x_c + \nu d, y_c + \nu h) = w_0 e^{-i\omega t} e^{i(k_{xc}(x_c+\nu d)+k_{yc}(y_c+\nu h))}, \tag{1.53}$$

where k_{xc} and k_{yc} are the wave number along the directions x_c and y_c respectively. Figure 1.10 shows a typical unwrapped strip in the configuration of Ventres. The vane cascade is immersed in a non viscous uniform mean flow with zero angle of attack, the components of which are $(U_{xc}, 0, 0)$.

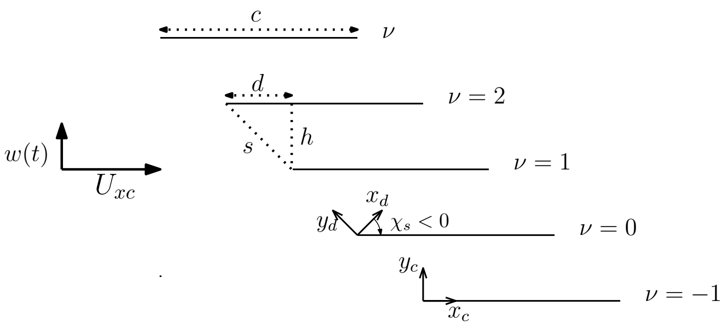

Figure 1.10: Unwrapped strip for the model of Ventres (reproduced from de Laborderie [11]).

In order to ensure the no-slip condition on the flat plate, a velocity field is produced by the impingement of the incident fluctuation. From the momentum and the continuity equations verified by the acoustic pressure, Ventres *et al.* [45] show that the problem is reduced to solving the following integral equation:

$$w(x_c + \nu d, y_c + \nu h) = \int_{-c/2}^{c/2} K_c(x_c - x', y_c) \frac{\Delta p_0(x') e^{i\nu\sigma}}{\rho_0 U_{xc}} \frac{dx'}{c/2}, \tag{1.54}$$

where

$$\sigma = k_{xc} d + k_{yc} h, \tag{1.55}$$

is the interblade phase angle. $\Delta p_0(x')$ is the unsteady pressure jump across the vane $\nu = 0$ and K_c corresponds to the kernel function of the problem, which accounts for the cascade as defined in [45]. This equation is numerically solved by a collocation method. After obtaining the unsteady loading on every vane at each radius, the strips are wrapped back to their initial cylindrical form. The loading is then used as a dipole distribution in the acoustic analogy of Goldstein [132], which gives the acoustic field within an infinite annular duct with a uniform axial mean flow (see section 1.4.3.2).

1.4.4.3 Models based on Glegg's cascade response

Glegg [127] developed a cascade response for a vane cascade of infinite span. Contrary to the cascade response of Ventres *et al.* [45], this model is 3D. This means that the wavenumber along z_c (k_{zc}) is no longer equal to zero, allowing for a better description of the physical phenomena. Additionally, the z-component of the mean velocity U_{zc} can be taken into account and is equivalent to consider a swept stator vane (see figs. 1.11a and 1.11b). Glegg considers an incident gust, which is assumed to be a harmonic wave, written as follows:

$$w(x_c, y_c, z_c) = w_0 e^{-i\omega t} e^{i(k_{xc}x_c + k_{yc}y_c + k_{zc}z_c)}, \tag{1.56}$$

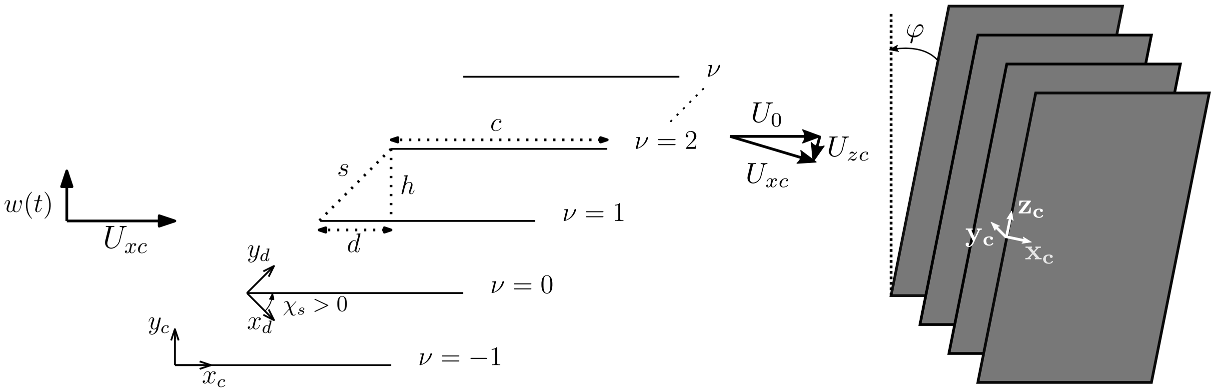

(a) Unwrapped strip for Glegg's model.

(b) 3D view of a vane cascade with a sweep angle φ and the corresponding impinging flow.

Figure 1.11: Glegg's model configuration (reproduced from Posson *et al.* [12]).

Similarly to the model of Ventres *et al.* [45], the objective is to determine the velocity, and more precisely in this case its potential ϕ, produced by the impingement of the gust in order to ensure the no-slip condition on the flat-plate. It follows that for each vane, the incident gusts have an identical amplitude relative to the leading edge, but will be shifted in phase by the same inter-blade angle as defined in eq. (1.55). This also applies to the vane response. Considering this and the fact that the vanes and their wake introduce a discontinuity in the potential field, the potential jump across the vane ν and its wake can be written as the delayed potential jump across the vane as follows:

$$\Delta\phi_\nu(x_c, z_c, t) = \Delta\phi_0(x_c - \nu d)e^{-i\omega t + i(\nu\sigma + k_{zc}z_c)}. \tag{1.57}$$

Since the vanes have an infinite span, the model cannot predict the dispersion of the spanwise wavenumber, which means that k_{zc} is conserved in the cascade response. From the continuity and momentum equations, the integral equation of the velocity potential can be deduced:

$$\begin{aligned}\phi(x_c, y_c) = \frac{1}{2\pi}\int_{-\infty}^{+\infty}\int_{-\infty}^{+\infty} & \frac{-i\epsilon D(\eta)}{(\omega - k_{zc}U_{zc} + \eta U)^2/c_0^2 - \eta^2 - \epsilon^2 - k_{zc}^2} \\ & \times\left[\sum_{\nu=0}^{V-1} e^{i\nu(\sigma + \eta d + \epsilon h)}\right] e^{-i\eta x_c - i\epsilon y_c} d\eta d\epsilon,\end{aligned} \tag{1.58}$$

where $U = \sqrt{U_{xc}^2 + U_{zc}^2}$ is the velocity magnitude, V the number of vanes and $D(\eta)$ the Fourier transform of the potential jump across the vane number 0:

$$D(\eta) = \frac{1}{2\pi}\int_0^{+\infty} \Delta\phi_0(x_c)e^{-i\eta x_c} dx_c. \tag{1.59}$$

Glegg solves the integral eq. (1.58) using the Wiener-Hopf technique with the following boundary conditions:

(a) the velocity potential must be continuous upstream of the vanes,

(b) the total velocity normal to the plate must be zero (impermeability condition),

(c) the pressure must be continuous at the trailing edge (Kutta condition [132]) and in the wake.

Solving eq. (1.58) requires to decompose the potential and the potential jump into four parts:

$$\phi_0 = \phi_0^1 + \phi_0^2 + \phi_0^3 + \phi_0^4 \tag{1.60}$$

$$\Delta\phi_0 = \Delta\phi_0^1 + \Delta\phi_0^2 + \Delta\phi_0^3 + \Delta\phi_0^4 \tag{1.61}$$

Each term is the solution of a specific problem with its own boundary conditions. The first term is the solution of a vortical gust impinging on a cascade of flat-plates with a leading edge and a semi-infinite chord; boundary conditions (a) and (b) are considered in this first problem. The second part considers a cascade of flat-plates of semi-infinite chord with a trailing edge, interacting with the field ϕ_0^1 obtained by solving the first problem; this problem is subject to boundary conditions (b) and (c). However, solving this second step introduces a new potential ϕ_0^2, which modifies the upstream part of the problem. This results in an acoustic field that does not satisfy the boundary condition (a). Two additional solutions, which are coupled, need to be introduced: ϕ_0^3 solution of the first problem but taking ϕ_0^2 and ϕ_0^4 into account, and ϕ_0^4 solution of the second problem but taking ϕ_0^3 into account. Obtaining an exact solution through the coupling of the two last steps requires to solve an infinite matrix system. As a consequence, the solution of the problem can only be approximated by truncating this system. In Posson's model, which is an extension of Glegg's model (see section 1.4.4.3.2), the extrapolation of Richardson [170] proposed by Majumdar and Peake [171] has been used in order to reduce the computational cost of the prediction and ensure a converged solution. In the present application of this model, around 2000 terms had to be computed to get a converged solution.

Once the potential jump on the flat plates is obtained, Glegg [127] gives an explicit formula of the scattered acoustic velocity potential outside of the cascade resulting from the impingement of the incident gust. It is expressed as the sum of acoustic modes of index k scattered by the cascade:

$$\phi^{\pm}(\mathbf{x},t) = \pm\frac{\pi w_0 C^2}{\beta s_e}\sum_{k=-\infty}^{\infty} \pm\frac{\zeta_k^{\pm} D(\lambda_k^{\pm})}{\sqrt{\kappa_e^2 - f_k^2}} e^{i[-\lambda_k^{\pm}(x_c - y_c d/h) + (\sigma - 2\pi k) y_c/h + k_{zc} z_c]} e^{-i\omega t}, \tag{1.62}$$

with:

$$\begin{aligned} M &= U/c_0 & \beta &= \sqrt{1-M^2} & \omega_g &= \omega - k_{zc}U_{zc} \\ s_e &= \sqrt{d^2 + \beta^2 h^2} & \tan\chi_e &= d/\beta h & \lambda_k^{\pm} &= \kappa M + \eta_k^{\pm} \\ \zeta_k^{\pm} &= \beta\sqrt{\kappa_e^2 - (\eta_k^{\pm})^2} & \kappa_e^2 &= \kappa^2 - (k_{zc}/\beta)^2 & \kappa &= \omega_g/(c_0\beta^2) \\ \eta_k^{\pm} &= -f_k \sin\chi_e \pm \cos\chi_e\sqrt{\kappa_e^2 - f_k^2} & f_k &= (\sigma - 2\pi k + \kappa M d)/s_e & & \end{aligned}$$

In practice, this infinite sum is reduced to the cut-on modes. Indeed, the mode k propagates only if it satisfies the cut-on criterion $\kappa_e^2 - f_k^2 > 0$. It should also be noted that the acoustic field is obtained without explicitly making use of the distribution of the acoustic sources on the vanes. This considerably reduces the computational cost of such a method in comparison to annular models. This particular feature has been kept by Hanson when extending Glegg's cascade response, as explained in the following section.

1.4.4.3.1 Hanson's model

Hanson's model [162, 172] is based on Glegg's cascade model. The main advance of Hanson's approach is the ability to model more realistically the impinging flow by taking into account the in-homogeneity and the anisotropy that characterize the flow in the inter-stage. Hanson also developed the formalism to change the coordinate system by successive rotations in order to take into account the specific features of complex blade geometries (variable stagger, sweep and lean angles). Moreover, Hanson adapted Glegg's model to a cylindrical system, which allowed him to consider the wavenumbers in the duct coordinate system with the actual number of blades and vanes. Hanson's model also resorts to the strip theory: the geometry is divided into several cylindrical cuts of thickness Δr. For each strip, the acoustic power is then computed and radiated only within the considered Δr strip using Glegg's approach. This method differs from the approach of Ventres and Posson since the pressure jump is not computed and the computation of the acoustic power is not correlated between two different radii. Finally, in Hanson's model, only a free-field propagation is considered, which means that there is no energy distribution over the duct acoustic modes.

Despite these two limiting assumptions, this model predicts the shapes and levels of the acoustic power spectra fairly well [43]. Additionally, the fact that the model does not consider an in-duct propagation reduces its computational cost significantly. This can be a particularly interesting asset, especially for parametric studies in an industrial context.

1.4.4.3.2 Posson's model

Posson's model [12, 46, 48] includes Hanson's developments allowing to account for complex geometical features and also resorts to the strip theory: each strip corresponds to Glegg's configuration in which a rectilinear cascade of zero-thickness flat plates of infinite span is subject to a 3D impinging gust. However, Posson extended Glegg's model in order to compute both the acoustic field in the inter-blade domain and the unsteady pressure jump across the vanes. By solving eq. (1.58), the latter eventually leads to the pressure distribution along the chord, which can be considered as an equivalent distribution of dipoles along the vane surface once the cascade has been wrapped back to its initial position. The vane cascade responses subject to each gust are then added up to obtain the source distribution corresponding to the real impinging flow. These sources are finally radiated through the duct using the generalized Goldstein's acoustic analogy (see section 1.4.3.2). The use of a linear cascade response in conjunction with an annular propagation is responsible for some issues already identified by Posson *et al.* [12]. One of these is the non-coincidence of the cut-off frequencies of the duct-modes with that of the linear cascade, which results in unphysical resonances. In order to tackle this issue, a first correction has been implemented in the model and validated on a test-case [46]. In the present case, this annular correction, which only works for unswept vanes, is not taken into account since the vane sweep angle is not negligible. In order to reduce the unphysical resonances, the frequency bands in the following sections have been selected in order to exclude the cut-off frequencies, following suggestions by Grace [private comm] [158].

1.4.5 Numerical approach

1.4.5.1 Direct noise simulation

As briefly explained in section 1.4.1, the direct approach for noise computation can be divided into two steps:

1. Performing a numerical simulation that computes both the aerodynamic source field and, at least, part of the resulting acoustic near-field.
2. Computing the acoustic far-field based on the near-field by using analytical or numerical propagation techniques. This second step is necessary only if the acoustic far-field could not be computed in the first step.

The first part requires to select the simulation approach that is the most adapted to the computation of the broadband RSI noise. As mentioned in section 1.3, different levels of flow description are available. Since the near-field noise needs to be computed, only unsteady approaches can be used, which prevents from using the steady RANS approach. As the broadband noise results from the interaction of turbulent flows with solid walls, the inherent stochastic nature of turbulence must be captured by the chosen approach, and its modeling must be as limited as possible. Consequently, unsteady statistical approaches such as URANS cannot be used since turbulence is entirely modeled. It could however be used to compute the deterministic sources and the resulting near-field tonal noise. It has for instance been used by Daroukh [10] to compute the tonal noise resulting from the RSI mechanism and from an inlet flow distortion. DNS and LES methods, including LBM, are thus the only simulation options for direct broadband noise computations. Due to its computational cost, the direct sound simulation using a DNS approach is limited to cases at low to moderate Reynolds numbers (*i.e.* channel flows [88], low-pressure turbines with limited span [89–93] or compressor and fan blades [173, 174]). It still remains a powerful tool for studying noise generation mechanisms and provides precious databases for the development of other noise predictions tools. Thanks to high performance computers, LES has then been extensively used for more complex flow configurations. Its multiple forms (wall-resolved LES, wall-modeled LES, hybrid RANS/LES) make it a more versatile tool, which can be applied to a wider range of flow configurations for direct noise computation.

Whatever the chosen simulation technique, the first step of direct noise simulation raises four major difficulties:

1. Even if the computational resources have been significantly increased over the past decade, some highly CPU-demanding flow configurations are still out of reach for modern turbulence simulation techniques, even for wall-modeled LES or hybrid RANS/LES approaches. In this case, resorting to less costly methods is the only option to obtain an estimate of the broadband noise.

2. Even though LES-approaches involve less modeling than statistical approaches, they require many modeling approximations, the impact of which on the noise predictions has not been thoroughly addressed yet.

3. At subsonic Mach numbers, the magnitude disparity between hydrodynamic and acoustic disturbances is so significant that only a very small fraction of the flow energy effectively radiates into the far-field [175]. This means that acoustic waves are prone to numerical errors. Numerical accuracy then appears as a stringent requirement for the direct approach. High-order discretization schemes with excellent dissipation and dispersion properties are required to transport the acoustic waves without damping and distortion. The use of such schemes significantly increases the required computational resources.

4. Artificial dissipation is generally used in CFD algorithms for stability purposes. Even if it only has a limited impact on the aerodynamic field, it may damp acoustic waves significantly because of their low magnitude and their propagative nature.

The second part of the direct approach consists in extrapolating the near-field noise to the far-field. Several methods are available:

- Acoustic analogies: these methods rely on the use of a porous closed surface, which encloses all the acoustic sources, along with an acoustic analogy that solves the wave-equation in the far-field. Provided that the surface is localized in the linear region, where only acoustic fluctuations are observed, they are able to radiate the acoustic information from the control surface to the far-field. Two main formulations are available: the Kirchhoff method [176–178] and the method based on Ffowcs Williams and Hawkings's analogy [22], sometimes called Porous Ffowcs Williams Hawkings analogy, which extends the original FW-H analogy to permeable control surfaces. These two approaches give identical results if there are not any quadrupole sources on the porous surface. The FW-H formulation has however shown to be more robust than the Kirchhoff method in the presence of flow nonlinearity [179, 180] .

- Numerical methods: provided that a wave equation is satisfied at the boundaries of the simulation domain, numerical approaches can be used to solve simplified equations on a domain extending the simulation domain of the first step. Linearized Euler Equations (LEE) can be solved on a mesh external to the simulation domain for instance. A number of methods solving the Helmholtz equation are also available. This is the case of the Boundary Element Method (BEM), which numerically computes a tailored Green's function for all kinds of geometries based on a surface mesh. The numerical Green's function is then embedded in an integral formulation of the Helmholtz equation, in conjunction with an equivalent acoustic source derived from the acoustic near-field computed in the first step. The Finite Element Method (FEM) also solves the Helmholtz equations but on an external 3D mesh, which makes it more CPU-demanding than the BEM.

Finally, there is one last method that couples both steps in one unique approach: the computation of both the sources and the acoustic far-field using the Lattice-Boltzmann Method (LBM). This method uses the same approach as LES or Hybrid RANS/LES methods, except that it solves the Boltzmann equation on a Cartesian mesh instead of the Navier-Stokes equations. This drastically reduces the CPU costs at moderate Mach numbers and makes it possible to carry out direct broadband noise simulations thanks to the low dissipation of the method. LBM is a promising alternative to classical Navier-Stokes LES, but its applicability to high speed compressible flows such as those encountered in fan-OGV computations is still limited, in particular because of the computational resources it requires. It has however been used for the study of low-speed fans [78, 85].

In a nutshell, this section has revealed that the important computational cost of the direct numerical approach, which is induced by the high required level of accuracy, may be prohibitive in the frame of a fan-OGV interaction noise study.

1.4.5.2 Hybrid methods

In order to bypass the prohibitive CPU cost of the direct noise simulation approach, hybrid methods have been developed to carry out studies on the RSI mechanism at a more reasonable cost. These methods are generally a two-step process that separates the computation of the acoustic sources from the propagation.

1. Analytical/Semi-analytical approach: this method couples a CFD computation with an analytical model. The flow parameters that charaterize the impinging flow are extracted from the CFD simulation to feed the analytical model, which computes the resulting unsteady loading. The latter is then considered as an equivalent dipole source distribution in an acoustic analogy in order to compute the associated radiated noise [43, 48, 163]. This approach only requires flow simulations using statistical turbulence models (RANS, URANS), making it possible to compute the RSI noise at an affordable cost especially in an industrial context. Nevertheless, the inherent assumptions made in the turbulence models and the necessary geometry simplifications of the models induce a loss of accuracy. These models may also be applied to mean flow data extracted from high-fidelity unsteady simulations (such as LES), for comparison purposes, although such unsteady simulations are not meant to feed statistical models in the first place.

2. Numerical approach [43] : this method couples an LES, which directly computes the unsteady loading on the vanes, with an acoustic analogy such as the Ffowcs Williams and Hawkings [181] free-field analogy, or the Goldstein [132] duct analogy to recover the acoustic far field. These methods allows to directly compute the unsteady loading on the vane, the accuracy of this computation being set by the mesh itself. Their main drawback is that the Green's function is only known for canonical cases (free-field, uniform flow, annular cylindrical ducts, with possible but complex extensions to slowly varying ducts, lined ducts, mean swirl flows). As a consequence, some specific features such as sheared flows are ineluctably neglected, which can impact the accuracy of the method. Moreover, such approaches only consider dipole sources, which is only a valid assumption at low Mach numbers.

3. Propagation using Linearized Euler Equations (LEE) [51,53,57,60,61,182] : this method is a two step calculation that decouples the sound generated by turbulence from its propagation. In the first step, a mean flow field is computed by solving the viscous RANS equations (or an inviscid mean flow from Euler's equations) and the Euler's equations are then linearized

around this mean flow. In a second step, the LEE are solved with an additional turbulent source term, which is referred to as the synthetic turbulence model [183–185]. This source may be a stochastic model that is used to synthesize the velocity turbulence field that will be convected by the mean flow to interact with the vanes, which generates leading edge noise. This approach is very attractive since it allows taking into account sheared mean flows as well as the actual geometry of the vanes. However, besides the underlying assumption about the turbulence required for the source modeling, its main drawback is that it may become quite expensive for complex geometries and high frequencies such as those encountered in fan-OGV broadband cases. Moreover, the synthetic turbulence modeling is not straightforward and the LEE may present stability issues in the presence of strong sheared mean flows from RANS simulations [186].

Fan broadband noise prediction methods — Summary

In this section, the main approaches available to carry out fan broadband noise studies have been presented. The duct modes have been introduced along with the duct cut-off conditions. The concept of acoustic analogy has then been presented, with a particular focus on Goldstein's analogy, which deals with sound propagation in a duct with a mean axial flow. An overview of the available methods for broadband RSI noise prediction has then been given. They can be classified into two categories: analytical modeling and numerical methods.

Analytical modeling

Several types of models dedicated to broadband RSI noise predictions are available. They all consider stators as a sum/cascade of flat-plates and compute the vane response induced by an incident flow in a two-dimensional strip, which is then used as an equivalent dipole source in the frame of some form of acoustic analogy. Three of the most advanced cascade models have been presented with their specific features: Ventres's model, Hanson's model and Posson's model. They all differ by the way they model the incident flow and the cascade response (2D or 3D), and the propagation step (free-field or in-duct propagation).

Numerical approach

The two categories of numerical approaches have been introduced:

- The direct noise simulation, in which the aerodynamic sources as well as the acoustic near-field (at least) are computed. The propagation is then performed through a numerical approach or an acoustic analogy.
- The hybrid noise simulation, in which the computation of aerodynamic sources and the propagation are decoupled.

The hybrid noise simulation appears as a good trade-off between the induced computational cost and the accuracy level it guarantees. Two approaches, with two different levels of accuracy, have particularly been identified: the coupling of analytical models with low order simulations (RANS), to carry out fast studies, and the coupling between a scale resolving simulation (LES) with an acoustic analogy, to get more accurate results.

1.5 Conclusion: research approach and objectives

This chapter has presented the fundamental knowledge required to carry out broadband noise predictions on the RSI mechanism. The theoretical background regarding the acoustic duct propagation and the acoustic analogies have been introduced. The multiple numerical simulation approaches, from statistical methods to full turbulent resolving methods, have been compared in terms of accuracy and computational costs. The noise simulation approaches, classified as analytical or numerical methods, have then been exhaustively listed. Once more, the accuracy of the methods has been weighted against their cost to identify the most adapted tool for the present study.

In the light of this analysis, two hybrid approaches have been identified as first-hand tools for the present study:

- An analytical approach that couples an analytical model with a RANS simulation.
- A wall-modeled LES coupled with a Ffowcs Williams and Hawkings analogy (abbreviated WMLES-FWH).

The two different levels of accuracy provided by these methods, balanced with their respective cost, make them complementary tools. On the one hand, the analytical approach provides fast noise estimates, which makes it possible to carry out reasonably accurate RSI noise pre-design or optimization studies in the industrial context. It however relies on stringent hypotheses whether it is in the RANS approach or in the analytical modeling itself. On the other hand, the WMLES-FWH approach is a cutting edge method that gives a more accurate insight into the turbulence phenomena at stake in the RSI mechanism. It also relies on less modeling than the analytical approach, which makes it a first hand-tool to precisely investigate the involved flow mechanisms and to assess the validity of the hypotheses made in the analytical models. Nevertheless, it requires the use of important computational resources, which prevents it from being used intensively.

In this context, the main objective of the present study is to develop and validate this dual hybrid approach, and assess its capacity to provide reliable broadband RSI noise predictions. More specifically, the objectives are to:

- Compare the noise predictions obtained from the three cascade analytical models presented in this chapter and assess the impact of their respective hypotheses on the noise predictions.
- Assess the correctness of some hypotheses made in the analytical models, especially regarding the turbulence modeling, based on an analysis of the turbulence data obtained from the WMLES.
- Develop a complete WMLES-FWH approach, assess its capacity to accurately predict the broadband noise sources and to provide reliable broadband noise predictions. The objective is to quantify the required level of accuracy of the simulation to get a good estimate of the broadband noise.
- Assess the contribution of the RSI mechanism to the total radiated broadband noise, with respect to other potential broadband noise sources.
- Confront both approaches and compare the cost/accuracy ratio on the considered configuration.

In order to achieve these goals, the two hybrid approaches have been applied to the ACAT1 fan stage mock-up, which has been experimentally tested in the framework of the European project TurbonoiseBB (see chapter 2 for more details). A complete aerodynamic study of the configuration has been performed using both RANS and WMLES methods. Their respective results have been confronted and compared to the experimental data, allowing for a better assessment of their respective accuracy. Noise predictions have then been performed in two ways:

- Mean flow and turbulence data have been extracted from RANS and WMLES methods, and used as inputs for two analytical models (Hanson's and Posson's models). The first objective is to compare the impact of the chosen analytical model for each type of simulation separately. The second objective is to compare the disparities induced by inputs retrieved from different simulation approaches on the prediction provided by each model, separately.

- The stator vane pressure fluctuations have been retrieved from the WMLES in order to be used as a source for the FW-H analogy.

The RANS and the WMLES approaches have been confronted and compared to experimental data. Finally, in order to thoroughly assess the impact of the different sources of approximation in analytical models, an extensive parametric study using the hybrid analytical approach has been carried out. Ventres's, Hanson's and Posson's models have been applied to the Source Diagnostic Test case (SDT) (see chapter 5 for more details) and their respective predictions have been directly compared.

The organization of the present study then follows this strategy: chapters 2-4 present the work performed on the ACAT1 configuration. Chapter 2 introduces the main characteristics of the ACAT1 fan-stage. The numerical set-ups for both the RANS and the WMLES are detailed together with the convergence study and the unsteady extraction methodology. Chapter 3 presents the aerodynamic results from both approaches and chapter 4 focuses on the acoustic predictions. Finally, chapter 5 presents the parametric analytical study performed on the SDT configuration.

CHAPTER 2

Numerical investigation on the ACAT1 configuration: method, computational domain, meshing and convergence checking.

Introduction

This chapter presents the fan stage on which the simulations and noise predictions from chapters 3 and 4 have been performed. The experimental facility/set-up, the specific geometry features and the flow conditions at which the configuration is operating are presented. The numerical set-ups are also described for both the RANS and the two LES: the computational domains, numerical parameters (solver, boundary conditions) as well as the structure and the quality of the meshes are explained in detail. The convergence monitoring methods and the proofs of convergence for both types of simulations are then provided. Finally, the flow extractions to retrieve unsteady data from the two LES are described in detail.

Contents

2.1 Benchmark configuration

Chapters 2-4 present the work that has been performed in the framework of the European project TurbonoiseBB extending from September 2016 to August 2020. It gathers companies (SAFRAN Aircraft Engines, Rolls-Royce PLC, Airbus Operations SAS, GKN Aerospace Sweden, Industria de Turbo Propulsores S.A.U (ITP Aero), SAFRAN Helicopter Engines, MTU Aero

Engines AG) as well as research partners (Office National d'Études et de Recherches Aerospatiales (ONERA), École Centrale de Lyon, University of Southampton, The University of Cambridge, Chalmers Tekniska Hoegskolan, Universidad Politecnica de Madrid, Stichting Nationaal Lucht- En Ruimtevaartlaboratorium) that are major actors of the European aeronautic industry. The purpose of this project is to develop and validate concepts and technologies (experimental or numerical) in order to get a better understanding of the source mechanisms involved in broadband noise production within an aircraft engine fan stage. It also aims at producing innovative OGV designs [186, 187] that directly modify these sources in order to reduce the subsequent radiated noise.

To this end, a comprehensive data base of aerodynamic and acoustic measurements was obtained from a test campaign performed on the "ACAT1" Fan stage at the Universal Fan Facility for Acoustics (UFFA) [188] of AneCom AeroTest (ACAT) in Wildau, Germany. Figures 2.1a-2.1d show an overview of the test facility. The ACAT1 is a turbofan model with an outer radius of 0.43 m equipped with 20 fan blades and 44 stator vanes. Two configurations have been tested: one with a short inter-stage and an additional one with a longer inter-stage. Both configurations have been tested at different operating conditions (approach, side-line and cut-back conditions) on two different working lines (a Sea Level Static (SLS) and a Low Noise (LN) working line), which differ by the blade loading of the fan. Figure 2.2 shows a schematic view of the test rig summarizing all the aerodynamic and acoustic measurements that have been performed during the test campaign. The present work focuses exclusively on the SLS working line, at approach condition, for the short inter-stage configuration. The short inter-stage configuration was chosen because it is more representative of future UHBR engines in terms of rotor-stator spacing. The flow conditions of the chosen operating point are given in table 2.1.

Geometrical parameters	Tip radius R_T (m)	0.435
	Hub radius at the rotor leading edge (m)	0.138
	Rotor mid span chord $c_{midspan,R}$ (m)	0.136
	Stator mid span chord $c_{midspan,S}$ (m)	0.066
	Rotor tip gap (mm)	0.78
Operating point	Rotation speed Ω (rpm)	3828.2
	Tip relative Mach number	0.57
	Inlet Mach number	0.23
	Inter-stage mean Mach number	0.35
	Total mass-flow rate (kg/s)	55.156
	Bypass ratio	7.6
	Ambient pressure $P_{t,amb}$ (hPa)	995.6
	Ambient temperature $T_{t,amb}$ (K)	292.8
	Turbulence intensity at the inlet (%)	0.3
	Turbulence length scale at the inlet (m)	0.04
Reference values	Density (ρ) (kg/m^3)	1.19
	Speed of sound (c_0) (m/s)	342

Table 2.1: Approach condition.

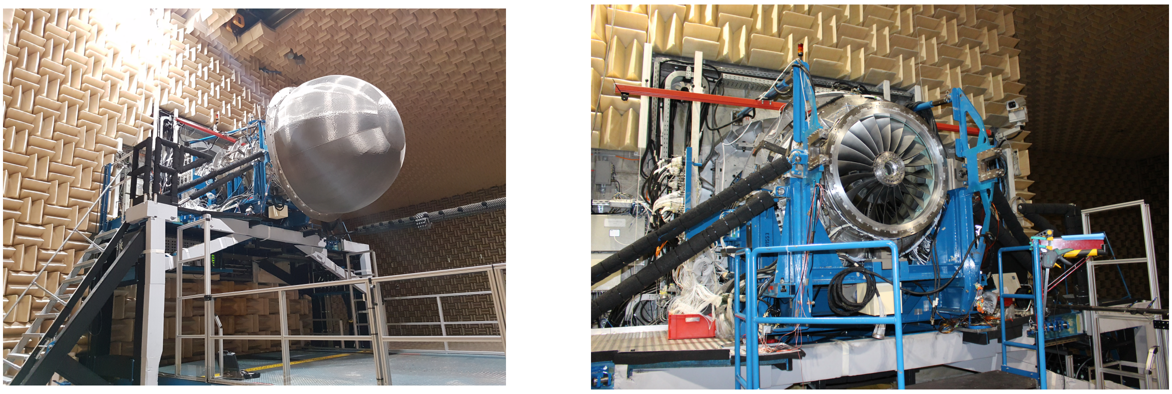

(a) UFFA rig.

(b) UFFA front view with no inlet.

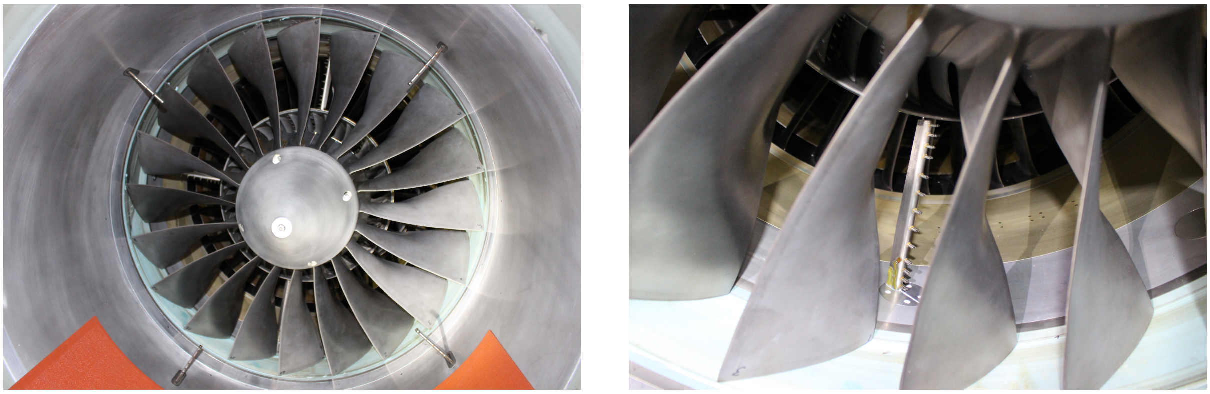

(c) Fan front view.

(d) Inter-stage pole rake.

Figure 2.1: Overview of the ACAT1 fan rig (© AneCom AeroTest, reproduced with permission).

2.2 Simulation set-ups

2.2.1 RANS simulation

2.2.1.1 Computational domain

The 3D view of the computational domain is depicted in fig. 2.3. The computational domain extends from 4 fan blade axial chords upstream of the rotor to 6 vane axial chords downstream of the stator. For the RANS computation described herein, it has been reduced to one rotor passage and one stator passage by the use of periodic boundary conditions. Since the objective of the present work is to study the Fan-OGV interaction, the Inlet Guide Vane (IGV) in the core flow has been removed to build the computational domain, making it possible to focus the mesh refinements on the zones of interest. The hot geometry of the fan blades, which accounts for the deformation of the fan blade induced by the rotation speed, is used in the present study.

2.2.1.2 Numerical parameters

Solver: The RANS simulation has been performed using the mixing-plane approach from the code ANSYS CFX v19.2. The high resolution CFX convection scheme has been used with Menter's k-ω SST turbulence model [189]. This model extends the Wilcox k-ω model [190] notably by accounting for the effect of the transport of the principal turbulent shear stress, leading to major improvements in predicting the flow in the presence of an adverse pressure gradient [189].

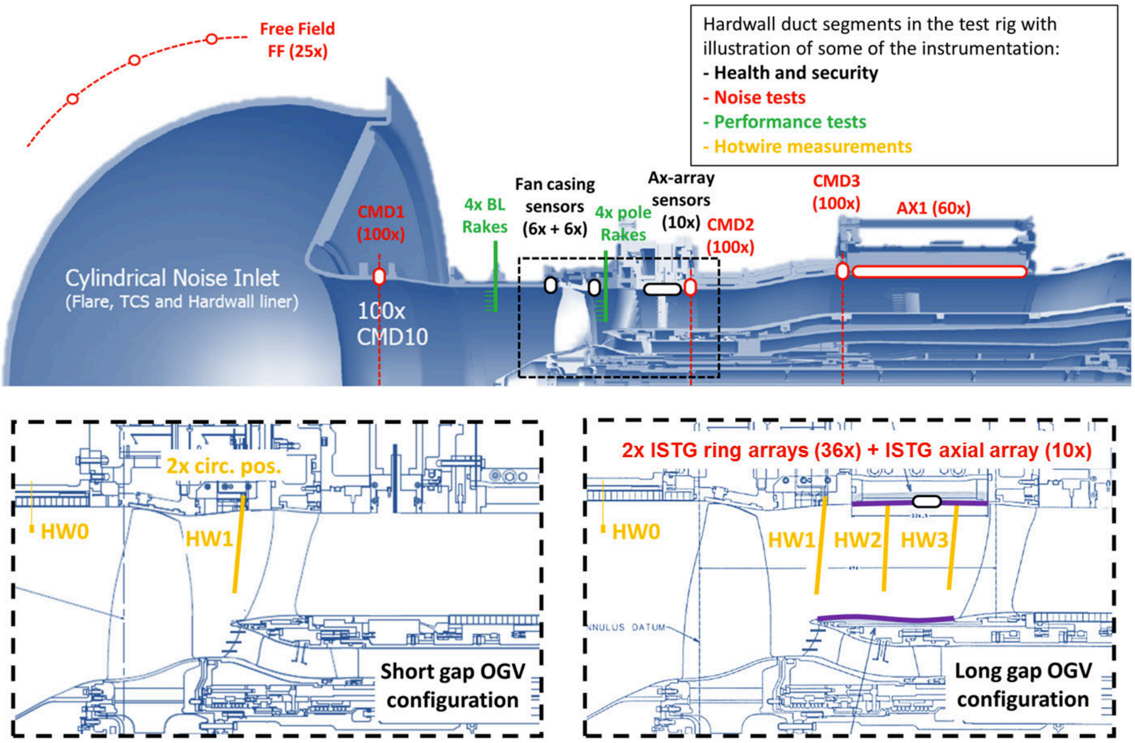

Figure 2.2: View of the UFFA fan rig of AneCom AeroTest. Ring arrays were used for acoustic measurements at the inlet (CMD1), inter-stage (ISTG) and bypass (CMD3) sections, and axial arrays at the inter-stage and in the bypass duct. Moreover, an array of 25 microphones, equally distributed from 0 to 120 degrees along an arc of radius 18.5 m centered on the fan axis at the nozzle intake, was used for far-field sound measurements upstream of the inlet.

Boundary conditions: Both the ambient pressure and temperature are prescribed at the inlet of the computational domain along with the turbulent quantities measured during the test campaign (see table 2.1). The bypass and core mass-flow rates are imposed at the bypass and core outlets respectively through the use of a throttle condition to target the experimental mass-flow. A no-slip adiabatic condition is imposed on all the solid surfaces. Finally, periodic boundary conditions are used on the lateral surfaces of the computational domain.

2.2.1.3 Mesh

Meshing strategy: The meshing software Centaur was used to generate the mesh. The latter is a hybrid unstructured grid composed of prism cells on walls, to accurately resolve the boundary layer, and of tetrahedral cells in the rest of the domain. Surface and volume refinements have been set (see figs. 2.4a-2.4d) in order to ensure the quality of the mesh:

- Surface refinements have mainly been used to accurately discretize the blade and the vane surfaces, especially the leading edges (LE), the trailing edges (TE) and the fillets. This has resulted in a rotor blade surface mesh with more than 150 cells in the axial direction and 200 cells in the radial direction. For the stator vane surface, there are at least 100 cells in

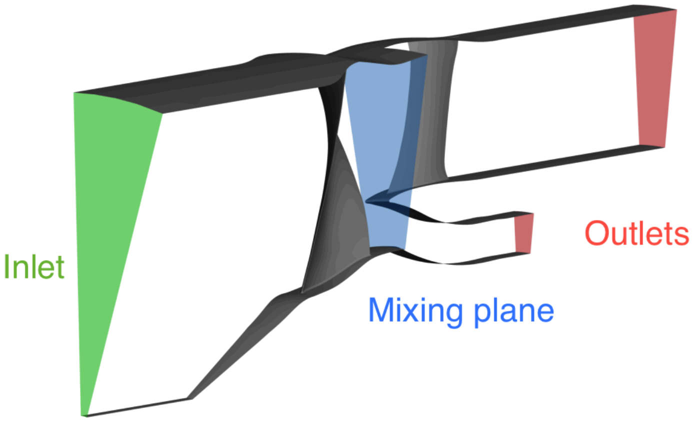

Figure 2.3: RANS computational domain.

the axial direction and more than 150 in the radial direction.

- Prismatic refinements: 25 prism layers with a stretching ratio of 1.25 have been used in the entire computational domain to capture the boundary layer. However, keeping the 25 layers in regions displaying an important curvature often results in stretched or compressed cells in the prism layers, leading to skewed tetrahedral cells at the transition between the outer prism layer and the rest of the volume mesh. To prevent this, a set of interlocked refinement blocks has been introduced at the leading and trailing edges of the rotor and the stator. These blocks progressively reduce the number of prism layers from 25 to 19 at the leading and trailing edges. This reduction of prism layers has been counterbalanced with an increased density of tetrahedral cells. The mesh size close to the wall is set to $1 \cdot 10^{-5}$ m on the hub and shroud and to $1.2 \cdot 10^{-6}$ m on the blade and vanes in order to reach the quality requirements for a wall-resolved simulation $y^+ < 1$.

- Volume refinement blocks: 4 main blocks have been used for both the fan and the OGV:
  - Wake blocks: hexahedra have been used in order to refine the mesh along the wake. The generation of the cells follows a bilinear law from a size equivalent to $2.2 \cdot 10^{-1}$ $c_{midspan,R}$ to $7.4 \cdot 10^{-1} c_{midspan,R}$. This guarantees at least 15 points in the wake in the circumferential direction, which ensures an accurate description of the physics.
  - Leading-edge and trailing-edge cylindrical blocks have been used to ensure a smooth transition from the coarse to the fine mesh near the walls. The cells in these blocks grow from an initial cell size prescribed at the cylinder center line to larger cells following a linear law imposed by a prescribed stretching ratio.
  - Tip gap: a particular care has been taken to avoid degenerate cells in this region. A smoother tetrahedral cell transition and correct prism layer parameters have eventually ensured to precisely discretize the tip region with cells of correct quality. Around 30 cells are used to discretize the tip gap.
  - Inter-blade region: a maximum mesh size equivalent to $1.5 \cdot 10^{-2}$ $c_{midspan,R}$ was imposed in the inter-blade region in order to guarantee a correct azimuthal description of the flow. Approximately 120 cells are used to azimuthally discretize the inter-blade region.

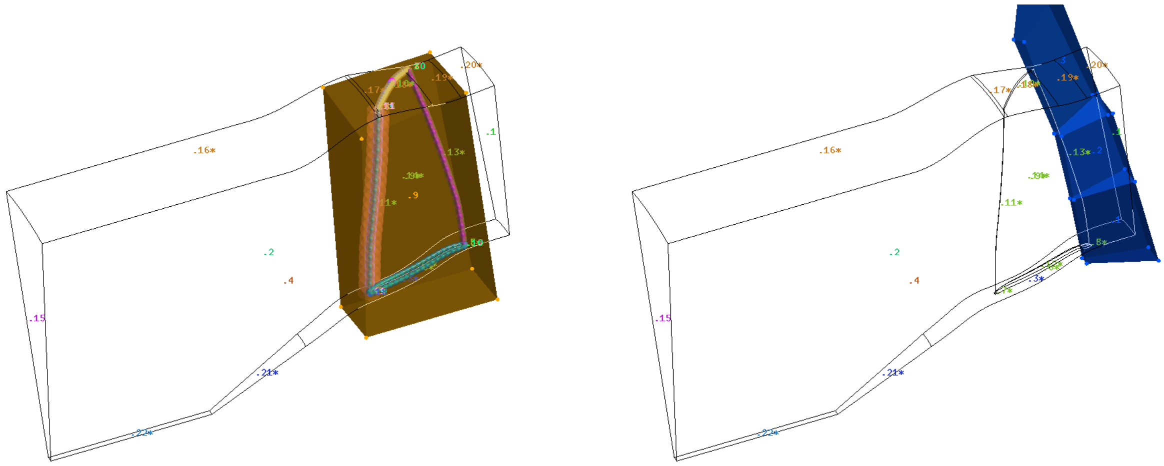

(a) Rotor refinement blocks.

(b) Rotor wake refinement block.

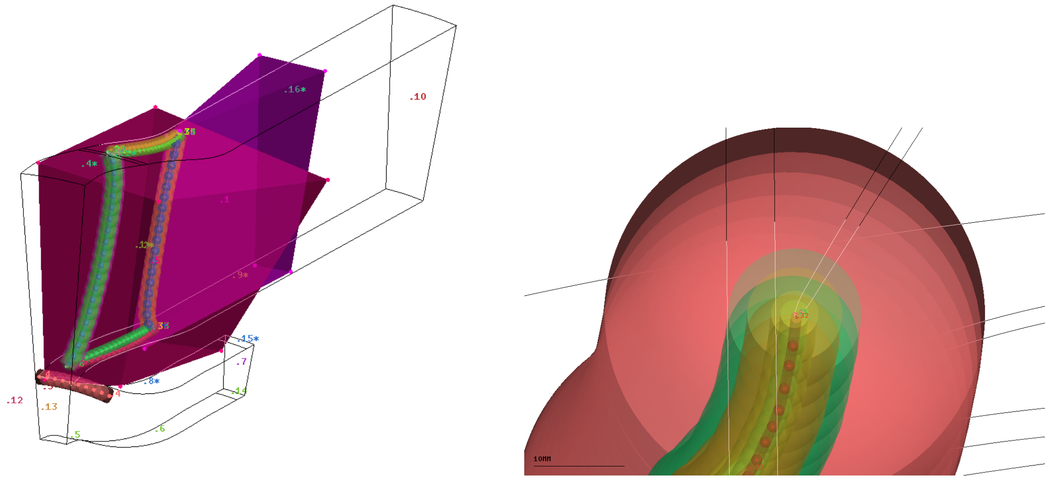

(c) Stator refinement blocks.

(d) Rotor leading-edge interlocked refinement blocks.

Figure 2.4: Overview of the mesh refinement blocks.

The final mesh displayed in figs. 2.5-2.7 is the result of a mesh-convergence study that has needed several iterations.
These parameters have eventually led to a mesh composed of 50 million cells in the rotor domain and of 20 million cells in the stator domain. The significant over-sizing of the mesh is mainly due to the wake-refinement blocks, which have been chosen excessively large to guarantee that the mesh follows the wakes. Consequently, a significant number of cells generated for the wake is actually not within the simulated wake. In addition, the use of such volume refinements creates cells that are almost isotropic, which significantly increases the number of cells in the wake compared to a structured mesh. The use of a refinement block fitted to the wake would have reduced the mesh size almost by half. However, since the computational cost of RANS computations is quite low, no mesh optimization aiming at reducing its size has been conducted.

Mesh quality: In terms of mesh quality, four main parameters have been monitored to ensure the reliability of the mesh:

- The cell aspect ratio (AR), which is the ratio of the longest edge length to the shortest

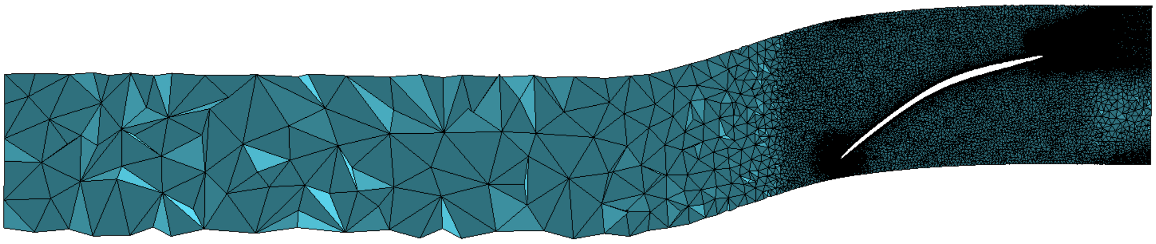

(a) Rotor.

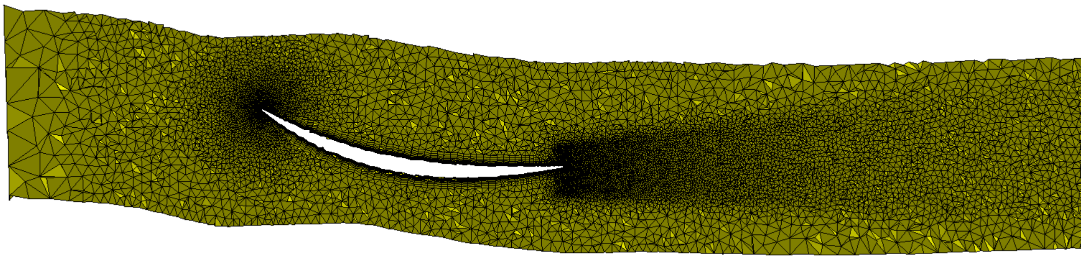

(b) Stator.

Figure 2.5: Mesh radial cut at rotor midspan, RANS simulation.

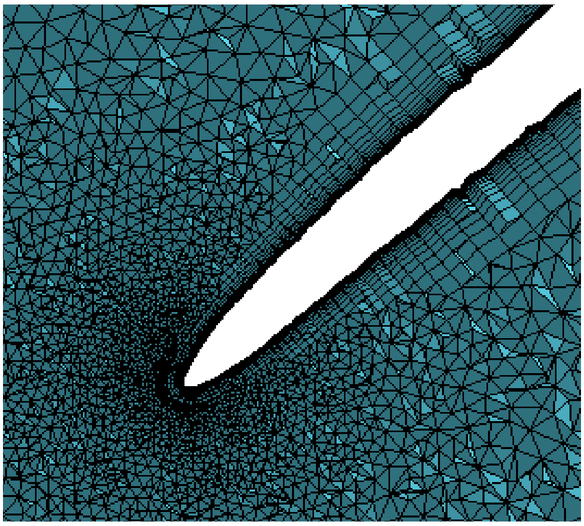

Figure 2.6: Rotor-blade LE mesh.

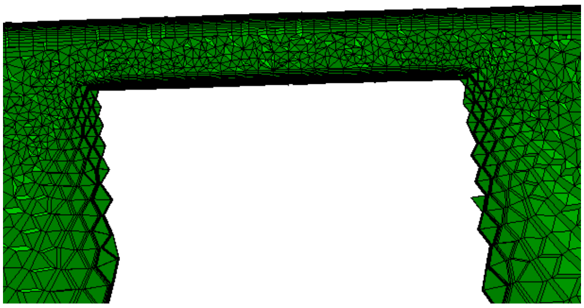

Figure 2.7: Rotor-blade tip-gap mesh, RANS simulation.

edge length of a given cell, is equal to 1 (ideal) for an equilateral triangle or a square. Values up to 100 are acceptable in the core of the flow whereas higher values can be found near the solid surfaces since prism cells, which are aligned with the flow direction, are used. It should also be mentioned that, in near wall regions, the wall mesh requirements (y^+ value) prevents from reaching low aspect ratios without excessively increasing the size of the surface mesh.

- The cell equivolume skewness, which is the ratio of the difference of the volume of an equilateral tetrahedron (*i.e.* ideal) with the same circumsphere of the current tetrahedron and the volume of the current tetrahedron to the volume of that equilateral tetrahedron (see eq. (2.1)). Cells of excellent to good quality have equivolume skewness values ranging from 0 to 0.5. Poor quality cells, with a skewness between 0.8 and 0.95, should only represent a small percentage of the mesh. Cells with skewness higher than 0.95 should be avoided as much as possible and be located in zones with small velocity gradients.

$$skew = \frac{V_{ideal} - V_{real}}{V_{real}}. \tag{2.1}$$

- The cell sliver, which is the ratio of the volume of an equilateral tetrahedron with the same average edge length as the current tetrahedron, to the volume of the current tetrahedron (see eq. (2.2)). Values above 10 should be avoided.

$$sliver = \frac{L_{avg}^3 \frac{\sqrt{2}}{12}}{V_{real}}. \tag{2.2}$$

- The dihedral angles (DiA), which is the angle between two faces of a given tetrahedron. A minimum value of 10° and a maximum value of 170° are acceptable.

Tables 2.2-2.6 show some statistics about the tetrahedron cells of both rotor and stator domains. The meshes are of good quality. Only a very limited number of cells that are not localized in critical zones do not respect the quality requirements. For the near wall region, the prism cells have an aspect ratio that has been maintained between 500 and 1000. Lower values of aspect ratio have been difficult to reach since the y^+ is close or lower than 1.

	Mean value	Maximum value	Percentage of tetrahedra with AR $>$ 100
Aspect ratio	1.23	132	$4 \cdot 10^{-6}\%$

Table 2.2: Mesh quality: aspect ratio.

	Mean value	Maximum value	Percentage of tetrahedra with skewness $>$ 0.95
Skewness	0.27	0.99	0.03 %

Table 2.3: Mesh quality: equivolume skewness.

	Mean value	Maximum value	Percentage of tetrahedra with sliver $>$ 10
Sliver	1.22	37	$8 \cdot 10^{-5}\%$

Table 2.4: Mesh quality: sliver.

	Mean value	Min value	Percentage of tetrahedra with DiA $<$ 10
Min dihedral angle	50	3	0.004%

Table 2.5: Mesh quality: minimum dihedral angle.

	Mean value	Max value	Percentage of tetrahedra with DiA > 170
Max dihedral angle	95	174	$6 \cdot 10^{-5}\%$

Table 2.6: Mesh quality: maximum dihedral angle.

Finally, as shown in fig. 2.8, the y^+ values on the solid surfaces of each sub-domain are below or close to 1, which is satisfactory for a wall resolved RANS simulation.

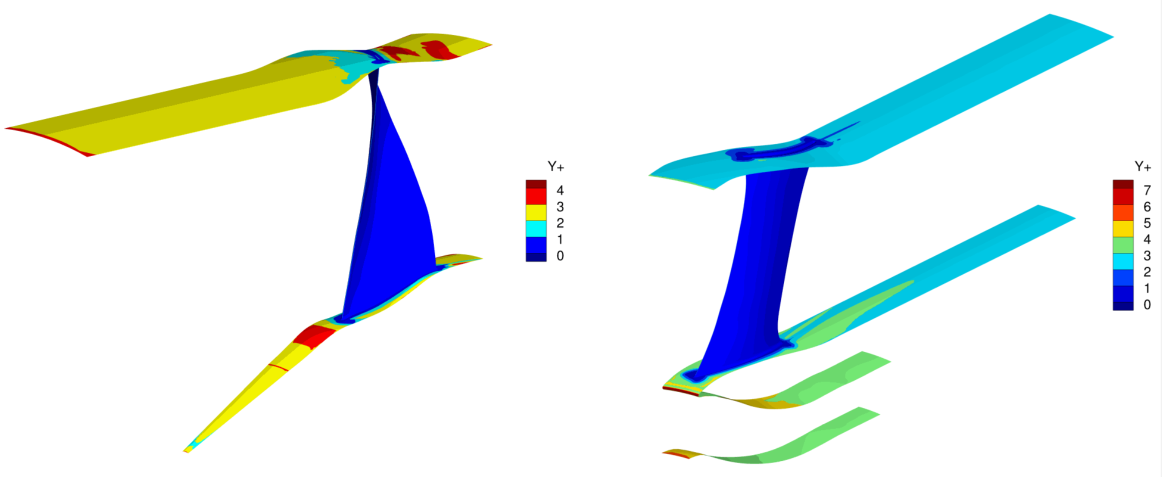

(a) Rotor.

(b) Stator.

Figure 2.8: y^+ values, RANS simulation.

Simulation Set-Ups: RANS simulation —— Summary

Computational domain

- 1 rotor blade -1 stator vane configuration.
- IGV removed.

Numerical parameters

- Solver: ANSYS CFX v19.2.
- Mixing plane approach.
- Turbulence modeling: Menter's k-ω SST turbulence model.
- Inlet boundary condition: ambient pressure and temperature, turbulent quantities measured in the test campaign imposed at the inlet.
- Outlet boundary conditions: measured mass-flow rates imposed at the bypass and core outlets.
- Side boundary condition: periodic boundary condition.
- Solid wall boundary condition: adiabatic walls with no-slip condition.

Mesh

- Hybrid unstructured mesh: prismatic cells on solid surfaces and tetrahedra in the rest of the domain.
- 70 million cells.
- Wall resolved simulation ($y^+ \approx 1$).
- The range of mesh quality parameter values guarantees a reliable simulation.

2.2.2 Large Eddy Simulations

2.2.2.1 Computational domain

In order to limit the computational costs of an LES, computational domains for turbomachines are commonly reduced using periodic boundary conditions. In the particular case of the AVBP solver, which is the code that has been used for the present LES (see section 2.2.2.2 for more details), the rotor-stator interface requires to have the same angular sector for the rotor and stator domains. For the ACAT1 geometry, the domain can thus be reduced to a quarter of the geometry, consisting of 5 fan blades and 11 vanes. Nevertheless, a 5-11 domain is still too large for a complete hub-to-tip fan/OGV LES. To further reduce the computational domain, a modification of the vane count, reducing it from 44 to 40 (9% reduction), has been performed. This has resulted in a 1 rotor blade-2 stator vane configuration ($2\pi/20$ periodicity), which allows to significantly reduce the computational costs. In order to maintain the stage performances while reducing the vane count, the stator vanes have been rescaled to keep the same solidity as the original OGV according to Rai and Madavan [191]. This modification consists in an axial rescaling (9% chord increase) and an azimuthal rescaling by the same factor. Through this process, the leading-edge position remains the same in order to maintain the fan-OGV distance of the original configuration. The camber line and the thickness-to-chord ratio are also conserved. Determinant parameters for broadband noise predictions, such as sweep, lean and stagger angles, are also maintained. Since the vane count is modified, such a geometric transformation will have a significant impact on the tonal component of the noise. However, it only has a limited impact on the broadband noise as shown by Leonard *et al.* [43] who performed a similar geometric transformation on the Source Diagnostic Test (SDT) configuration. A RANS study showing that the rescaling has had almost no impact on the performance parameters, on the pressure distribution on the OGV skin, and on the RSI broadband noise is presented in appendix B. The 3D view of the final computational domain is depicted in fig. 2.9.

2.2.2.2 Numerical parameters

Solver: The turbomachinery capacity of the AVBP code developed by Cerfacs [192] has been used to carry out the compressible LES on the ACAT1 configuration. The method used consists in the coupling of two LES domains, the first one dedicated to the rotor, and the second one to the stator. The two computational domains are coupled using an overset grid method [97], implemented using the coupling library CWIPI, through which conservative variables are exchanged between the two instances. The filtered compressible Navier-Stokes equations describing the mass, momentum and energy equations for a perfect gas are solved. Equations are solved using a finite-volume Lax-Wendroff time explicit scheme with second-order accuracy in time and space [193]. The CFL number has been set to 0.7 to ensure the stability of the

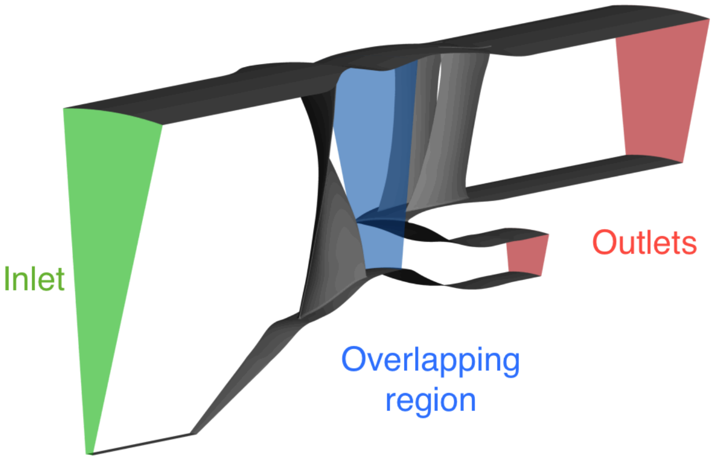

Figure 2.9: LES computational domain.

numerical simulation. The Wall-Adapting Local Eddy-viscosity (WALE) subgrid-scale closure, developed by Nicoud and Ducros [123], is used to model the unresolved turbulent contributions.

Boundary conditions: The inlet and outlets are treated using non-reflecting characteristics boundary conditions (NSCBC) [194]. At the inlet, the experimentally measured total temperature and pressure are imposed and the flow is purely axial with no turbulence injection [195]. At the outlet, the flow reaches a radial equilibrium that matches the mean static pressure extracted from a surface average of the static pressure at the outlet of the RANS simulation. Periodic boundaries are imposed on both lateral sides of the domain. On all the solid walls, the boundary layer is modeled using a wall law inducing a no-slip condition at the walls (see the work of Nicoud *et al.* [196] for more details on the law itself). A linear law is imposed if the normalized wall distance is $y^+ < 11$, and a logarithmic law otherwise (Schmitt *et al.* [197]).
Two simulations have been performed with two different levels of mesh refinement: a medium sized mesh (LES1) with an average y^+ of 35 on the blades and vanes, and a refined mesh (LES2) with an average y^+ of 20 on the blades and vanes. These y^+ values are consistent with those recommended by Piomelli [14] and Wagner *et al.* [15] for wall-modeled LES.
The time step as well as the number of iterations per blade passage for both simulations are presented in table 2.7.

	Time step (s)	Number of iterations per blade passages
LES1	$3.7 \cdot 10^{-8}$	22000
LES2	$2.75 \cdot 10^{-8}$	29000

Table 2.7: Numerical parameters.

The present numerical method has been validated on compressors [94], turbines [95] and turbofans [43, 44, 98, 99].

2.2.2.3 Mesh

Meshing strategy: The Centaur software was used to generate the LES grids. The two LES meshes (LES1 and LES2) have the same global topology as the RANS mesh (see fig. 2.10). Still, some modifications have been introduced in the refinement blocks to better cope with the LES mesh requirements. In particular the hydrodynamic cut-off frequency (f_h) and the acoustic cut-off frequency (f_a) are of paramount interest. These values are mentioned in the following paragraphs and are computed using the following relationships:

$$f_h = \frac{U_c}{L}, \tag{2.3}$$

$$f_a = \frac{c_0 + U_c}{L}, \tag{2.4}$$

where U_c is the convection velocity (corresponding to 120 m/s in the inter-stage), c_0 is the speed of sound, and L is the smallest resolved length scale that is equal to 22 times the cell size, considering that a frequency is resolved when using at least 22 points per wavelength with the Lax-Wendroff scheme. The specific features of the two LES meshes are the following:

- Prismatic refinements:
  - LES1: 8 prism layers with a stretching ratio of 1.18 have been used in the entire computational domain to capture the boundary layer. The interlocked refinement blocks progressively reduce the number of prism layers from 8 to 3 at the leading edge, and from 8 to 4 at the trailing edge. The mesh size close to the wall is set to $1.8 \cdot 10^{-4}$ m in the entire domain to obtain an average y^+ of 35 on the blades and vanes. This guarantees cut-off frequencies of $f_h = 30$ kHz and $f_a = 116$ kHz on all the solid walls.
  - LES2: 14 prism layers with a stretching ratio of 1.08 have been used in the entire computational domain to capture the boundary layer. The interlocked refinement blocks progressively reduce the number of prism layers from 14 to 6 at the leading edge, and from 14 to 8 at the trailing edge. The mesh size close to the wall is set to $1.0 \cdot 10^{-4}$ m in the entire domain to obtain an average y^+ of 20 on the blades and vanes. This guarantees cut-off frequencies of $f_h = 55$ kHz and $f_a = 209$ kHz on all the solid walls.
- Volume refinement blocks:
  - The intervane refinement block in the stator domain has been extended up to the overlapping region in order to correctly transport the rotor wakes into the stator domain since no block fitted to the wake can be set in the stator domain.
  - A block imposing a uniform mesh in the overlapping area has been used to facilitate the data transfer between the two AVBP instances involved in the computation.
  - The wake block of the rotor domain has been replaced by a set of 12 cylindrical refinement blocks. The cylinder positions have been set on the basis of the velocity field retrieved from the RANS simulation, in order to limit the extent of the wake blocks and reduce the number of cells outside of the actual wake. The cylinders have a larger radius in the LES2 to better follow the wakes. In the stator domain, the hexahedra blocks from the RANS mesh have been kept.
  - All the block meshing parameters have been modified for the LES1 and LES2 meshes in order to cope with LES mesh requirements in terms of time-step, mesh size, and accuracy. Tables 2.8-2.13 show the different meshing parameters for both simulations and each refinement block.

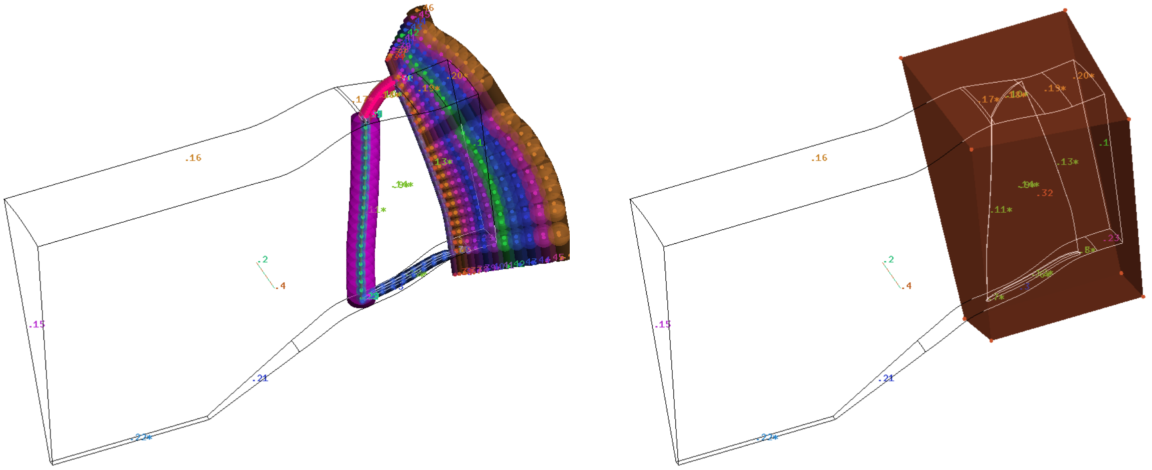

(a) Rotor refinement blocks.

(b) Rotor interblade refinement block.

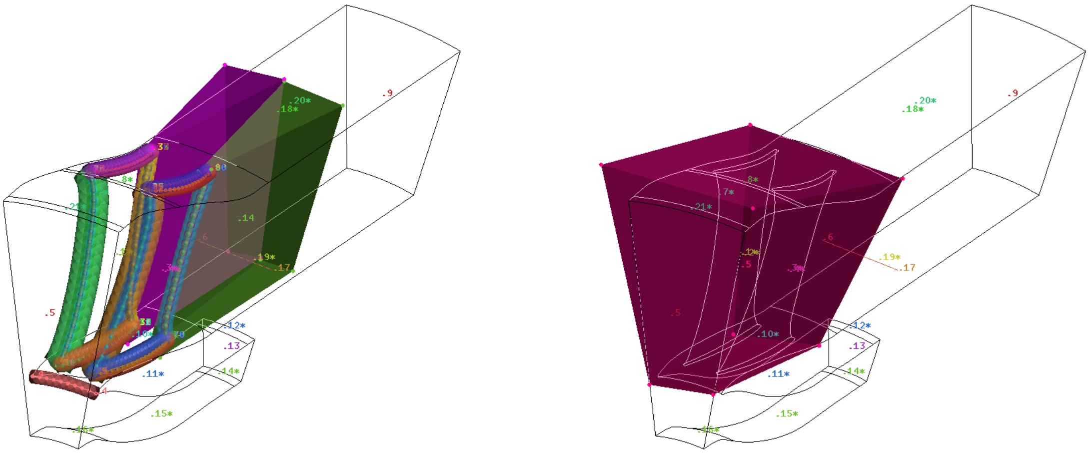

(c) Stator refinement blocks.

(d) Stator interblade refinement block.

Figure 2.10: Overview of the mesh refinement blocks.

	Cell size (% of $c_{midspan,R}$)	f_h (Hz)	f_a(Hz)
LES1	1.4	2850	11000
LES2	1.4	2850	11000

Table 2.8: Mesh parameters: maximum cell size.

	Cell size (% of $c_{midspan,R}$)	f_h (Hz)	f_a(Hz)
LES1	$2.6 \cdot 10^{-1}$	15500	60000
LES2	$1.5 \cdot 10^{-1}$	27000	105500

Table 2.9: Mesh parameters: leading and trailing edge blocks.

	Cell size (% of $c_{midspan,R}$)		f_h (Hz)		f_a(Hz)	
Cylinder number	1^{st}	12^{th}	1^{st}	12^{th}	1^{st}	12^{th}
LES1	$2.2 \cdot 10^{-1}$	$7.4 \cdot 10^{-1}$	18000	5500	70000	21000
LES2	$1.8 \cdot 10^{-1}$	$7 \cdot 10^{-1}$	22000	5700	83 000	22000

Table 2.10: Mesh parameters: rotor wake blocks.

	Cell size (% of $c_{midspan,R}$)		f_h (Hz)		f_a(Hz)	
Position	TE	Downstream TE	TE	Downstream TE	TE	Downstream TE
LES1	$2.2 \cdot 10^{-1}$	2.2	18000	1800	70000	7000
LES2	$1.8 \cdot 10^{-1}$	1.5	22000	5700	83 000	22000

Table 2.11: Mesh parameters: stator wake blocks.

	Cell size (% of $c_{midspan,R}$)	f_h (Hz)	f_a(Hz)
LES1	1.4	2900	11000
LES2	$7.4 \cdot 10^{-1}$	5500	21000

Table 2.12: Mesh parameters: rotor interblade block.

	Cell size (% of $c_{midspan,R}$)	f_h (Hz)	f_a(Hz)
LES1	1.4	2850	11000
LES2	$5.8 \cdot 10^{-1}$	6800	26100

Table 2.13: Mesh parameters: stator interblade block.

The resulting numbers of mesh cells are detailed in table 2.14 and an overview of the meshes is displayed in figs. 2.11-2.14.

	Rotor ($\cdot 10^6$)	Stator ($\cdot 10^6$)	Total ($\cdot 10^6$)
LES1	56	39	95
LES2	125	85	210

Table 2.14: Mesh size: number of cells per subdomain.

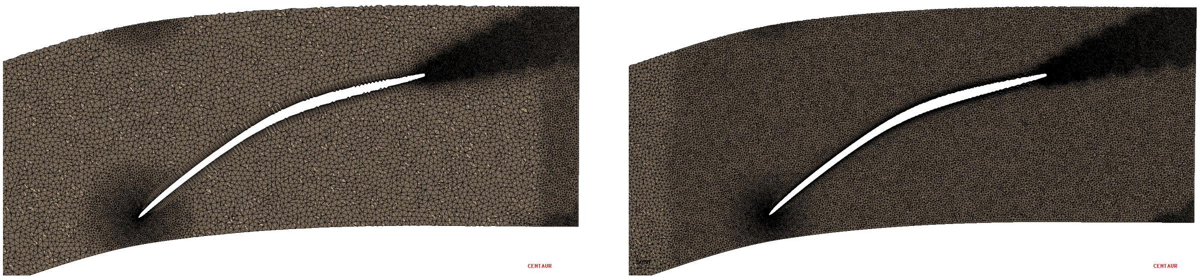

(a) LES1.

(b) LES2.

Figure 2.11: Mesh radial cut at midspan, rotor domain.

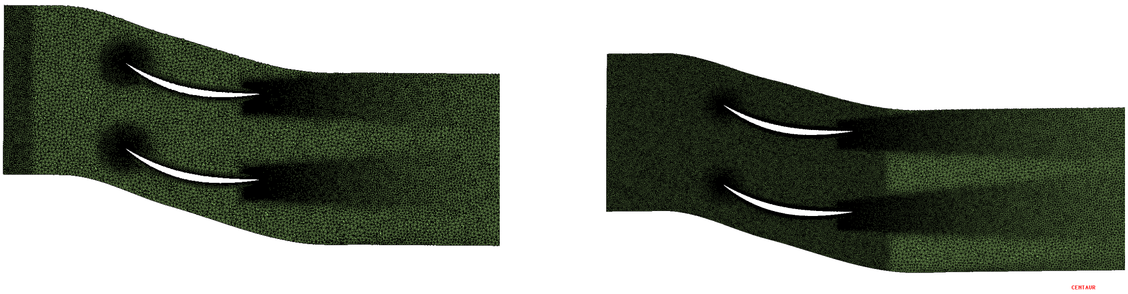

(a) LES1.

(b) LES2.

Figure 2.12: Mesh radial cut at midspan, stator domain.

Mesh quality: In terms of mesh quality, the same quality indicators as for the RANS (see section 2.2.1.3) have been monitored for the LES meshes. The mesh statistics gathered in tables 2.15-2.19 show that the LES1 and LES2 meshes are of good quality compared to standards given in the literature.

In the case of wall-modeled LES, the dimensionless wall distance to a surface in the normal direction (designated indifferently using y^+ or n^+), and in the tangential directions (s^+ for the streamwise direction and r^+ for the third local direction) have to cope with certain requirements that are recalled in table 2.20 along with the wall-resolved LES requirements.

The n^+ values in the entire domain for both LES1 and LES2 are shown in fig. 2.15. Figures 2.16-2.23 display maps of the n^+, s^+ and r^+ values on the blade and vane surfaces for both simulations, confirming that the meshes are consistent with the wall requirements for wall-modeled LES.

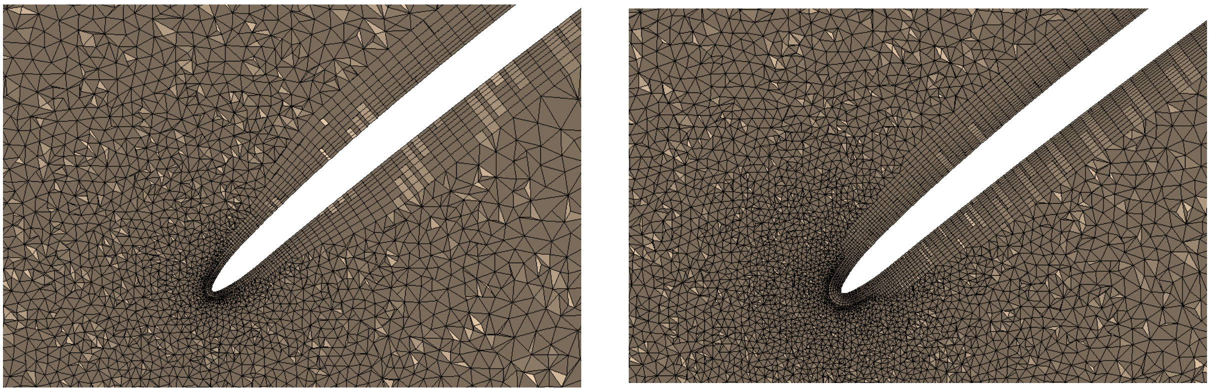

(a) LES1. (b) LES2.

Figure 2.13: Mesh radial cut at midspan, rotor leading-edge.

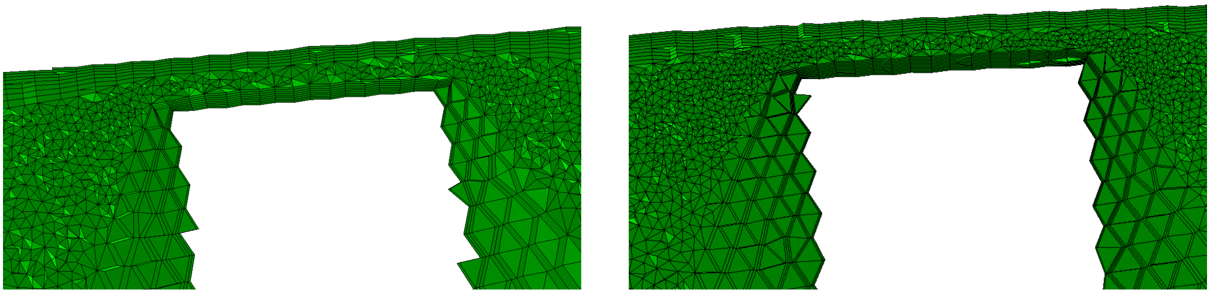

(a) LES1. (b) LES2.

Figure 2.14: Mesh axial cut, rotor tip-gap.

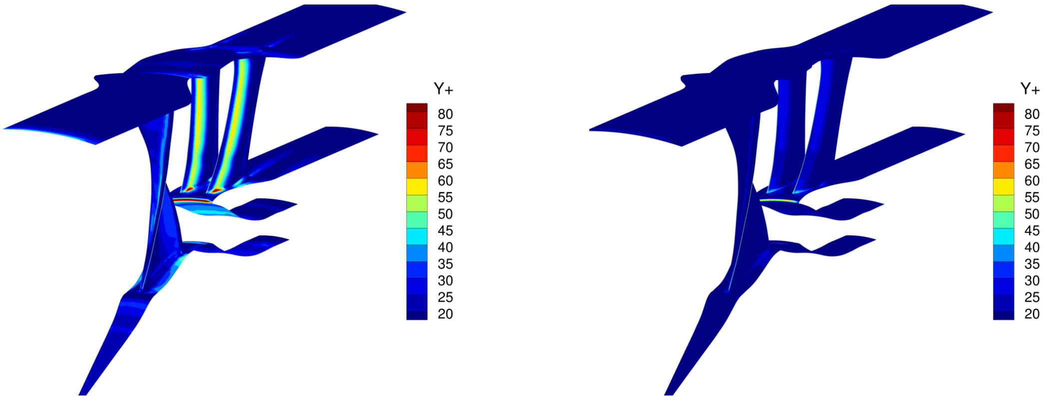

(a) LES1. (b) LES2.

Figure 2.15: n^+ values (different color maps).

	Mean value	Maximum value	Percentage of tetrahedra with AR $>$ 100
LES1	1.23	278	$6 \cdot 10^{-6}\%$
LES2	1.23	313	$1 \cdot 10^{-5}\%$

Table 2.15: Mesh quality: aspect ratio.

	Mean value	Maximum value	Percentage of tetrahedra with skewness > 0.95
LES1	0.27	0.99	0.03 %
LES2	0.27	0.99	0.03 %

Table 2.16: Mesh quality: equivolume skewness.

	Mean value	Max value	Percentage of tetrahedra with sliver > 10
LES1	1.21	25	$3 \cdot 10^{-5}\%$
LES2	1.21	57	$1 \cdot 10^{-4}\%$

Table 2.17: Mesh quality: sliver.

	Mean value	Min value	Percentage of tetrahedra with DiA < 10
LES1	50	3	0.0003%
LES2	50	2.5	0.002%

Table 2.18: Mesh quality: minimum dihedral angle.

	Mean value	Max value	Percentage of tetrahedra with DiA > 170
LES1	95	176	$3 \cdot 10^{-5}\%$
LES2	95	175	$7 \cdot 10^{-5}\%$

Table 2.19: Mesh quality: maximum dihedral angle.

	Wall-resolved LES	Wall-modeled LES
s^+	50-150	100-600
r^+	10-40	100-300
n^+	1	30-150
Number of points in $0 < n^+ < 10$	3-5	-

Table 2.20: Wall mesh requirements for LES [14] [15].

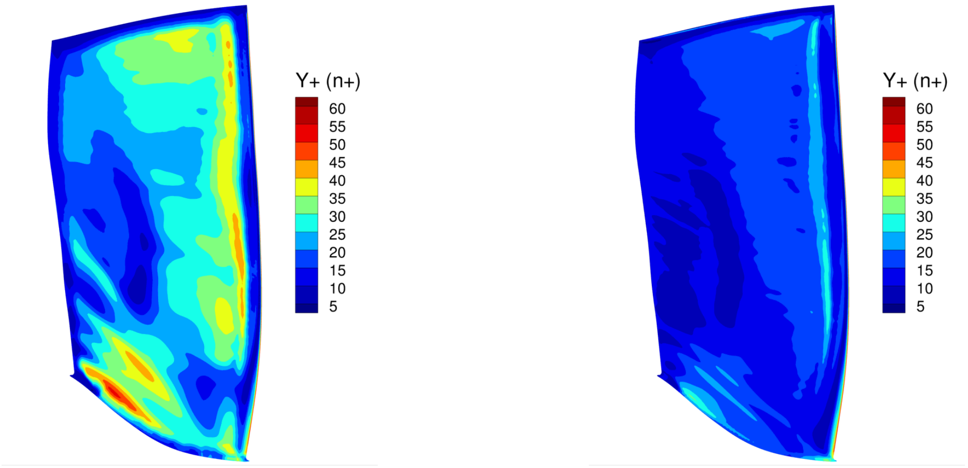

(a) LES1.

(b) LES2.

Figure 2.16: n^+ values, rotor suction side.

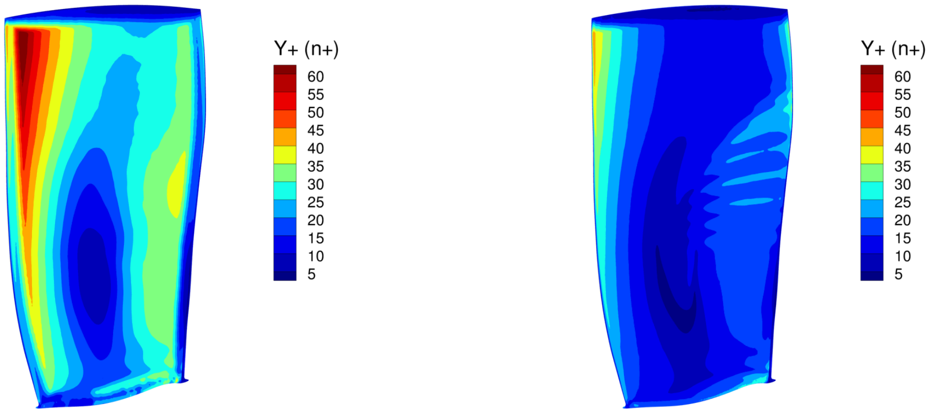

(a) LES1.

(b) LES2.

Figure 2.17: n^+ values, rotor pressure side.

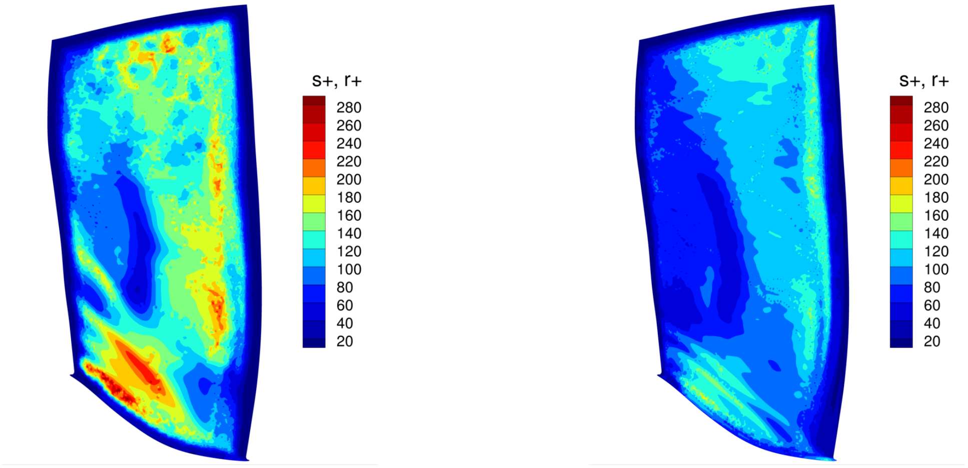

(a) LES1.

(b) LES2.

Figure 2.18: s^+ and r^+ values, rotor suction side.

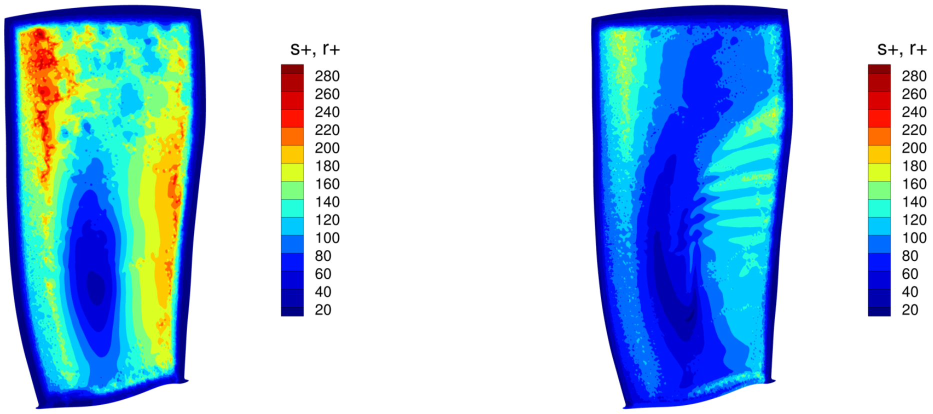

(a) LES1. (b) LES2.

Figure 2.19: s^+ and r^+ values, rotor pressure side.

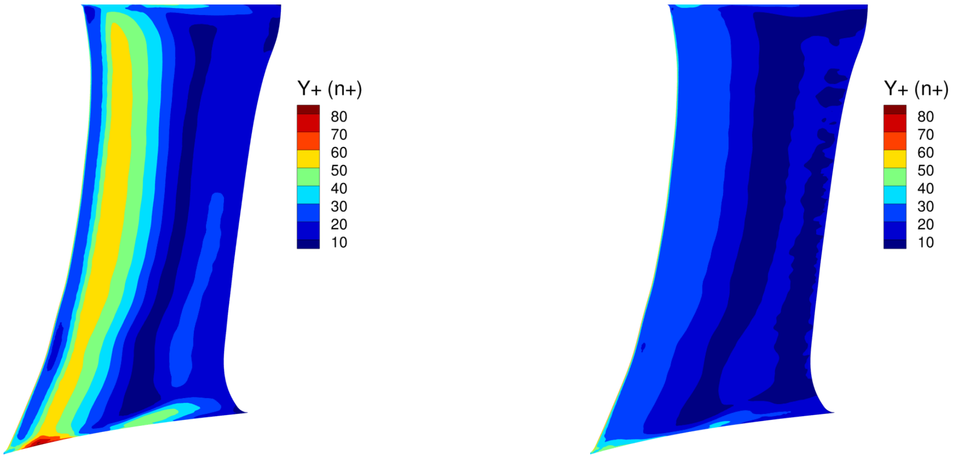

(a) LES1. (b) LES2.

Figure 2.20: n^+ values, stator suction side.

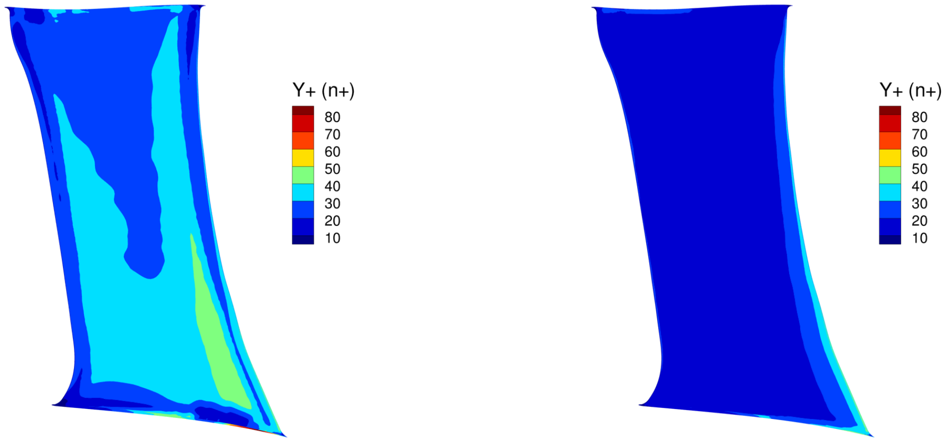

(a) LES1. (b) LES2.

Figure 2.21: n^+ values, stator pressure side.

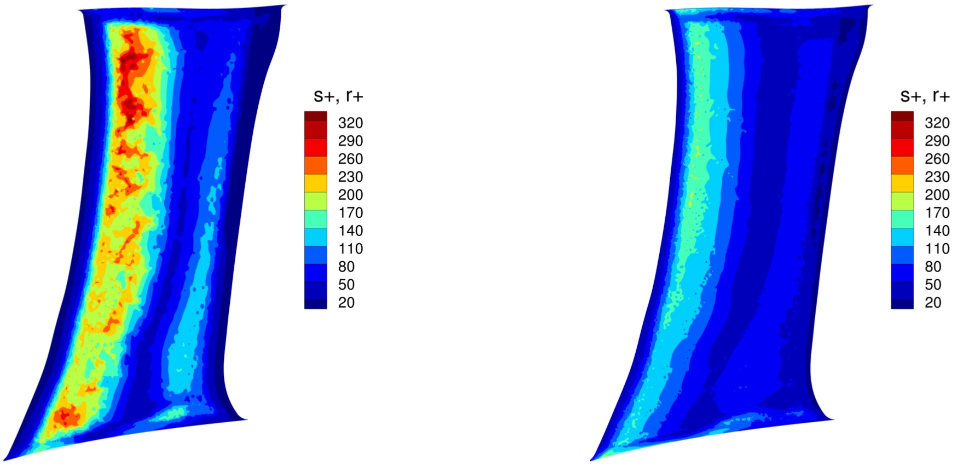

(a) LES1.

(b) LES2.

Figure 2.22: s^+ and r^+ values, stator suction side.

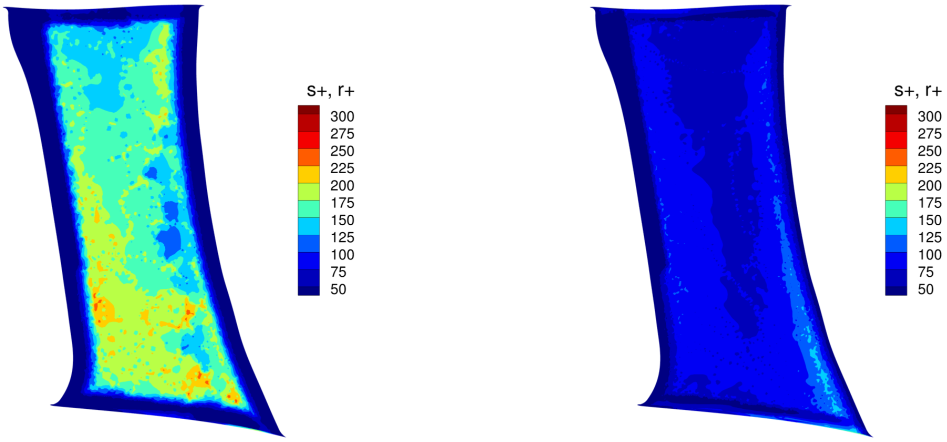

(a) LES1.

(b) LES2.

Figure 2.23: s^+ and r^+ values, stator pressure side.

Simulation Set-Ups: LES simulation — Summary

Computational domain

- Rescaled OGV to reduce the computational domain while maintaining the stage performance.
- 1 rotor blade - 2 rescaled stator vane configuration.
- IGV removed.

Numerical parameters

- Solver: TurboAVBP.
- Subgrid scale: WALE model.
- Non reflecting characteristic boundary conditions:
    - Inlet boundary condition: experimental ambient pressure and temperature, **no** injected turbulence.
    - Outlet boundary conditions: mean total pressure and temperature retrieved from the RANS simulation.
    - Side boundary condition: periodic boundary condition.
    - Solid wall boundary condition: boundary layer modeled using a wall law inducing a no-slip condition.

Mesh

- Hybrid unstructured mesh: prismatic cells on solid surfaces and tetrahedra in the rest of the domain.
- Two levels of mesh refinement:
    - Mesh LES1: 95 millions of cells.
    - Mesh LES2: 210 millions of cells.
- Wall mesh characteristic :
    - Mesh LES1: 8 prism layers. $n^+ < 60$, $s^+ < 300$, $r^+ < 300$.
    - Mesh LES2: 14 prism layers. $n^+ < 40$, $s^+ < 150$, $r^+ < 150$.
- The range of mesh quality parameter values guarantees reliable simulations.

2.3 Convergence check

2.3.1 RANS simulation

The convergence of the RANS simulation has been checked by monitoring both RMS values of the residuals (stabilization after a decrease of around three orders of magnitude) and the convergence of key variables (inlet mass-flow rate, total pressure at the outlets, torque on the blades and vanes all rendered dimensionless by their respective final value). The converged state has been reached after around 1000 iterations as shown in figs. 2.24 and 2.25.

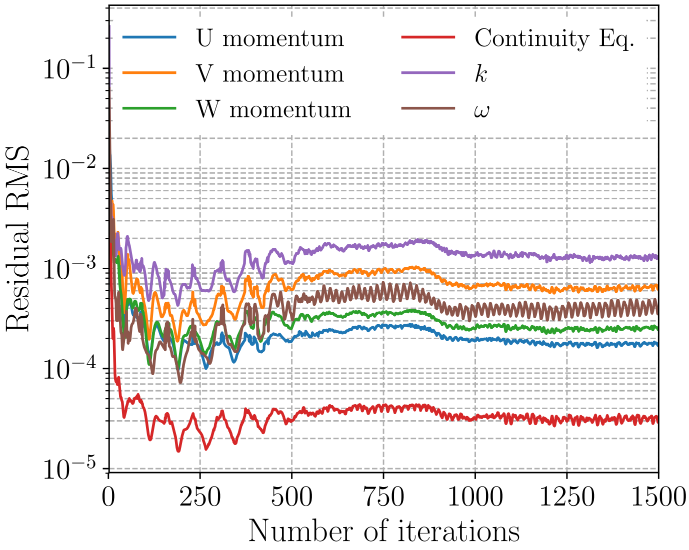

Figure 2.24: Evolution of the RMS values of the residuals with respect to the number of iterations (RANS simulation).

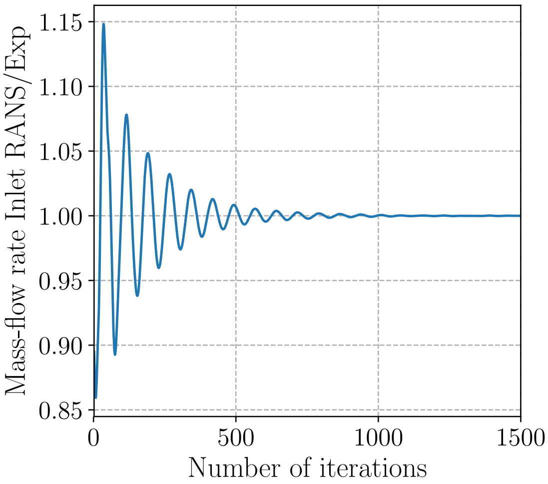

(a) Inlet mass-flow rate (RANS simulation).

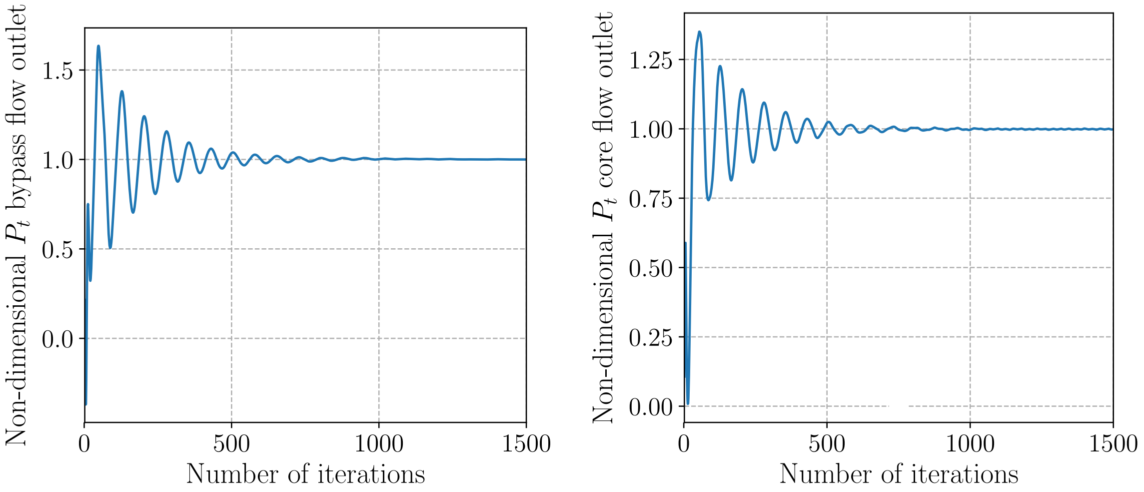

(b) P_t at the bypass flow outlet.

(c) P_t at the core flow outlet.

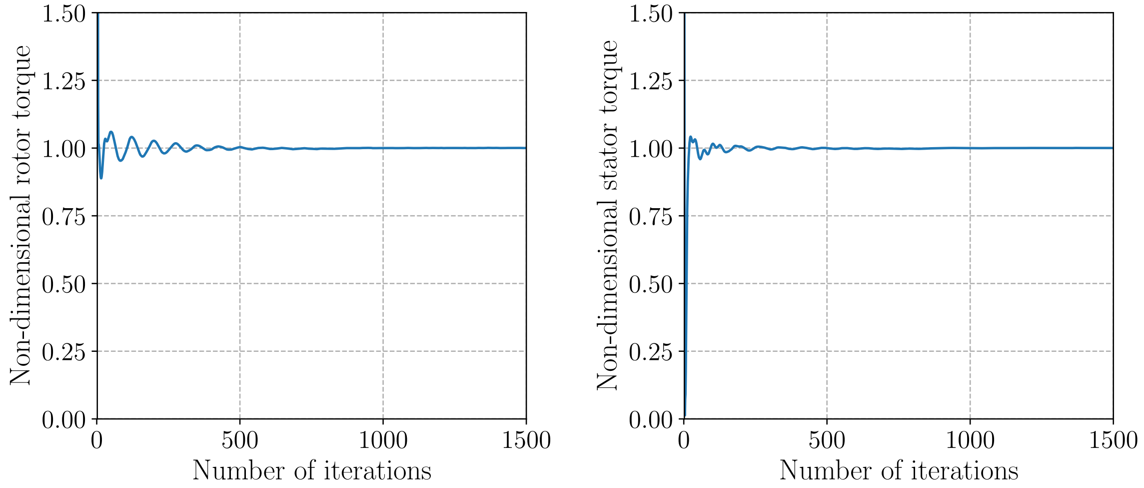

(d) Rotor torque.

(e) Stator torque.

Figure 2.25: Evolution of key variables with respect to the number of iterations (RANS simulation). P_t and torque values have been rendered dimensionless by their respective final value.

2.3.2 Large Eddy Simulations

2.3.2.1 Convergence monitoring strategy

Mean quantities: The convergence of the simulation has been checked by monitoring common integrated quantities (mass-flow rate at the inlet and outlets, fan pressure ratios in the bypass and core flows) as well as local quantities such as the pressure or the velocity using local control points (hereafter referred to as "probes"), the locations of which are shown in fig. 2.26. The probes located upstream of the splitter are fixed in the rotating frame of reference. The stabilization of integrated quantities ensures the convergence of the mean flow.

Statistics: As was performed by Leonard *et al.* [43] on the SDT configuration, the convergence of flow statistics has been checked by analyzing the signals retrieved from the probes with the method developed by Mockett *et al.* [198]. This method enables to estimate the statistical error

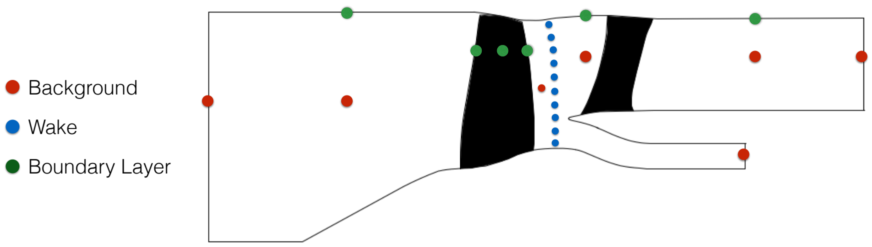

Figure 2.26: Probe locations.

of a finite time signal and is particularly suited to identify the end of the transient regime of an LES. It has been applied to all the probes to estimate the best time to start recording the statistics.

The main principles of this method are briefly presented hereafter. Let $x(t)$ be a signal of length T. Mockett *et al.*'s method is a two-step method. Firstly, the signal $x(t)$ is divided into a series of windows of length T_w. For $T_w \ll T$, a first estimate of the statistical error can be obtained using :

$$\epsilon(T_w) \approx \frac{\sqrt{\langle(\hat{\phi}_{T_w} - \hat{\phi}_T)^2\rangle}}{\hat{\phi}_T}, \tag{2.5}$$

where $\hat{\phi}$ is the estimate of a statistical quantity (mean or standard deviation), $\hat{\phi}_T$ is the estimate obtained using the entire signal, $\hat{\phi}_{T_w}$ is the estimate of each subsignal of length T_w, and $\langle\ \rangle$ denotes averaging over the available data windows. By varying the window size, the error trend as a function of sample length can be estimated. As mentioned by Mockett *et al.*, this estimate naturally becomes decreasingly accurate as T_w approaches T since the number of available windows decreases. Unless long time-resolved benchmark signals are available (*e.g.*from comparable experiments), the usefulness of this method alone is therefore limited.

To further extend the method to estimate the statistical errors and predict their evolution for longer signals, analytical expressions to estimate the error on the average and standard deviation have been derived in the specific case of bandwidth-limited Gaussian white noise (of bandwidth B). Indeed, in this case, the error on the mean and standard deviation can be expressed as [199]:

$$\epsilon[\mu_x] = \frac{1}{\sqrt{2BT}}\frac{\sigma_x}{\mu_x}, \tag{2.6}$$

$$\epsilon[\sigma_x] = \frac{1}{\sqrt{4BT}}, \tag{2.7}$$

where μ_x and σ_x are respectively the mean and the standard deviation of the Gaussian white noise. These relationships remain valid for $BT \geq 5$. In the present case, since the signals do not correspond to bandwidth-limited Gaussian white noise, the mean and standard deviation are replaced with the values computed from the entire signal. B is then the only remaining unknown and is used as a curve-fitting parameter that is obtained as the lowest B for which the gaussian estimates intersect the curves obtained from eq. (2.5). The fact that the minimum intersecting B is sought means that the error estimate is actually maximized.

Figure 2.27 shows the fitting step for both mean and standard deviation on the pressure signal retrieved from one of the previously mentioned probes. As expected, the Gaussian error estimate over-predicts the error.

These two tools are then used to detect the initial transient content of a given signal. For a

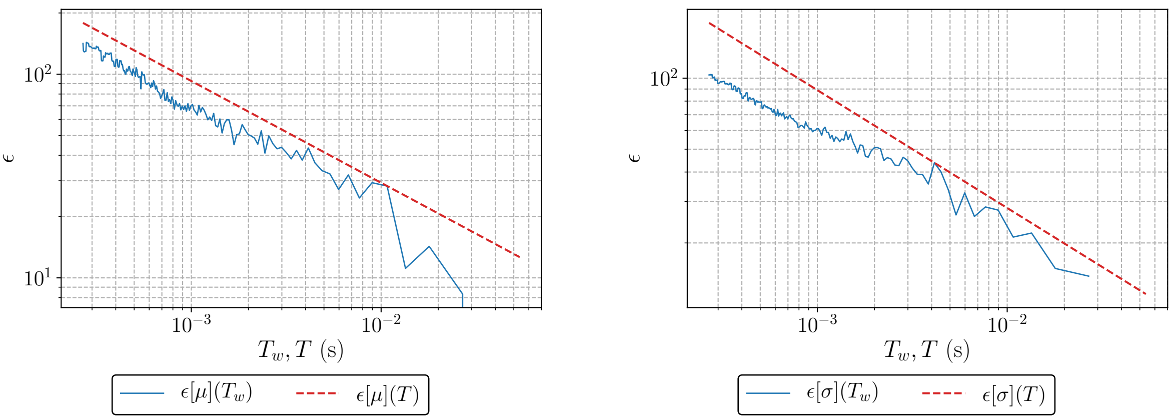

(a) Mean.

(b) Standard deviation.

Figure 2.27: Fitting step of Mockett's method.

signal of length T, exhibiting a transient character for $0 < t < t_t$ where t_t denotes the onset time of stationarity, the study of the distortions of both the mean and standard deviation over time makes it possible to identify the end of the transient signal.

To this end, the signal is successively shortened by removing samples from the beginning of the signal, with the shifted start time denoted t_0. The absolute statistical random error $\epsilon(\hat{\phi})(t_0)$ is computed using eqs. (2.5)-(2.7) for both the mean and the standard deviation as t_0 is varied. Mockett *et al.* indicate that the initial transient present for $t_0 < t_t$ will cause an increase in the absolute statistical error relatively to the signal without transient (for $t_0 > t_t$). Once the initial transient is entirely removed and the signal is shortened further, the absolute statistical error is then expected to rise because of the reduction of the time signal T. This means that t_t actually corresponds to a minimum of $\epsilon(\hat{\phi})(t_0)$ and also that a sufficient sample size over which the statistically steady state has been reached is required to accurately detect this minimum.

In order to detect this minimum, and consequently obtain a single value for t_t, Mockett *et al.* recommend to compute the mean $(\epsilon(\hat{\mu})(t_0))$ and standard deviation $(\epsilon(\hat{\sigma})(t_0))$ absolute errors and search for the minimum of the product of these quantities. Due to the shrinking of the sample when t_0 approaches T, the computed errors become increasingly unreliable, which could cause spurious minima for large t_0. For this reason t_0 is limited to $0 < t_0 < T/2$.

2.3.2.2 LES1

Mean quantities: Figures 2.28 and 2.29 present the evolution of the performance parameters with respect to the simulation time. These values were obtained from a mass-flow rate weighted average over an axial field cut at the splitter location, upstream of the stator. The mass-flow rates match the experimental data with a relative error below 1% after 2 complete rotations. Regarding the pressure ratios Π, both bypass and core fan pressure ratios have been stable from the beginning of the simulation with a relative error below 1% with respect to the experimental data.

Regarding the probe signals, they have been extracted every 250 time steps, which corresponds to a sampling rate of around 110 kHz. They have not been recorded from the beginning of the simulation but only after around 4 rotations. Nevertheless, they can be exploited to confirm the convergence of other mean quantities over the recorded time. Figure 2.30 shows the evolution of the static pressure and the axial velocity, rendered dimensionless by the mean value of the raw signal, for different probe locations. All the probe signals display an almost constant running

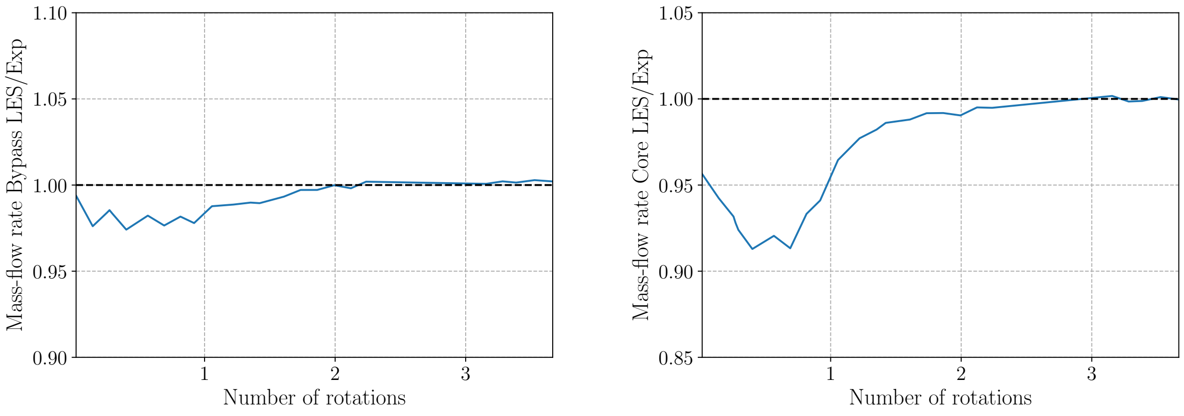

(a) Bypass.
(b) Core.

Figure 2.28: Evolution of the mass-flow rate in the bypass and in the core sections.

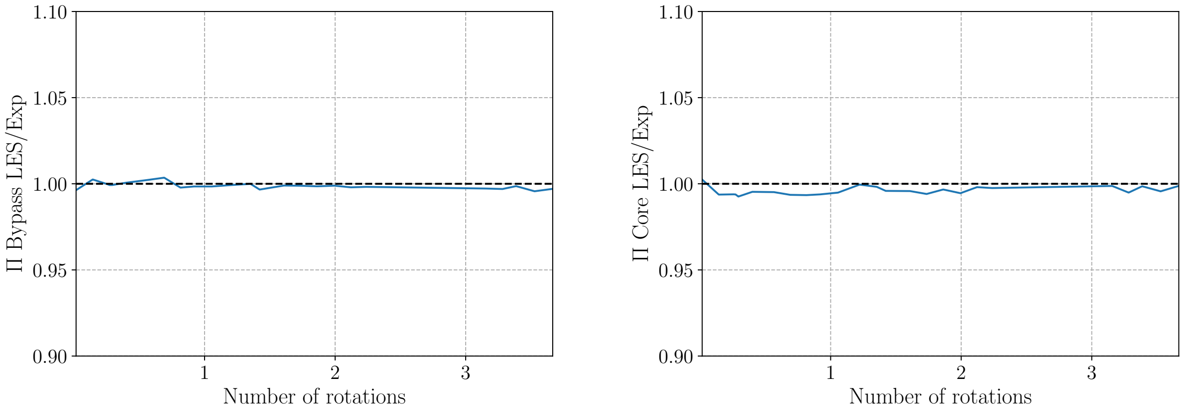

(a) Bypass.
(b) Core.

Figure 2.29: Evolution of the fan pressure ratio in the bypass and in the core sections.

average. Along with the stabilization of the performance parameters, this confirms the converged state of the mean flow.

Statistics: Following Mockett *et al.*'s method (see section 2.3.2.1), fig. 2.31 shows the evolution of the product of the mean and standard deviation absolute errors for some of the previously presented probes (see appendix C for the other probes). Both the raw product and its running average are plotted for a better reading. For all the presented probes, the absolute minimum of the product is reached before 105 blade passing periods, which indicates that the simulation is statistically converged after this point. Some spurious local minima due to the shrinking of the signal also appear later without preventing a clear identification of t_t. Some probes display an absolute minimum that is located at the very beginning of the sample. This is due to the fact that the probes were not introduced from the beginning of the simulation, which induces that some of the recorded signals may not exhibit any transient character. This is the case of probe 5 for instance.

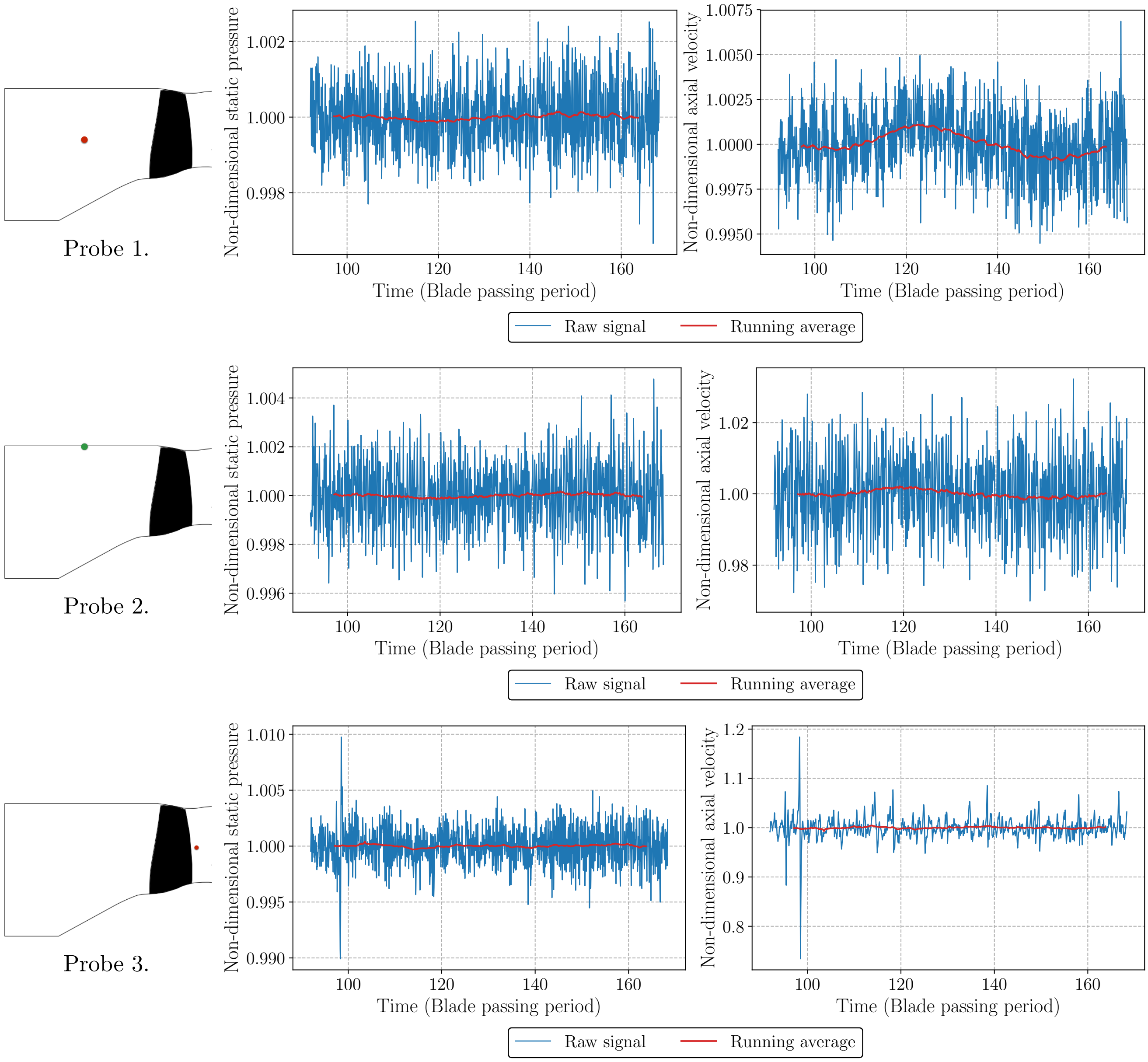

Figure 2.30: Instantaneous pressure/velocity signals and running average at different probe locations.

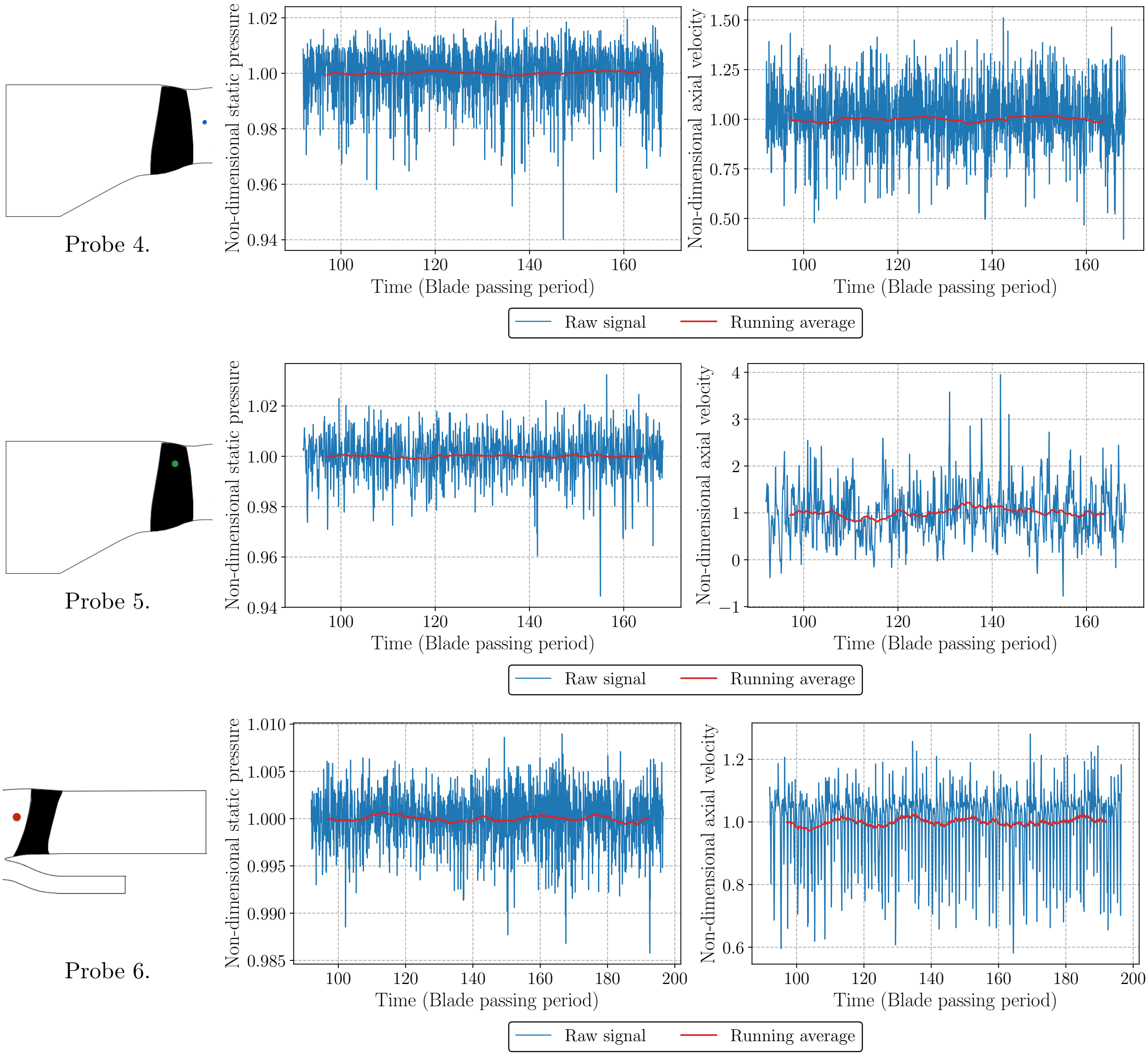

Figure 2.30: Instantaneous pressure/velocity signals and running average at different probe locations.

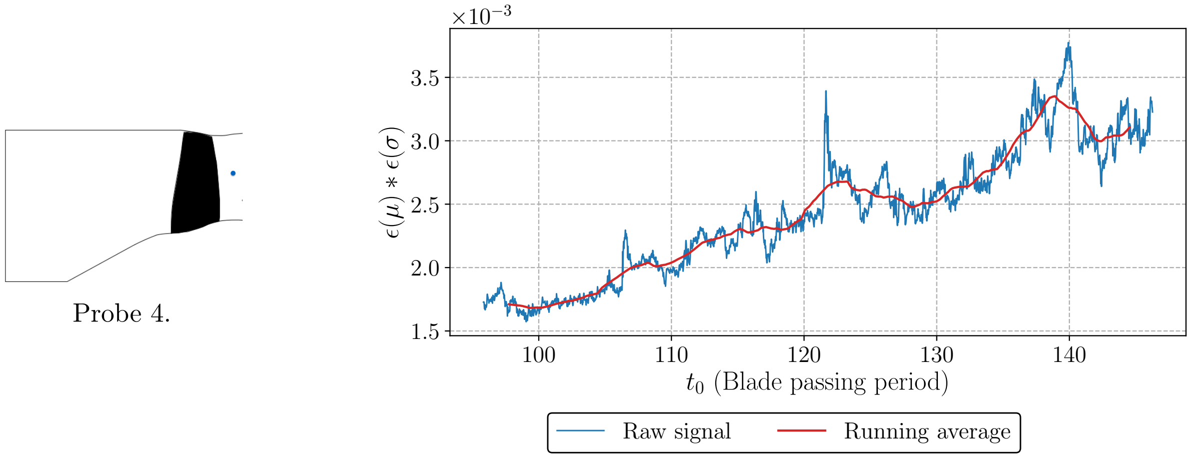

Probe 4.

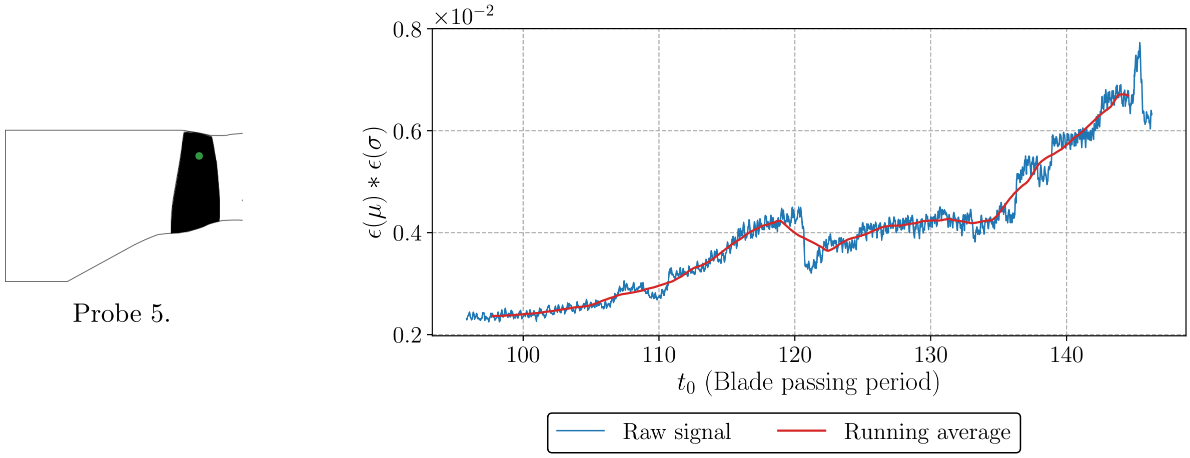

Probe 5.

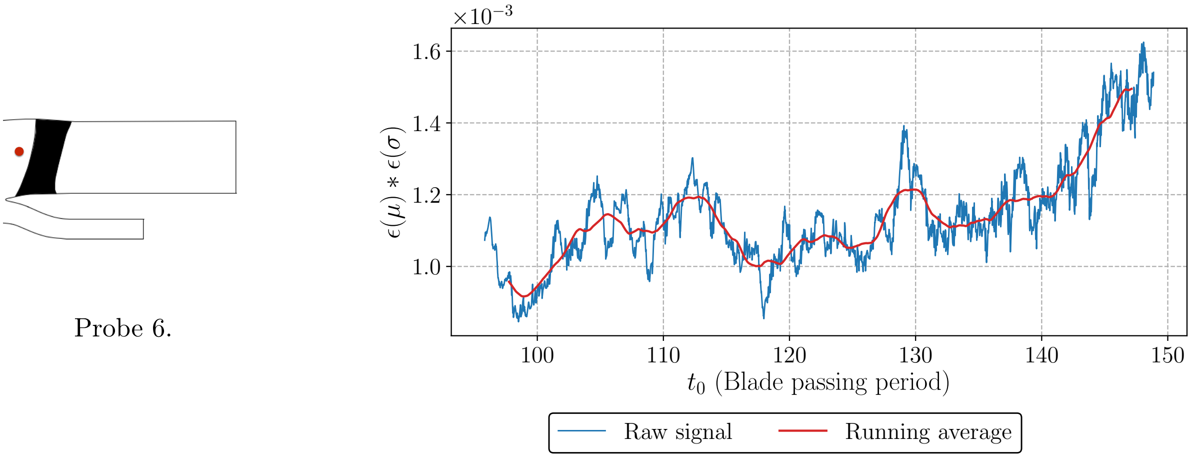

Probe 6.

Figure 2.31: Evolution of the product of the mean and standard deviation of the probe pressure signals following Mockett *et al.*'s methodology.

2.3.2.3 LES2

Mean quantities: Figures 2.32 and 2.33 present the evolution of the performance parameters with respect to the simulation time. Even though the LES2 has been initialized using an LES1 solution, the outlet mass-flow rates have needed 2 rotations to reach a constant value, whereas the fan pressure ratio has been stable from the beginning of the simulation. One can note that the mass-flow rates at both outlets have slightly drifted from the experimental data. This point, which is discussed in chapter 3, is inherent to the modifications induced in the flow by the mesh refinement and does not question the convergence of the simulation.

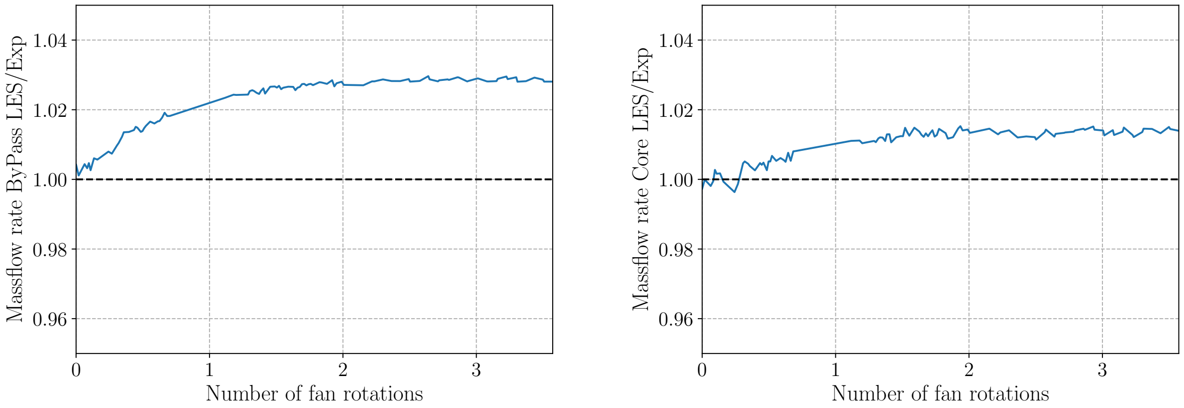

(a) Bypass.

(b) Core.

Figure 2.32: Evolution of the mass-flow rate in the bypass and in the core sections.

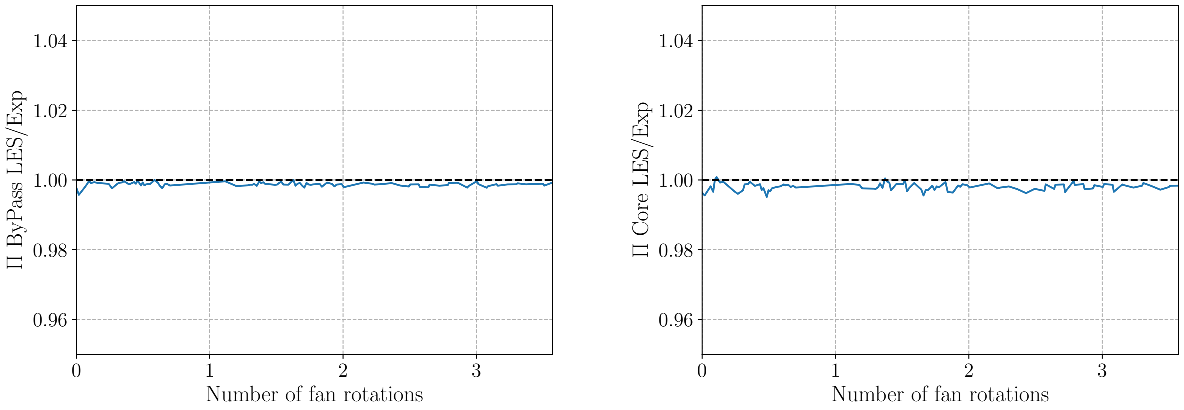

(a) Bypass.

(b) Core.

Figure 2.33: Evolution of the fan pressure ratio in the bypass and in the core sections.

Regarding the probe signals, they have been extracted every 300 time-steps, which corresponds to a sampling rate of 120 kHz. Figure 2.34 shows the evolution of the static pressure and the axial velocity rendered dimensionless using the mean value of the raw signals, for different probe locations.

These probe signals show that the mean flow convergence is reached after at least 30 blade passing periods, which corresponds to 1.5 fan rotations.

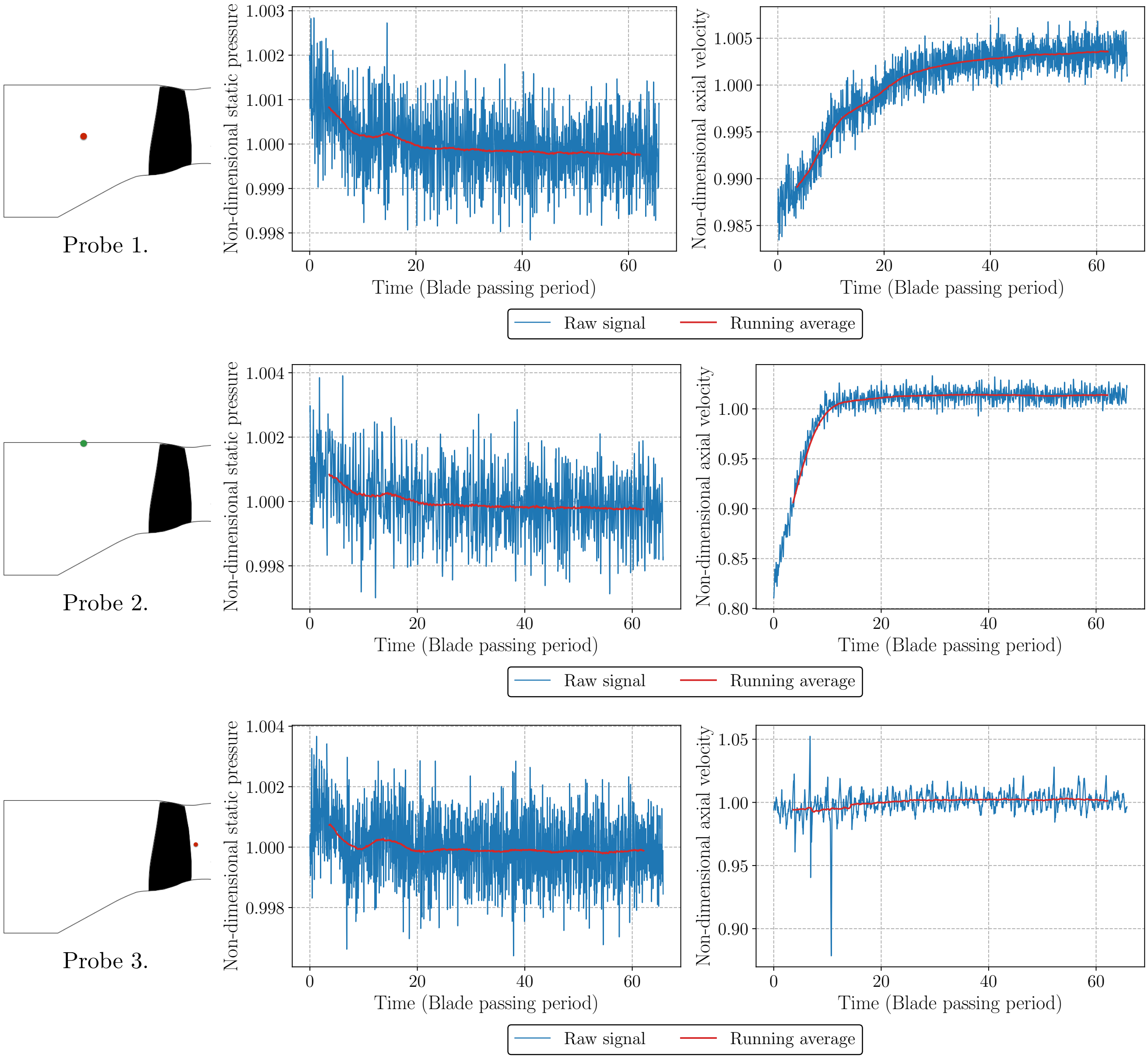

Figure 2.34: Instantaneous pressure/velocity signals and running average at different probe locations.

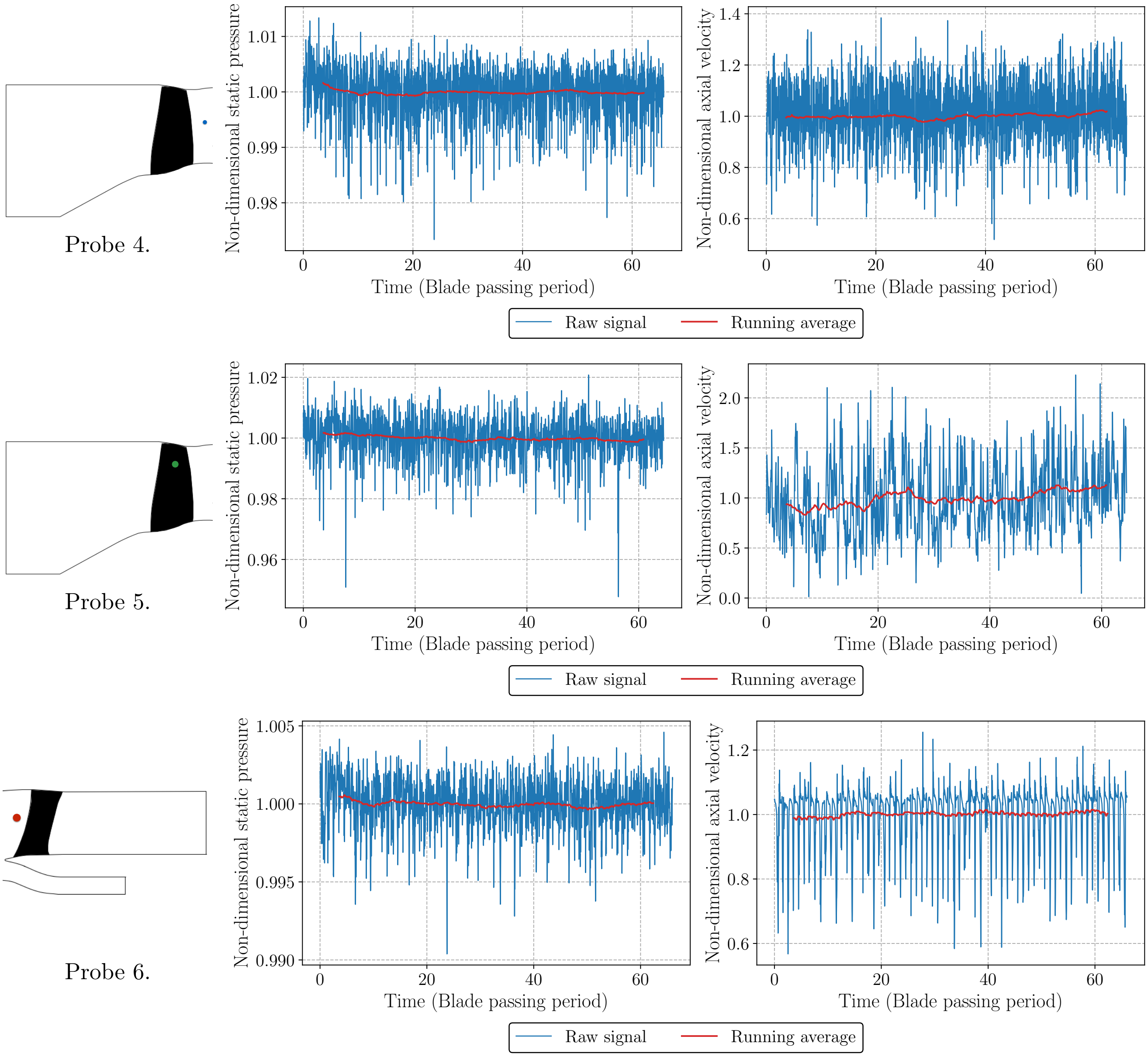

Figure 2.34: Instantaneous pressure/velocity signals and running average at different probe locations.

Statistics: Figure 2.35 shows the evolution of the product of the mean and standard deviation absolute errors for some the previously presented probes, as performed for LES1 (see appendix C for the other probes). The end of the transient period, which corresponds to the absolute minimum of the previously mentioned product, is reached before 33 blade passing periods. The simulation is considered as statistically converged from this point.

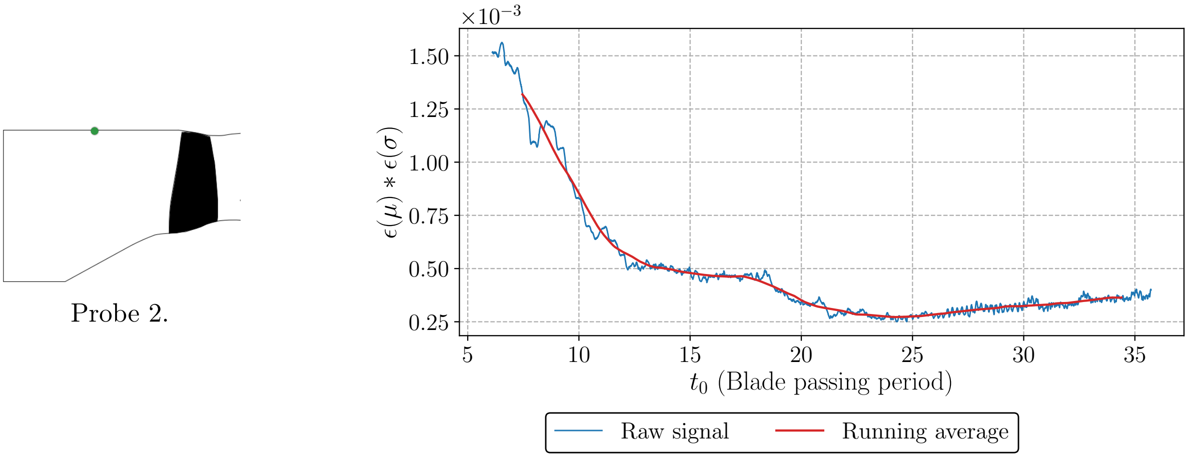
Probe 2.

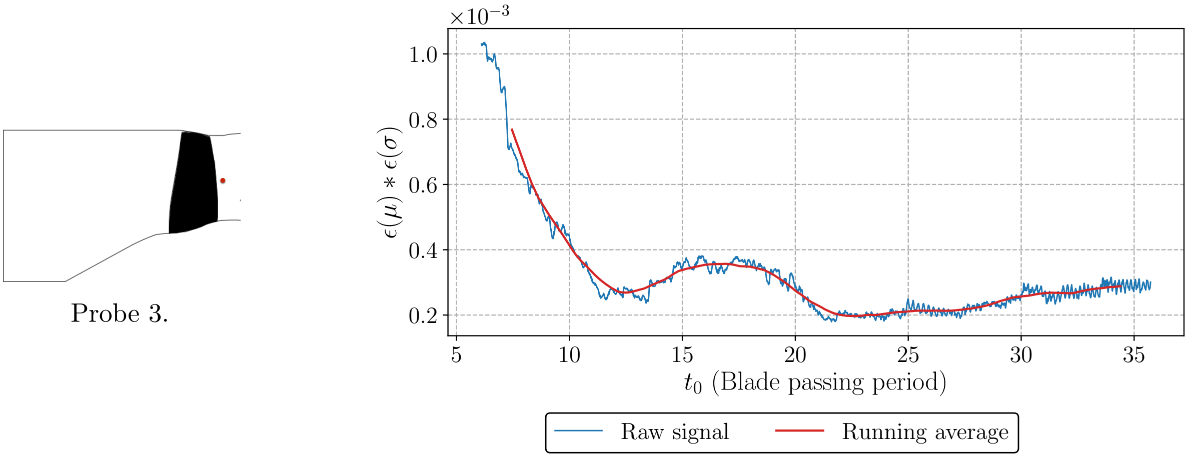
Probe 3.

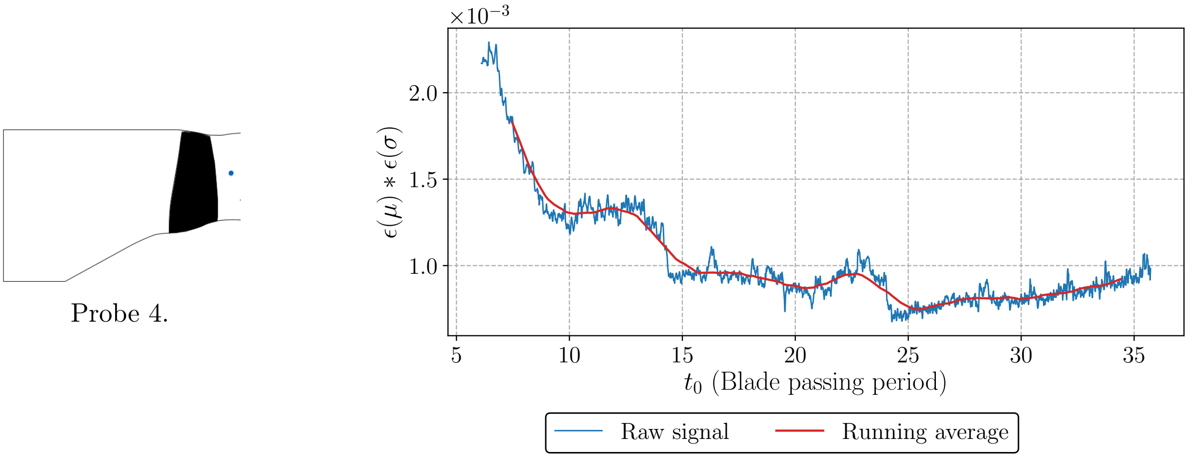
Probe 4.

Figure 2.35: Evolution of the product of the mean and standard deviation of the probe pressure signals following Mockett *et al.*'s methodology.

Convergence check — **Summary**

RANS

- RMS residual values stabilized and decreased by 3 orders of magnitude after 1000 iterations.
- Stabilization of key variables after 1000 iterations.

LES

- LES1:
  - Convergence of the mean flow reached after 2 fan rotations.
  - Statistical convergence monitored using Mockett *et al.*'s approach. Convergence of the statistics reached after 5 fan rotations.
- LES2:
  - Convergence of the mean flow reached after 1.5 fan rotations.
  - Statistical convergence monitored using Mockett *et al.*'s approach. Convergence of the statistics reached after 1.7 fan rotations.

2.4 Flow extractions

Figure 2.36 shows the flow extractions that have been performed during the acquisition runs (iterations after the statistical convergence). The velocity as well as the pressure fields have been extracted at the axial positions IN1, HW1 and LE1 and radial positions R1 and R2. HW1 is also the location where the hot-wire (HW) measurements have been performed. The pressure field on the fan and OGV skins have also been extracted.
All these extractions have been performed every 250 iterations for LES1 and every 300 iterations for LES2, which corresponds to sampling frequencies of about 110 kHz and 120 kHz, respectively.

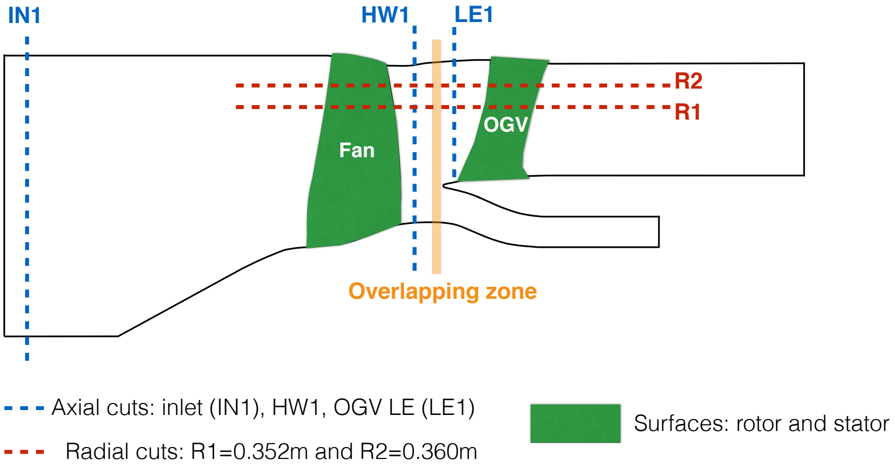

Figure 2.36: Sketch of the unsteady flow extractions.

2.5 Conclusion

In this chapter, a first insight into the experimental campaign that has been conducted on the ACAT1 fan stage has been given. The short gap geometry at approach conditions, which is the selected configuration for the present study, has been presented. The flow conditions of this configuration have been presented along with the corresponding main geometrical parameters. The numerical set-ups of the two chosen approaches (RANS and LES) have been described with details about the selected solvers, the modeling choices and the meshing strategy. The mesh statistics have been thoroughly analyzed for both the RANS and the LES meshes to show that the generated meshes respect the quality requirements for a wall-resolved RANS simulation and wall-modeled LES. In particular, the differences in the refinement between the LES1 and the LES2 meshes have been emphasized in order to clearly identify the different levels of accuracy of these two simulations. The convergence checking methodology has then been exhaustively presented and proofs of convergence have been provided for the two simulation approaches. The convergence study has notably enabled to detect the end of the transient regime of both LES and determine the starting point of the unsteady flow extractions that have been described in the last section of this chapter.

CHAPTER 3

Numerical investigation on the ACAT1 configuration: aerodynamic analysis

Introduction

This chapter presents the aerodynamic analysis of the RANS simulation and the two LES, whose numerical set-ups have been presented in the previous chapter. Results are validated against the performance parameters, the inter-stage pole rakes, and the hot-wire measurements at the HW1 position. A simultaneous comparison of the three simulations is carried out in order to emphasize the modifications induced by the simulation approaches and by the mesh refinement.

Contents

3.1 Performance parameters

Tables 3.1 and 3.2 present the performance parameters at approach condition obtained from the RANS computation and from the two LES. These values have been obtained from a mass-flow rate weighted average over an axial field cut at the splitter location, upstream of the stator. The agreement of the RANS results with the experimental data is excellent within the measurement uncertainty: the computed bypass pressure ratio is close to the experimental value (0.36% error) as well as the pressure ratio of the core flow (0.2% error). The total Fan Pressure Ratio (FPR), computed from the mass-flow rate weighted average of the core and bypass FPR, is also close to the experimental data. Similar comments can be made for the performance parameters obtained with the LES1. Regarding the LES2, however, larger discrepancies are observed, especially in the bypass flow. This is mainly due to a significant modification of the flow topology on the stator vane, which will be shown in the following sections.

	Massflow rate (kg/s)		
	Bypass	Core	Total
Experiment	48.745	6.411	55.156
RANS	48.745	6.411	55.156
LES1	48.787 (+0.09%)	6.395 (−0.25%)	55.186 (+0.05%)
LES2	50.108 (+2.8%)	6.500 (+1.4%)	56.647(+2.7%)

Table 3.1: Mass-flow rates obtained from the simulations at approach condition.

	Fan pressure ratio		
	Bypass	Core	Total
Experiment	1.110	1.100	1.109
RANS	1.106 (−0.36%)	1.098 (−0.2%)	1.105 (−0.34%)
LES1	1.106 (−0.36%)	1.095 (−0.45%)	1.105 (−0.36%)
LES2	1.109 (−0.01%)	1.098 (−0.19%)	1.107 (−0.18%)

Table 3.2: Fan pressure ratios obtained from the simulations at approach condition.

3.2 Mean flow

This section is devoted to the comparison of the mean flow obtained from the three numerical simulations. As the RANS simulation is a steady approach, no additional averaging has been required for this simulation. It should be pointed out that the mixing plane approach implies a circumferential averaging between the rotor and the stator sub-domains, which prevents from observing the rotor wakes in the stator domain. Concerning the high-fidelity simulations, LES1 and LES2 have been averaged over approximately 5 and 2 fan rotations, respectively. In this case, the averaging process is performed in the reference frame of each sub-domain: the rotating frame for the rotor and the stationary frame for the stator. As a consequence, even though the rotor wakes are convected through the rotor-stator interface, this averaging process makes them vanish in the stator mean solution.

3.2.1 Meridional plane

A convenient way to get a qualitative overview of the mean flow is to use the meridional plane. It provides a view of the axial momentum weighted azimuthal average of each variable of interest, at each radial and axial positions of a user-defined target grid. In the present case, the meridional plane contours for the absolute Mach number (fig. 3.1), the static pressure (fig. 3.2), the total pressure (fig. 3.3) and the flow angle $\alpha = \arctan(V_\theta/V_x)$ (fig. 3.4) have been plotted on a grid using 80 points in the axial direction and 40 points in the radial one. The blades and vanes are indicated using black solid lines. For the most part, the different fields are consistent from one simulation to another as only minor discrepancies can be observed. Regarding the absolute Mach number (fig. 3.1), the main difference appears on the duct walls, especially on the shroud where the LES1 displays lower Mach number values than the two other simulations. This may indicate a thicker boundary layer for the LES1, which might be a consequence of a lack of mesh refinement in this region since the LES2 does not exhibit such flow features. In fig. 3.2, the only difference is observed downstream of the OGV where the RANS seems to predict a more intense compression of the flow since the static pressure levels over the whole vane span are higher than those of the two other simulations. A slightly higher total pressure is observed downstream of the vane in the LES1 and the LES2, as depicted in fig. 3.3. As for the flow angle, it is almost identical for the three simulations as shown in fig. 3.4, except in the inter-stage tip region where the LES2 displays lower values than both the RANS and the LES1. The flow angle is close to zero downstream of the stator, showing that the flow is correctly straightened up by the OGV. In the core flow, however, the flow angle remains quite significant because the IGV has been removed from the computational domain.

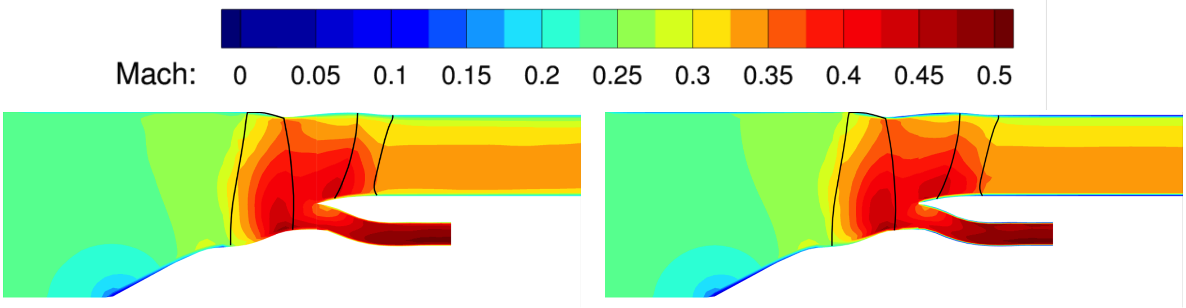

(a) RANS

(b) LES1

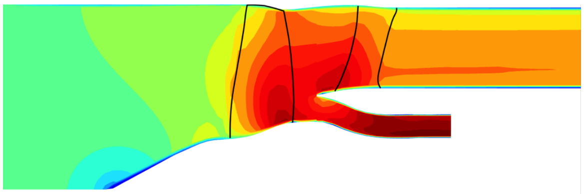

(c) LES2

Figure 3.1: Meridional plane, absolute Mach number.

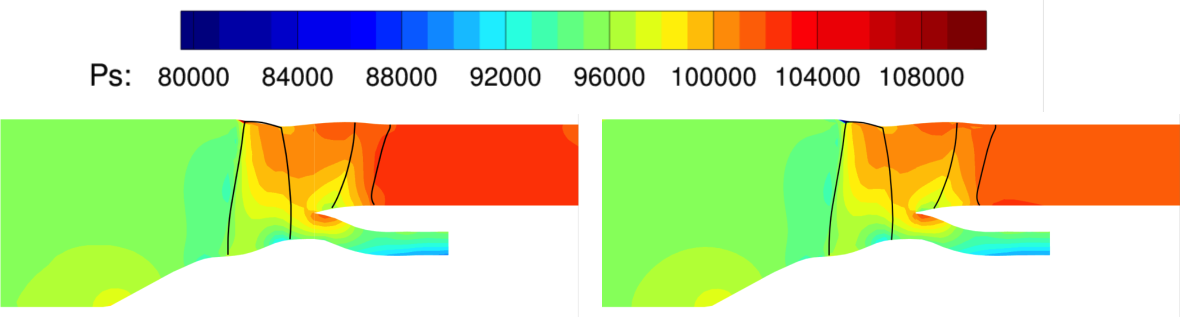

(a) RANS (b) LES1

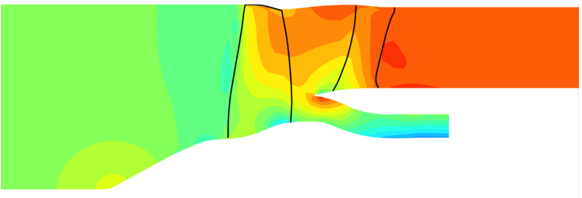

(c) LES2

Figure 3.2: Meridional plane, static pressure.

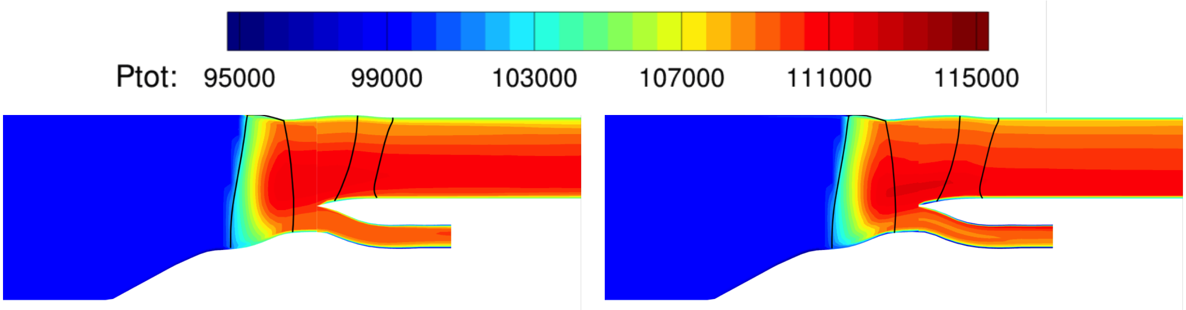

(a) RANS (b) LES1

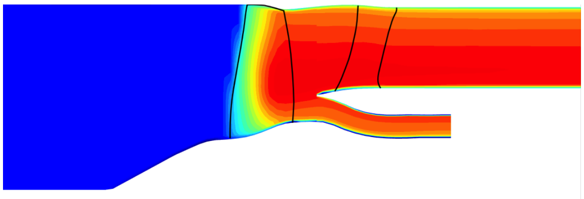

(c) LES2

Figure 3.3: Meridional plane, total pressure.

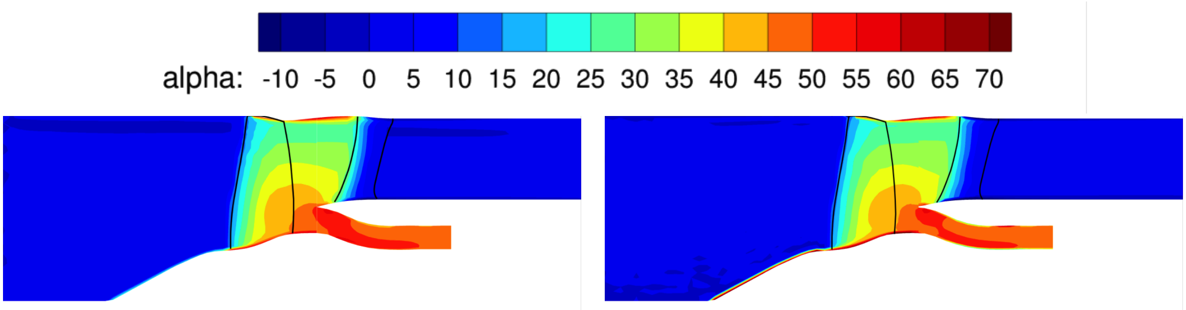

(a) RANS

(b) LES1

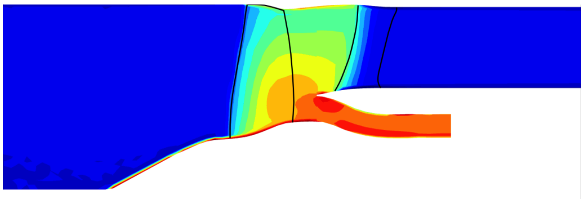

(c) LES2

Figure 3.4: Meridional plane, flow angle.

3.2.2 Radial profile

The previous section has shown that the meridional view of the three simulations are relatively similar, qualitatively speaking. In order to be more quantitative, the inter-stage total pressure and total temperature profiles have been plotted in fig. 3.5 along with the experimental data measured by the pole rakes at the same location (X=-2.653 m). At this axial location, the cross-section includes both the core flow inlet section and the whole bypass flow section. The variables are divided by their respective experimental ambient values that were prescribed at the inlet of the simulations. The thick grey line indicates the splitter location.

All the simulations are in very good agreement with the experimental data, for both the total pressure and the total temperature. Regarding the total pressure, the LES1 displays the largest discrepancies with a slight overestimation from the splitter up to 40% of the duct height, and a constant underestimation in the rest of the bypass duct. The RANS and the LES2 show negligible differences with the experiment from the splitter up to 70% of the duct height. From this point, the RANS slightly underestimates the total pressure while the LES2 total pressure remains close to the experiment. It is not surprising that the largest discrepancies at the tip are observed for the RANS, since the SST turbulence model may have trouble to correctly predict the flow in the presence of anisotropic flows such as those encountered in the tip clearance region. Similar comments can be made for the total temperature.

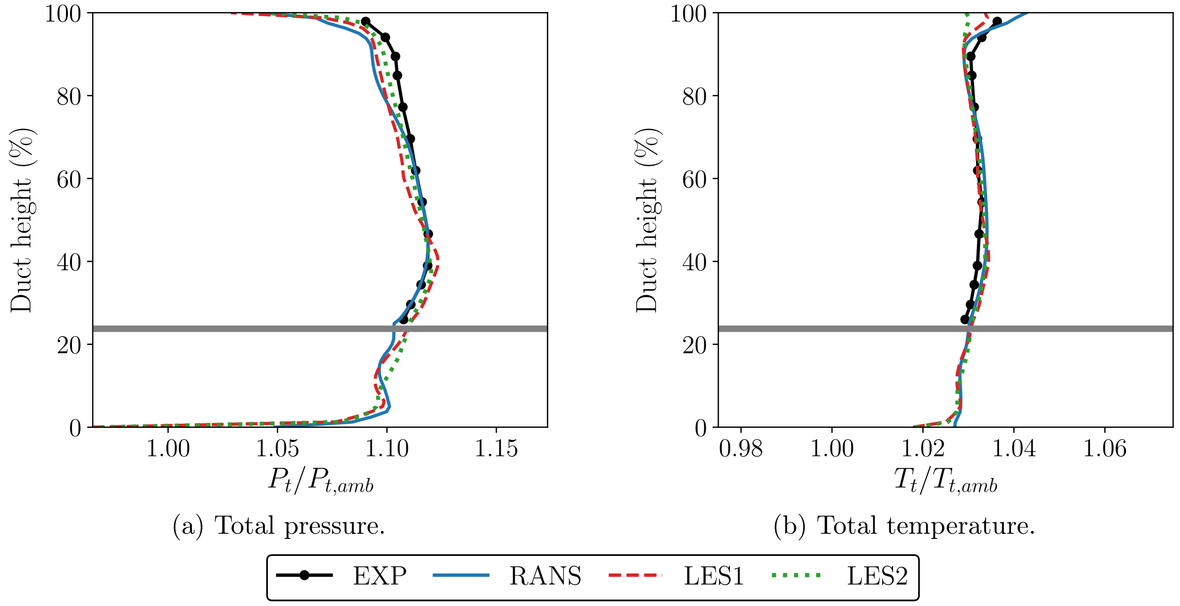

(a) Total pressure.

(b) Total temperature.

Figure 3.5: Mean total pressure and total temperature radial profiles in the inter-stage. The experimental data have been measured using the inter-stage pole rakes at the axial position X=-2.653 m, located upstream of the splitter (see fig. 2.2). The thick grey line indicates the location of the splitter.

3.2.3 Blade-to-blade mean flow

A first overview of the mean flow topology is depicted in figs. 3.6 and 3.7, which show a blade-to-blade view of the mean absolute Mach number and of the Turbulence Kinetic Energy (TKE) contours at different radial positions. The TKE corresponds to the k variable in the case of the RANS. For the LES, the TKE is defined as:

$$TKE = \frac{1}{2}\left(u'^2_{rms} + v'^2_{rms} + w'^2_{rms}\right), \tag{3.1}$$

where u'_{rms}, v'_{rms} and w'_{rms} are the RMS of the resolved velocity fluctuations in the x, y and z directions, respectively.

At 25% rotor span (see figs. 3.6a-3.6c and figs. 3.7a-3.7c), the flow upstream of the rotor down to half of its chord is very similar for the three simulations. At the leading edge of the rotor, however, a higher acceleration of the flow can be observed on the suction side for the two LES with respect to the RANS. At the same location, both LES predict an increase in the TKE, which suggests a transition of the boundary layer from laminar to turbulent. In the second half of the blade, a pocket of higher Mach number is formed on the suction side, its extent being larger for the two LES than for the RANS. The main discrepancies are observed for the rotor wakes, which have different thickness, axial evolution, and turbulence levels in each simulation. In the RANS simulation, the thickening of the wake is very progressive, leading to a wake that keeps almost the same thickness as it leaves the rotor trailing edge. The wakes from the LES1, on the contrary, display a sudden widening as they leave the rotor trailing edge. In this case, the velocity deficit in the wake is much smaller than the one observed in the RANS, whereas the TKE values are significantly larger. At this radius, the LES2 predicts the thinnest wakes, with the smallest velocity deficit, and a wake TKE that is slightly below the levels observed in the LES1. Since the Mach number contours of both LES are almost identical except in the wakes, it is likely that the differences observed between them are caused by the refined mesh on the blade skin of the LES2, which may modify the structure of the boundary layers and of the resulting wakes. This point will be specifically addressed in sections 3.2.5 and 3.2.6. The slight shift of the operating point might also contribute to this phenomenon.

At 50% rotor span (see figs. 3.6d-3.6f and figs. 3.7d-3.7f), the Mach number contours in the rotor domain are almost identical for the three simulations. The rotor wakes are, indeed, much more similar than those at 25% rotor span. A slightly higher acceleration is still observable at the leading edge of the rotor for both LES. The TKE contours, however, reveal important differences between the three simulations. They all seem to predict a thick turbulent boundary layer on the suction side of the blade right after the leading edge, which then results in larger rotor wakes. The turbulence levels of the boundary layers substantially vary from one simulation to another, the LES1 and the RANS showing the highest and the lowest levels, respectively. In both LES, a second production point of TKE can be seen at about 60% rotor chord. Important discrepancies appear in the stator domain. The boundary layer on the vane suction side of the LES1 seems to be much thicker near the trailing edge, which leads to wider stator wakes. This phenomenon is neither observed in the RANS nor in the LES2, which consequently predict thinner wakes, the wakes of the RANS being the thinnest. The TKE contours show an increase in the TKE levels near the stator trailing edge, especially in the LES1, which suggests a laminar-turbulent transition. It will be shown in the next sections that the TKE production points, identified on both the rotor and the stator, are actually linked to strong 3D flow features (see section 3.2.4) and to a profound modification of the structure of the boundary layers, which is related to their laminar/turbulent state but also to their local separations from the blade and vane surfaces (see section 3.2.5).

Similar comments can be made at 75% rotor span (see figs. 3.6g-3.6i and figs. 3.7g-3.7i). In this case, the turbulence levels of the boundary layer on the rotor suction side, and the interaction of the latter with the downstream wake, are even more pronounced.

Finally, at 95 % rotor span (see figs. 3.6j-3.6l and figs. 3.7j-3.7l), the three simulations display relatively different flow topologies. In the rotor domain, the tip clearance flow strongly interacts with the inter-blade flow and with the downstream wake, which leads to a thicker wake in this region with respect to the other radial positions. This interaction is particularly pronounced in the LES2 in which a region with a Mach number of about 0.35, which seems to result from this interaction, covers half of the blade passage. This is also confirmed by the TKE contours. This phenomenon is less intense in the LES1 and in the RANS, but is still present. This particular feature has a noticeable effect on the flow topology in the stator domain. In comparison with the LES, the RANS displays a weaker acceleration of the flow on the stator suction side and a more important deceleration on the pressure side. The Mach number behind the stator row is also smaller than that observed in the LES. The stator wakes are a lot more similar than at other radial positions, with still thinner wakes for the LES2.

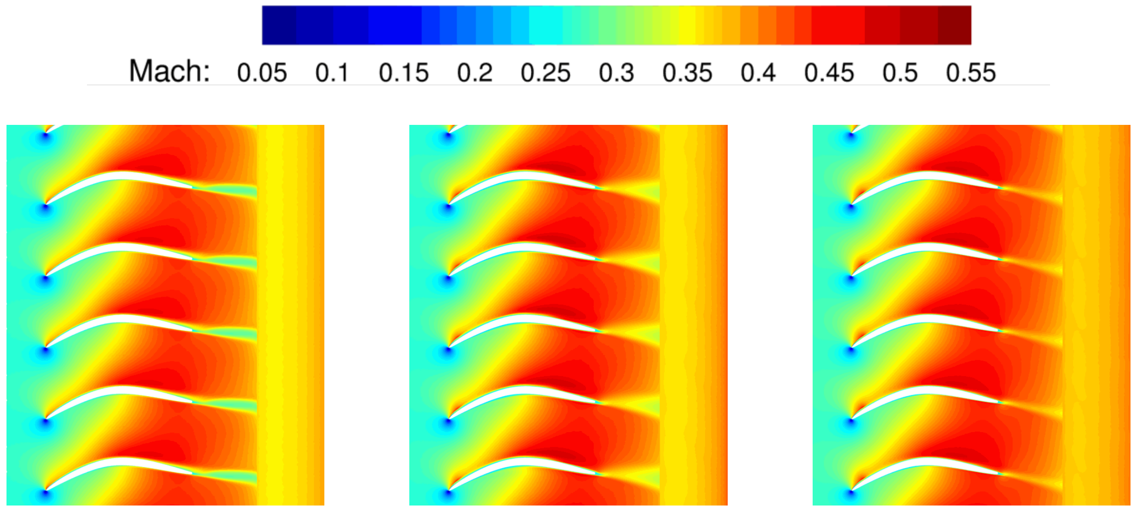

(a) RANS - 25% rotor span. (b) LES1 - 25% rotor span. (c) LES2 - 25% rotor span.

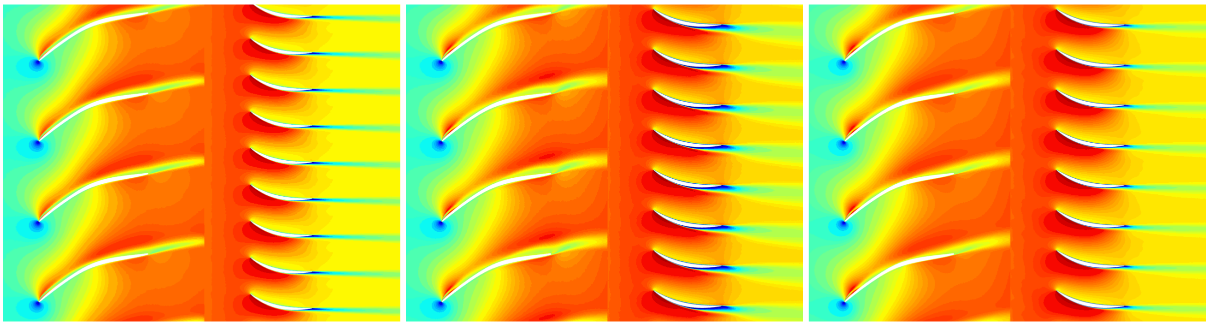

(d) RANS - 50% rotor span. (e) LES1 - 50% rotor span. (f) LES2 - 50% rotor span.

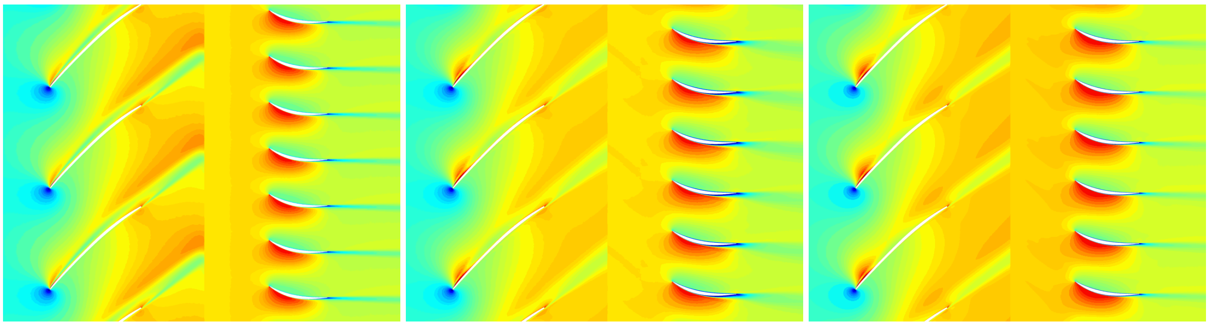

(g) RANS - 75% rotor span. (h) LES1 - 75% rotor span. (i) LES2 - 75% rotor span.

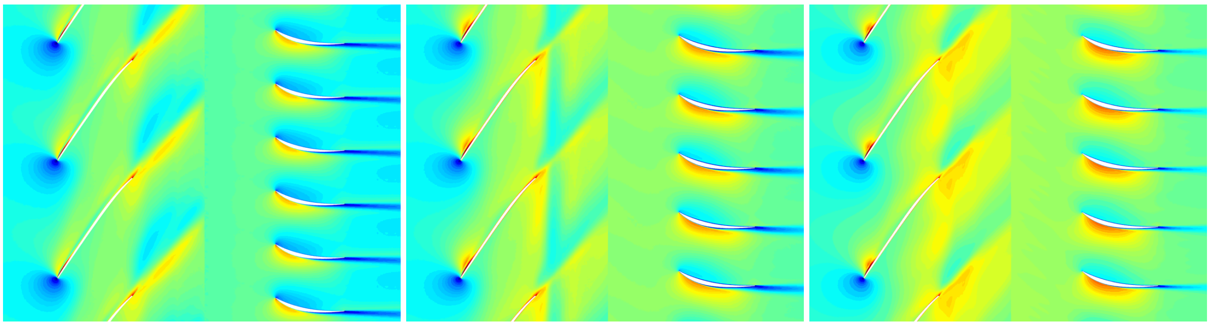

(j) RANS - 95% rotor span. (k) LES1 - 95% rotor span. (l) LES2 - 95% rotor span.

Figure 3.6: Mean Mach number field at different duct heights for each simulation.

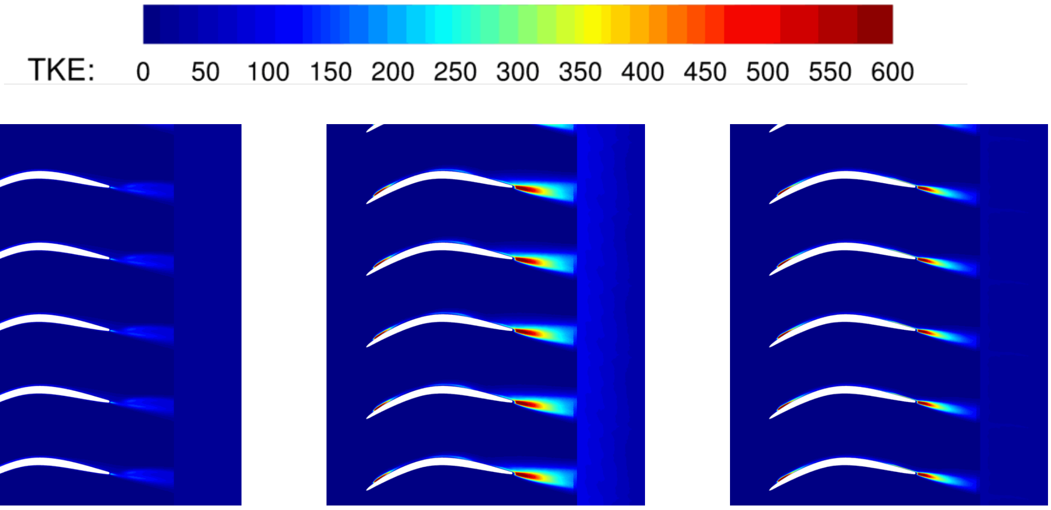

(a) RANS - 25% rotor span. (b) LES1 - 25% rotor span. (c) LES2 - 25% rotor span.

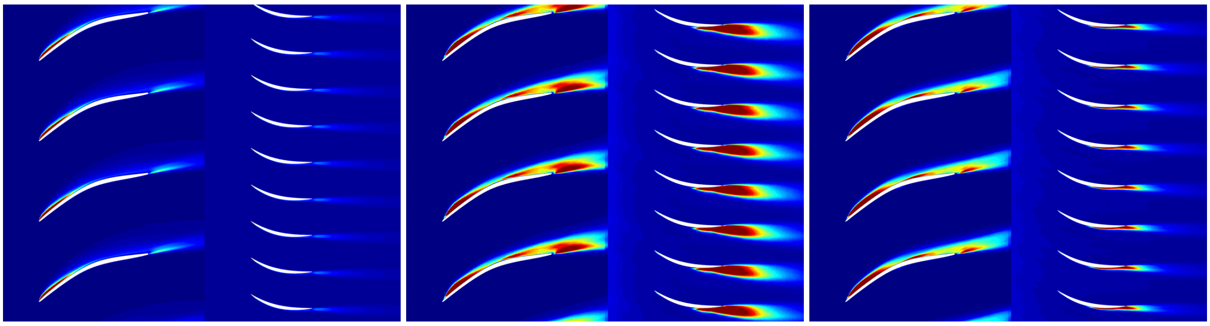

(d) RANS - 50% rotor span. (e) LES1 - 50% rotor span. (f) LES2 - 50% rotor span.

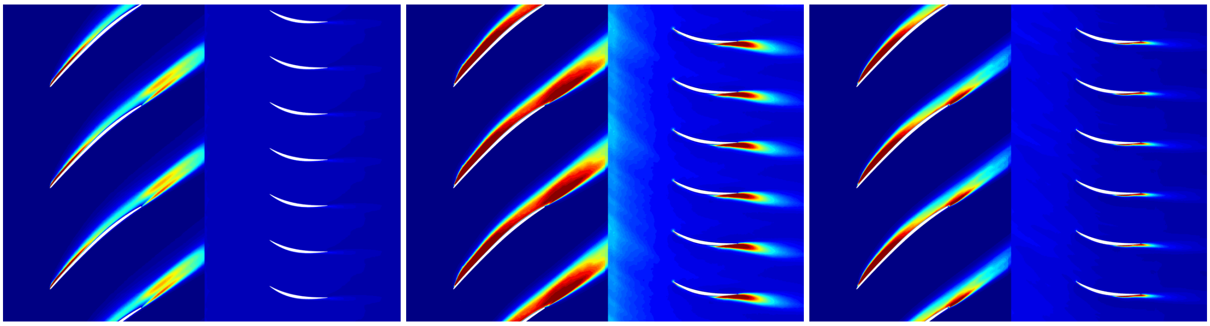

(g) RANS - 75% rotor span. (h) LES1 - 75% rotor span. (i) LES2 - 75% rotor span.

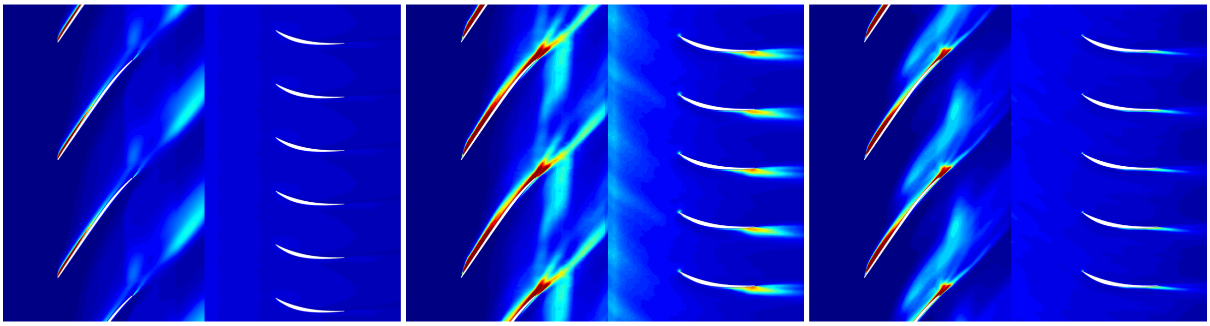

(j) RANS - 95% rotor span. (k) LES1 - 95% rotor span. (l) LES2 - 95% rotor span.

Figure 3.7: TKE field at different duct heights for each simulation.

3.2.4 3D flow topology

The previous 2D analysis has given a first overview of the main flow features in the ACAT1 fan stage at approach condition. A 3D analysis is however necessary to get a comprehensive understanding of the complexity of the flow, and to clearly identify the involved phenomena. To this aim, the streamlines colored by the vorticity magnitude have been plotted close to the fan (figs. 3.8 and 3.9) and to the OGV (figs. 3.10 and 3.11) in the rotating and stationary reference frames, respectively. In the case of the rotor, all simulations exhibit a strong radial flow with streamlines leaving the rotor TE at a much higher radial position than at the LE. This is particularly noticeable in both LES for which streamlines close to the hub at the LE, leave the fan at the TE at almost 70% rotor span. Additionally, streamlines going in the upstream direction can be observed in both LES at about 50% rotor span, near the TE, which suggests the presence of a recirculation region. In all simulations, a strong radial vortical structure develops at the LE of the fan. In the RANS, it extends from 40% rotor span up to the tip and displays a saw tooth profile. Its radial extent is much longer in both LES, covering almost 80% of the rotor span. In both LES, this radial structure appears to be partly formed of streamlines originating from the lower part of the fan LE and traveling up to the rotor tip, where they eventually feed the tip gap flow. This phenomenon is less visible in the RANS case as most of the streamlines originally caught in this structure leave it to continue their path down to the trailing edge. This is confirmed by fig. 3.9, which shows the tip gap flow streamlines only. In the RANS, the streamlines originates from the upper part of the fan LE, while the lower part streamlines directly feed the tip gap flow in both LES. Such a radial structure was also observed by Pérez Arroyo *et al.* [200] on the SDT configuration at approach condition, suggesting that it is a characteristic flow feature at low fan speeds. The intense TKE levels observed near the rotor LE in section 3.2.3 are thus partly due to the LE radial vortex. Nevertheless, equivalent TKE levels are found downstream of this structure especially above 25% rotor span, which suggests that it also contributes to the boundary layer transition. Furthermore, in all simulations, LE streamlines that are not necessarily caught in the radial vortex appear to move alternatively towards the upstream and downstream directions, indicating a potential flow recirculation that will be studied in the next section.

Regarding the flow around the stator, the RANS displays streamlines that are aligned with the stage axis over most of the OGV span. A slight radial flow can be observed near the hub and the shroud where the boundary layers on the duct walls interact with the flow near the vane surface. At the TE, at about 10% OGV span, a recirculation region can be observed. Both LES display significant differences with the RANS simulation. From the leading edge down to 60% stator chord, the flow remains aligned with the axial direction, as observed in the RANS results. From that point, a radial flow, which tends to bring the streamlines closer to the stator midspan, can be observed in both LES. The LES1 displays an intense radial vortical structure at 60% stator chord extending over the entire vane span. This vortical structure is very similar to the one observed at the rotor LE and is mainly composed of streamlines originating from the duct wall boundary layers, as shown in fig. 3.11. As with the rotor, some streamlines, which are not necessarily caught in the radial vortex, are moving alternatively towards the upstream and downstream directions, suggesting a recirculation region. This region also corresponds to the location of the intense TKE production observed in the previous section in the LES1. The radial vortex is however not present in the LES2, which suggests that it is a consequence of a lack of mesh refinement in the LES1. Its absence also explains the lower increase in TKE observed in the LES2 at this location, which indicates a weaker boundary layer transition.

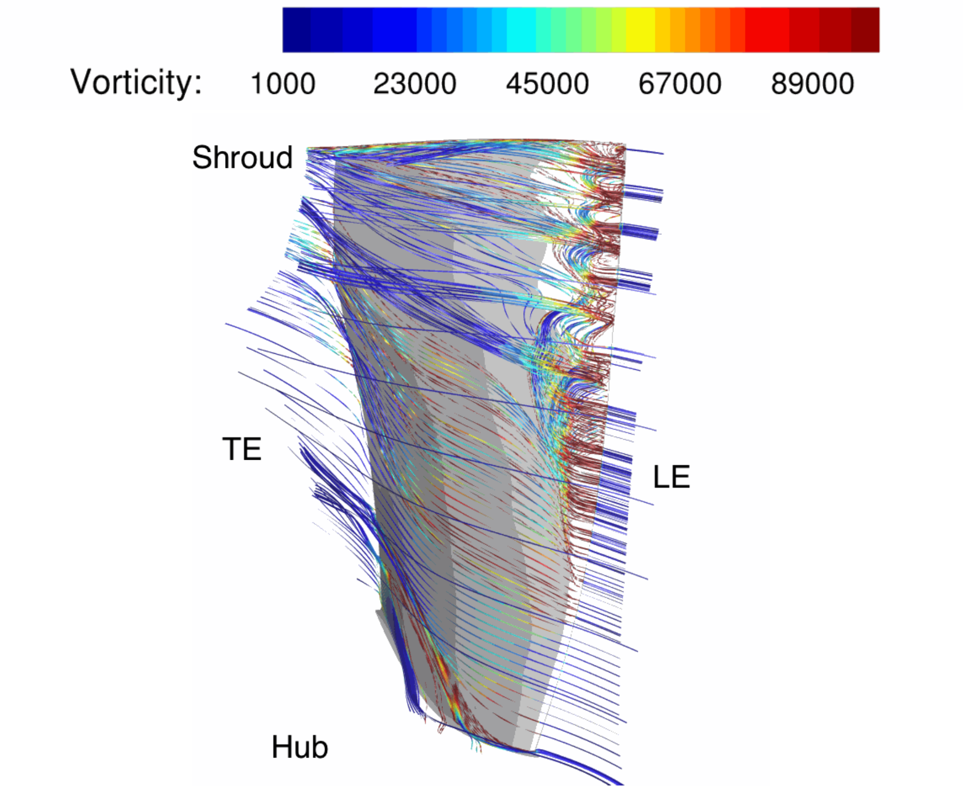

(a) RANS.

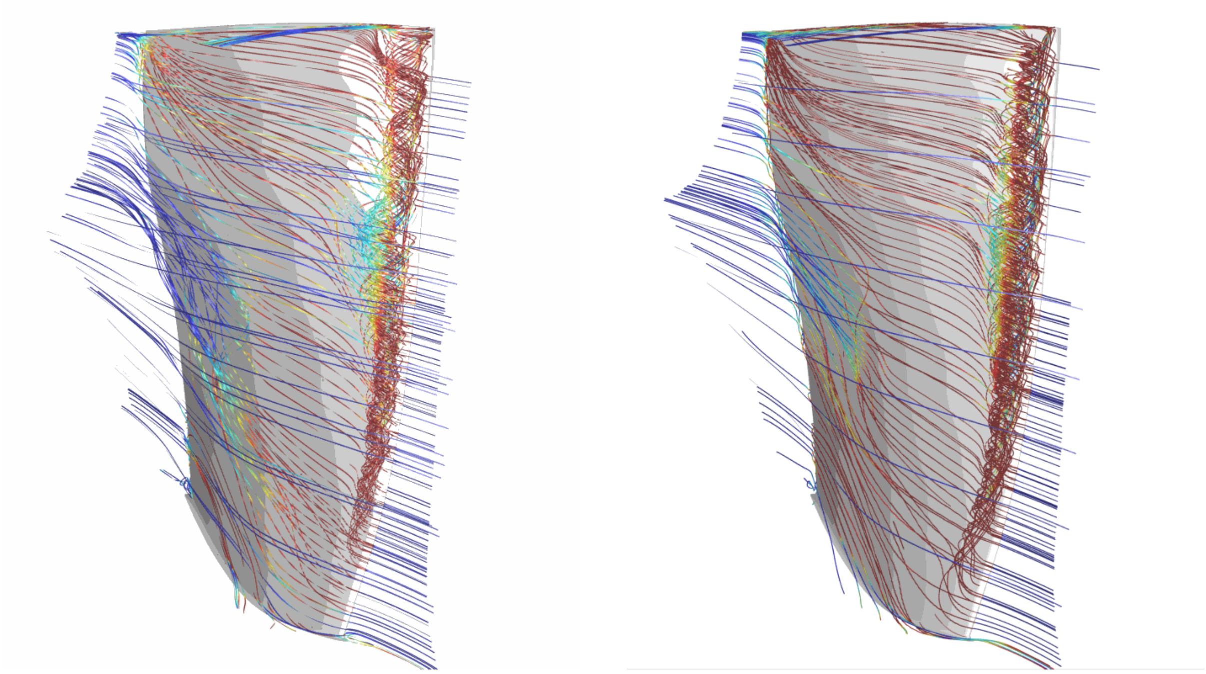

(b) LES1.

(c) LES2.

Figure 3.8: Streamlines in the rotor domain (suction side).

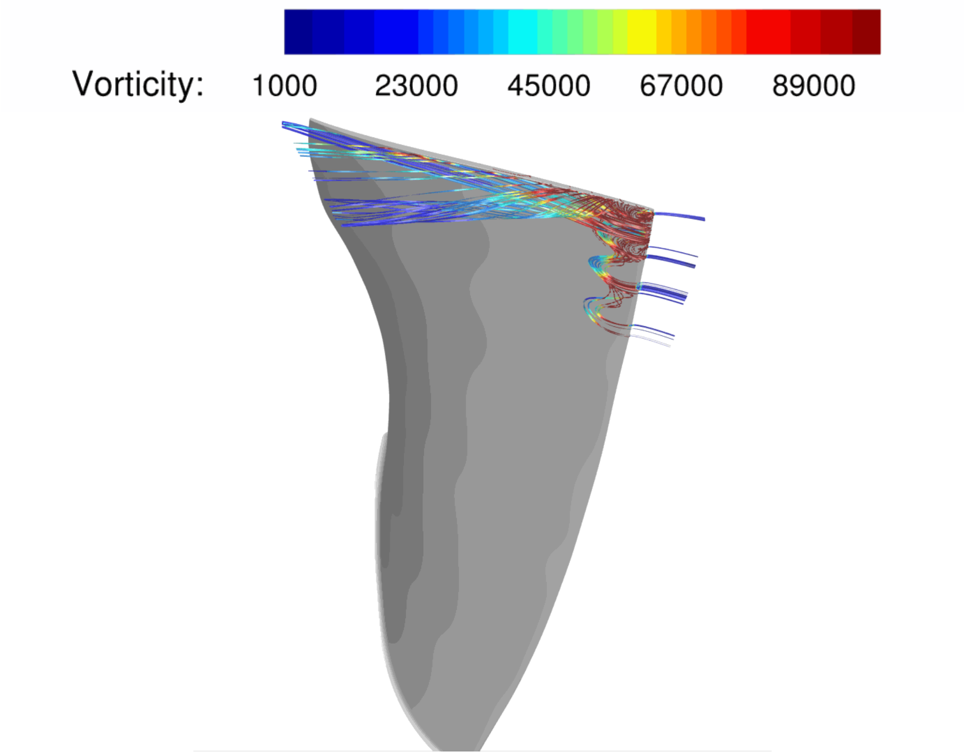

(a) RANS.

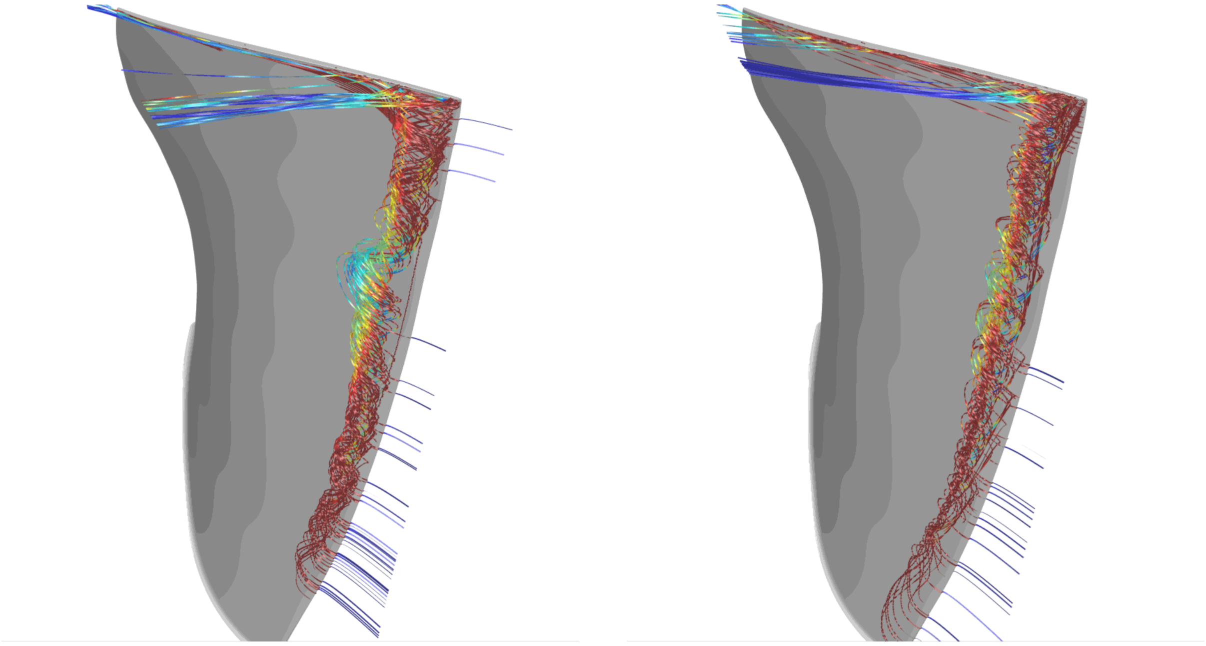

(b) LES1.

(c) LES2.

Figure 3.9: Streamlines in the rotor tip clearance (suction side).

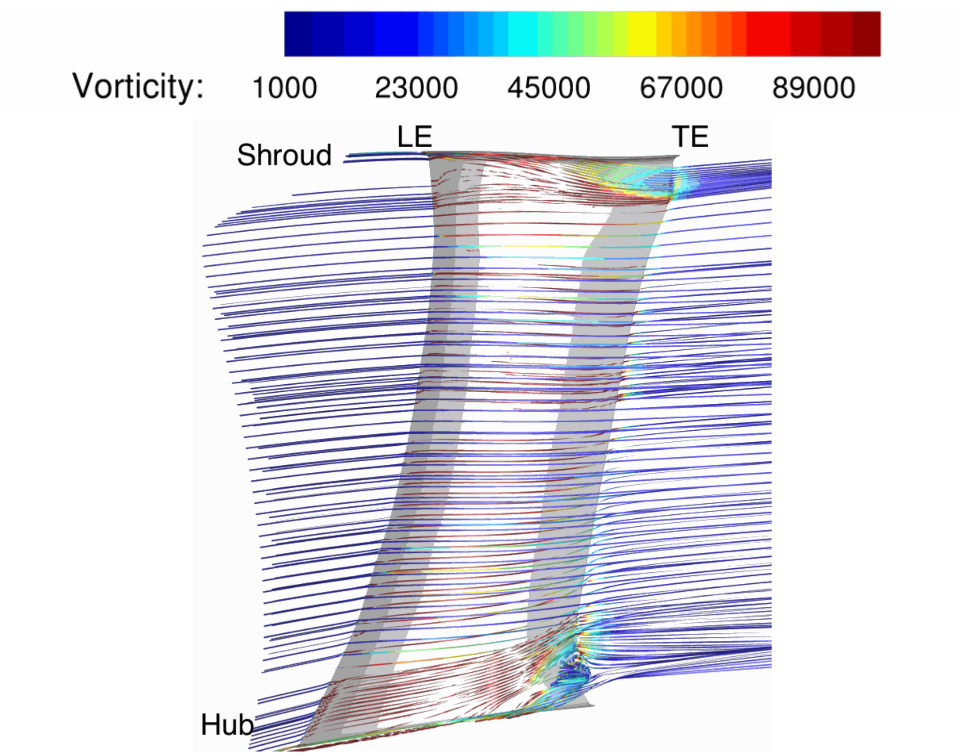

(a) RANS.

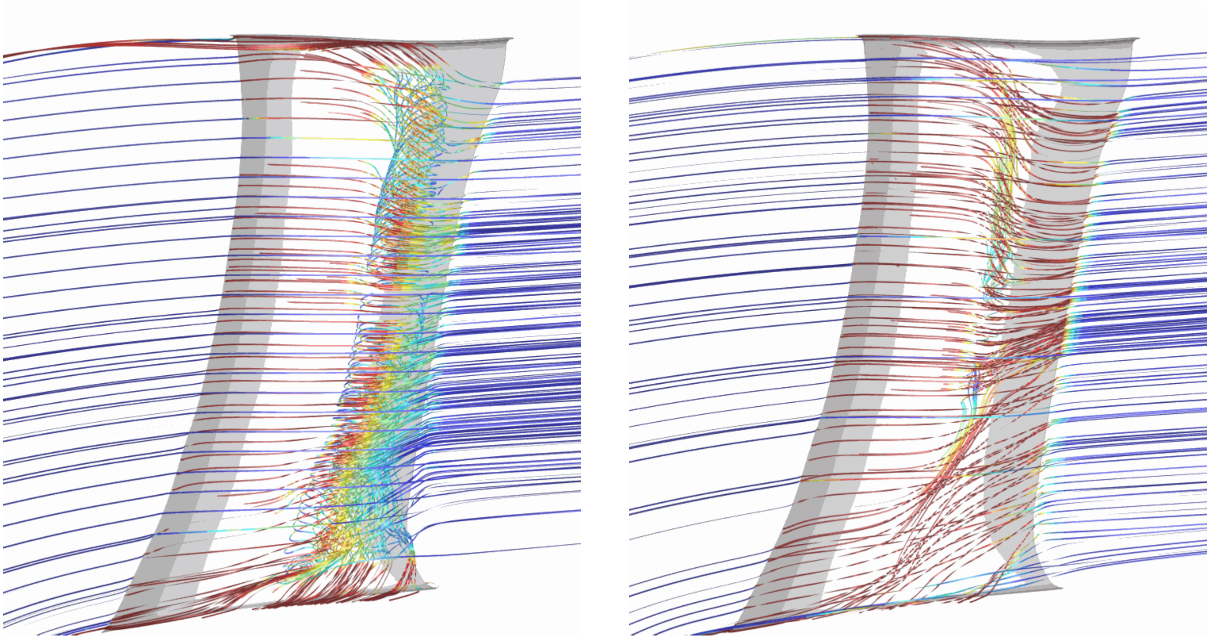

(b) LES1.

(c) LES2.

Figure 3.10: Streamlines in the stator domain (suction side).

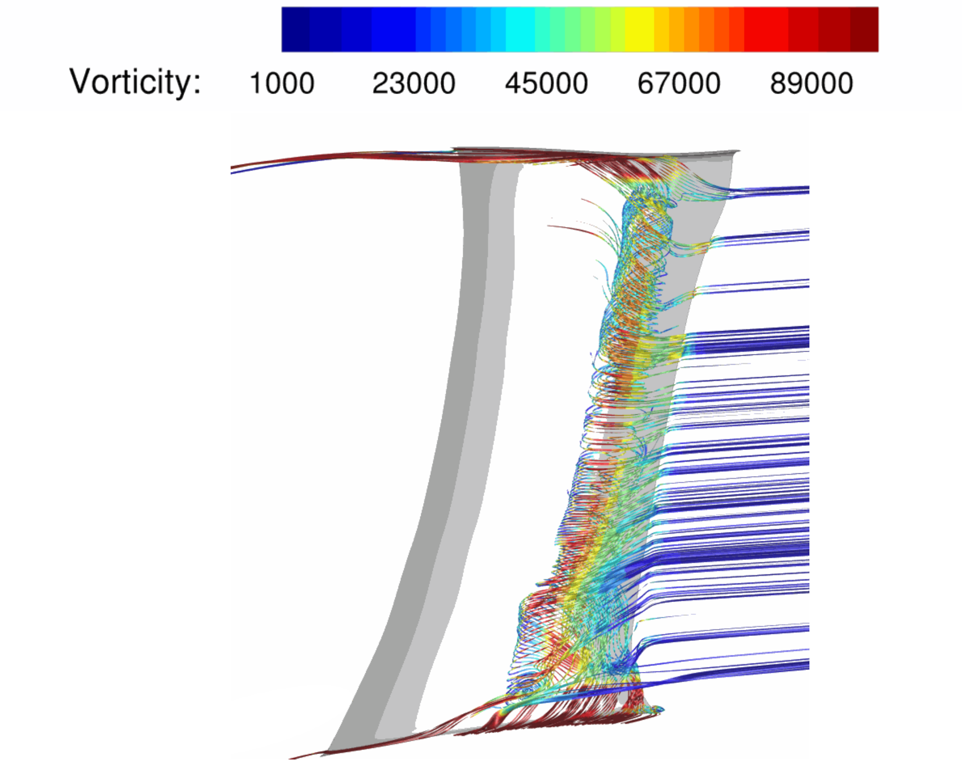

Figure 3.11: Stator radial structure streamlines in the LES1 (suction side).

3.2.5 Boundary layer analysis

As observed in section 3.2.3, the structure of the boundary layers on the blades and vanes seems to significantly impact the topology of the downstream flow, especially the wakes. This section specifically addresses this topic and aims at emphasizing the main properties of these boundary layers.

3.2.5.1 Boundary layer state

The previous section has already shown that the radial vortical structures observed on both the rotor and the stator take part in the TKE production observed in section 3.2.3. These intense turbulent levels, however, are not restricted to the radial vortex locations, which indicates a modification of the turbulent state of the boundary layer. In order to better understand what is responsible for this, the TKE contours over the first 30% of the rotor chord have been plotted for the three simulations, at 75% rotor span (see fig. 3.12). For both LES, the first percents of rotor chord display a null TKE, which characterizes laminar boundary layers. When reaching around 10% of the rotor chord, the TKE quickly intensifies, indicating the transition of the oncoming laminar boundary layer. This transition seems to result from a complex interaction between the LE radial vortex and the LE flow separation identified in the previous section. In order to be more quantitative, the boundary layer profiles based on the velocity component V_s tangent to the blade surface have been extracted from the three simulations at 75% rotor span (see fig. 3.13). The velocity profiles at the rotor leading edge reveal that a significant flow separation occurs ($V_s < 0$ m/s) in all simulations and extends from the leading edge down to 15% of the fan chord length. In both LES, this precisely corresponds to the downstream limit of the LE vortex and to the starting point of the TKE production. Thus, a laminar separation bubble forms right at the rotor LE and simultaneously interacts and partially merges with the radial vortex. These cumulative effects then cause the transition to turbulence and the reattachment of the boundary layer. This transition is not observed in the RANS since no transition model has been used. The boundary layer is thus turbulent right from the rotor leading edge and a turbulent flow separation occurs. Furthermore, the RANS flow separation is much more pronounced than that of both LES, as shown in figs. 3.13a and 3.13b.

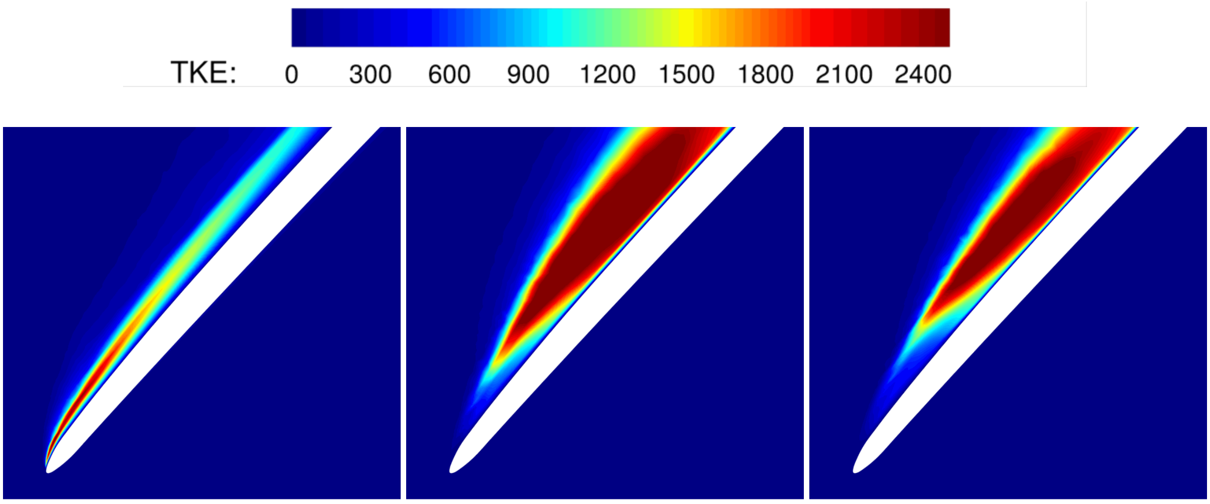

(a) RANS. (b) LES1. (c) LES2.

Figure 3.12: TKE contours at the rotor leading edge, 75% rotor span.

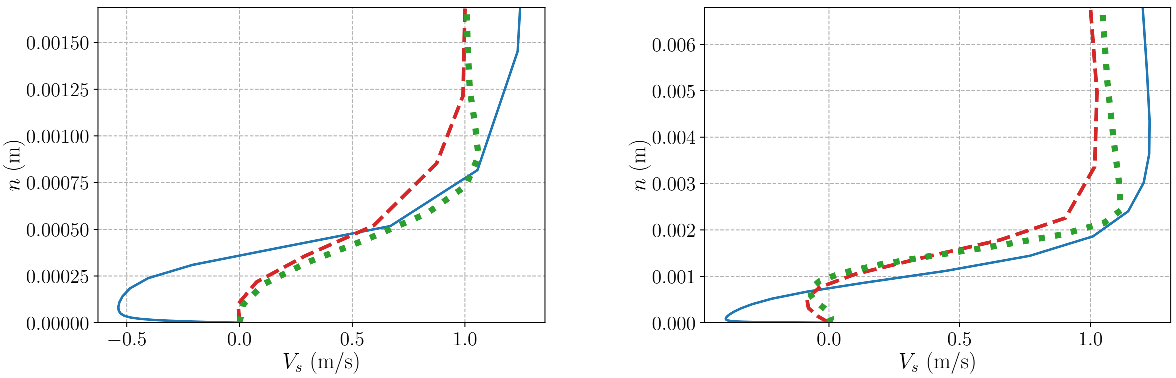

(a) 1% rotor chord.

(b) 5% rotor chord.

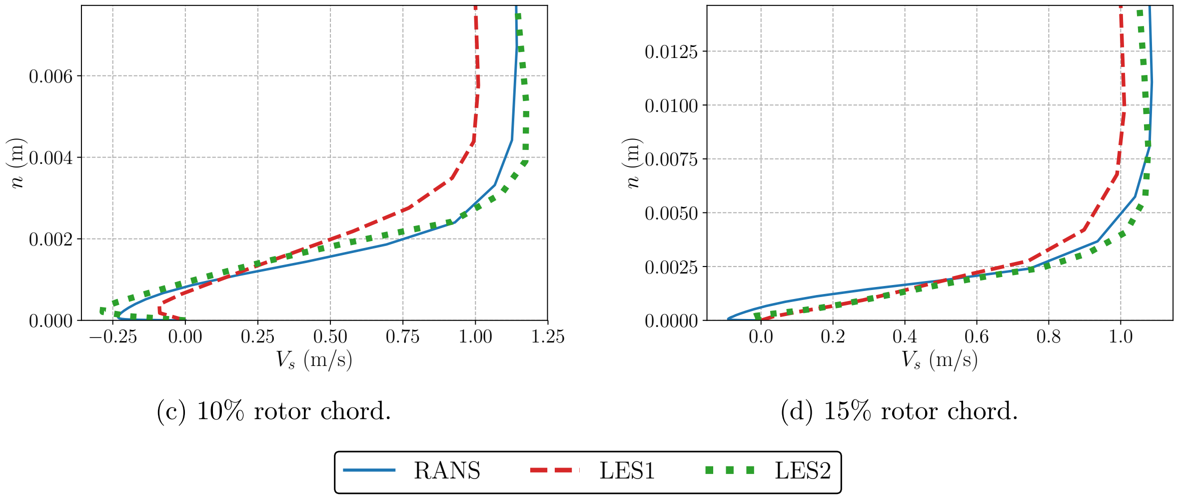

(c) 10% rotor chord.

(d) 15% rotor chord.

Figure 3.13: Boundary layer profiles on the rotor suction side at 75% rotor span.

Regarding the stator, a closer view of the TKE contours around the vanes is shown in fig. 3.14. At the stator leading edge of both LES, high TKE levels, which vanish after a few chord percents, can be observed. As the flow does not display any particular flow feature in this region (see fig. 3.10), this suggests a turbulent boundary layer that tends to return to a laminar state, until it reaches the second transition that occurs at 60% stator chord. In the LES1, as with the rotor, the radial vortex is responsible for part of the TKE production at this location but also contributes to the transition of the boundary layer. The absence of this vortical structure in the LES2 leads to lower TKE levels and to a weaker boundary layer transition. None of these phenomena appears in the RANS, which displays negligible turbulent levels. The boundary layer profiles at 75% rotor span plotted in fig. 3.15 show that a flow separation occurs in the LES1 before reaching 70% of the vane chord, which corresponds to the location of the previously observed radial vortex and flow recirculation. No evidence of flow separation is observed for the RANS and the LES2. The slight bending observed in the LES2 profile at 60% vane chord indicates a laminar acceleration.

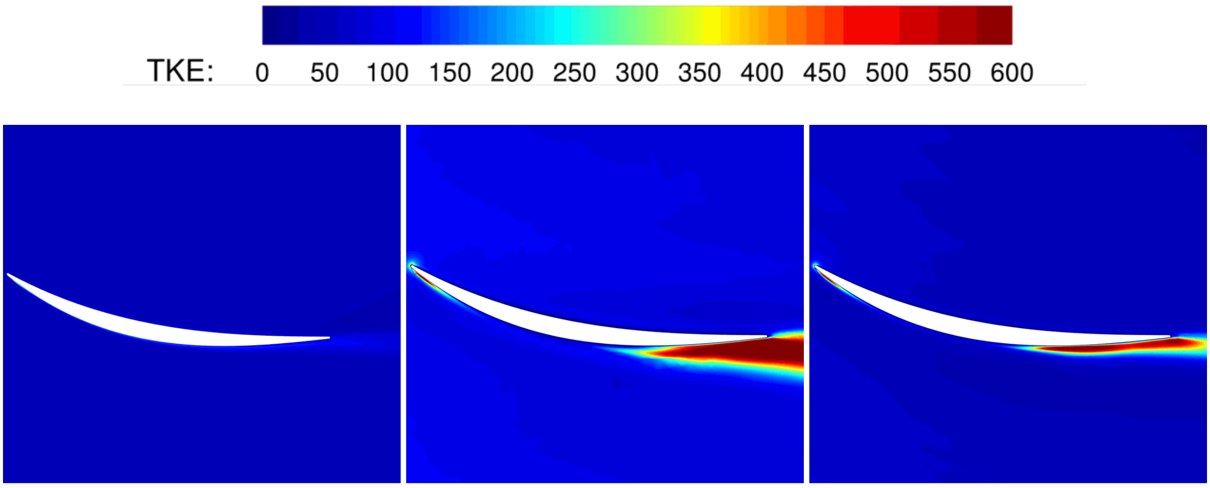

(a) RANS.

(b) LES1.

(c) LES2.

Figure 3.14: TKE contours at the stator leading edge, 75% rotor span.

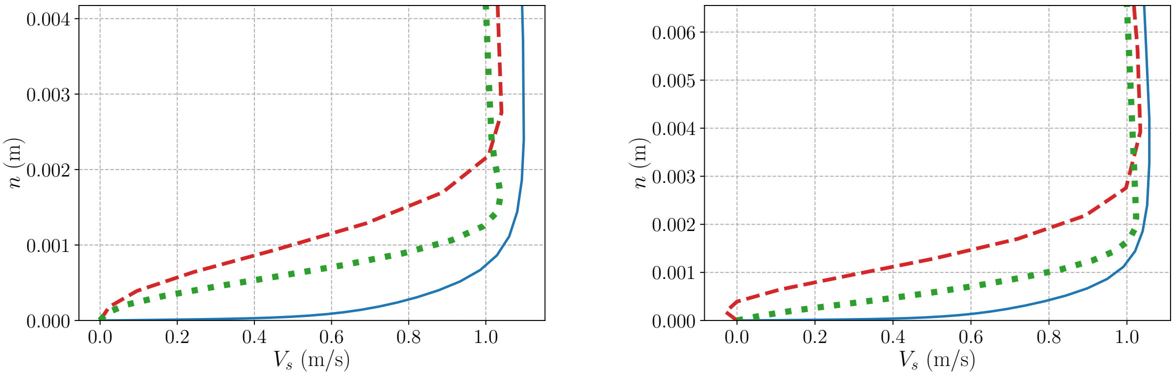

(a) 60% stator chord.

(b) 70% stator chord.

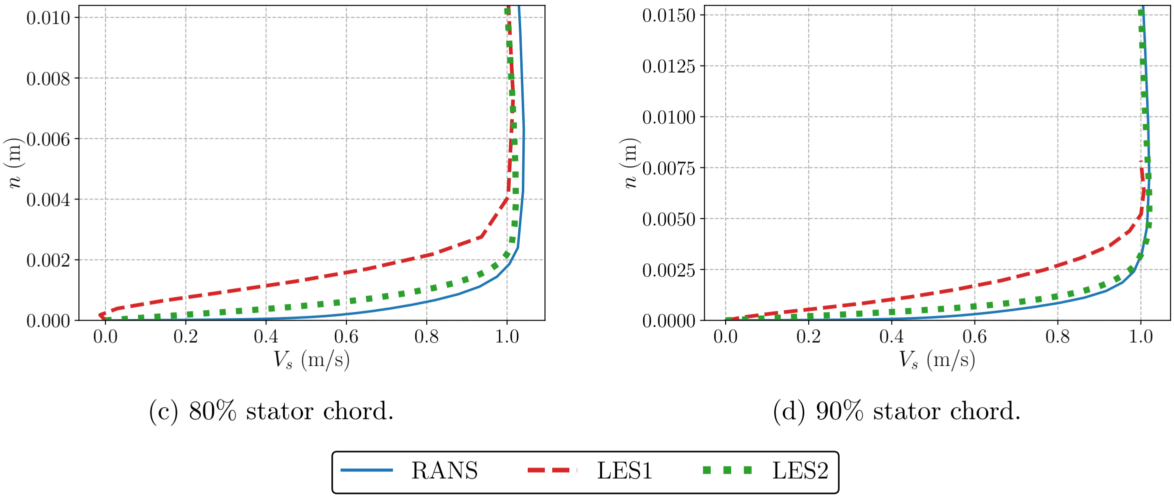

(c) 80% stator chord.

(d) 90% stator chord.

Figure 3.15: Boundary layer profiles on the stator suction side at 75% rotor span.

3.2.5.2 Flow separations

As highlighted in the above section, flow separations can be observed on both the fan and the OGV. They are actually quite common at approach condition since the fan is operating at higher angles of attack than at cruise condition. In order to have a global view of the zones affected by such flow separations, the mean friction coefficient C_f has been computed on the suction side of the blades and vanes and is displayed in figs. 3.16 and 3.17 along with the streaklines. C_f is defined as follows:

$$C_f = \frac{\tau_w}{\frac{1}{2}\rho_\infty V_\infty^2}, \tag{3.2}$$

where ρ_∞ and V_∞ are the density and the velocity of the fluid at the inlet, respectively. τ_w is the wall shear stress defined as:

$$\tau_w = \mu \left(\frac{\partial V_s}{\partial n} \right)_{wall}, \tag{3.3}$$

where μ is the dynamic viscosity of the fluid, V_s is the flow velocity tangent to the wall and $\left(\frac{\partial V_s}{\partial n}\right)_{wall}$ is the wall value of the derivative of V_s in the wall normal direction.

Figure 3.16 unveils that the previously observed flow separation at the fan leading edge actually covers 75% to 95% of the rotor span and the first 15% of the rotor chord, which includes the area covered by the LE radial vortex. In the case of the RANS, the flow separation extends from 25% of the fan span up to the tip of the rotor. In both LES, it covers a longer area and seems to be divided into two parts over most of the blade span, as suggested by the friction lines. However, this splitting of the detached area seems to result more from the averaging process than from a real behavior of the flow. Indeed, as it will be shown in the analysis of the unsteady flow (section 3.3.1), the intermittent behavior of the separation bubble results in fluctuations of its size that may lead to such a mean solution, as also observed by Deuse and Sandberg [201] in their study of the Controlled Diffusion (CD) airfoil geometry.

At 75% span, the extent of the detached zone in the RANS covers half of the area covered by that of both LES. This is not the case over the whole fan span, such as at 65% rotor span where a significantly larger LE separation is observed in the RANS.

In the RANS case, the flow reattaches downstream of this flow separation before reaching half of the blade chord and remains attached down to the trailing-edge. For both LES, the flow reattaches before reaching a quarter of the blade chord and remains attached down to the trailing-edge except between 30% and 60% of the rotor span, where a second flow detachment occurs at 60% rotor chord. In the LES2, this second flow separation has a shorter streamwise extent than in the LES1. The location of this second flow separation coincides with the second TKE production point observed in figs. 3.6e and 3.6f.

Regarding the vane (fig. 3.17), significant differences can be observed between the three simulations. For the RANS, the flow remains attached on almost all the suction side. Small isolated separation zones appear at the LE close to the casing and at the TE at 10% vane height. The LES1 displays a radically different flow pattern, with a substantial flow separation occurring at around 65% stator chord, which extends over almost the entire vane span and coincides with the radial vortex observed in fig. 3.11. Between 20% and 95% of the vane span, the flow reattaches before reaching the trailing edge while below 20% it remains detached. This flow separation disappears in the LES2 as a result of the wall mesh refinement, which has led to a better description of the near wall flow. Once again, these observations are consistent with the location of the TKE production point on the vane that has been underlined in fig. 3.7.

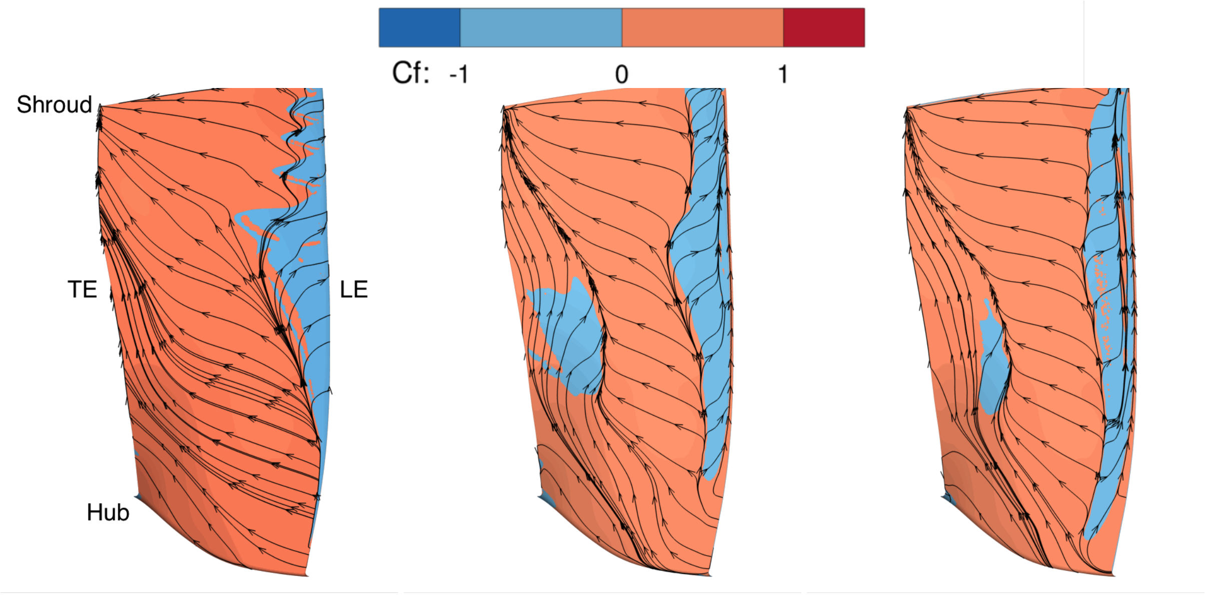

(a) RANS. (b) LES1. (c) LES2.

Figure 3.16: Mean friction coefficient and streaklines on the fan suction side.

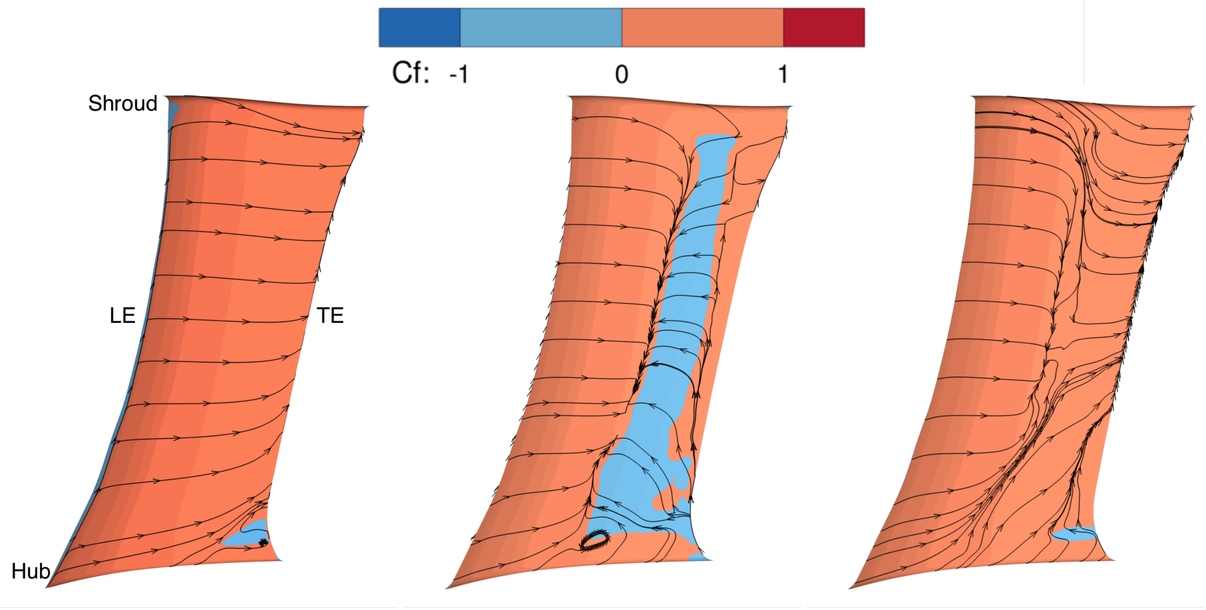

(a) RANS. (b) LES1. (c) LES2.

Figure 3.17: Mean friction coefficient and streaklines on the vane suction side.

3.2.5.3 Boundary layer thickness

As mentioned in section 3.2.3, the concomitant effects of the flow separations and the laminar-turbulent boundary layer transition lead to thicker boundary layers on the suction side of the blades and the vanes, with intense TKE levels, which eventually interact with the downstream wakes. This can be quantitatively assessed by computing the boundary layer thickness δ as depicted in fig. 3.18 at 75% rotor span. The procedure to compute δ is detailed in appendix D.

On the fan, a thick boundary layer is predicted for all three simulations. The LE flow

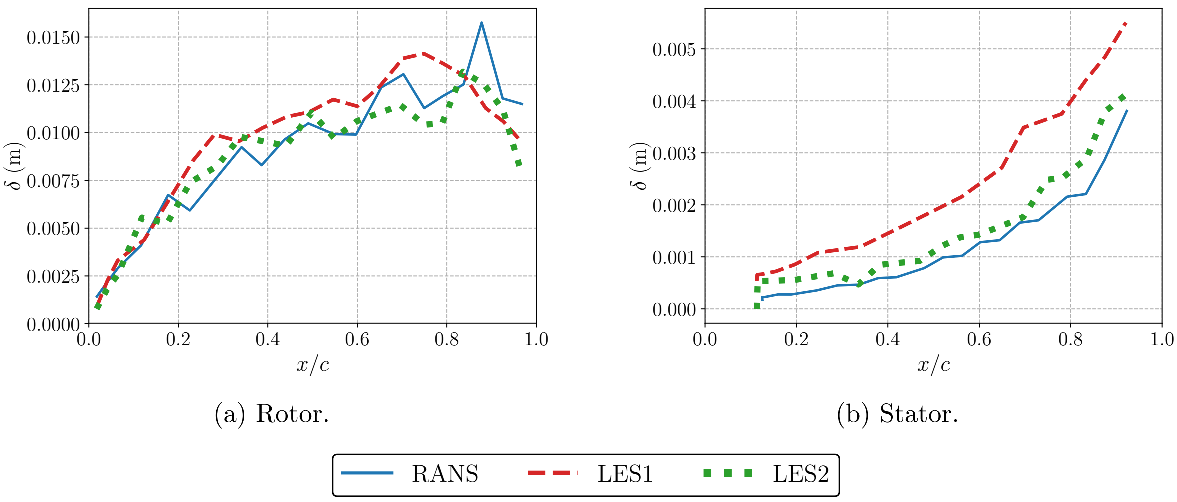

(a) Rotor.

(b) Stator.

Figure 3.18: Boundary layer thickness on the rotor and stator suction sides at 75% rotor span.

separation results in a boundary layer that reaches more than half of its maximum thickness along the first 20% of the chord length. The absolute value, as well as the axial evolution of δ are very similar for all three simulations. As for the vane boundary layer, the LES1 predicts a thicker one than both the LES2 and the RANS along the entire vane chord. The axial evolution of δ is smoother than on the rotor since no LE flow separation is observed on the vane. At around 65% OGV chord, however, a sudden increase in δ is observed for both LES, which coincides with the location of the boundary layer transition observed on the stator.

All these observations are consistent with the comments made in the previous sections: flow separations and/or laminar-turbulent transitions occur on both the blades and the vanes, which generates higher TKE levels that inevitably interact with the downstream wake.

3.2.6 Pressure coefficient

The previous sections have revealed that the flow topology on the rotor and stator skins differ from one simulation to another. This has a direct impact on the wall pressure distribution, which can be analyzed using the pressure coefficient C_p defined as follows:

$$C_p = \frac{P - P_\infty}{\frac{1}{2}\rho_\infty V_\infty^2}, \tag{3.4}$$

where ρ_∞, V_∞ and P_∞ are the density, the velocity and the static pressure of the fluid at the inlet, respectively. The mean C_p profiles have been extracted on both the rotor and the stator skins and are shown in figs. 3.19 and 3.20 for different radial positions. On the rotor pressure side, the three simulations provide identical results. On the rotor suction side, they predict comparable profiles above 20% of the fan chord for all radial positions. Below 20% of the chord, however, significant discrepancies appear between the RANS and both LES. Indeed, both LES give similar results in this region and display a plateau of constant C_p extending from the leading edge down to 15% of the rotor chord at all radial positions. This plateau is typical of a laminar separation bubble as shown by Sanjosé *et al.* [174], Wu *et al.* [173] and Deuse and Sandberg [201], in their studies on the CD airfoil. In the RANS, a similar plateau, which is a lot shorter than those observed in the two LES, can be observed at the same location for radial positions above 25% rotor span. The significant extent differences noticed between the RANS and both LES seem to be directly linked to the turbulent state of the oncoming flow.

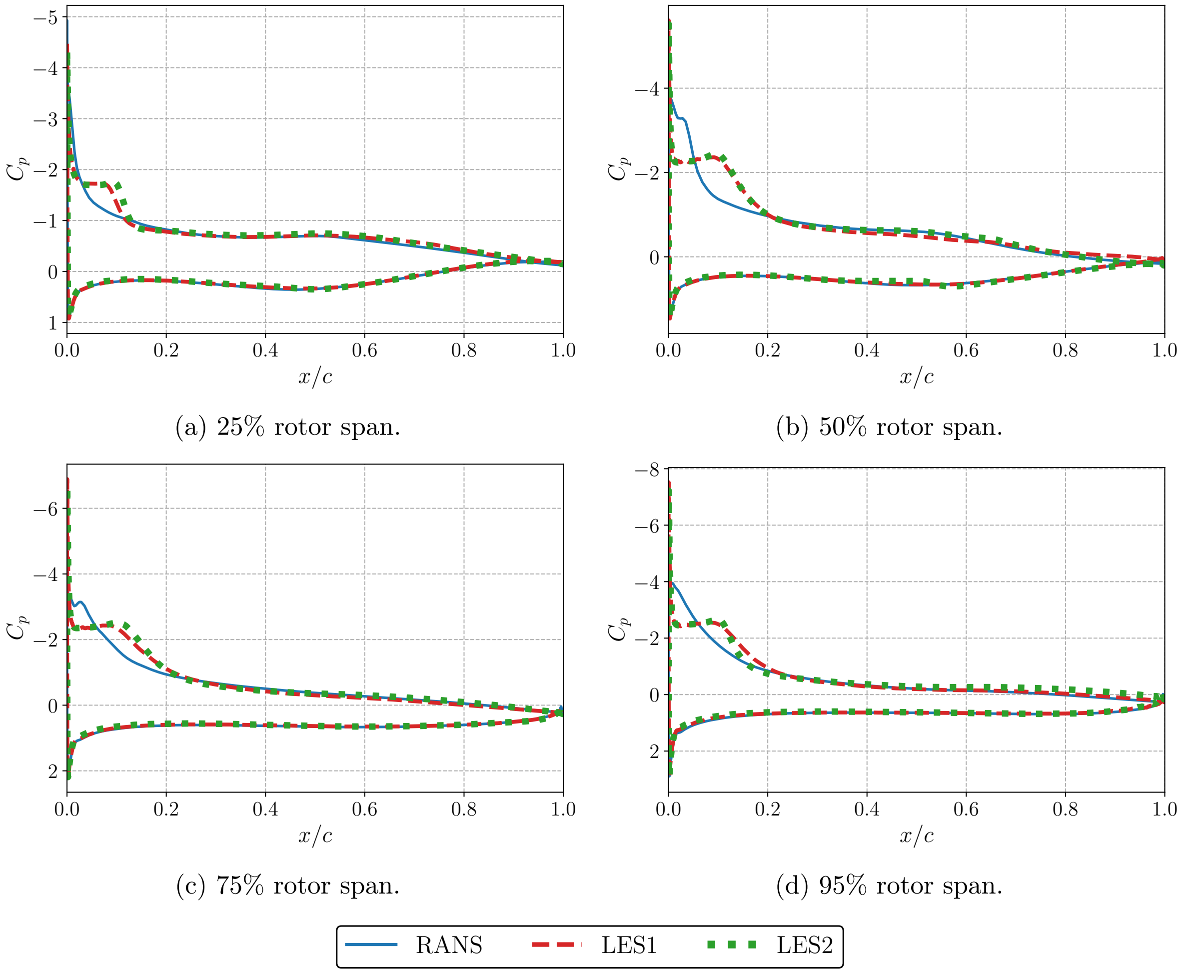

(a) 25% rotor span.

(b) 50% rotor span.

(c) 75% rotor span.

(d) 95% rotor span.

Figure 3.19: Pressure coefficient on the rotor blade at different radial positions.

Regarding the OGV, similarly to the rotor, the results on the pressure side are identical for all the simulations. On the suction side, the C_p profiles at 25%, 50%, and 75% stator span of each simulation look very similar from the leading edge down to 65% stator chord. From that point, the LES1 C_p profiles reach a small plateau that extends over 15% of the stator chord. This occurs at the same location as the transition of the boundary layer, which is induced by the flow separation observed in the previous section. Such a noticeable plateau is not observed for the LES2, which is consistent with the absence of separated areas. However, a slight change of slope at 65% chord indicates a boundary layer transition. At 95% stator span, significant disparities can be observed. They can be mainly attributed to the flow disparities upstream of the stator, as mentioned in section 3.2.3.

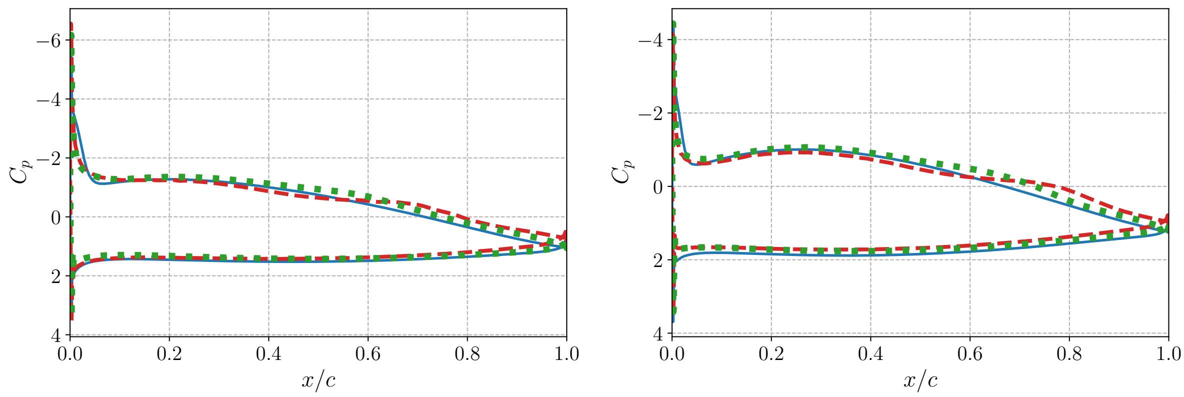

(a) 25% stator span.

(b) 50% stator span.

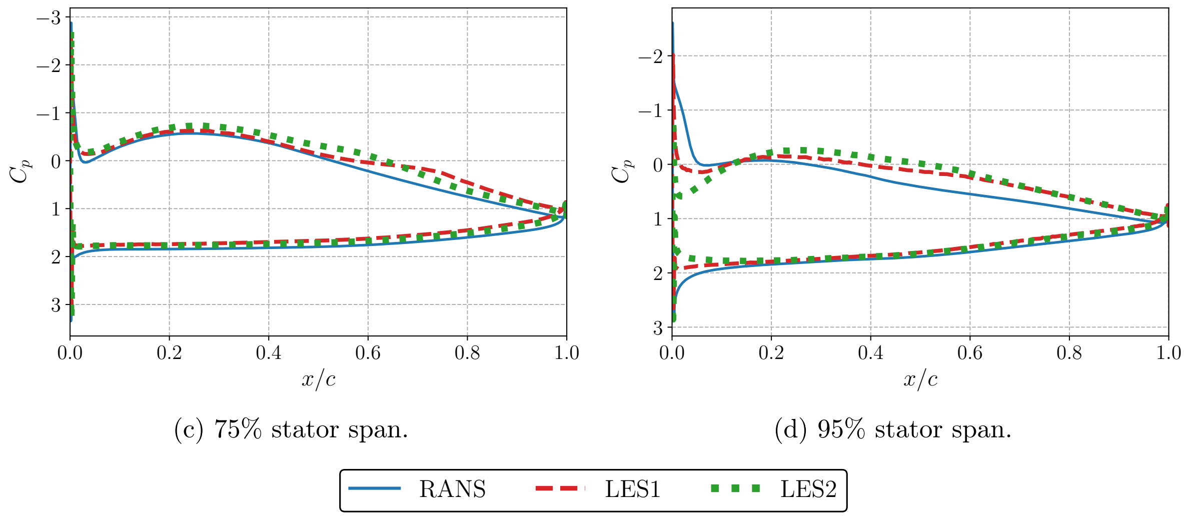

(c) 75% stator span.

(d) 95% stator span.

Figure 3.20: Pressure coefficient on the stator vane at different radial positions.

3.2.7 Fan wake analysis

The two hybrid noise simulation approaches that have been selected obviously rely on an accurate prediction of the fan wakes since they are at the heart of the RSI mechanism. Both their structure (velocity deficit, width) and their turbulent properties (turbulence kinetic energy, integral length scale) must be precisely captured by the simulation in order to perform reliable noise predictions. As a consequence, it is of paramount importance to ensure that the wakes, and the boundary layers they originated from, are sufficiently discretized and properly convected through the domain. The above section has already underlined the numerous specific features of the fan boundary layers and has shown how significant their interactions with the downstream wakes are. The present section focuses on the wake structure and compares the simulation results to the HW measurements performed at the HW1 position (X=-2.685 m, see fig. 2.2).

3.2.7.1 Velocity and turbulence kinetic energy maps

Figures 3.21-3.24 compare the three velocity components and the TKE retrieved from the three simulations with the HW measurements.

For all simulations, the axial velocity (fig. 3.21) is in very good agreement with the experimental data. The overall shape of the wakes is well recovered in terms of thickness and tilting. However, discrepancies can be observed near the casing where the boundary layer is thicker in the RANS than in both LES, the thinnest boundary layer being observed in the LES2. Unfortunately, this part of the flow cannot be validated against the experimental data since the HW measurements have not been performed close to the casing wall. In spite of that, the experimental data exhibit a large tip gap vortex that none of the present simulations is able to capture. A finer mesh may be needed in this flow region to better capture this flow feature [69, 202]. A slight overestimation, which is within the experimental uncertainty, can be observed in the background flow over the whole blade span, for all simulations. This contradicts the performance results presented in table 3.1 in which only the LES2 overestimates the mass-flow rate. The HW measurements are thus not consistent with the performance measurements. This may result from the HW calibration issues that have been reported during the test campaign. Still, the discrepancy is only of a few meters per second, which does not make the measurements totally unreliable.

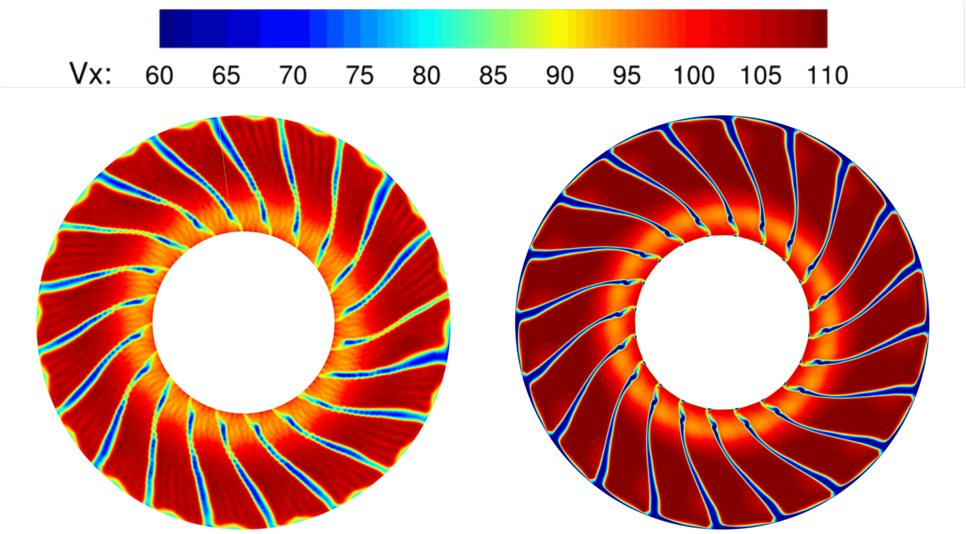

(a) HW measurements. (b) RANS.

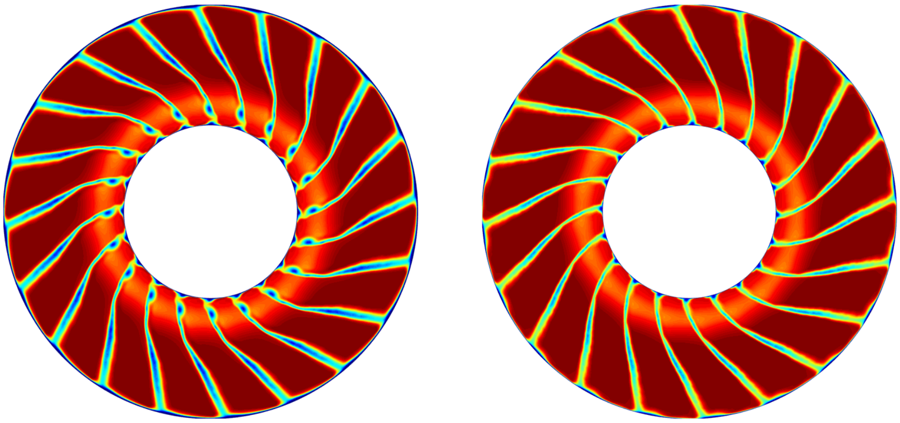

(c) LES1. (d) LES2.

Figure 3.21: Axial velocity field at position HW1.

The wake velocity deficit is overestimated by the RANS, but well recovered by the LES1 except in the tip region of the rotor where the velocity deficit notably decreases, which is not observed in the HW measurements. In the case of the LES2, the wake velocity deficit is, however, slightly underestimated. These comments actually depend on the wake that is chosen for the comparison. Indeed, it should be underlined at this point that the experimental wakes vary from one blade to another, a few blades shedding particularly thick wakes (*e.g.* 4 o'clock blade). The computation assumes a perfect axisymmetry that should be ideally obtained in the experiment. Similarly, the experimental data are questionable in the gap region where the flow is expected to exhibit intense swirl that is likely to flaw the HW measurements.

The azimuthal velocity (fig. 3.22) is in very good agreement with the experimental data. A slight overestimation is observed in the core flow for all simulations, which could be partly explained by the absence of the IGV in the numerical set-up.

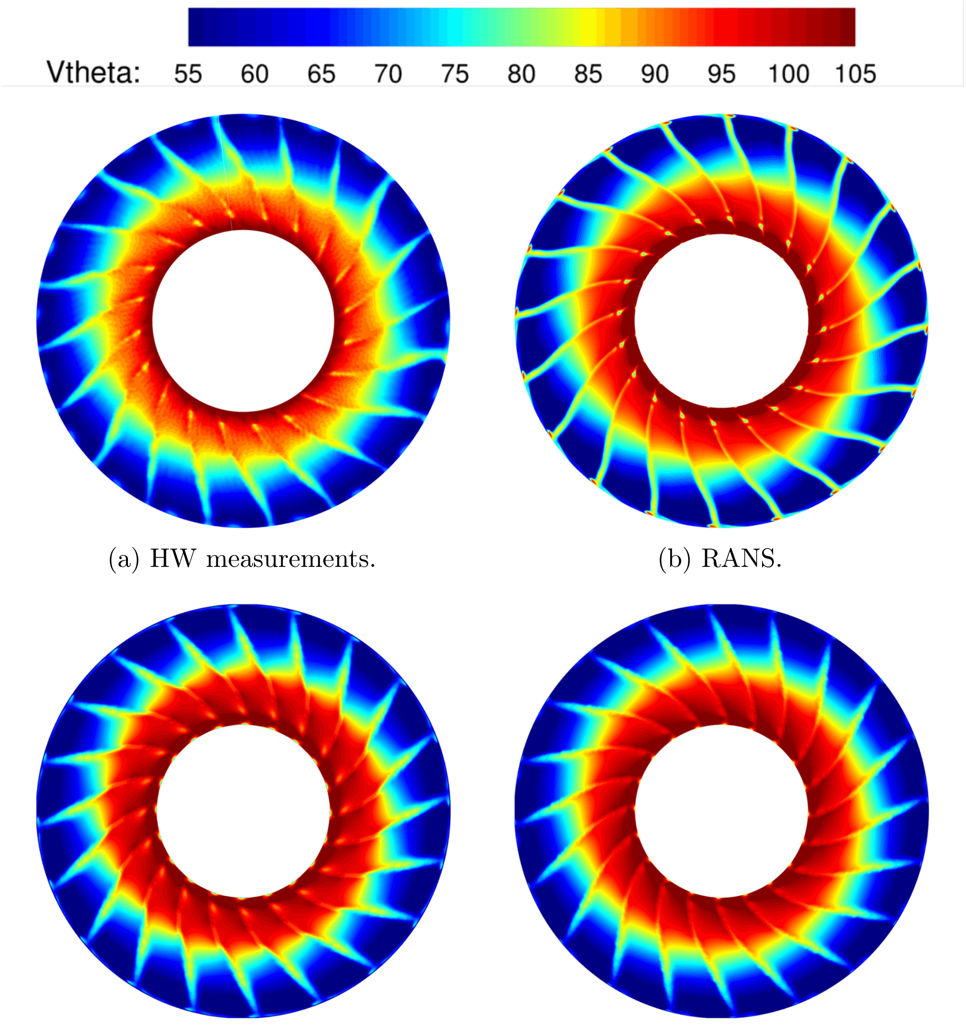

(a) HW measurements. (b) RANS.

(c) LES1. (d) LES2.

Figure 3.22: Circumferential velocity field at position HW1.

The radial velocity (fig. 3.23) is the velocity component that shows the largest discrepancies. This component is well captured in the wake and in the upper part of the background flow. However, a substantial overestimation is observed close to the casing, especially in the two LES, and in the core flow. The largest disparities are observed in the LES2. This global overestimation might be partially explained by the lack of accuracy of the experimental estimate using hot-wires, since comparable discrepancies have been observed on other configurations [203]. The radial velocity is indeed very small compared to the two other components, therefore slight differences in the main components account for relatively large variations of the radial velocity.

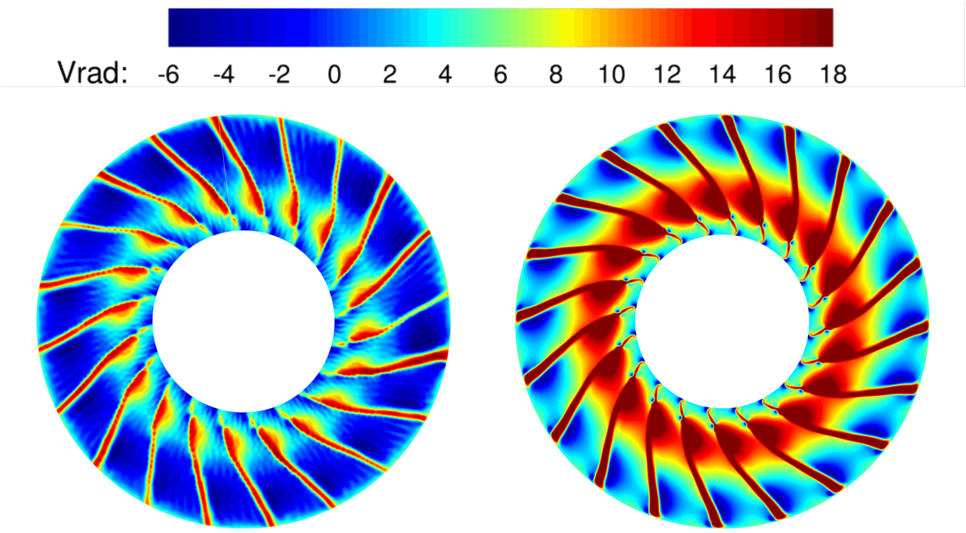

(a) HW measurements. (b) RANS.

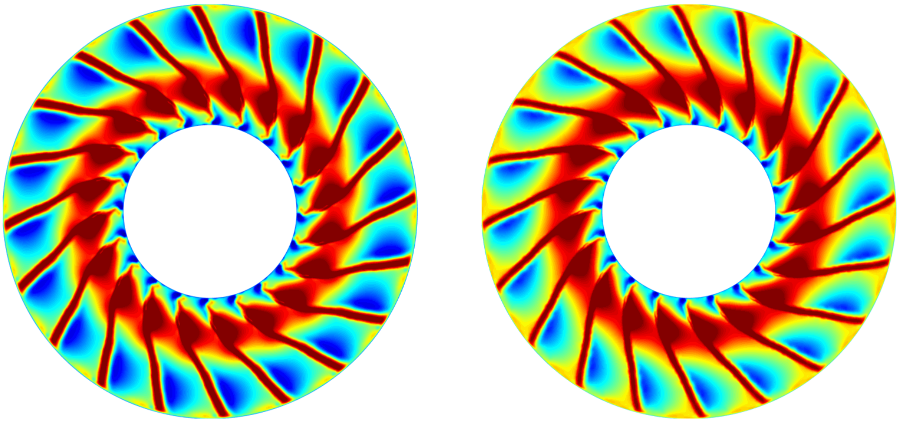

(c) LES1. (d) LES2.

Figure 3.23: Radial velocity field at position HW1.

Finally, the turbulence kinetic energy (fig. 3.24) is significantly overestimated by all the simulations. The LES1 predicts the highest TKE levels while the LES2 predicts the lowest ones. This actually results from the significant flow detachment observed at the rotor leading edge, which might be more important in the simulation than in the experiment. As observed in the previous sections, this flow separation induces high levels of TKE close to the rotor suction side, which then interact with the wakes. This can be more clearly observed in fig. 3.25, especially in the LES1 for which the highest TKE levels are located on the side of the wake that corresponds to the suction side of the blade. It is however more difficult to notice the same flow separation when looking at the HW measurements, except on isolated wakes (at 12, 2 and 3 o'clock for instance). As already mentioned for the axial component, it should be pointed out that the HW measurements show significant wake-to-wake variations that cannot be reproduced by the simulation. Furthermore, many RANS studies on the same case (see Kissner *et al.* [204]) and a ZDES study by François *et al.* [205] and by Polacsek *et al.* [206] have shown similar discrepancies with the experimental data, suggesting a potential lack of accuracy of the HW measurements. The overall agreement of the simulations with the experiment is still quite satisfactory. Even though the TKE overestimation observed in the RANS and the LES1 may be detrimental to the noise predictions, the latter will lead to interesting outcomes, as shown in chapter 4. Additionally, a significant reduction of the TKE levels has been achieved with the LES2, which in conjunction with the remarks made on the experimental data, guarantees the trustworthiness of both the aerodynamic and acoustic predictions.

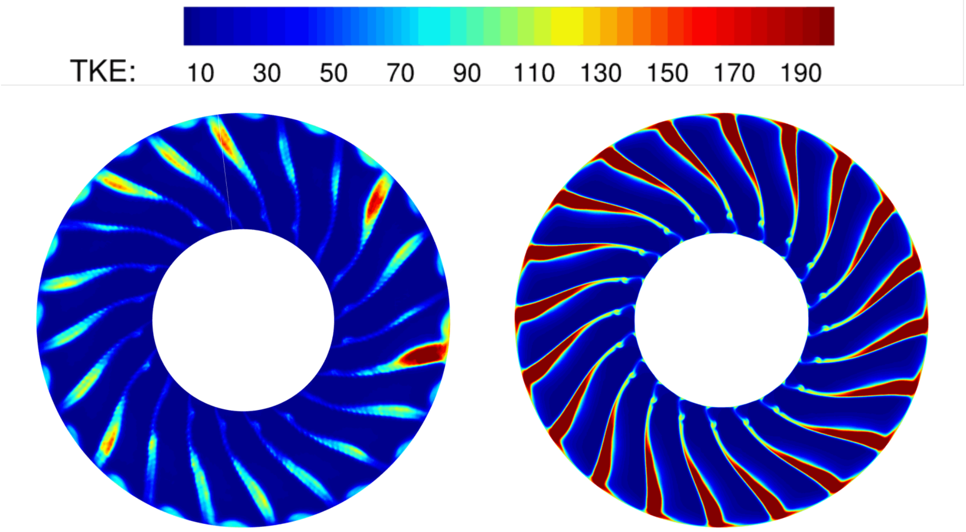

(a) HW measurements.

(b) RANS.

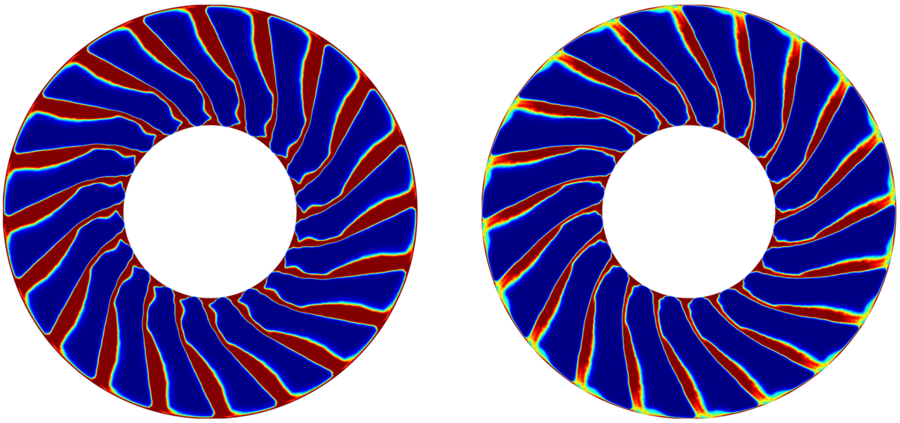

(c) LES1.

(d) LES2.

Figure 3.24: Turbulence kinetic energy at position HW1.

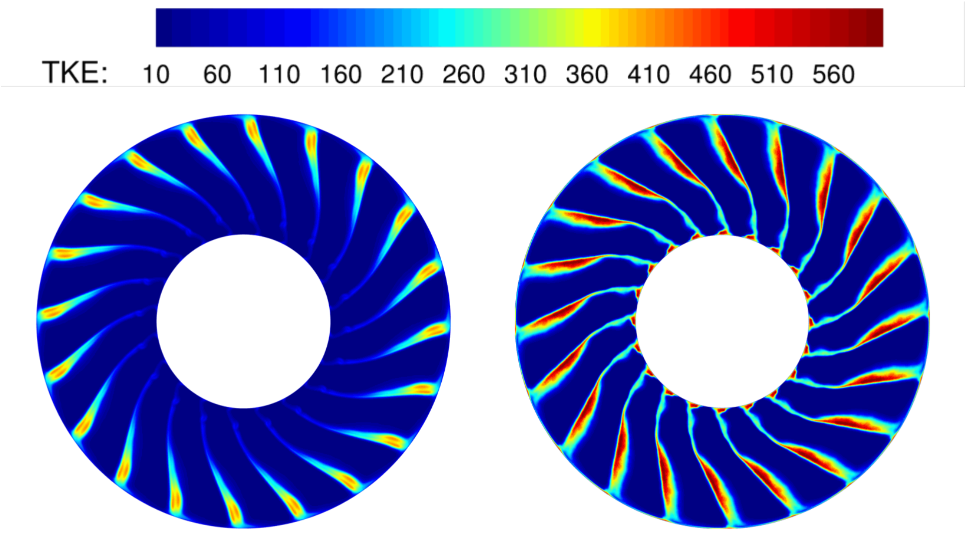

(a) RANS.

(b) LES1.

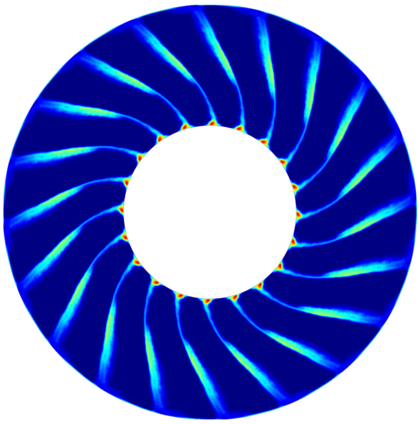

(c) LES2.

Figure 3.25: Turbulence kinetic energy at position HW1, convenient color map scale.

3.2.7.2 Azimuthal profiles

The above section has enabled to qualitatively compare the simulation results against the hot-wire measurements, and to have a comprehensive overview of the structure of the fan wakes. However, the blade-to-blade variations observed in the experimental data prevent from precisely appreciating their similarities and disparities with the simulations. In order to have a more quantitative analysis, the mean wake azimuthal profiles of each velocity component, and their RMS values, have been plotted for different radial positions, along with the corresponding experimental revolution range. The latter is basically the area delimiting the range of variations observed in the experimental data at each radius, and over the full annulus. Thereby, the blade-to-blade variations are taken into account without isolating each wake.

At 25% rotor span (fig. 3.26), the experimental revolution range is remarkably thinner than at other radial positions, indicating smaller blade-to-blade variations. Regarding the axial velocity, the RANS profile are in good agreement with the experimental data. Indeed, the velocity deficit is well predicted and the velocity in the background flow matches the experimental values. Both LES underestimate the velocity deficit, but recover the background values. However, the three simulations tend to predict a thinner wake than in the experiment. Both azimuthal and

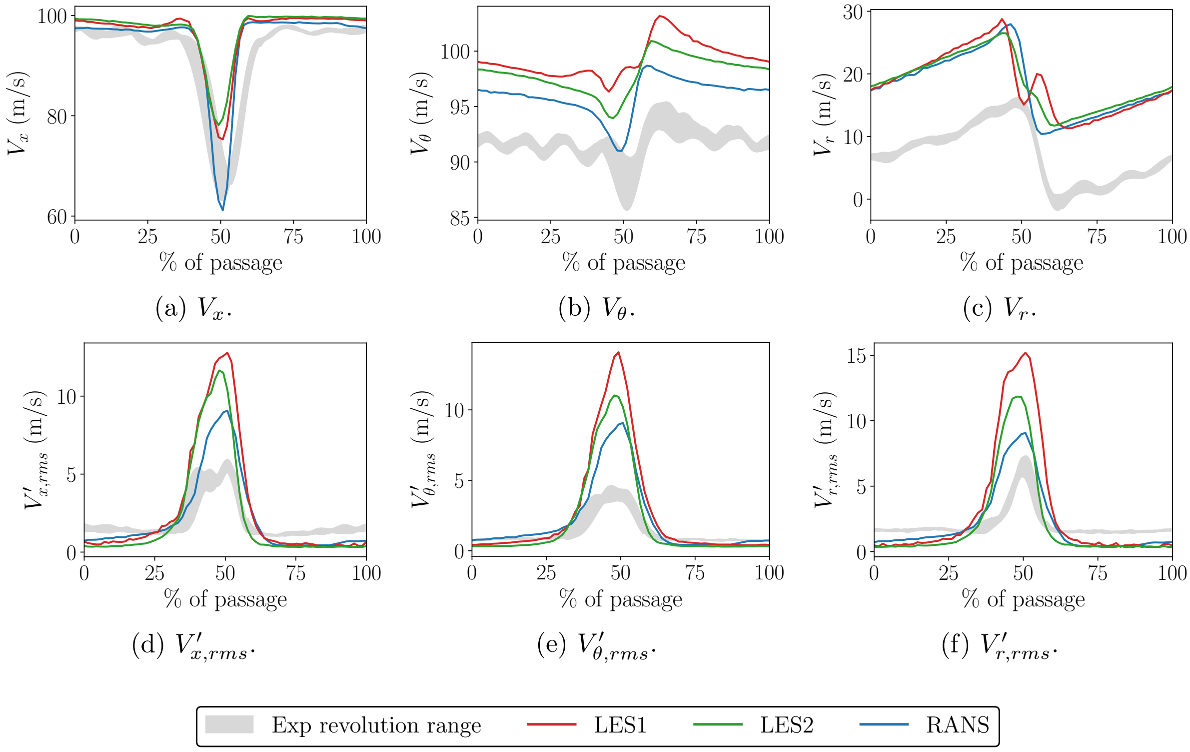
(a) V_x.

(b) V_θ.

(c) V_r.

(d) $V'_{x,rms}$.

(e) $V'_{\theta,rms}$.

(f) $V'_{r,rms}$.

Figure 3.26: Velocity component azimuthal profiles at 25% rotor span.

radial velocities are overestimated by the simulations, the RANS results being the closest to the experimental data. The overall shape of the experimental profile is well recovered by all simulations, which ensures that the correct behavior of the flow is captured. In the LES1, however, an unexpected hump can be observed at 60% of the passage. The wake RMS values are overestimated by all simulations at this radius, especially in the case of the LES1. The fan LE flow separation, which is already present at this radius in both LES, may actually be responsible for the larger RMS values observed in both LES with respect to the RANS. As a whole, the RMS profiles are sharper than the experimental ones and the background values are well captured.

At 50% rotor span (fig. 3.27), the axial velocity deficit and the wake width are this time well captured by all the simulations. An overestimation of the background axial velocity is however observed. As mentioned in section 3.2.7.1, this overestimation of the background velocity is noticed over almost the whole blade span, which indicates a mismatch between the HW and the performance measurements. The azimuthal velocity profiles are in good agreement with the experimental data especially for the two LES, which match both the background and the wake values. The radial velocity is still over-predicted at this radial position, but is in better agreement with the experimental measurements than at 25% rotor span, especially for both LES, which give estimates that are closer to the measurements with respect to the RANS. The wake RMS values are again overestimated by both LES for each component, whereas the RANS is able to recover both the background and the wake levels. A substantial improvement in terms of absolute levels is however achieved with the LES2. Furthermore, both LES results display profile shapes that faithfully reproduce those observed in the experiment, contrary to the RANS ones. This observation combined with the previously mentioned HW calibration issues, which may have partly caused the larger gap observed between the LES and the measurements, support the fact that the LES approach better recovers the underlying physics in the wakes than the RANS.

The significant blade-to-blade variations observed at 75% blade span (fig. 3.28) result in a

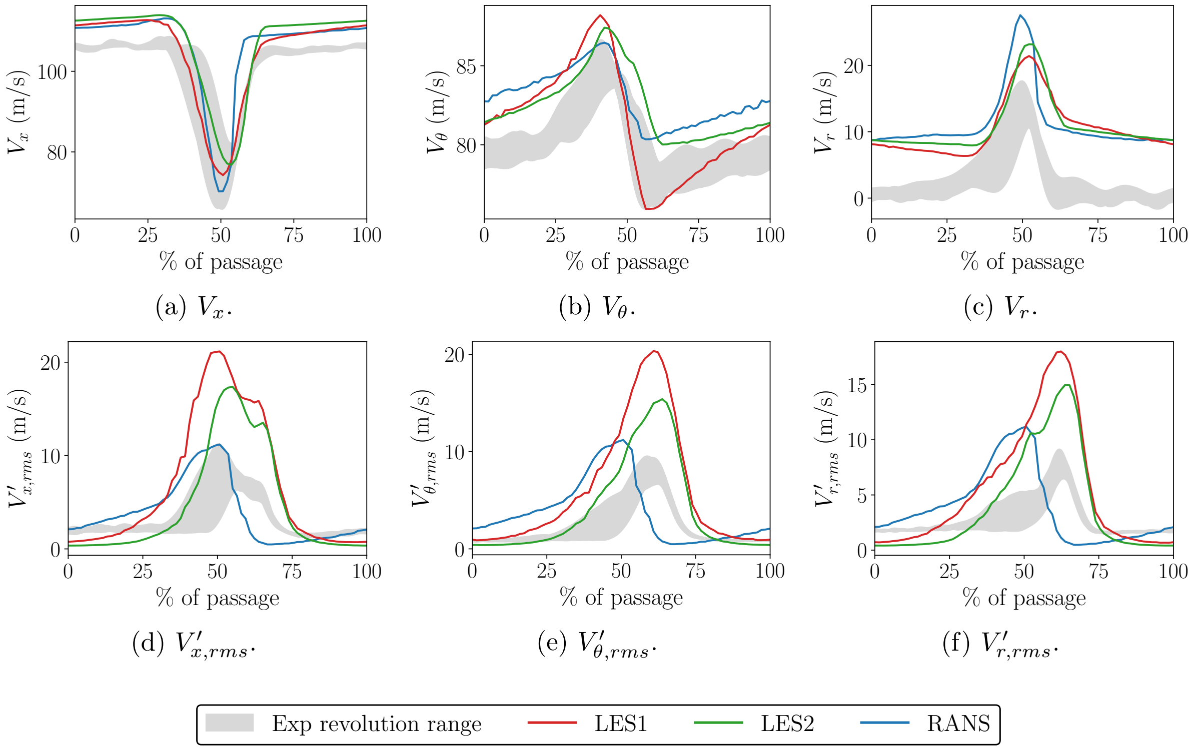

(a) V_x.

(b) V_θ.

(c) V_r.

(d) $V'_{x,rms}$.

(e) $V'_{\theta,rms}$.

(f) $V'_{r,rms}$.

Figure 3.27: Velocity component azimuthal profiles at 50% rotor span.

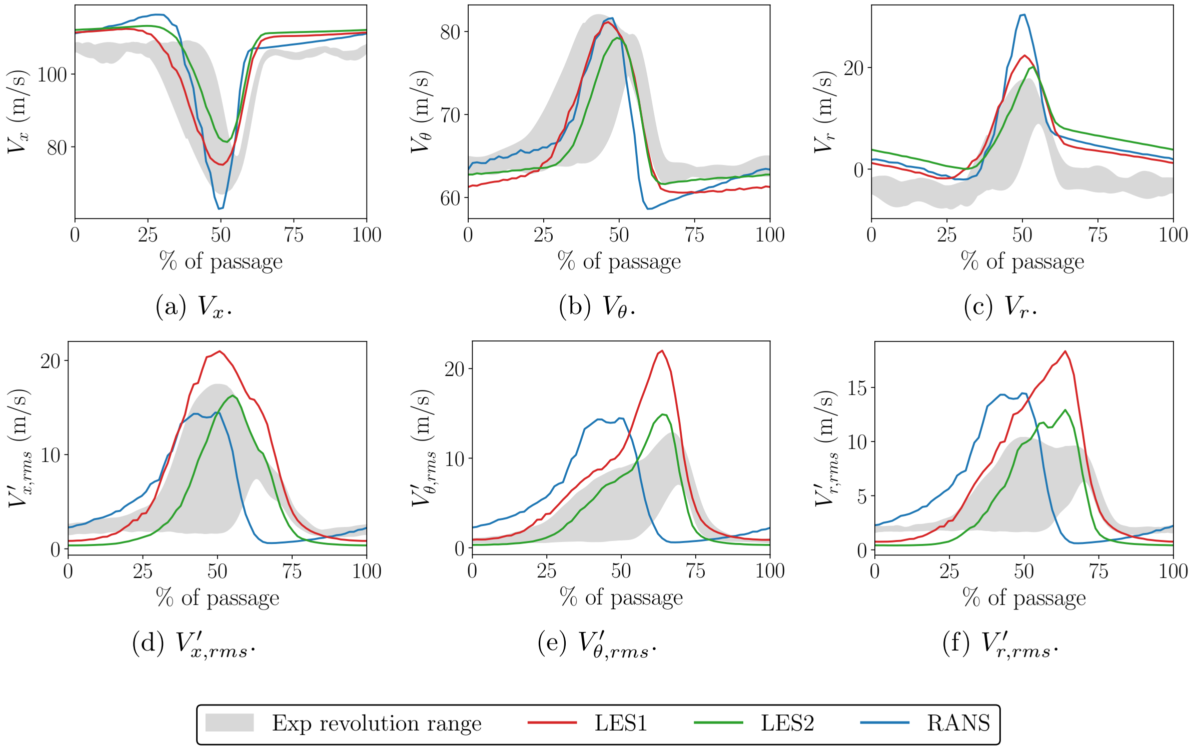

(a) V_x.

(b) V_θ.

(c) V_r.

(d) $V'_{x,rms}$.

(e) $V'_{\theta,rms}$.

(f) $V'_{r,rms}$.

Figure 3.28: Velocity component azimuthal profiles at 75% rotor span.

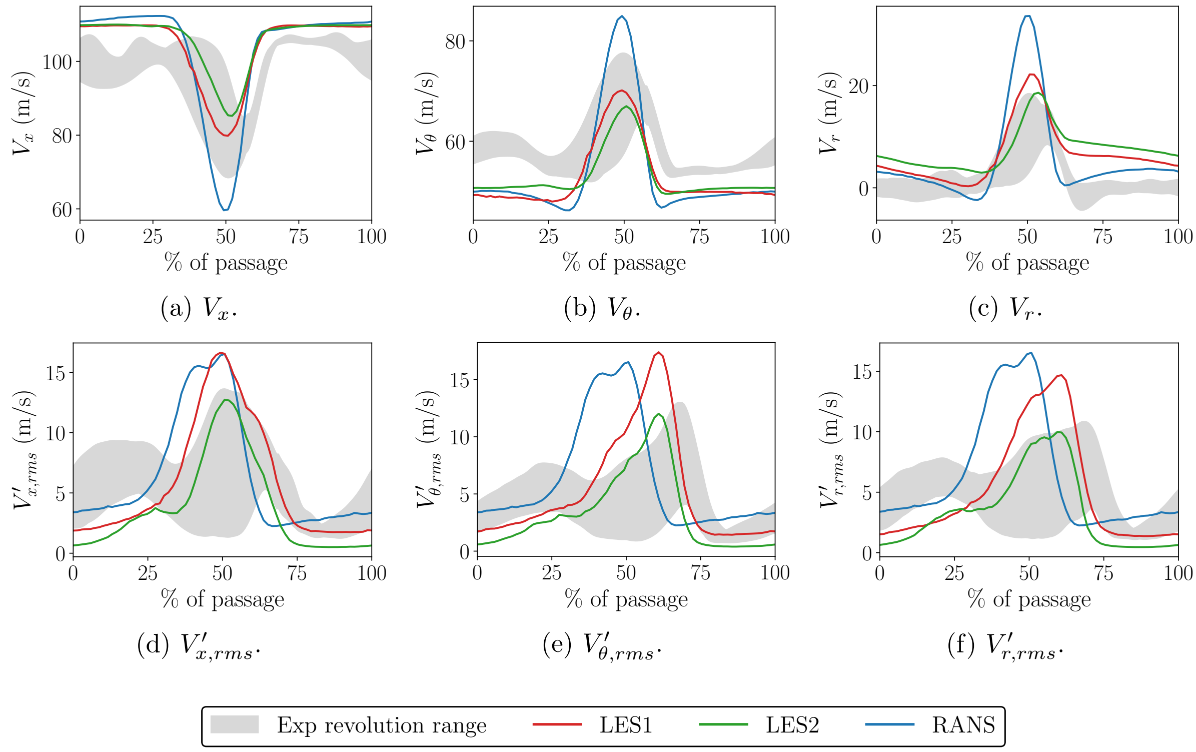

(a) V_x. (b) V_θ. (c) V_r.

(d) $V'_{x,rms}$. (e) $V'_{\theta,rms}$. (f) $V'_{r,rms}$.

Figure 3.29: Velocity component azimuthal profiles at 95% rotor span.

wide experimental revolution range. At this radial position, the RANS overestimates the axial velocity deficit whereas both LES are in fairly good agreement with the measurements. All the simulations recovers quite well the experimental wake width but still overestimate the background values. The circumferential velocity profile is in excellent agreement with the experimental data, especially in the case of the LES2, which perfectly matches the experimental values. The RANS and the LES1 slightly overestimate the background values. Regarding the radial velocity, an over-prediction can still be observed, particularly for the RANS. The LES2, on the contrary, shows a better agreement with the experimental profile than what has been observed at lower radial positions. Concerning the RMS profiles, similarly to what has been observed at 50% rotor span, both LES predict profiles with shapes faithfully reproducing the experimental ones, contrary to the RANS. In terms of magnitude, the RANS recovers the axial RMS velocity but slightly overestimates the azimuthal and radial ones. The LES1 provides higher values for all three components. The LES2, on the contrary, is in very good agreement with the HW measurements, with profiles that are almost entirely within the range of experimental values. Considering that the HW technique is more prone to errors regarding the mean flow (because of the calibration errors) than for the fluctuations, this confirms the significant improvements achieved by the LES2.

The last radial position, located at 95% rotor span (fig. 3.29), displays the largest discrepancies for the RANS simulation. Indeed, it significantly overestimates the axial velocity deficit as well as the magnitude of both the radial and the circumferential velocity components. Both LES, on the contrary, are in very good agreement with the measurements in terms of magnitude and shape for the axial and azimuthal velocity components, while the radial component is still overestimated. Important blade-to-blade variations are observed for the experimental RMS values, as indicated by the wide experimental revolution range. This makes the reading of the results more difficult but still shows that the shape of the profiles are better captured by the LES approach for all velocity components. In terms of magnitude, only the LES2 recovers the experimental levels, as the LES2 profiles are all close to the upper limit of the experimental range. Both the RANS and the LES1 tend to overestimate the RMS levels for all components.

General comments can be made on the previous observations:

- The RANS provides satisfactory results for all the velocity components in terms of magnitude and shape. The magnitude of the predicted RMS values is also globally recovered. The shape of the RMS profile, however, significantly differ from the experimental ones. Furthermore, a degradation of the results is observed close to the rotor tip, which confirms the known difficulty of the RANS to correctly simulate the tip gap flow.
- A global overestimation of both the velocity components and their RMS values is observed for the LES1, even though the shape of the profiles is faithfully reproduced.
- The LES2 provides the most accurate results. Both the shape and the magnitude of the velocity components and their RMS values are well recovered. A slight overestimation can still be observed for each component. Nevertheless, this is mainly attributed to the lack of accuracy of the HW method, and to the calibration issues that have been mentioned in the previous sections.

Mean flow — Summary

Meridional plane and radial profiles

- Meridional plane: minor disparities observed between the three simulations for the Mach number, static pressure, total pressure and flow angle fields.
- Radial profiles: very good agreement of the total pressure and total temperature radial profiles with the experimental data. Slight underestimation of the total pressure near the casing, especially for the RANS and the LES1.

Blade-to-blade mean flow

- Overall similar channel flows for all simulations
- Disparities observed in the rotor near wall region and wakes:
  - Thick boundary layer on the rotor suction side caused by a laminar-turbulent transition for both LES, and by an intense TKE production at the rotor leading edge for the RANS.
  - Substantial disparities in the boundary layer turbulence levels of each simulation.
  - Strong interaction of the turbulent boundary layer with the downstream wake inducing significant wake TKE level disparities between the simulations.
- Discrepancies observed in the stator near wall region and wakes:
  - Low TKE levels observed on the stator suction side in the RANS.
  - Turbulent transition of the boundary layer observed in both LES, leading to an increase in TKE levels and in the wake thickness.

3D flow topology

- Rotor domain:

    - Significant radial flow.
    - Development of a radial vortical structure at the LE, extending over more than 60% of the rotor span in all simulations.
    - Strong interaction between the LE vortex and the tip clearance flow.
    - Highlighting of a recirculation region induced by the LE vortex.

- Stator domain:
    - Flow aligned with the rotation axis over most of the vane surface in the RANS simulation.
    - Strong radial flow observed in the LES1 leading to a radial vortical structure at 60% chord similar to the rotor LE vortex.
    - Slight radial flow observed in the LES2.

Boundary layer analysis

- Identification of flow separations:
    - Significant flow separation observed at the rotor leading edge for all simulations.
    - Flow separation observed at 60% rotor chord, at midspan, for both LES.
    - Large flow detachment covering the last 40% of the stator vane chord in the LES1.
- Several laminar-turbulent transitions induced by flow separations, strong interactions with 3D flow features, and adverse pressure gradients.
- Intense thickening of the boundary layer induced by the turbulent transitions.

Pressure coefficient

- Comparable pressure coefficient profiles on the rotor and stator pressure sides for all simulations.
- Slight disparities observed on the rotor and stator suction sides.
- Highlighting of C_p plateaus, on both the rotor and stator suction sides, caused by flow separations, intense 3D flow features, and boundary layer transitions.

Fan wake analysis

- Overall good agreement of the simulations with the HW measurements.
    - Slight overestimation of the mean axial and azimuthal velocity components by all simulations.
    - Overestimation of the mean radial velocity by all the simulations attributed to the lack of accuracy of the HW method.
    - Significant over-prediction of wake TKE levels by all the simulations attributed to a probable more intense rotor leading edge flow separation, and to a lack of accuracy of the HW measurements.
    - Significant improvement of the RMS levels observed with the LES2.

3.3 Instantaneous and unsteady flow

In the previous sections, the main flow features of the three simulations have been emphasized thanks to the analysis of the mean flow. The present section deals with the unsteady phenomena that occur in both LES. In particular, it aims at emphasizing the dynamic nature of some flow features and analyze the turbulent structures and statistics in detail.

3.3.1 Blade-to-blade instantaneous flow

Figure 3.30 shows the instantaneous Mach number field at different radial positions for both LES. For all radial positions, the LES1 displays a thick or more dissipated wake at the transition between the rotor and the stator domains, which is due to the coarser mesh in this region. This has not been observed in the mean solution since the wakes vanish because of the averaging process. This phenomena is not observed anymore in the LES2 thanks to its much finer mesh, except at 25% rotor span because the inter-stage refinement block does not extend down to the core flow region.

At 25% rotor span, the flow is very similar between the two simulations, except that the LES2 rotor wakes are thinner than those of the LES1.

Above 25% rotor span, the turbulent nature of the flow can be clearly observed in both simulations. The flow is laminar on the rotor pressure side while a thick turbulent boundary layer develops on its suction side. The previously analyzed rotor LE flow detachment, which is partly responsible for this laminar-turbulent transition, has an intermittent behavior that results in the formation of vortices that graze along the blade suction side, and eventually feed the downstream wake. This phenomenon is well illustrated by the video in fig. 3.31, which shows the vortical structures created by the LE flow separation and convected down to the trailing edge. Depending of the radial position, several differences can be observed in the stator domain between the two LES. At 50% rotor span, the flow detachment that occurs on the stator suction side in the LES1 triggers an intense vortex shedding at the trailing edge. This explains the significant stator wake thickness observed in section 3.2.3. This is not observed in the LES2 except at 75% rotor span for which a much less intense vortex shedding is observed. Moreover, in both LES, half of the stator vanes exhibit wider wakes than the other half ($2\pi/20$-periodicity). This phenomenon is also observable at 75% rotor span and is particularly exacerbated at 95% rotor span, especially in the LES1. This results from the interaction of the rotor wakes with the stator vanes, which triggers the transition to turbulence every two vanes since there are 20 rotor blades and 40 stator vanes. At 95% rotor span, the tip gap flow is well captured by the LES2 and slightly dissipated by the LES1. It directly interacts with the wake of the neighboring blade, at its trailing edge.

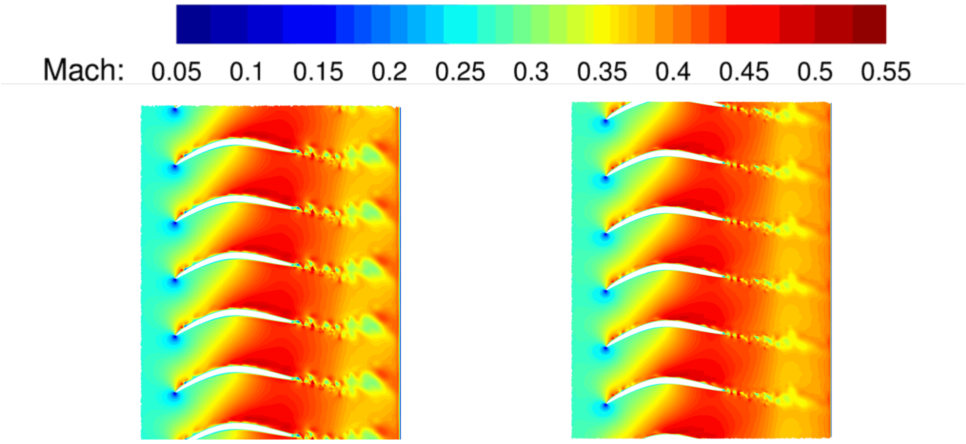

(a) LES1 - 25% rotor span. (b) LES2 - 25% rotor span.

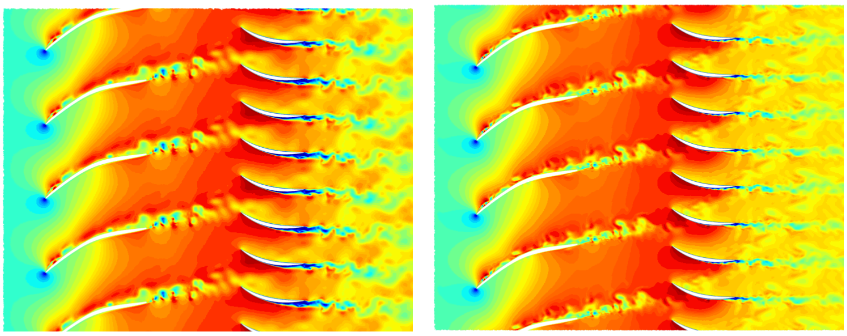

(c) LES1 - 50% rotor span. (d) LES2 - 50% rotor span.

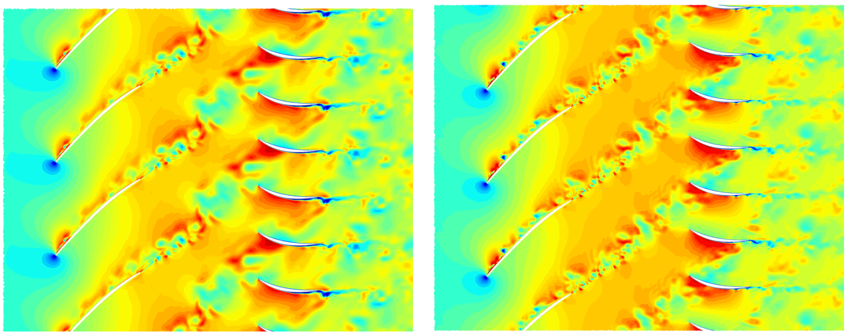

(e) LES1 - 75% rotor span. (f) LES2 - 75% rotor span.

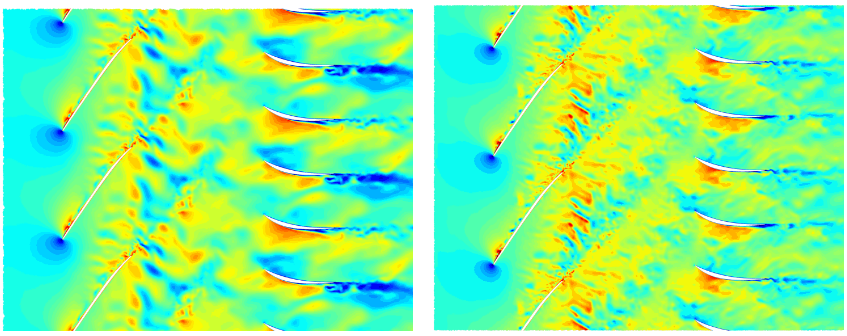

(g) LES1 - 95% rotor span. (h) LES2 - 95% rotor span.

Figure 3.30: Instantaneous Mach number field at different duct heights for both LES.

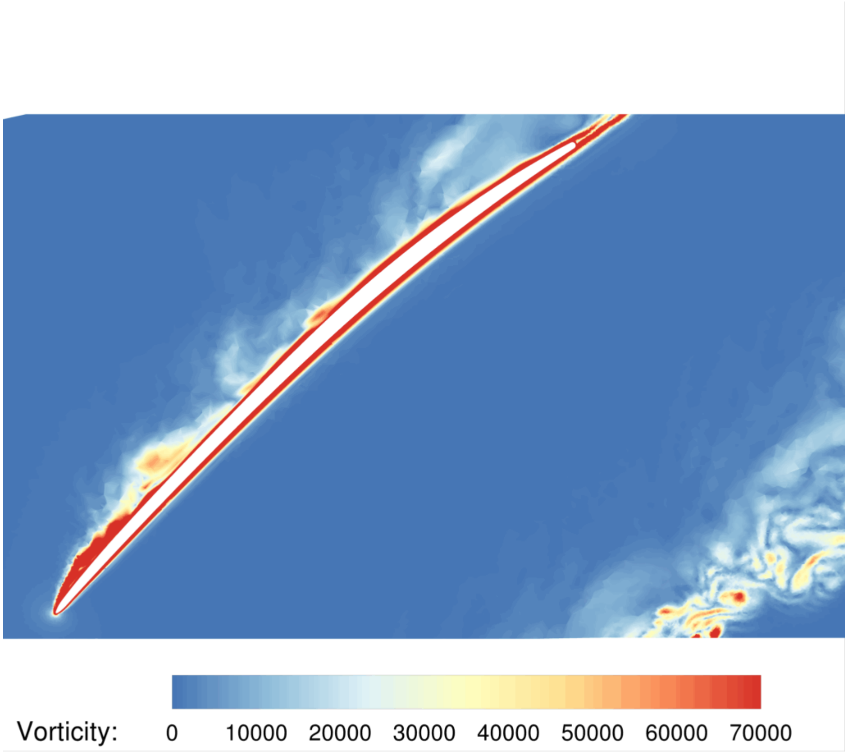

Figure 3.31: Animation of the LE flow separation: vorticity field (double click on the picture or follow this link[1]to start playing the video).

3.3.2 Q-criterion

A convenient way to see the development of turbulent structures is to use iso-surfaces of Q-criterion, where Q stands for the second invariant of the velocity gradient tensor, which is defined as follows:

$$Q = \frac{1}{2}\left(\|\Omega\|^2 - \|\mathbf{S}\|^2\right), \tag{3.5}$$

where $\mathbf{S} = \frac{1}{2}\left(\nabla\vec{V} + \nabla\vec{V}^T\right)$ and $\Omega = \frac{1}{2}\left(\nabla\vec{V} - \nabla\vec{V}^T\right)$ are the symmetric and antisymmetric part of the velocity gradient, respectively. Such iso-surfaces are shown in figs. 3.32 and 3.33 for both LES. The same iso-surface value has been chosen for both simulations in order to see the different turbulence resolutions.

The first view presented in fig. 3.32 shows the development of the turbulent structures on the rotor suction side that result from the LE flow separation. Larger coherent structures are created in the LES1, whereas the LES2 displays an increased density of smaller structures. These disparities are partly related to the presence/difference of intensity of the LE flow detachment, such as below 20% of the rotor span where the flow is clearly turbulent in the case of the LES2, but quasi-laminar in the LES1. They also illustrate the more accurate description of turbulence resulting from the finer mesh of the LES2. The radial flow observed in section 3.2.4 is also well illustrated in these pictures.

The different patterns of the turbulent structures along the blades have a direct influence on the structure of the downstream wakes, which are mainly made of large stretched structures in

---

[1] https://youtu.be/exf1wzJjsmA

the LES1, while both elongated and smaller structures can be observed in the LES2. A horseshoe vortex forms at the junction of the rotor leading edge and the hub in both simulations. Its vortical structure is well captured by the LES2 while it seems to be smoothed by the LES1. On the stator pressure side, the flow seems to remain laminar over the whole vane axial extent.

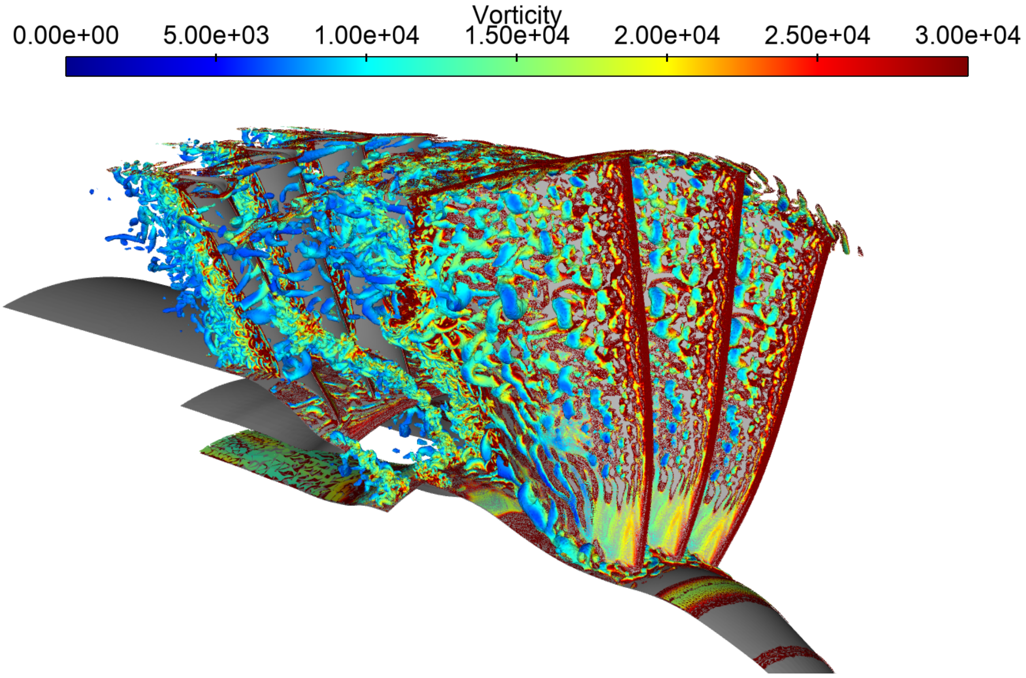

(a) LES1.

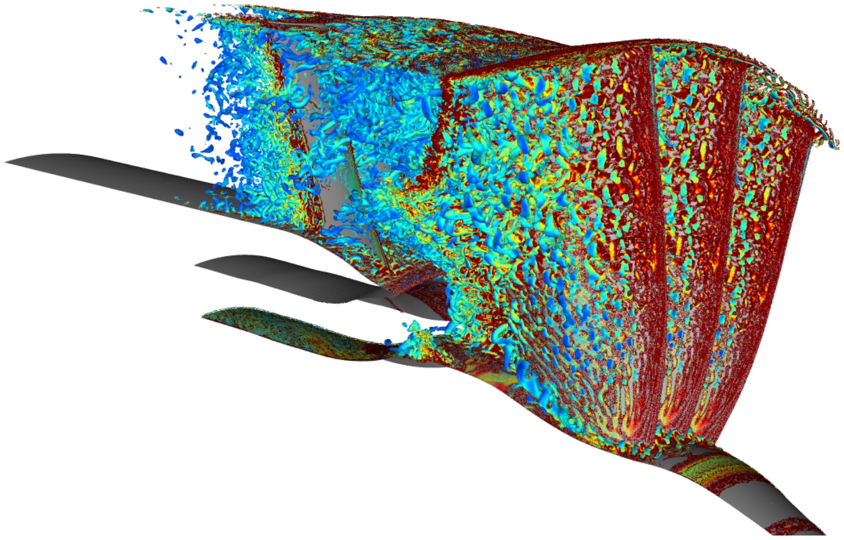

(b) LES2.

Figure 3.32: Q-criterion iso-surface colored by the vorticity magnitude (front part view).

Figure 3.33 shows a view of the rear part of the computation domain. It confirms the previous observations made on the rotor wakes. For the chosen iso-surface value, the LES1 wakes look scattered in comparison with the dense LES2 wakes, which are well defined throughout the inter-vane channel. For both simulations, the flow is laminar on the whole rotor blade pressure side, except on isolated turbulent spots and between 10% and 60% of the rotor span near the trailing edge. The second leg of the horseshoe vortex can be observed. Once again, its vortical structure is much clearer in the LES2 than in the LES1. Regarding the flow on the vane, as observed in section 3.2.5, the boundary layer is quasi-laminar from the LE down to 65% of the vane chord. It then transitions to a turbulent state in both computations. This transition is more intense in the LES1 because of the significant flow separation occurring at this location.

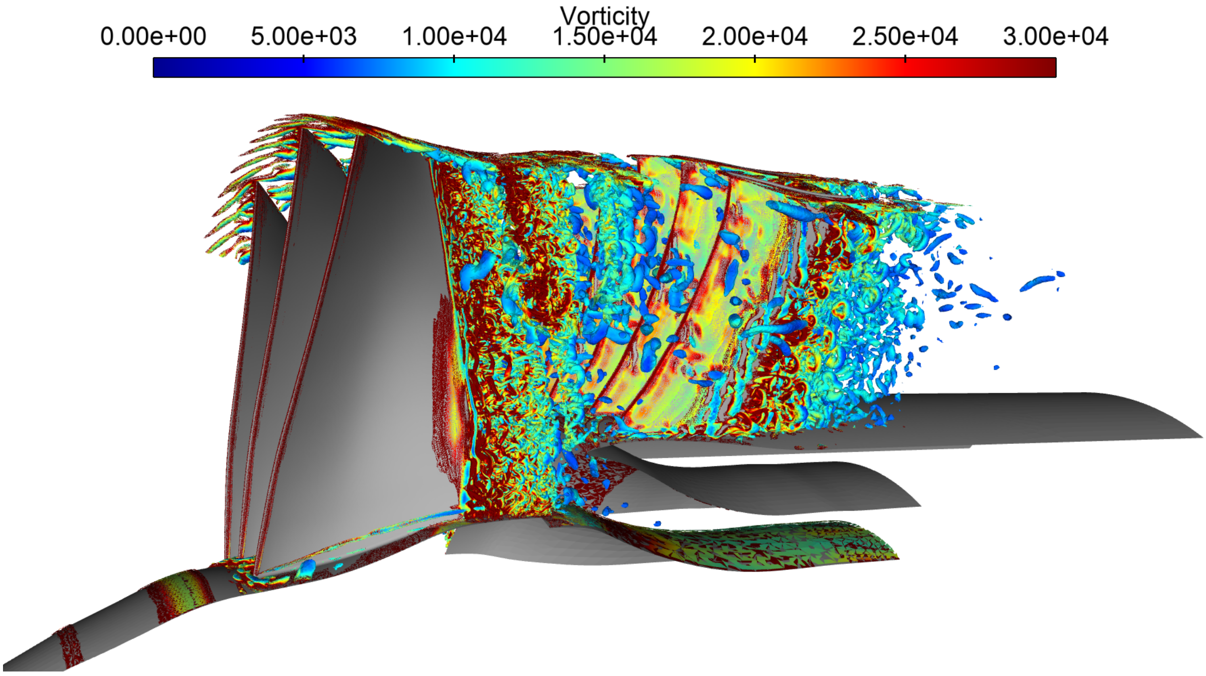

(a) LES1.

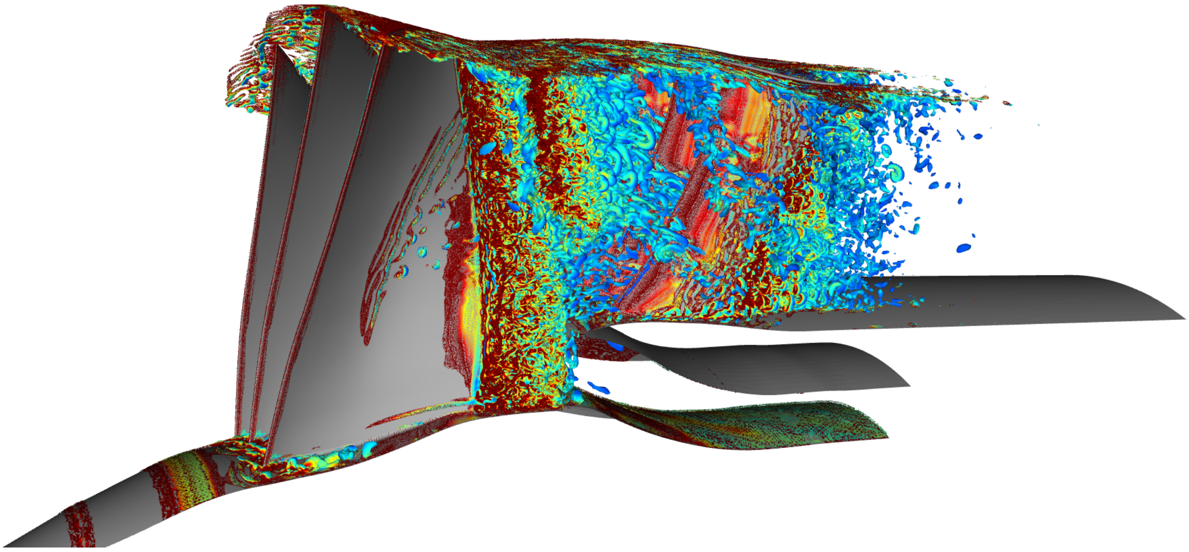

(b) LES2.

Figure 3.33: Q-criterion iso-surface colored by the vorticity magnitude (rear part view).

3.3.3 Velocity spectra

In order to have a better insight into the turbulence statistics, the Power Spectral Density (PSD) of each velocity component at the HW1 position at 50% rotor span is displayed in fig. 3.34. The simulation results are plotted along with the HW measurements at the same position. The details related to the Fourier transform of each simulation signal are summarized in table 3.3. As already noticed in section 3.2.7.2 when commenting the RMS levels, the LES1 overestimates the PSD levels over the whole chosen frequency range and for all velocity components, whereas the LES2 provides spectra that are much closer to the experimental data. More precisely, the LES1 overestimates the axial velocity by 5 to 10 dB between 1 kHz and 5 kHz while the overestimate for the LES2 remains below 5 dB at low frequencies, and decreases down to 2 dB above 4kHz. Above 5 kHz, the results of the two simulations overlay. The fact that higher PSD levels are observed at low frequencies for the LES1 is actually consistent with the fact that larger coherent structures are observed in this simulation, compared with the LES2. At about 7-8 kHz, a sudden drop in the experimental PSD occurs, for all velocity components. A deeper analysis of the experimental data has revealed that this drop actually results from the relatively important thickness of the hot-wires (enlarged diameter justified by mechanical constraints and probe damages during AneCom tests), which leads to a cut-off frequency of the spectrum of roughly 8 kHz. This partly explains the fact that all the simulations tend to overestimate the RMS levels, since the measurements actually underestimate the true turbulence levels. Polacsek *et al.* [206] have estimated that the RMS levels issued from the measurements are underestimated by a factor of about 1.5, which would significantly reduce the remaining slight overestimation observed in section 3.2.7.2 for the LES2.

For the circumferential velocity spectra, the LES1 displays an almost constant gap of 10 dB from low frequencies up to the experimental cut-off frequency. The LES2 provides more accurate results, with a gap of 1-2 dB up to 3 kHz. Above this frequency, this gap progressively increases to reach a maximum value of 5 dB at 7 kHz. Above 7 kHz, the PSD levels retrieved from both simulation almost overlay.

Finally, the LES1 radial velocity spectrum displays a similar behavior as the circumferential one. The LES2 spectrum, on the contrary, is in very good agreement with the measurements with a gap ranging from 1 to 3 dB from low frequencies up to the experimental cut-off frequency. Above 8 kHz, both simulation spectra overlay.

	LES1	LES2
Sampling frequency (kHz)	110	120
Number of averaging windows (Hann windows)	10	5
Overlap	50%	50%
Δf (Hz)	282	206

Table 3.3: Fourrier transform parameters for the PSD computations.

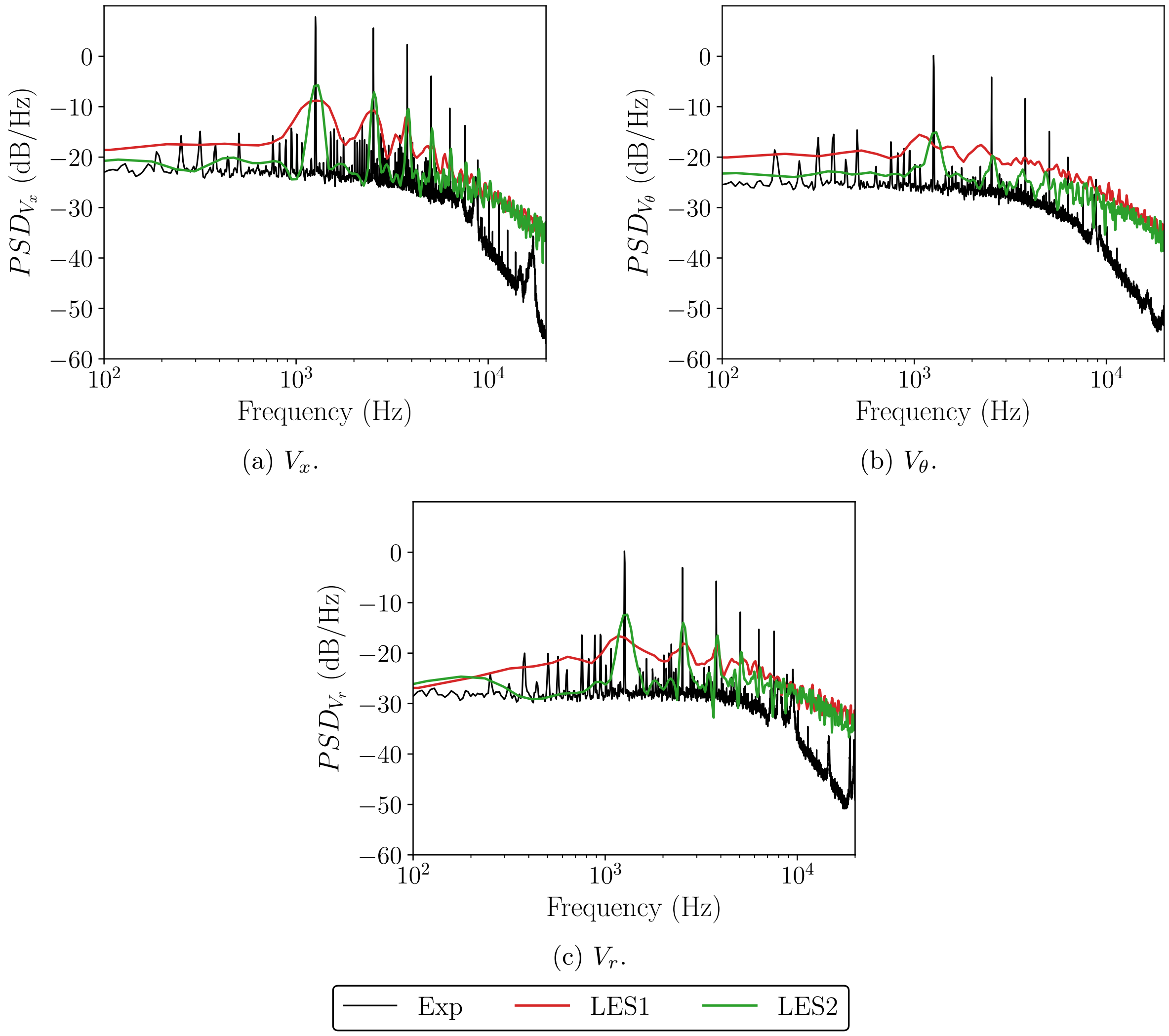

(a) V_x. (b) V_θ. (c) V_r.

Figure 3.34: PSD (dB/Hz) of the fluctuations of each velocity component at the HW1 position, at 50% rotor span.

Instantaneous and unsteady flow — Summary

Blade-to-blade instantaneous flow

- Turbulent flow structures created by the intermittent rotor LE flow separation.
- Vortex shedding observed at the stator trailing edge.
- The wake and near wall flow on the stator display a $2\pi/20$ periodicity (one out of two vanes) due to the interaction of the 20 rotor wakes with the 40 stator vanes.

Q-criterion

- Large coherent turbulent structures created by the rotor LE flow detachment.
- Larger and more stretched structures observed in the LES1.
- Increased density of turbulent structures noticed in the LES2 due to its finer mesh.

- Highlighting of the turbulent transition on the vane suction side.

Velocity spectra

- PSD levels significantly overestimated by the LES1 (5-10 dB gap).
- Better results obtained with the LES2 (2-5 dB gap)
- Drop in the experimental PSD above 8 kHz:
  - Identification of a cut-off frequency (8 kHz) induced by the thickness of the hot-wires.
  - Questionable trustworthiness of the measurements above 8 kHz.
  - Underestimation of the experimental PSD induced by the spectrum drop explaining the *a priori* overestimated RMS levels of the simulations.

3.4 Conclusion

In this chapter, a comprehensive aerodynamic analysis has been carried out on the ACAT1 fan stage using three different computations: a wall resolved RANS simulation, and two wall-modeled LES of different levels of refinement. The RANS and the LES1 are in excellent agreement with experimental performance parameters while small disparities, attributed to major flow topology modifications, are observed for the LES2. The mean flow of each simulation has been thoroughly analyzed and compared to the available experimental measurements. The three simulations provide very consistent results and are globally in very good agreement with the experimental data. The main flow disparities appear in the boundary layers and the wakes. The critical flow features such as the rotor LE radial vortex, the multiple flow separations, the induced turbulent transitions, and their relative impact on the wake structure and TKE levels have been highlighted, showing noticeable differences between the simulations. In particular, the RANS and the LES1 provide significantly overestimated wake TKE levels, while those of the LES2 are in much better agreement with the HW measurements. This unexpected overestimation may result from the HW calibration issues that have been reported during the test campaign.

The analysis of the unsteady data retrieved from both LES has then enabled to get a better overview of the turbulence structures and statistics. In particular, the development of the turbulent structures due to the dynamic behavior of the rotor LE flow detachment has been highlighted. In the LES1, larger and more stretched turbulent structures are observed while the LES2 displays an increased density of smaller structures. Turbulence spectra have also been compared to the HW spectra, showing overestimated levels for the LES1 but satisfactory ones for the LES2. These spectra have also revealed that the hot-wire measurements actually underestimate the RMS levels because of a cut-off frequency induced by the thickness of the hot-wires.

CHAPTER 4

Broadband Rotor-Stator interaction noise predictions on the ACAT1 configuration

Introduction

The present chapter describes the RSI broadband noise predictions performed on the ACAT1 fan stage using two different approaches. The first one uses CFD-informed analytical models while the second one is a hybrid numerical approach coupling both LES with the Ffowcs Williams and Hawkings free-field analogy. The noise estimates obtained from both methods are directly compared to the sound measurements. For each method, the noise estimates based on each simulation are simultaneously compared in order assess the impact of the differences observed in the aerodynamic analysis of the three simulations.

Contents

4.1 Measurements

The experimental Sound poWer Level (SWL) displayed in the following result comparisons have been computed using the microphone measurements. The upstream SWL obtained from the forward arc has been computed by integrating the sound pressure spectra measured by the far-field microphones weighted by the sine of the radiation angle. The downstream SWL has been computed using the pressure signals at the outer casing of the bypass section by assuming a particular energy distribution over the acoustic cut-on modes. This method is referred to as Wave Number Decomposition (WND) and is detailed in Tapken *et al.* [40].

4.2 Noise predictions using CFD-informed analytical models

4.2.1 Analytical models

For this study, two models representing the state of the art of analytical broadband RSI noise prediction have been applied to predict the noise: the model of Hanson [49], and the model of Posson *et al.* [12, 46, 48] as implemented in the *Optibrui* platform, jointly developed by Université de Sherbrooke, Ecole Centrale de Lyon, Airbus, Safran Ventilation Systems and Valeo. Both models are based on Glegg's cascade response [127] and resort to the strip theory in which the stator is divided into several strips. Each strip corresponds to Glegg's configuration in which a rectilinear cascade of zero-thickness flat plates of infinite span is subject to a 3D impinging gust. In the present study, 30 strips have been used for each model. The equivalent flat plate stagger angle has been set using a weighting considering 90% of the LE stagger angle and 10% of the TE stagger angle (see section 5.2 for more details). The two models mainly differ in the way the acoustic propagation is modeled. In Hanson's model, the propagation is performed within each strip accounting for mean axial flow whereas in Posson's model, the unsteady loading is used as an equivalent dipole source within an in-duct analogy (Goldstein's analogy [132]) taking into account a uniform axial flow and distributing the acoustic energy over the duct cut-on modes (see section 1.4.4 for more details). Each model has been informed with flow parameters extracted from the RANS and from the two LES. It should be emphasized that the LES was not meant to feed the analytical models nor are the analytical models meant to be fed by LES statistics, although they technically can. Taking advantage of the existing LES and more specifically, of its statistics, is however a great opportunity to obtain a finer assessment of these models by comparing the analytical responses to a variety of mean flow fields.

4.2.2 Input parameters

4.2.2.1 Extraction methodology

Analytical models require several input parameters in order to reconstruct the stator incident flow and compute the resulting load fluctuations:

- The axial velocity
- The absolute velocity
- The turbulence intensity (TI) in the wake and in the background flow
- The turbulence integral length scale (TLS) in the wake and in the background flow
- The wake half width

The turbulence state of the incident flow is modeled with the Liepmann isotropic spectrum, which is computed using the turbulence intensity and the turbulence integral length scale.

A well adapted and fairly accurate way to extract these parameters is to assume a Gaussian shape for the wake, based either on the absolute velocity deficit or on the turbulence kinetic energy. Performing a Gaussian fit on the extracted wakes then enables to separate the background flow from the wake variables by applying a 20% threshold (see fig. 4.1).

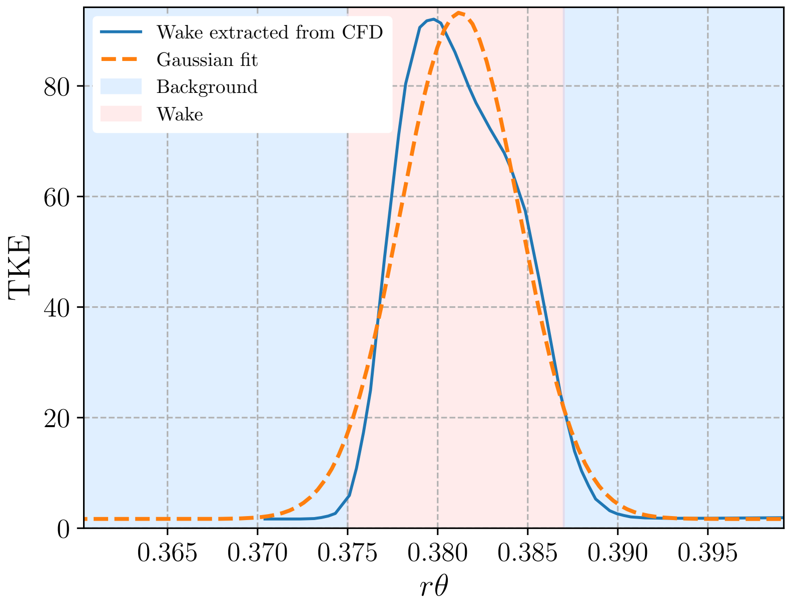

Figure 4.1: Wake extraction using a Gaussian fit.

Multiple processes for estimating the streamwise turbulence length scale based on numerical simulations are available. For RANS simulations, the first one, proposed by Pope [86], makes direct use of the turbulent variables k and ω through the following relationship:

$$\Lambda_p = 0.43\frac{\sqrt{k}}{C_\mu \omega}, \tag{4.1}$$

with $C_\mu = 0.09$. Another estimate can be obtained using the wake width L_w with the empirical relationship of Jurdic *et al.* [207] :

$$\Lambda_j = 0.21 L_w, \tag{4.2}$$

where L_w corresponds to the full width at half maximum of the Gaussian function used for the fitting process, and is computed using the standard deviation σ of the Gaussian function through the following relationship: $L_w = 2\sqrt{2ln(2)}\sigma$. For the latter relationship, the wake and background TLS are the same. This estimate can obviously be used also when retrieving data from LES. Another integral length scale estimate can be obtained using the unsteady data extracted from the temporal recording made on an axial cut through the computation of the temporal autocorrelation function:

$$R_{uu}(\mathbf{x},\tau) = \frac{\overline{u^{'}(\mathbf{x},t)u^{'}(\mathbf{x},t+\tau)}}{u^{'2}_{rms}(\mathbf{x})}, \tag{4.3}$$

where $u'(\mathbf{x},t)$ is the axial velocity fluctuation at position $\mathbf{x}$ and time t, and $u'_{rms}(\mathbf{x})$ the root mean square of the velocity fluctuations at position $\mathbf{x}$. The autocorrelation can then be used to compute the temporal integral scale [86]:

$$\Lambda_t = \int_{\tau=0}^{\infty} R_{uu}(\mathbf{x},\tau)d\tau. \tag{4.4}$$

Under Taylor's frozen turbulence assumption [86, 207], an integral length scale can finally be computed as follows:

$$\Lambda_c = \overline{U}\Lambda_t, \tag{4.5}$$

where $\overline{U}$ is the mean axial velocity component transporting the turbulence.

These flow parameters have to be extracted as close as possible to the stator leading edge in order get a representative description of the flow that is actually interacting with the vane cascade. In the case of the RANS, the data cannot be directly extracted in the stator domain since the mixing plane approach performs a circumferential average at the interface between the rotor and stator domains, preventing the rotor wakes from being convected down to the stator leading edge. As a consequence, the wakes can only be extracted upstream of the mixing plane. Performing broadband noise predictions based on input parameters extracted this far from the vane would lead to overestimated predictions since the models would have been informed with flow parameters (turbulence intensity and integral length scale) that have not decayed enough. To tackle this issue, wake extrapolation methods have been developed. They extrapolate the wakes down to the LE of the stator, increasing the reliability of the noise predictions. Leonard *et al.* [43] developed such an extrapolation method based on a Fourier series decomposition, which proved to give fairly precise results. Jaron *et al.* [208] developed a method based on physical considerations that takes into account the potential field due to the rotor. In the present study, the wake information has been reconstructed at the stator LE by extracting the flow at 200 axial positions from the rotor TE down to the mixing plane. For each axial cut, the wake profile has been extracted on 120 radial positions and 320 azithumal positions. Each azimuthal profile is then fitted using a Fourier series decomposition with a maximum of 9 harmonics. For each radial position, the axial evolution of the phase and amplitude coefficients of the velocity components has been fitted using Jaron's method. Since the method of Jaron is neither dedicated to the TKE (k variable of the Menter SST model) nor to the specific dissipation rate (ω variable of the Menter SST model), the axial evolution of their Fourier coefficients has been fitted with a mean square method to a sum of two exponential functions for the amplitude (typical for a diffusive process), and a linear function for the phase (consistent with a constant convection velocity).

The Fourier coefficients are then extrapolated down to the stator LE based on these fitting functions and used to reconstruct the 2D map of the wake at this position. Figure 4.2 shows that the extrapolations fit very closely the extracted values in the region where both data are available, which gives some confidence in the downstream region where the extrapolation stands alone. In fact the fitting is very satisfactory over the whole blade span, except for radii very close to the hub and to the casing where the boundary layer prevented the fitting from being as accurate as in the rest of the domain, for all harmonics. The hub part of the wake is not an issue in our case since it is extrapolated into the core flow.

For both LES, the extraction has been performed at the LE1 position (see fig. 2.36). To do so, a phase locked average has been performed over about 4 rotations for the LES1 and 3 rotations for the LES2, making it possible to recover the velocity components, the TI, the wake width and Λ_j for both simulations. The same approach as Odier *et al.* [99] has been used to compute Λ_c based on the unsteady data retrieved at the same location, and over the same simulation times.

Figures 4.3 and 4.4 show the axial velocity and the TKE contours near the stator leading edge resulting from the RANS extrapolation and from the phase-locked average of each LES. It should be noted that the LE1 cut and the stator leading edge are not exactly at the same location. However, since the distance between the leading edge and the axial cut of both LES is relatively small, the flow disparities between these two positions are expected to be relatively small as well, which ensures a reliable comparison between the two extractions. Furthermore,

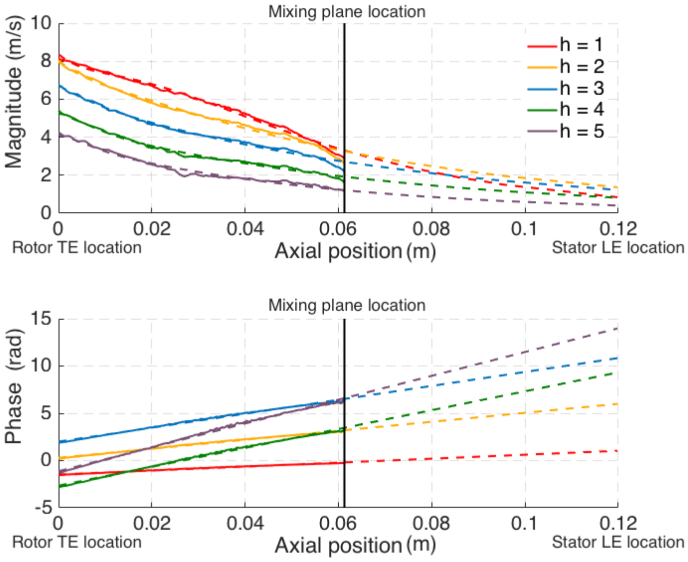

Figure 4.2: Fourier decomposition of the 5 first harmonics (h) of the axial velocity at rotor mid span: extracted values (solid lines) and extrapolated values (dashed lines).

the slightly smaller radial extent of the RANS cut, with respect to the LES ones, is due to the fact that the outer radius of the duct slightly decreases in the inter-stage zone, preventing from completely extrapolating the tip-gap flow since the extrapolation is performed at each radius.

The validation of this extrapolation against experimental data cannot be conducted since no HW measurements have been performed at the stator LE. However, given that both LES provide similar results, the extrapolated field can be directly compared with them while considering the differences already observed in chapter 3. Figures 4.3 and 4.4 show that the extrapolation process tends to overestimate the tilting of the wake. Indeed, the RANS wakes are a lot more leaned than the LES ones whereas their tilting is similar at the HW1 position. Moreover, the expected decrease in the wake velocity deficit is overestimated by the extrapolation, as the RANS wake velocity deficit is significantly less important than that of the two LES, contrary to what has been observed at the HW1 position. The relative wake width and the TKE level disparities seem to be of the same order of magnitude as at the HW1 position, with a global decrease in the wake TKE levels that goes along with a wake broadening.

4.2.2.2 Input comparison

Figures 4.5 and 4.6 show the radial evolution of the input parameters resulting from the previously explained extraction process. The LES values are plotted along with the RANS extractions.

The absolute and axial velocities (figs. 4.5a and 4.5b) extracted from both LES and the RANS are relatively similar, with values that are slightly higher at the stator midspan for the RANS. The turbulence intensity, however, shows significant disparities. On the one hand, the background TI (fig. 4.5c) of both LES is slightly lower than in the RANS. This might be due to the fact that no turbulence has been prescribed at the inlet of the LES, whereas an inlet turbulence intensity of 0.03% has been imposed in the RANS. On the other hand, the wake TI is higher for both LES, especially for the LES1, which can reach values up to twice the RANS wake TI between 15% and 80% of the stator span (fig. 4.5d). The LES2 displays intermediate wake TI

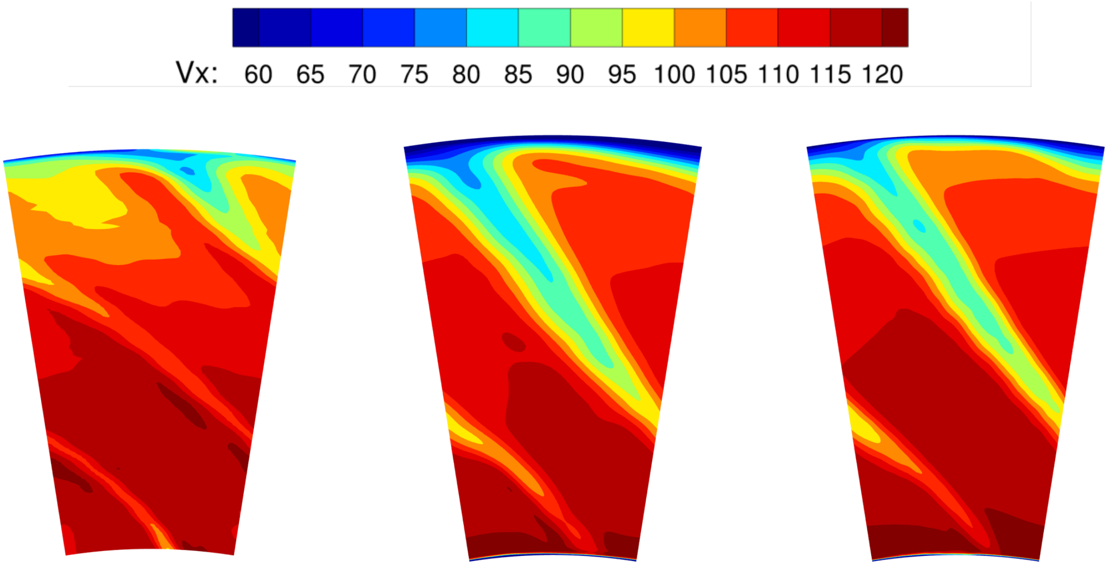

(a) RANS.

(b) LES1.

(c) LES2.

Figure 4.3: Axial velocity component at the stator leading edge.

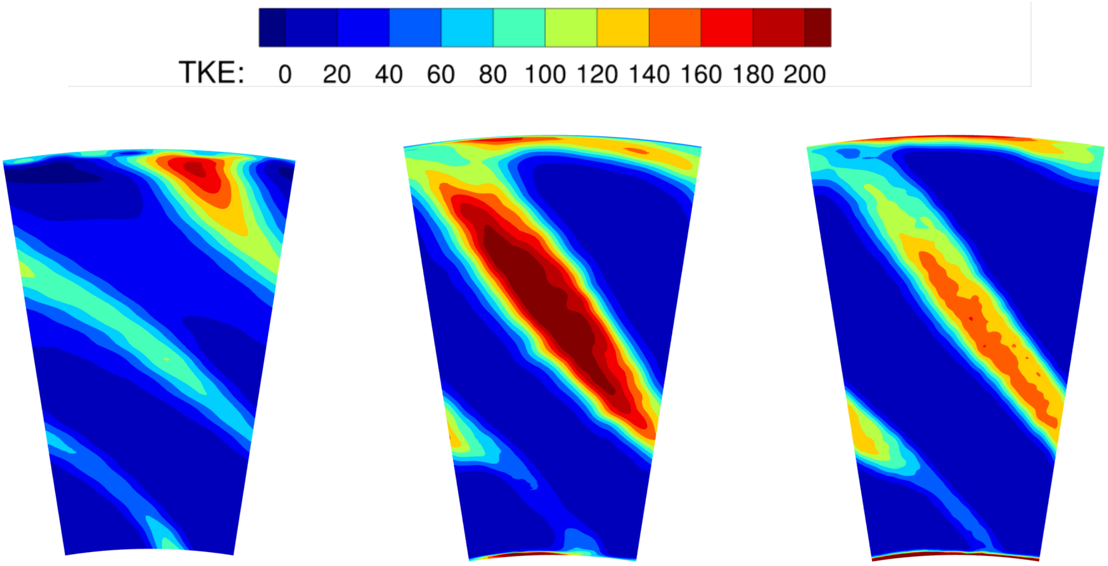

(a) RANS.

(b) LES1.

(c) LES2.

Figure 4.4: Turbulence kinetic energy at the stator leading edge.

levels that are between the LES1 and the RANS ones, except between 0% and 30% of the vane span where the wake TI levels are slightly higher than those of the LES1. These observations are consistent with the aerodynamic analysis of chapter 3, which has shown that the rotor LE flow separation leads to higher TKE levels for the LES1, while the RANS displays the lowest ones. The tip gap region is characterized by a decrease and a sudden increase in the TI, showing the interaction of the wake with the tip gap flow. For both background and wake TI, both LES unveil a sudden increase in TI near the hub and the casing. However, in the case of the RANS, this increase cannot be observed at the hub because the extrapolation process does not account for the presence of the splitter.

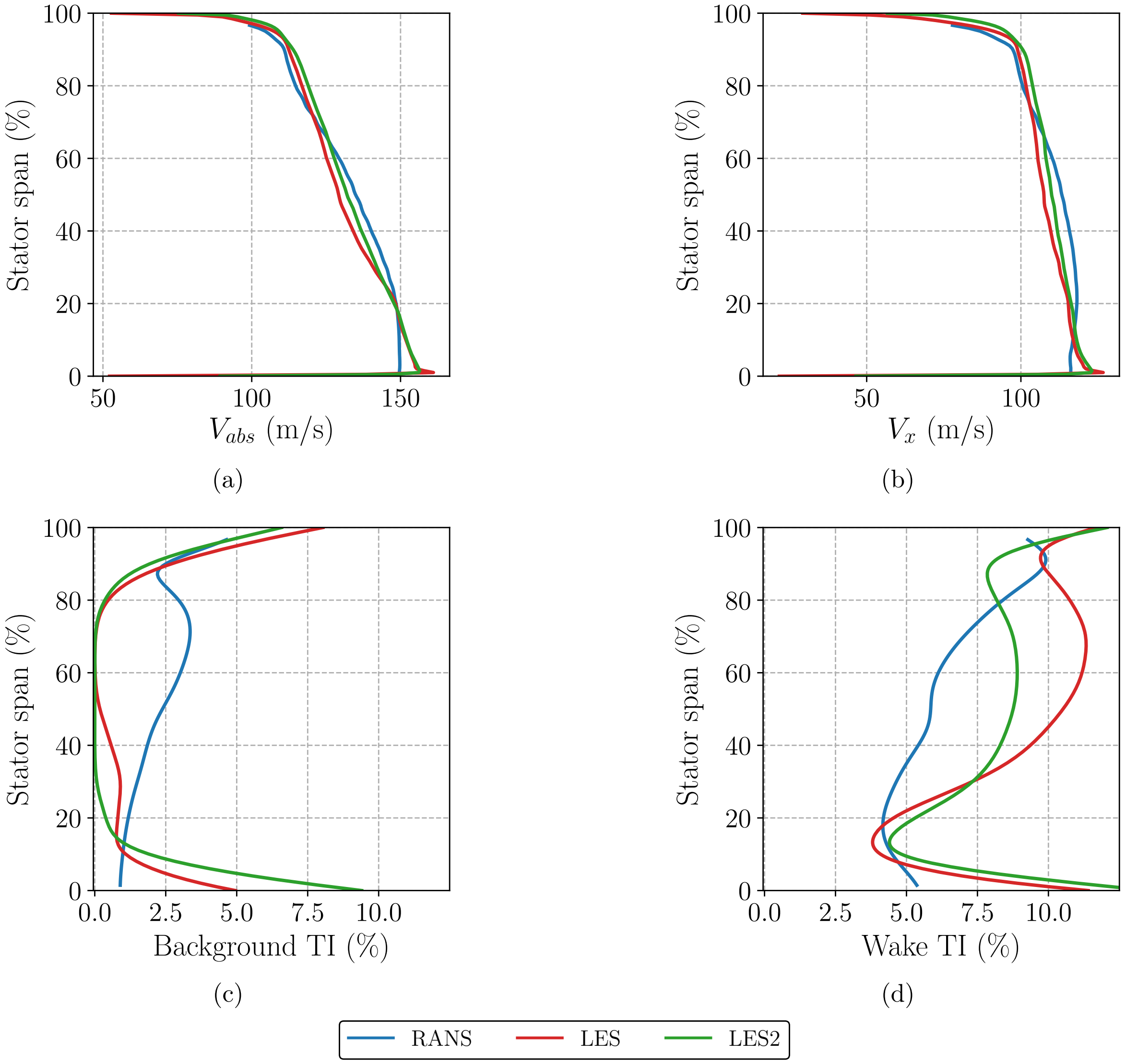

Figure 4.5: Comparison of the model input parameters extracted from both RANS and LES.

The different TLS estimates are plotted in fig. 4.6. The radial evolution of Λ_j is very similar for all simulations, except at 15% stator span where a slight decrease in the TLS, which may result from the interaction of the wake with the splitter, is observed for both LES. The values are higher for the LES1 since the wake is wider than in both the RANS and the LES2 over the whole vane span. Once again, this is the consequence of a more substantial interaction between the separated flow and the downstream wake in the LES1. As expected, according to Jacob *et al.* [67] and Grilliat *et al.* [209], the same increase in Λ_j is observed near the tip gap region where the wake substantially thickens because of its interaction with the tip gap flow. The Λ_p estimate provides wake values that are comparable to those of the RANS Λ_j except above 80% of the stator span where Λ_p decreases instead of increasing.

Λ_c displays a quite different behavior from Λ_j. In the background flow and for both LES, Λ_c is almost constant from the hub up to 80% of the vane span with significantly larger values than those obtained with Λ_j. Smaller background Λ_c values are obtained for the LES2 with respect to the LES1. Near the tip, its shape is similar to the Λ_p estimate, with a decrease in the estimated

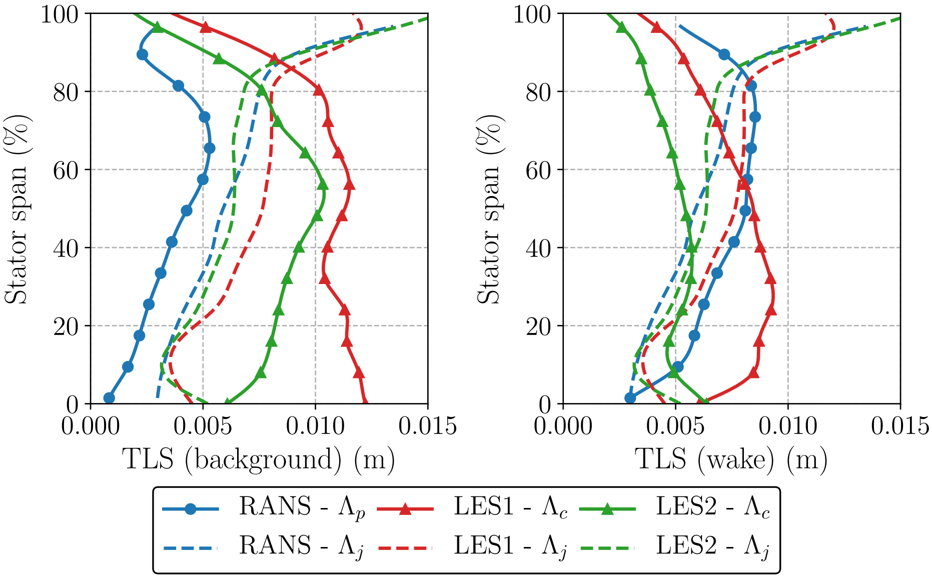

Figure 4.6: Comparison of the different TLS estimates extracted from both RANS and LES.

TLS in the vicinity of the casing. In the wake, the radial evolution of Λ_c significantly departs from Jurdic's estimate. For both LES, Λ_c increases from the hub up to 30% of the vane span and then decreases up to the casing. For the LES1, the Λ_c values are higher than those of Λ_j from the hub up to 60% of the stator span. From that point, Λ_j gives larger values than Λ_c, which can reach more than twice the Λ_c values at the very tip. In the case of the LES2, Λ_c provides values that are similar to those of Λ_j up to 40% of the stator span. Above this radial position, Λ_c values are much smaller than those of Λ_j. In both LES, the wake TLS is smaller than that in the background, whereas Λ_p predicts the opposite. The unexpected larger background Λ_c may be an artifact of the post-processing as the TLS is assessed in a region that hardly displays any turbulent features, leading to such a result.

The results obtained for Λ_c question the validity of Jurdic's estimate in such a flow configuration. It seems that the flow detachment observed on the fan leading edge has significantly modified the wake structure and has led to a flow configuration that does not correspond to the one in which the Jurdic correlation has been established.

4.2.3 Results

The input parameters presented in the previous section have been used to inform Hanson's and Posson's models in order to carry out broadband RSI noise predictions. Figures 4.7 and 4.8 show the predictions using both models informed with the integral length scale estimates that are available for each simulation. The RANS (figs. 4.9 and 4.10) and the LES (figs. 4.11 and 4.12) results have also been plotted separately for better legibility. The plots will be commented in the next section along with the discussion regarding the impact of the TLS estimate on the predictions.

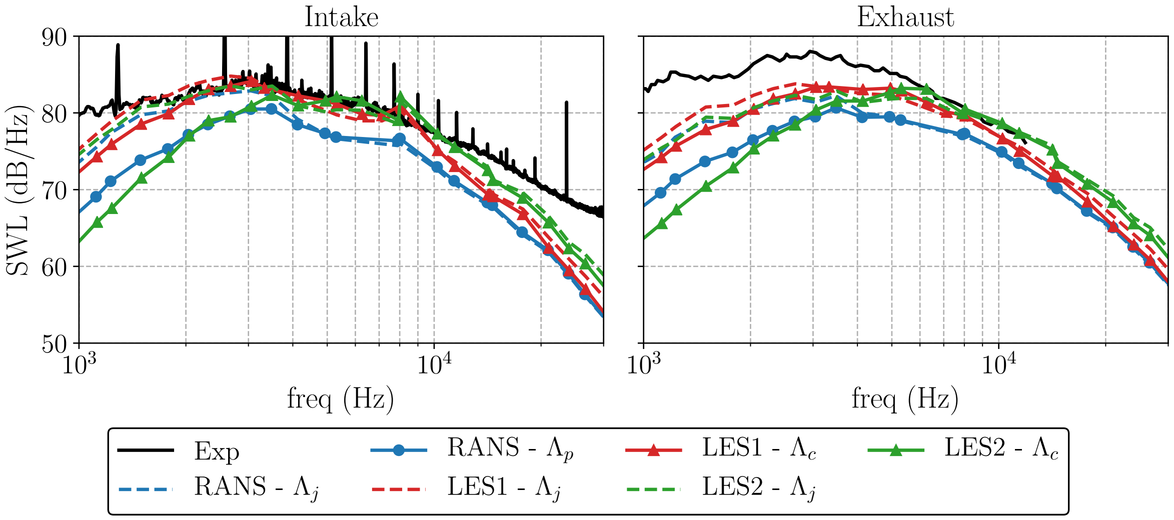

Figure 4.7: Upstream SWL (left) and downstream SWL (right) spectra predicted by Posson's model.

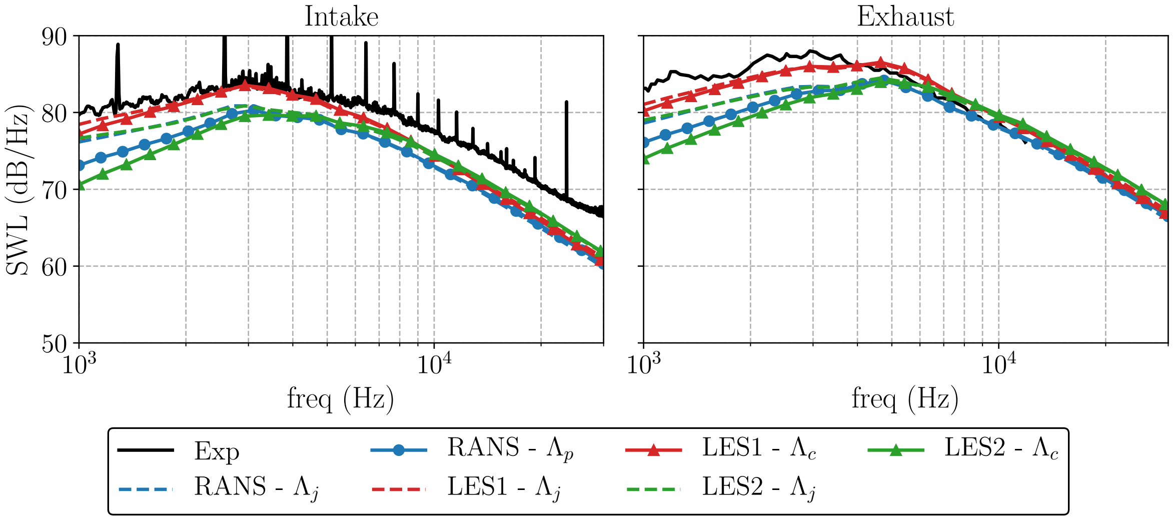

Figure 4.8: Upstream SWL (left) and downstream SWL (right) spectra predicted by Hanson's model.

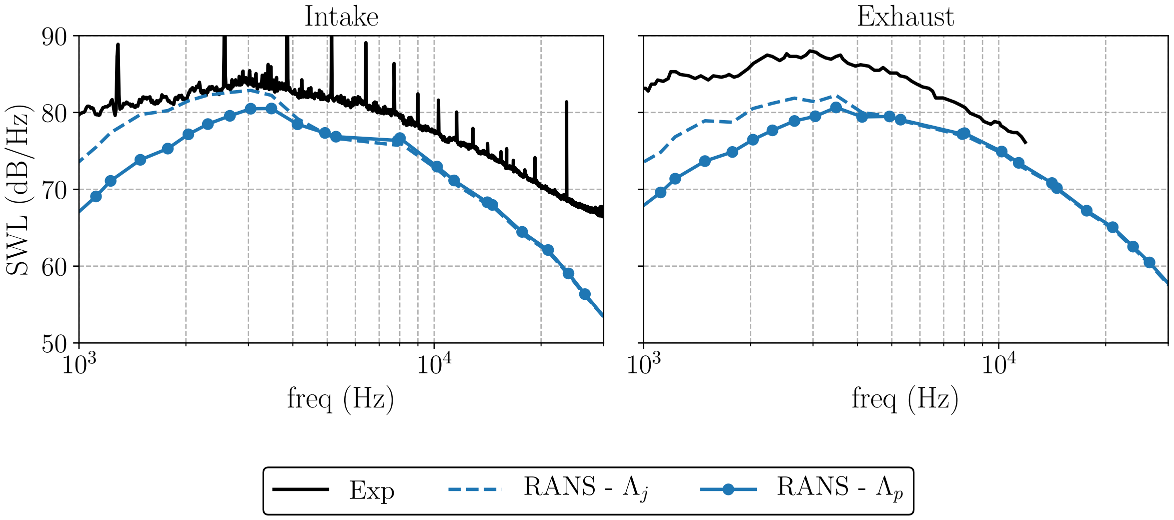

Figure 4.9: Upstream SWL (left) and downstream SWL (right) spectra predicted by Posson's model (RANS only).

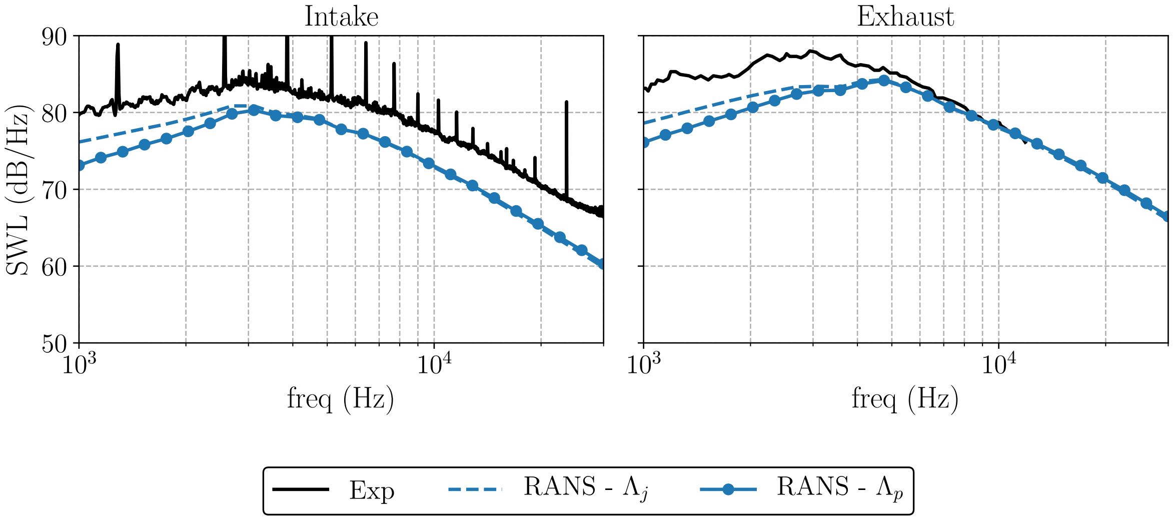

Figure 4.10: Upstream SWL (left) and downstream SWL (right) spectra predicted by Hanson's model (RANS only).

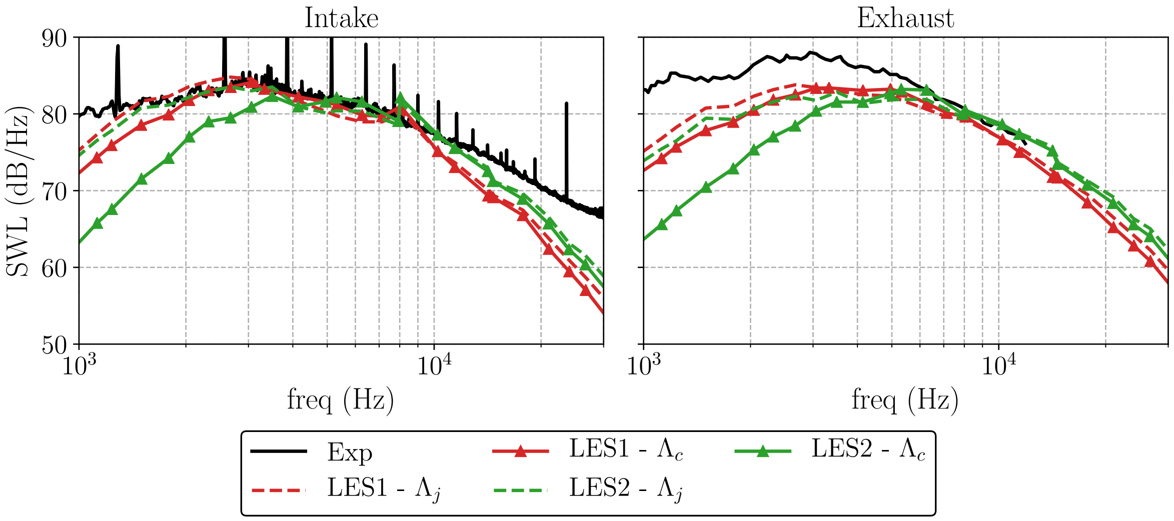

Figure 4.11: Upstream SWL (left) and downstream SWL (right) spectra predicted by Posson's model (LES only).

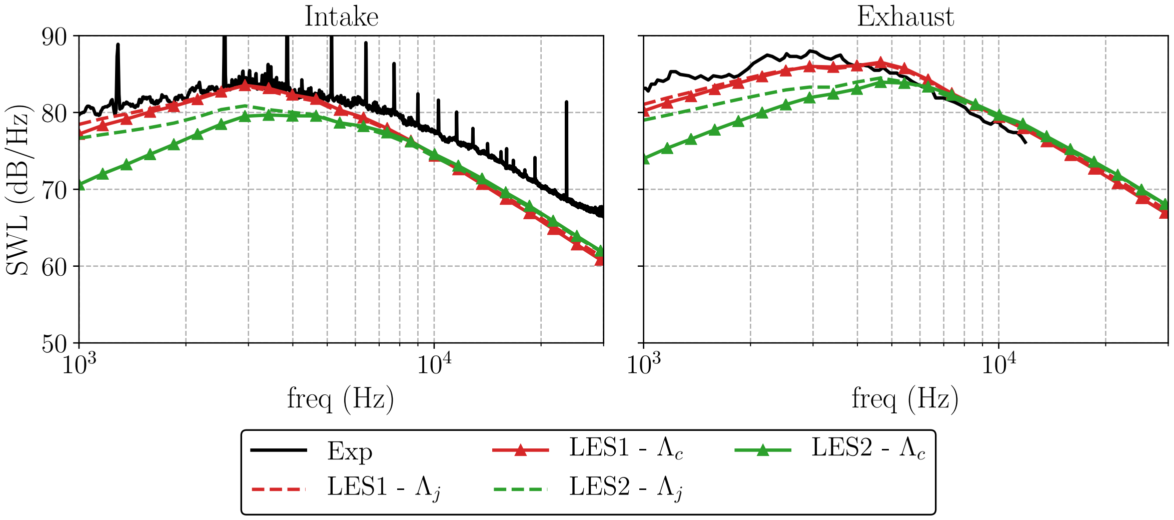

Figure 4.12: Upstream SWL (left) and downstream SWL (right) spectra predicted by Hanson's model (LES only).

4.2.3.1 Impact of the turbulence length scale estimate on the noise predictions

The choice of the TLS estimate has a significant impact on the noise predictions. In the RANS case, larger turbulent structures are found at the tip of the stator with Jurdic's estimate (see fig. 4.6), which eventually leads to higher noise levels at low frequency for both models (see figs. 4.9 and 4.10). The gap between Pope's and Jurdic's approaches can reach values up to 7 dB for Posson's model and 4 dB for Hanson's model. This means that it is paramount to correctly simulate the tip-gap flow and to determine which TLS estimate is the most reliable when retrieving data from RANS simulations. Such a behavior is still noticeable for the LES1 (see figs. 4.11 and 4.12) but with a much smaller magnitude, despite similar wake TLS disparities at the tip between Λ_c and Λ_j (see fig. 4.6). Indeed, at low frequency, the difference between the two model estimates is less than 1 and 3 dB for Hanson's and Posson's models, respectively. To better understand this result, a strip-by-strip study has been carried out using Hanson's model informed with both the RANS and the LES1 data. Figures 4.13 and 4.14 show the noise radiated by each strip separately, for the TLS estimates available for each simulation. Only the upstream noise is displayed since similar effects are observed downstream. Strips 1 and 30 are the closest to the bypass hub and to the casing, respectively. In the RANS case, the Λ_j and Λ_p predictions provide similar noise estimates for the 20 first strips. Among the 10 last strips, however, significant discrepancies appear at low frequencies with SWL levels that can be 10 dB higher for the Λ_j predictions, which confirms the previous observations. On the contrary, the LES1-based strip-by-strip study reveals disparities in the first 10 strips (see fig. 4.14). At low frequency, the Λ_c predictions display SWL levels than can be 5 to 10 dB higher than the Λ_j predictions depending on the considered strip. From strip 11 to strip 30, the disparities observed between the Λ_c and Λ_j predictions are of the same order as those observed between Λ_p and Λ_j in the RANS case. Consequently, the much larger wake and background TLS values obtained with Λ_c, from the hub up to 30% of the stator span, partly counterbalance the low frequency SWL increase due to the significant Λ_j values at the tip. This eventually results in a reduced gap between the Λ_c and Λ_j LES1 predictions, with respect to the gap between the Λ_j and Λ_p RANS predictions. In the case of the LES2, the low frequency disparities between the noise predictions obtained with the two available TLS estimates are even larger than those observed for the RANS. Indeed, the gap between the two approaches can reach values up to 10 dB for Posson's model and 6 dB for Hanson's model (see figs. 4.11 and 4.12). This can be attributed to the fact that, above 40% of the stator span, the LES2 wake Λ_c values are significantly lower than the Λ_j ones as shown in fig. 4.6. Below 40% stator span, Λ_c and Λ_j are of the same order of magnitude. It should also be noted that this increased gap between the predictions obtained with the two estimates occurs in spite of significantly larger background Λ_c values with respect to Λ_j. This implies that the counterbalance effect observed for the LES1 is actually due to the larger near hub Λ_c values in the wake, rather than those in the background flow.

For both models and for all simulations, the noise predictions obtained with the two available TLS estimates for each simulation almost overlay above 5 kHz despite noticeable TLS disparities (see figs. 4.7 and 4.8). This is particularly the case for Hanson's model (figs. 4.10 and 4.12) and for the RANS-informed predictions using Posson's model (fig. 4.9). For the LES-informed predictions using Posson's model (fig. 4.11), the TLS disparities have had a slight impact at high-frequencies as well. Indeed, in addition to the near-casing strip effect, the TLS differences have induced a slight tilting of the spectra, leading to an almost constant 1 dB gap above 5 kHz between the two predictions performed for each LES.

As also shown by Leonard *et al.* [43] on the NASA Source Diagnostic Test case (SDT), the power spectra obtained with Jurdic's approach are closer to the experimental data in terms of shape and absolute levels, whether it is for the RANS-informed (figs. 4.9 and 4.10) or the

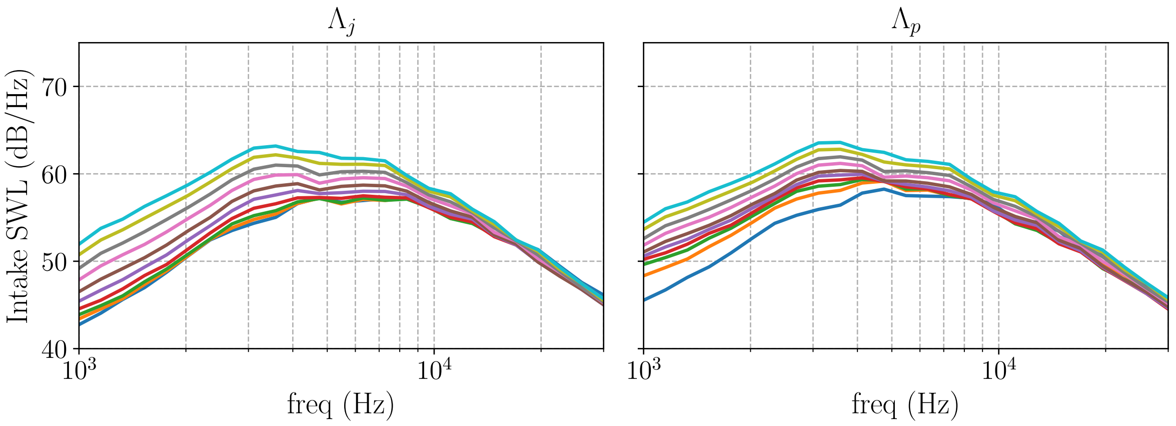

(a) Strips 1 to 10.

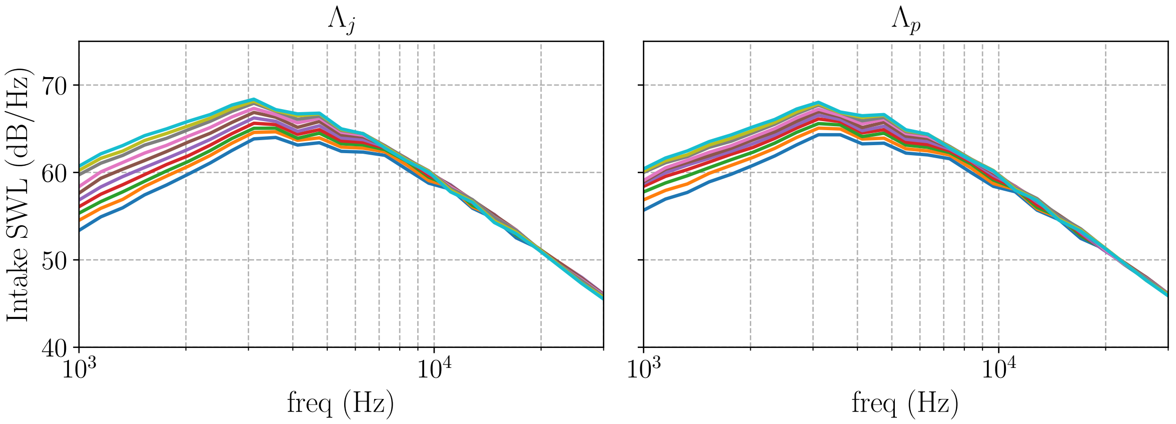

(b) Strips 11 to 20.

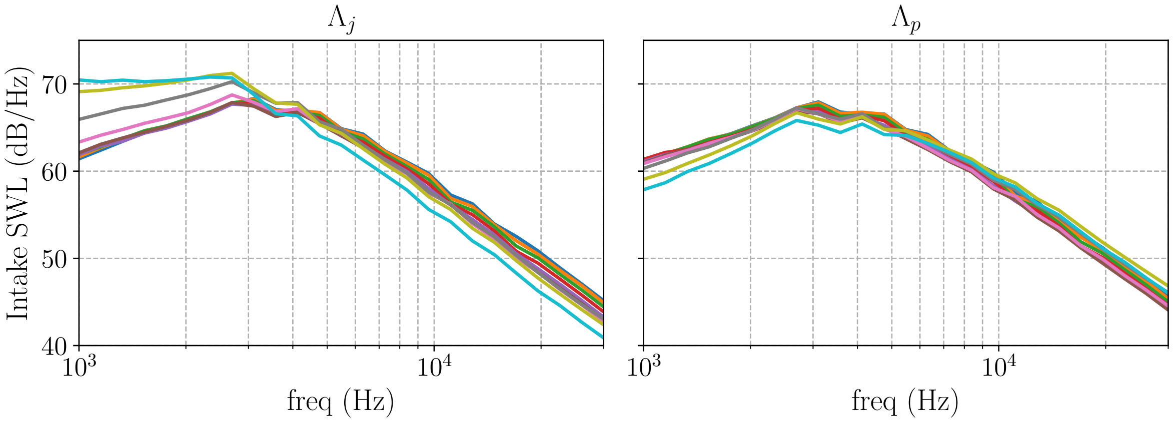

(c) Strips 21 to 30.

Figure 4.13: Strip-by-strip results using Hanson's model informed with the RANS data. Λ_j results (left) and Λ_p results (right).

LES-informed predictions (figs. 4.11 and 4.12). However, this does not mean that Jurdic's approach provides the most reliable estimate for two main reasons. Firstly, the LES2 Λ_c estimate, which is arguably the most reliable estimate in the present study, displays significant discrepancies with Λ_j in terms shape and absolute values as shown in fig. 4.6. Furthermore, for the ACAT1

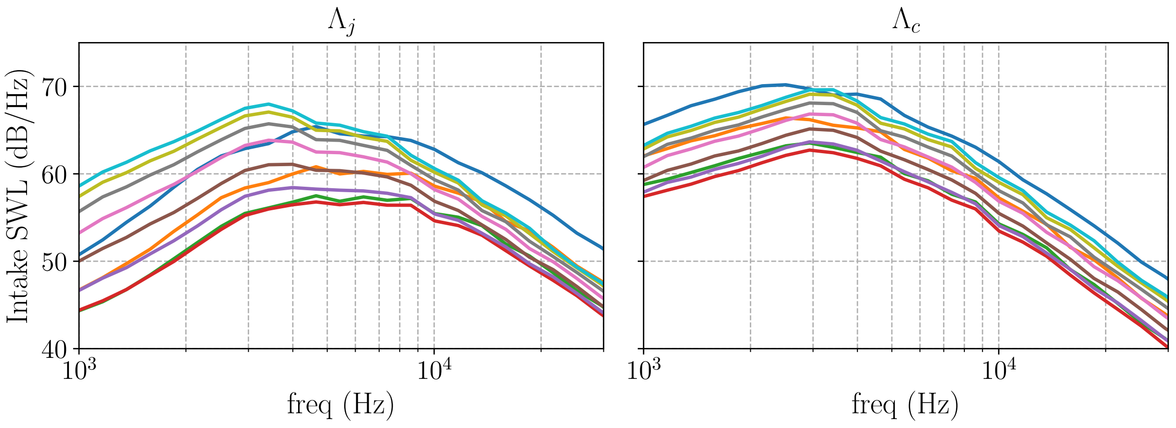

(a) Strips 1 to 10.

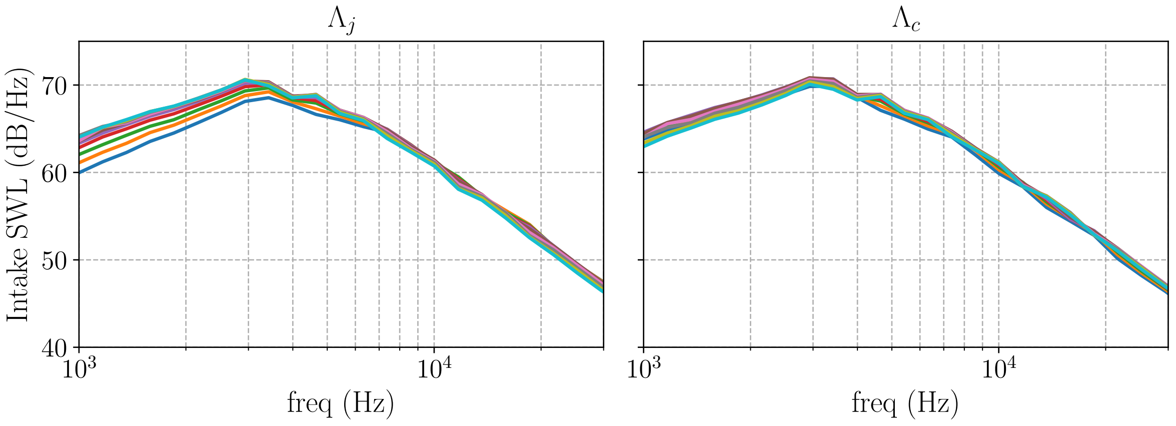

(b) Strips 11 to 20.

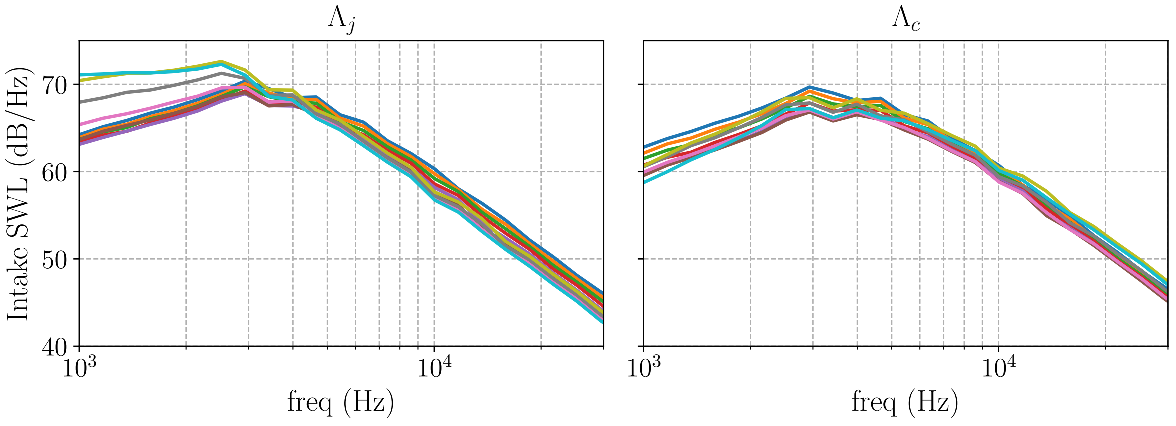

(c) Strips 21 to 30.

Figure 4.14: Strip-by-strip results using Hanson's model informed with the LES1 data. Λ_j results (left) and Λ_c results (right).

configuration, the Λ_j estimate does not seem to recover the true behavior of the flow in the tip region since an increase in the TLS is observed close to the casing, whereas Λ_c decreases. The Λ_p estimate, on the contrary, recovers the correct behavior in the tip region as shown in fig. 4.6. For both analytical models, it also provides noise predictions that are much closer to the

LES2 Λ_c predictions (see figs. 4.7 and 4.8). Secondly, it should be underlined that the sound measurements include the noise produced by all the sources within the fan stage, while the analytical models only estimate the noise generated by the RSI mechanism. As a consequence, the noise levels predicted by the analytical models are actually expected to be lower than those of the measurements, especially if the RSI mechanism is not the only significant noise source. This may actually be the case of the ACAT1 configuration since all the analytical predictions underestimate the radiated noise over most of the chosen frequency range, despite an overestimated TKE for all simulations. This is especially the case for the LES1, which predicts RMS levels for the velocity components that can be twice as large as the measured values (see chapter 3 for more details). This question will be addressed more specifically in section 4.3.

The previous comments thus raise the question of the most reliable TLS estimate to use when performing noise predictions with RANS-informed analytical models. When retrieving data from an LES, the best choice is to rely on the unsteady data and limit the number of modeling assumptions. Λ_c is a good example of such an estimate but still relies on Taylor's frozen turbulence assumption. Other estimates relying on spatial correlations, such as those proposed by Grace *et al.* [56], would give more accurate results but require an increased amount of extracted data to be computed. When retrieving data from a RANS simulation, however, the choice is less obvious. On the one hand, the Jurdic estimate (see eq. (4.2)) predicts larger turbulent structures near the casing with respect to Λ_c, which significantly increases the noise levels at low frequencies. On the other hand, the Pope estimate (see eq. (4.1))recovers a radial evolution in the wake similar to that of the LES2 Λ_c, but simultaneously underestimates the TLS in the background. It also predicts larger turbulent structures in the wake than in the background, which is not consistent with the Λ_c estimate. Since the background flow has proven to be less determinant than the wake flow, the Pope estimate might be a better option in the present case. Some alternatives to these two RANS TLS estimates also exist (see the studies by Kissner *et al.* [204] and Guérin *et al.* [210] for more details) but have not proven to be more accurate than those tested in the present study. The previous comments are conditioned by the accuracy of the RANS extrapolation process.

Finally, significant disparities in the noise predictions are observed depending on the simulation from which the input parameters are extracted. At first sight, the LES1 results look satisfactory as they are the closest to the noise measurements. However, this apparent better agreement is actually due to the significantly overestimated TKE in the LES1, and to the additional broadband noise sources present in the experiment as shown in section 4.3. As a consequence, an LES that is not fine enough can lead to less accurate analytical noise predictions than a RANS, since the RANS-informed predictions are much closer to the LES2 predictions, which arguably use the most reliable input parameters.

4.2.3.2 Impact of the chosen analytical model

Figures 4.15-4.17 show the direct comparison of the CFD-informed predictions obtained from Hanson's and Posson's models, for each simulation. Regardless of the simulation type or the considered TLS estimate, Posson's model tends to underestimate the noise at low frequency relatively to Hanson's model. This is mainly attributed to the duct cut-off effect which has a noticeable impact, especially at low frequencies for which a major part of the first modes is cut-off. The frequency for which the maximum SWL is observed is well captured by the model of Posson for both upstream and downstream predictions. Hanson's model, however, only captures the frequency of the SWL peak for the upstream prediction. This capacity to capture the frequency of the SWL peak does not depend on the chosen TLS estimate. In terms of shape, Hanson's model is closer to the upstream experimental spectrum whereas Posson's model recovers quite faithfully the shape of the downstream experimental spectrum. This may be due to the fact that Posson's model uses the inner and outer radii of the bypass section as references for the in-duct propagation, leading to a more important cut-off effect for the upstream part but to a more faithful downstream prediction. In terms of absolute levels, Hanson's model provides an overall better estimate of the intake and exhaust SWL than Posson's model. In the case of the LES2-Λ_c predictions for instance, both models underestimate the upstream noise from medium to high frequencies, with a gap ranging from 2 to 8 dB for the highest frequencies. For the downstream prediction, Hanson's model recovers the experimental noise levels above 5 kHz. Below this frequency, it underestimates the noise by 4 to 10 dB depending on the considered TLS estimate. Depending on the TLS estimate, a significant underestimation by 10 to 15 dB can be observed for Posson's model below 5 kHz, while the experimental levels are well recovered above. Conclusions have to be drawn carefully since the duct geometry both upstream and downstream of the OGV, as well as rotor reflections, are likely to impact the sound transmission. In that perspective, Posson's model better takes into account the transmission across the stator and the downstream duct, since it expresses the solution as a sum of cut-on annular duct modes. Consequently, the apparent under-prediction of Posson's model may actually be the most trustworthy for the RSI mechanism, which would indicate the presence of other non-negligible noise sources in the experiment. The fact that both models still under-predict the radiated noise in spite of the fact that the TI levels are significantly higher than in the experiment also supports this latter point.

Furthermore, the present results contradict the study of Leonard *et al.*'s on the SDT case [43] in which the model of Hanson tends to slightly overestimate the downstream SWL, especially at low frequencies. Similarly to the present study, they showed that Posson's model underestimates the noise radiated downstream of the stator. However, the gap between the experiment and the predictions did not exceed 5 dB when using Jurdic's TLS estimate. Once again, this supports the fact that additional noise sources are present in the ACAT1 configuration, as it will be shown in the next section. Nevertheless, it should also be noted that not all the phenomena of the RSI mechanisms are taken into account. For instance, the rotor shielding effect as well as the swirling flow upstream of the stator have not been taken into account and may have a significant influence on the SWL, as shown by Posson *et al.* [211] and Masson *et al.* [163]. This significant underestimation of the noise may also be the consequence of the numerous assumptions made in the model, which might not be completely correct in the specific case of the ACAT1 configuration.

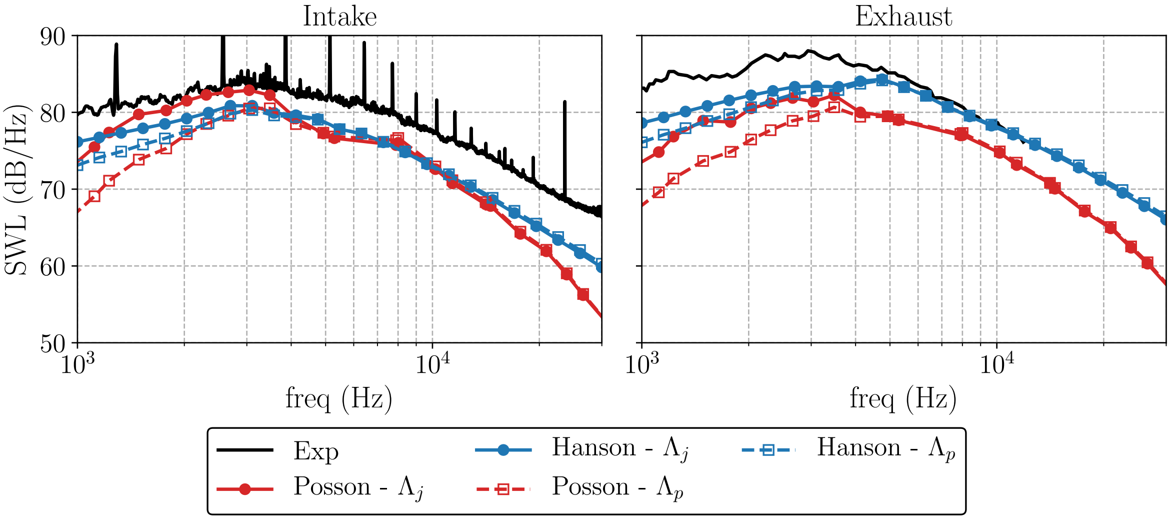

Figure 4.15: Comparison of the RANS-informed predictions using Hanson's and Posson's models.

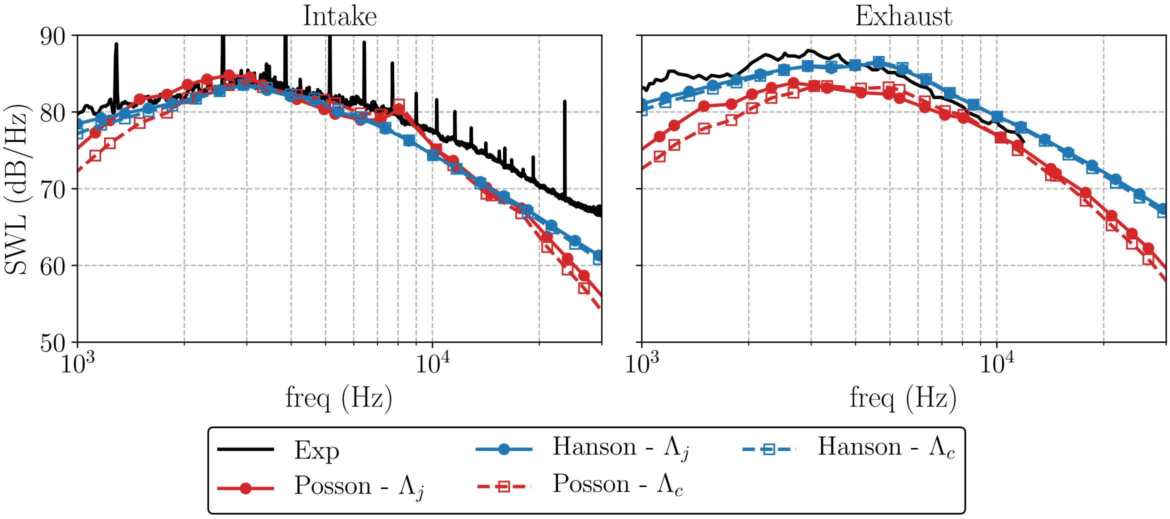

Figure 4.16: Comparison of the LES1-informed predictions using Hanson's and Posson's models.

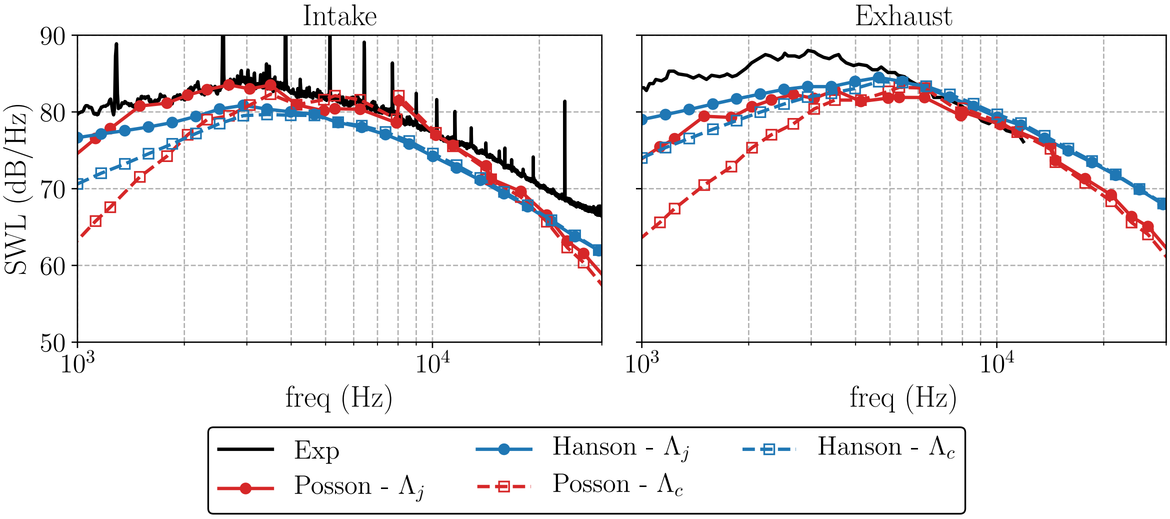

Figure 4.17: Comparison of the LES2-informed predictions using Hanson's and Posson's models.

Noise predictions using CFD-informed analytical models———— Summary

Analytical models

- Two analytical models based on Glegg cascade response have been used:
  - Hanson's model: cascade response, propagation within each strip accounting for mean axial flow.
  - Posson's model: cascade response, in-duct propagation using Goldstein's analogy with mean axial flow.
- Number of radial strips: 30.

Input parameters

- Input parameters extracted as close as possible to the stator LE:
  - RANS: flow extrapolation from the rotor domain down to the stator LE required because of the mixing-plane approach.
  - LES: data extraction at the LE1 position using a phase locked average and the unsteady data.
- Estimation of the TLS using three different approaches:
  - Λ_j: Jurdic's approach based on the wake width (RANS and LES). Predicts larger TLS near the casing because of the wake thickening.
  - Λ_c: based on the temporal autocorrelation of the axial velocity fluctuations and on Taylor's frozen turbulence hypothesis (LES only). Predicts large turbulent structures in the background flow and a decreasing TLS close to the casing.
  - Λ_p: Pope's approach based on the k and ω variables (RANS only). Predicts larger structures in the wake than in the background flow but provides a radial evolution closer to Λ_c.

Results

- Significant impact of the TLS estimate on the noise predictions.
  - Higher noise levels at low frequencies induced by Λ_j because of the larger structures predicted at the stator tip.
  - Λ_j predictions are the closest to the noise measurements, which does not guarantee their reliability given the discrepancies observed with the LES2 Λ_c.
  - Λ_p: most adapted TLS estimate for the RANS-informed predictions in the present study.
- Experimental noise levels better recovered by Hanson's model, but Posson's model more reliable since duct properties are taken into account.
- Global underestimation of the noise by both models despite an overestimated TKE, even for the LES2 Λ_c predictions, suggesting the presence of other dominant noise sources in the experiment.

4.3 Noise predictions using a hybrid numerical approach

In this section, a hybrid numerical approach coupling both LES with the Ffowcs Williams and Hawkings analogy is undertaken to estimate the noise radiated by the ACAT1 fan stage. In a first part, the turbulent properties of the flow impinging onto the stator row are further analyzed. In a second part, the potential noise sources on the fan and the OGV are presented. Finally, the RSI noise predictions as well as the rotor self noise predictions are analyzed.
These three parts rely on an extensive use of the Fast Fourier Transform (FFT). The FFT parameters used for the PSD computations are summarized in table 4.1.

	LES1		LES2	
Sampling frequency (kHz)	110		120	
Overlap	50%		50%	
Number of averaging windows (Hann windows)	10	5	5	3
Δf (Hz)	282	141	206	124

Table 4.1: FFT parameters for the PSD computations.

For each result, the number of averaging windows will be mentioned to clearly identify the frequency resolution of the signals.

4.3.1 Incident turbulent flow

Section 4.2.2.2 has given a first overview of the main turbulence properties of the flow impinging onto the stator row. Another essential property to investigate is the coherence function, which measures the correlation of the turbulent structures in a chosen direction with respect to their size. The coherence function of the velocity component u_i can be expressed as follows:

$$\gamma^2_{u_i}\left(x,\theta,r,x',\theta',r',\omega\right) = \frac{\left|\Phi_{u_i}\left(x,\theta,r,x',\theta',r',\omega\right)\right|^2}{\Phi_{u_i}(x,\theta,r,\omega)\Phi_{u_i}\left(x',\theta',r',\omega\right)}, \tag{4.6}$$

where $\Phi_{u_i}\left(x,\theta,r,x',\theta',r',\omega\right)$ is the cross spectral density (CSD) of the velocity component u_i and $\Phi_{u_i}(x,\theta,r,\omega)$ is the power spectral density of the same velocity component at the point (x,r,θ). In the present case, the data have been extracted from both LES at the LE1 position along a selected radius so that θ and x are constant. The coherence function then becomes a radial coherence function and can be rewritten $\gamma^2_{u_i}\left(r,r',\omega\right)$. Figures 4.18 and 4.19 show the radial coherence as a function of the frequency and the radius for the LES1 and the LES2, respectively. The coherence function has been plotted for the velocity component in the cascade reference frame, the reference radius being located at midspan. u_{xc}, w and u_r correspond to the velocity along the vane chord, the upwash velocity (normal to the chord) and the radial velocity, respectively. They have been computed assuming that the geometric chord of the real vane is equal to the chord of the equivalent flat plate.

At midspan, the coherence is equal to 1 for all the velocity components since the CSD is equal to the PSD. For the LES1, some interferences, which are mainly due to the sampling frequency and to the mesh resolution, appear at high frequencies. They almost disappear in the LES2 coherence maps. The shorter LES2 signals, however, induce a higher background coherence noise. For both LES and for all velocity components, significant coherence values are observed at the BPF and its harmonics since the periodic part of the velocity signals has not been removed. The two first BPF harmonics are observable for u_{xc}, while only the first harmonic is captured for the two other components. Apart from these isolated frequencies, for both LES and for all the velocity components, the coherence quickly decreases, which means that the turbulent structures share equivalent properties in the three directions. The radial extent over which the turbulent structures are correlated seems to be similar for all the velocity components and relatively short with respect to the stator span. This is confirmed by fig. 4.20, which shows the evolution of the radial coherence length scale, defined in eq. (4.7), for each velocity component with respect to the frequency. Each simulation shows a mean radial coherence length scale equivalent to 30-35% of the stator span for all the velocity components, which is more than the 20% of the stator span observed by De Laborderie *et al.* [212] in its study on the CME2 low pressure compressor.

$$L_{r,u_i}(\omega) = \int_{R_H}^{R_T} \sqrt{\gamma^2_{u_i}(r, r', \omega)}\mathrm{d}r' \tag{4.7}$$

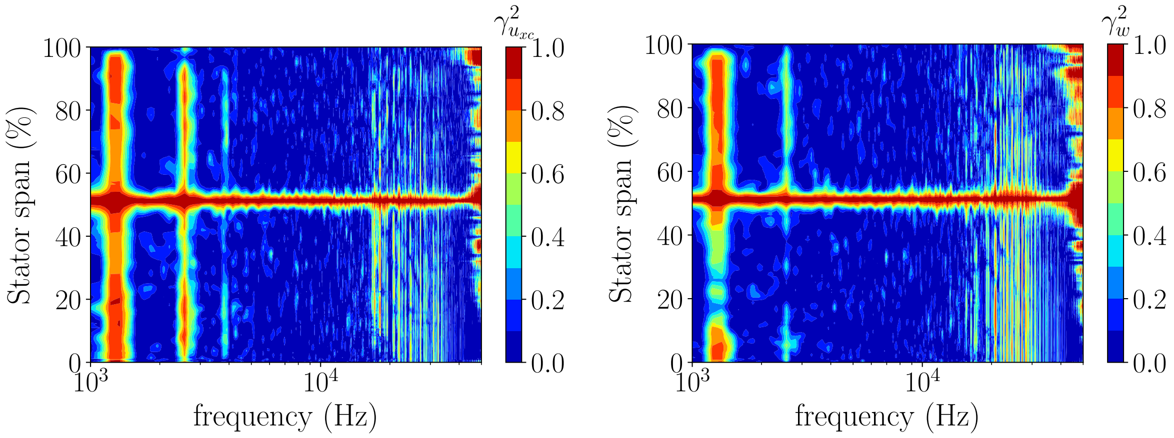

(a) u_{xc}.

(b) w.

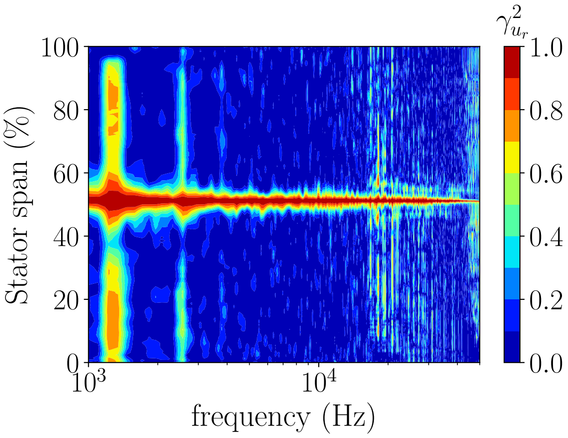

(c) u_r.

Figure 4.18: LES1 radial coherence function contours for each velocity component in the cascade frame of reference. Reference radius at stator midspan (10 windows).

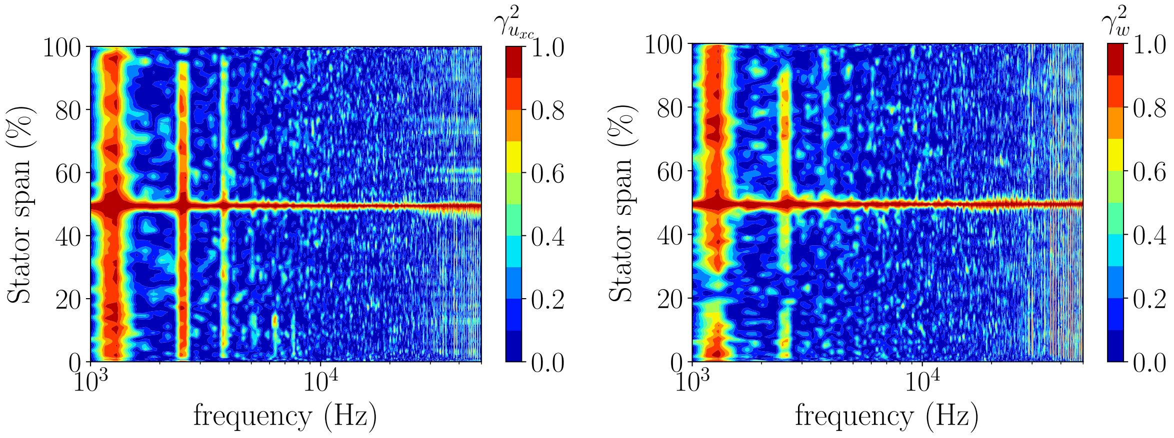

(a) u_{xc}.

(b) w.

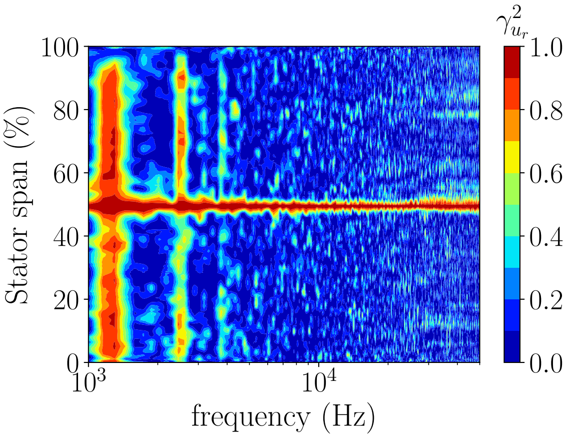

(c) u_r.

Figure 4.19: LES2 radial coherence function contours for each velocity component in the cascade frame of reference. Reference radius at stator midspan (5 windows).

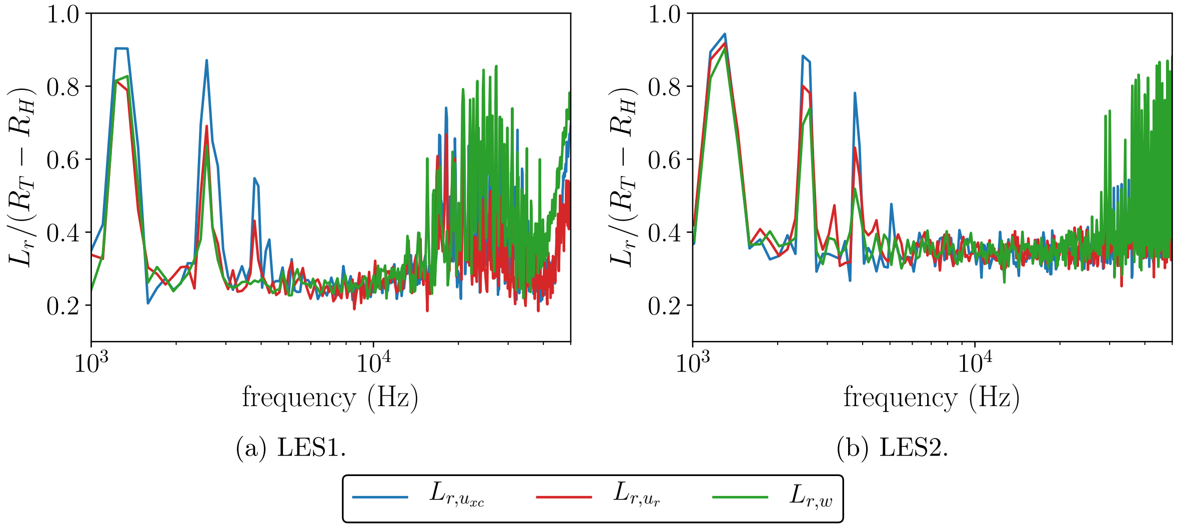

(a) LES1.

(b) LES2.

Figure 4.20: Radial coherence length scale for each velocity component.

4.3.2 Broadband noise sources

4.3.2.1 Source localization

As mentioned in chapter 1, the present noise prediction approach uses the pressure fluctuations on the rotor and stator surfaces as sources to be fed into the Ffowcs Williams and Hawkings analogy. The real broadband noise sources are embedded in these pressure fluctuations since no assumptions are made on the blade and vane geometries (thickness, camber, stagger angle, sweep) nor the flow conditions (flow angle, viscosity, load, isotropic turbulence). Moreover the compressibility of the unsteady highly resolved simulation inherently takes into account the scattering by the blades and vanes of the sound generated in its vicinity and thus avoids determining the Green's function of the blades and vanes. Nonetheless, cascade effects are only partially taken into account as the mutual influence is limited to a varying number of neighboring blades depending on the grid resolution for a given discretization scheme. The duct cut-off effect is also not taken into account by this approach. Before performing any noise predictions, it is thus of prime interest to analyze the broadband noise sources on the blade and vane surfaces. A practical way to get an overview of the potential noise sources is to examine the root mean square of the pressure fluctuations on the surfaces of interest. Figure 4.21 shows the P_{rms} on the stator surface. For both LES, high levels of P_{rms} can be observed at the stator leading edge. This phenomenon is typical of the RSI mechanism and results from the impact of the turbulent rotor wakes onto the stator. The LES2-RMS levels at the stator LE are remarkably lower than those of the LES1, indicating a weaker rotor-stator interaction. This observation is consistent with the lower TKE found in the LES2 rotor wakes (fig. 4.4). Another explanation could be that the LES1 turbulent wakes contain more large scale structures than the LES2: these are undergoing stronger distortions as they hit the vane leading edge and are thus radiating more efficiently. A second zone of important RMS levels, starting at about 60% stator chord, can be observed in both LES. This zone corresponds to the boundary layer turbulent transition observed in chapter 3. Higher RMS levels are found in this zone in the LES1 since a much stronger turbulent transition occurs because of the boundary layer separation. Given that the rear-part pressure fluctuations are not negligible with respect to the leading edge ones, they may contribute to some extent to the total radiated noise.

Regarding the fan sources, fig. 4.22 reveals that significant RMS levels can be observed at the same location as the rotor leading edge flow detachment. The magnitude of the fluctuations in both LES is similar and are as intense as those at the stator leading edge. As a consequence, depending on the efficiency of the radiation process, this source may substantially contribute to the total radiated noise. These two latter points will be investigated more precisely in the next section.

In order to have a better idea of how these fluctuations are spread over the studied frequency range, the PSD of the pressure fluctuations ϕ_{pp} has been computed along the chord of the stator and of the rotor at 50% stator span and 75% rotor span, respectively. For the stator (see fig. 4.23), the leading edge pressure fluctuations are spread over the whole frequency range, with higher values from 1 to 10 kHz in both simulations. As already mentioned, the LES2 ϕ_{pp} values are slightly lower at this position than those of the LES1. The pressure fluctuations in the rear-part of the OGV (60% to 100% of the stator chord) are the most intense between 1 and 8 kHz for both simulations, indicating the creation of a wide range of turbulent structures of different sizes. As suggested by the RMS values, the LES1 ϕ_{pp} levels are 10 dB higher than in the LES2, indicating a much stronger boundary layer transition. For both simulations, intense ϕ_{pp} levels are observed at the BPF and its harmonics over the whole vane chord because of the convection of the rotor wakes throughout the inter-vane channel. For the LES1, the lower sampling frequency of the signal as well as the lower mesh resolution lead to a wide zone of low ϕ_{pp} magnitude at

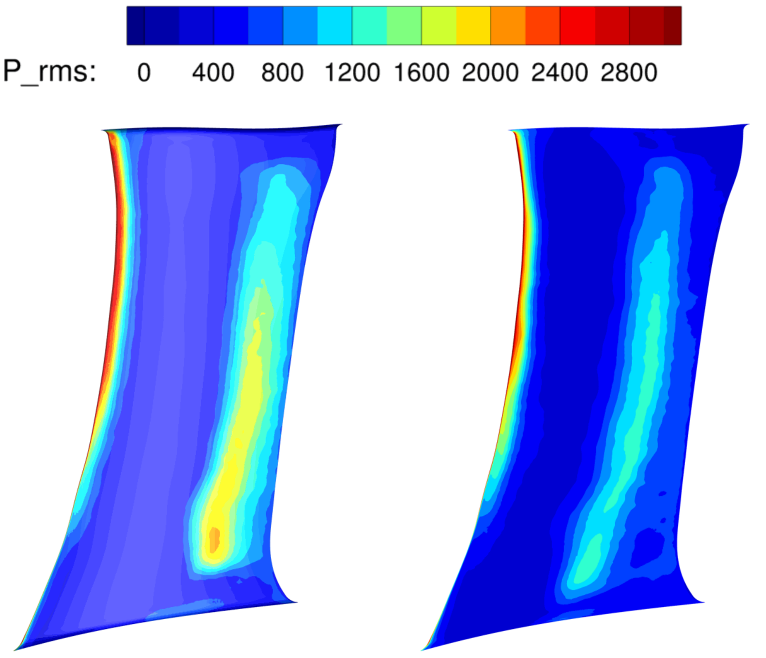

(a) LES1. (b) LES2.

Figure 4.21: P_{rms} values on the stator suction side.

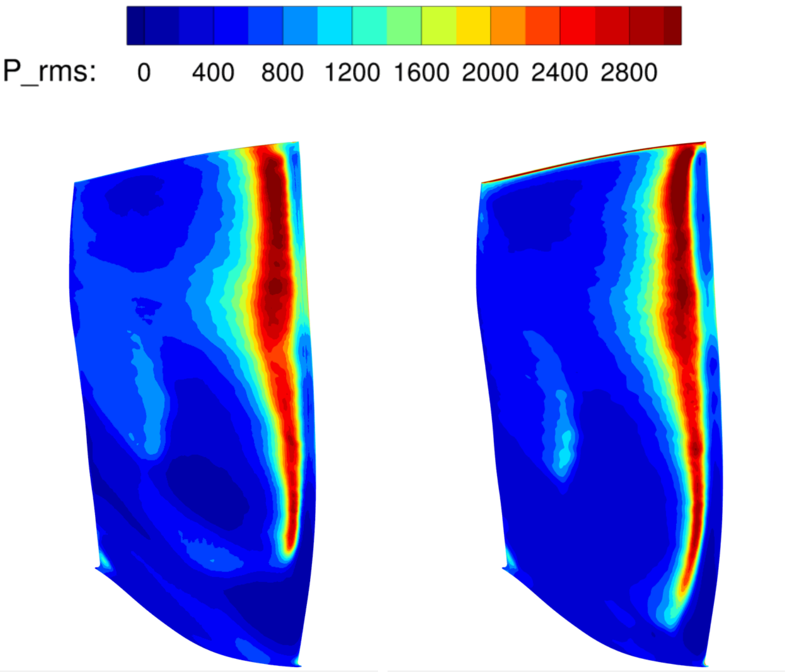

(a) LES1. (b) LES2.

Figure 4.22: P_{rms} values on the rotor suction side.

high frequency, which disappears in the LES2. A similar zone can also be observed in the case of the rotor (see fig. 4.24). The LES1 and LES2 ϕ_{pp} maps on the rotor are relatively similar:

the highest levels are observed near the leading edge, where the flow separation occurs, and are spread over a significant part of the chosen frequency range as the first noticeable decrease in ϕ_{pp} only occurs at 10 kHz. The boundary layer transition resulting from the flow separation creates significant pressure fluctuations between 1 and 10 kHz over the entire blade chord, which once again indicates the creation of a wide range of turbulent structures of different sizes. In both simulations, a global decrease in ϕ_{pp} by 10 to 15 dB is observed from the leading edge down to the trailing edge.

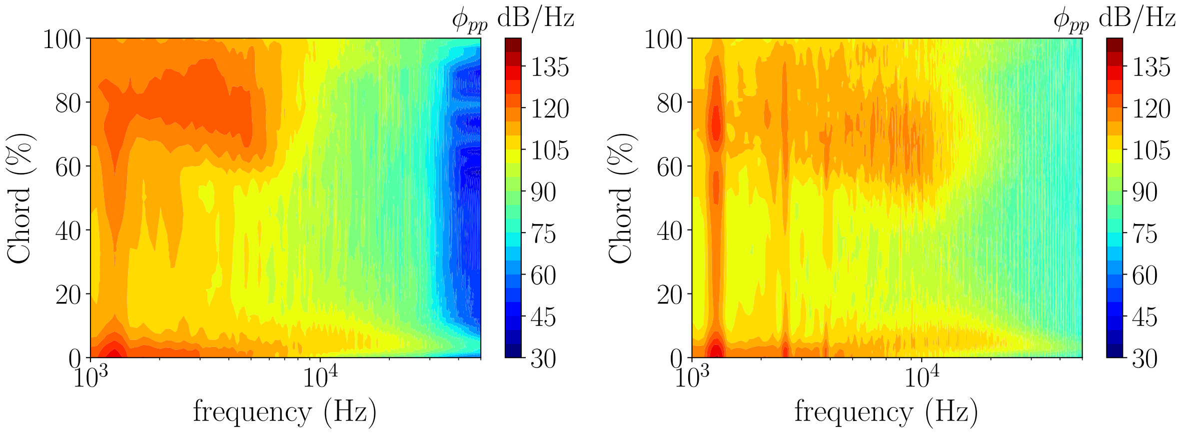

(a) LES1 (10 windows).

(b) LES2 (5 windows).

Figure 4.23: PSD of the pressure fluctuations on the stator surface at 50% stator span.

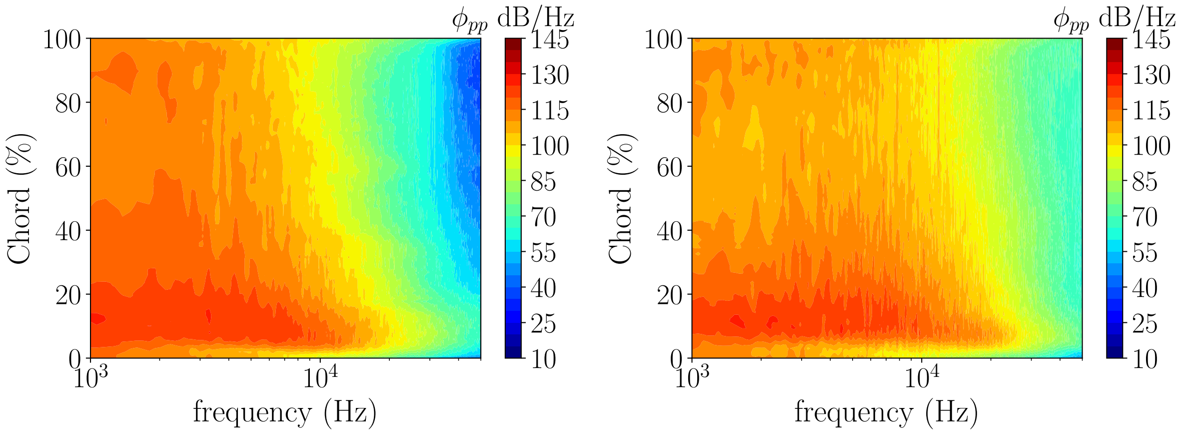

(a) LES1 (10 windows).

(b) LES2 (5 windows).

Figure 4.24: PSD of the pressure fluctuations on the rotor surface at 75% fan span.

All these observations confirm that, apart from the RSI mechanism, other broadband noise sources, which are mainly related to flow separations and boundary layer transitions, can be identified in the ACAT1 fan stage at approach conditions. Furthermore, the order of magnitude of the pressure fluctuations associated with these sources is comparable to that of the RSI mechanism, which may significantly contribute to the total radiated noise.

4.3.2.2 Vane response

Similarly to the analysis made on the incident flow, it is of great interest to study the radial coherence of the vane response to the RSI mechanism. To do so, the coherence of the pressure on the vane surface γ_p has been computed for both LES, at 0.5% vane chord over the whole stator span (see fig. 4.25). As with the velocity components, the midspan position has been chosen as the reference location, which explains the high coherence value at 50% stator span. From this position, γ_p quickly decreases in both simulations except at the BPF and its harmonics, as with the coherence of the velocity components. This indicates that the radial extent over which the vane response is correlated is also quite short with respect to the stator span. This is confirmed by fig. 4.26, which shows the evolution of the radial coherence length scale of the pressure fluctuations $L_{r,p}$ on the stator suction side at 0.5% stator chord over the whole vane span. In both simulations, $L_{r,p}$ is of the same order of magnitude as the radial coherence length scale of all velocity components. This is actually consistent with the hypothesis made in Posson's model, which considers that the cross-spectral density of the pressure jump on the vane is negligible above a certain radial coherence length scale, which is chosen to be equal to the radial coherence length scale of the incident upwash velocity. The validity of this hypothesis seems to depend on the considered configuration since De Laborderie [11] found that the coherence length scale of the vane response can be 3 to 4 times larger than that of the upwash velocity when dealing with a low pressure compressor.

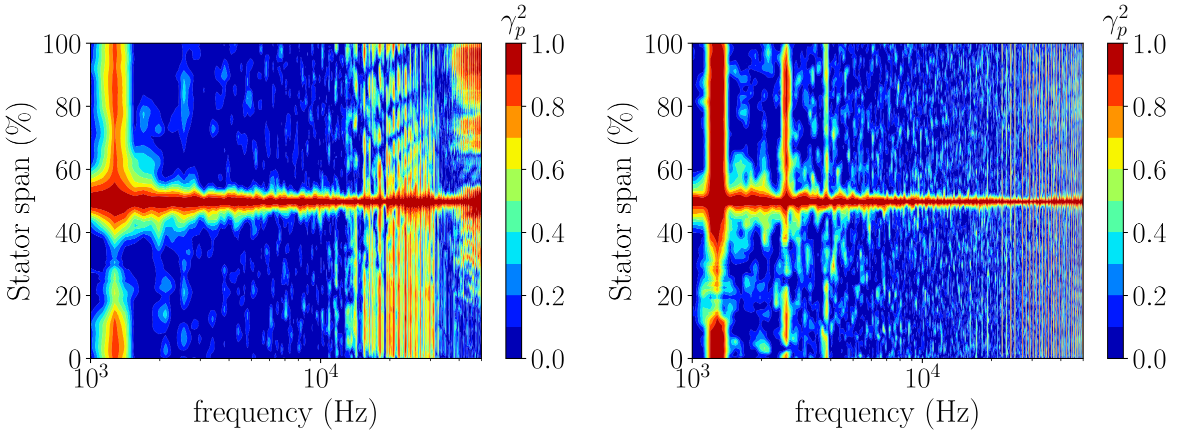

(a) LES1 (10 windows).

(b) LES2 (5 windows).

Figure 4.25: Radial coherence function contours of the pressure fluctuations on the stator vane suction side at 0.5% stator chord. Reference radius at stator midspan.

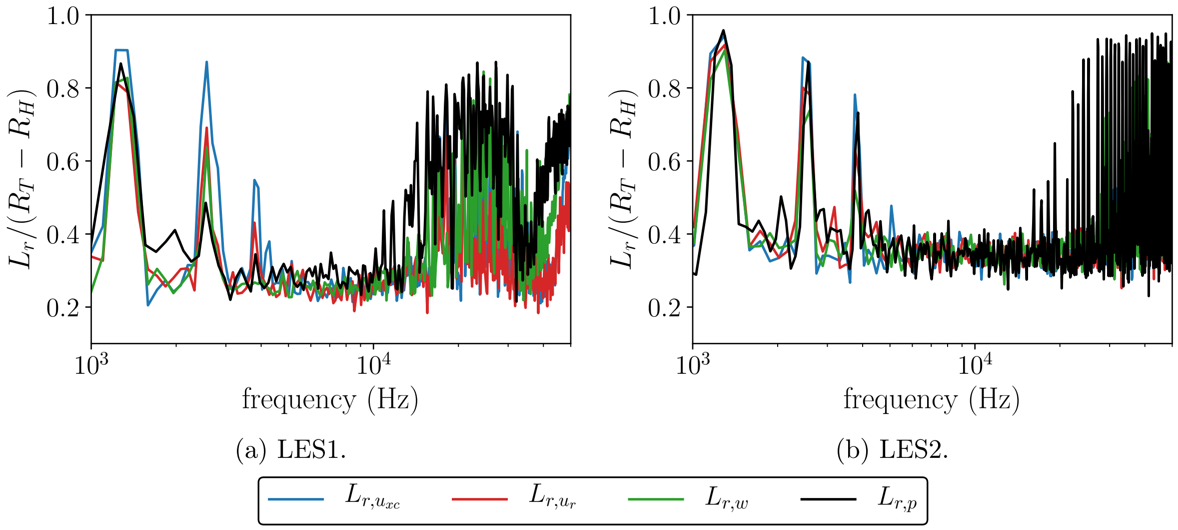

(a) LES1.

(b) LES2.

Figure 4.26: Radial coherence length scale for each velocity component and for the pressure fluctuations at the stator leading edge.

4.3.3 Acoustic results

The previous LES-informed analytical model approach has been performed for comparison purposes but does not represent a viable noise prediction approach given the cost of an LES. LES is in fact better suited for high-order numerical hybrid methods dedicated to broadband noise predictions. As previously explained, this kind of method is a two-step approach that decouples the computation of the acoustic sources, performed through a scale-resolving simulation such as LES, from the propagation, usually performed through the use of an acoustic analogy. In the present case, the sources correspond to the wall pressure fluctuations on the stator and on the rotor surfaces, which have been extracted from the simulation over about 4.5 and 3 rotations for the LES1 and the LES2, respectively. These pressure fluctuations have then been used as dipole sources within the Ffowcs Williams and Hawkings free-field analogy, as implemented in the tool *SherFWH* developed by the Aeroacoustics Group of Université de Sherbrooke [213]. SherFWH is an implementation of the formulations of Casalino [214] and Najafi-Yazdi *et al.* [215]. As already mentioned, FW-H's analogy propagates the sound in the free-field, which means that the duct geometry is neglected as well as the noise shielding induced by the presence of the rotor and stator rows. Moreover, extracting the sources directly on the vane/rotor surface implies that the quadrupole sources, related to the volume term of the FW-H analogy [22], are neglected. This is actually a fairly reasonable assumption since the relative tip Mach number of the rotor is of 0.57, which makes it possible to neglect both monopole and quadrupole sources [22].

Figure 4.27 shows the noise predictions considering only the stator sources for both LES. For both the upstream and the downstream noise, the FW-H predictions based on the LES1 recover quite faithfully the overall shape of the experimental spectra. In terms of absolute levels, however, a significant over-prediction of the radiated noise is observed. This is especially the case for the upstream prediction, which displays a 12 dB gap from low to medium frequencies. Above 5 kHz, however, this gap decreases to 4 dB and remains constant up to higher frequencies. The over-prediction of the noise for the downstream part is not as important as for the upstream one. The difference with respect to the experiment is only of 2 dB on most of the studied frequency range, except at low frequencies where it can reach 5 dB.

The LES2 predictions are in much better agreement with the experimental spectra. For both the upstream and the downstream predictions, the gap with the experiment from low to medium frequencies is still present but has been reduced by almost 5 dB. This leads to a downstream prediction that almost recovers the low frequency experimental noise levels. This low frequency noise reduction is consistent with the shrinking of the wake turbulent structures observed in section 3.3 for the LES2 with respect to the LES1. For frequencies above 5 kHz, however, the noise is still overestimated by about 4 dB since the predictions of both LES almost overlay.

This overall overprediction is actually expected for two main reasons. Firstly, the RMS levels predicted by both LES are overestimated, especially in the LES1. Secondly, the FW-H analogy only considers a free-field propagation, which neglects the duct cut-off effect as well as the real distribution of the acoustic energy over the duct modes. As shown by Pérez Arroyo *et al.* [44], the use of Goldstein's analogy [132], which takes into account these duct specific features, could lead to a 5 to 10 dB reduction of the predicted noise over the whole frequency range with respect to the FW-H based prediction. Part of this overestimation can also be attributed to the other noise sources that have been identified in the previous sections. For instance, the flow detachment and/or the boundary layer transition occurring at the rear part of the stator vane may also take part in the broadband noise production to a larger extent than in the experiment. In order to assess how significant their contribution to the radiated noise is, the vane has been split in two parts: the front part, consisting of the first 40% of the vane maximum axial chord over the entire vane span, and the aft part, which consists of the 60% left. Considering this splitting, the PSD Φ_{Full} induced by the pressure fluctuations on the full vane at a particular observer point can be rewritten as follows:

$$\Phi_{Full} = \Phi_{Front} + \Phi_{Aft} + 2Re(\Phi_{Front,Aft}), \tag{4.8}$$

where Φ_{Front} and Φ_{Aft} are the PSD induced by the front and the aft parts of the vane, respectively, $\Phi_{Front,Aft}$ is the cross-spectral density between the front and the aft parts, and $Re()$ denotes the real part of the quantity in parentheses. These three terms (Φ_{Front}, Φ_{Aft}, and $2Re(\Phi_{Front,Aft})$) have been plotted along with the full-vane based prediction in figs. 4.28 and 4.29 for the LES1 and the LES2, respectively.

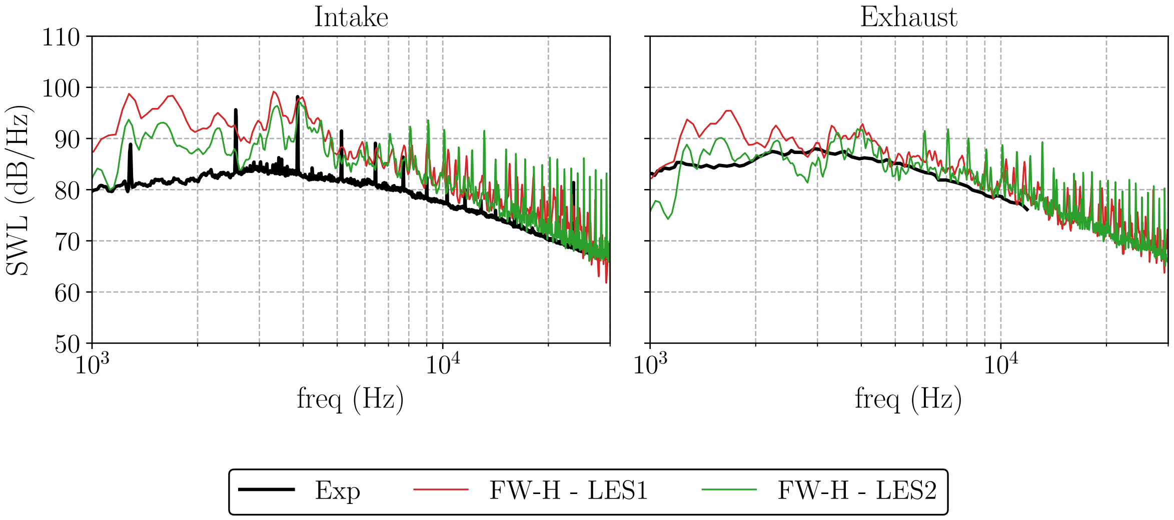

Figure 4.27: Upstream SWL (left) and downstream SWL (right) spectra obtained from the Ffowcs Williams and Hawkings analogy (LES1: 5 windows, LES2: 3 windows).

For both LES the aft part of the vane is responsible for most of the noise radiated by the vane,

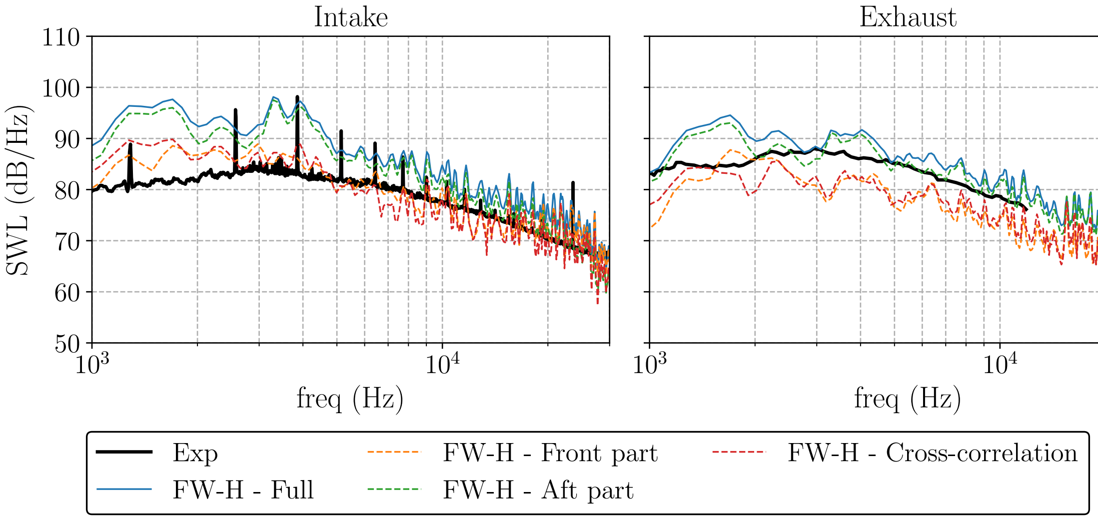

Figure 4.28: LES1 upstream SWL (left) and downstream SWL (right) spectra obtained from the Ffowcs Williams and Hawkings analogy, for each sub-part of the vane (10 windows).

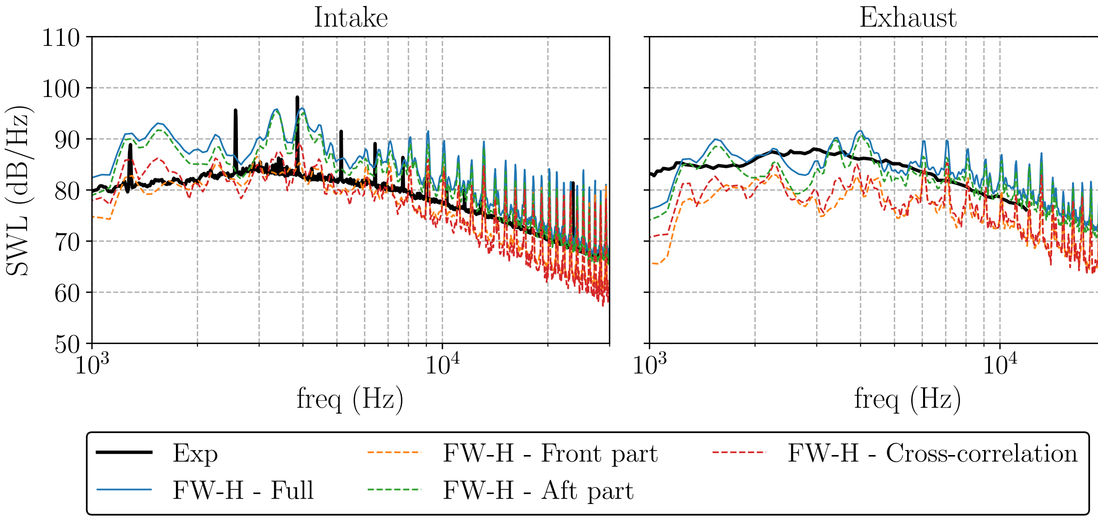

Figure 4.29: LES2 upstream SWL (left) and downstream SWL (right) spectra obtained from the Ffowcs Williams and Hawkings analogy, for each sub-part of the vane (5 windows).

which means that in the present computation, the noise due to the boundary layer transition may be more important than expected. Moreover, a similar offset of the three noise components is observed between the LES1 and the LES2, which indicates that the weaker boundary layer transition in the LES2 is not responsible on its own for the noise reduction at low frequencies. The cross-spectra also show that the front and aft parts of the vane pressure fluctuations are correlated indicating a possible downstream shift of the RSI sources. These observations all show that the noise mechanisms related to the boundary layer, to its turbulent transition and to its scattering by the trailing edge also play an important role in the broadband noise production. Similar observations were made by De Laborderie *et al.* [11, 212] on a low-compressor that exhibited unexpected dominant broadband noise sources in addition to the RSI mechanism. Additionally, in order to assess the accuracy of the analytical predictions, figs. 4.30 and 4.31

show the comparison of the OGV front part noise predicted by the FW-H analogy, with the corresponding LES-informed analytical predictions using Hanson's model, for the LES1 and LES2, respectively. Hanson's model has been chosen for the comparison since its hypotheses are the closest to the FW-H analogy, compared with Posson's model. For both simulations, the analytical predictions recover quite well the upstream SWL, with a slight underestimation at low frequencies. The discrepancies are slightly larger for the downstream predictions, with similar SWL values at low frequencies but a 4 to 5 dB overestimation at high frequencies for the analytical predictions. The Hanson RANS predictions using Λ_p have also been plotted in fig. 4.31, showing the capacity of the RANS-informed models to provide reliable noise predictions. Indeed, the RANS-informed analytical predictions are almost as close as the LES2-informed predictions to the FW-H estimates. This also confirms that the *a priori* noise underestimation observed in the analytical predictions results from additional noise sources in the experiment, which can only be captured by more advanced methods.

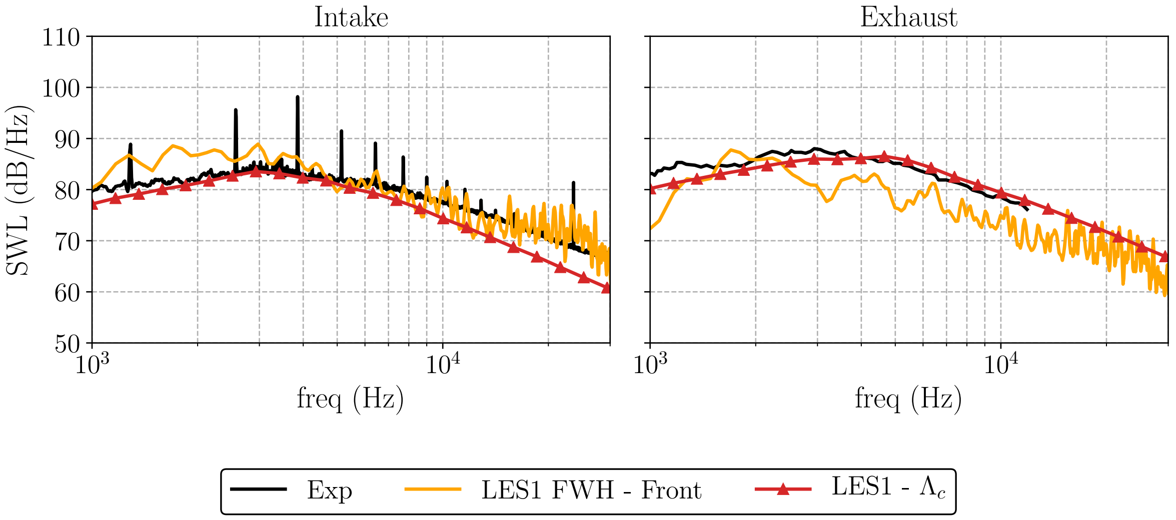

Figure 4.30: Comparison of the noise predictions obtained from the Ffowcs Williams and Hawkings analogy (LES1 front part only, 10 windows), and from Hanson's model informed with LES1 data. Upstream SWL (left) and downstream SWL (right) spectra.

Still, taking into account the duct properties would most likely lead to an underestimation of the total noise if only the vane sources are considered, which means that other noise sources, such as the rotor LE flow separation and the rotor TE noise, must contribute to the total radiated noise. To investigate this hypothesis, noise predictions using the pressure fluctuations recorded on the rotor skin have been performed for both LES. The results are plotted in fig. 4.32. The LES1 and LES2 spectra are consistent with the observations made in section 3.3. The LES1 leading edge flow separation tends to create larger and stretched structures, which results in higher noise levels at low frequencies and lower ones at high frequencies. On the contrary, the LES2 leading edge flow detachment creates smaller structures, which leads to spectra that look like the LES1 ones but tilted anticlockwise since lower noise levels are found at low frequencies, while higher ones are observed at high frequencies. In terms of magnitude, the rotor noise of both LES displays comparable and even higher levels than the noise radiated by the front part of their respective stator. In the case of the LES2, the rotor produces noise levels above 8 kHz that are similar to those produced by the entire OGV. Hence, the rotor significantly takes part in the broadband noise production, because of the LE flow separation, of the turbulent structures it generates, but also because of the scattering of the latter structures and of the induced turbulent

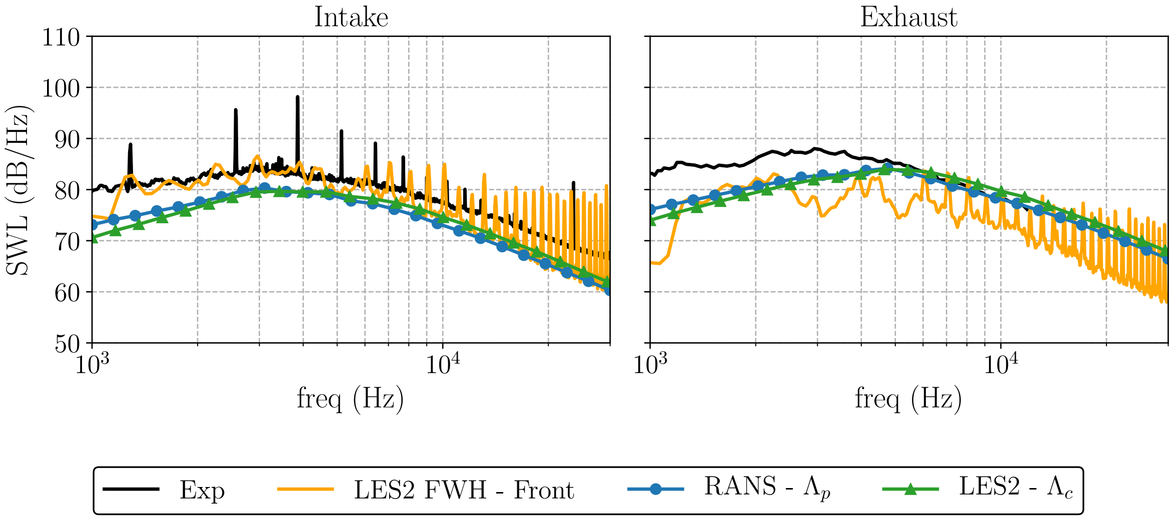

Figure 4.31: Comparison of the noise predictions obtained from the Ffowcs Williams and Hawkings analogy (LES2 front part only, 5 windows), and from Hanson's model informed with RANS and LES2 data. Upstream SWL (left) and downstream SWL (right) spectra.

boundary layer by the trailing edge. These sources were also identified by Deuse *et al.* [201] in their study of the CD airfoil self-noise, at a much lower chord based Reynolds number ($\sim 10^5$), and were shown to be amplified at Mach numbers close to that of the present configuration.

These multiple additional broadband noise sources significantly contribute to the total radiated noise, which explains why the analytical model predictions do not match the experimental noise spectra since they only take into account the RSI mechanism.

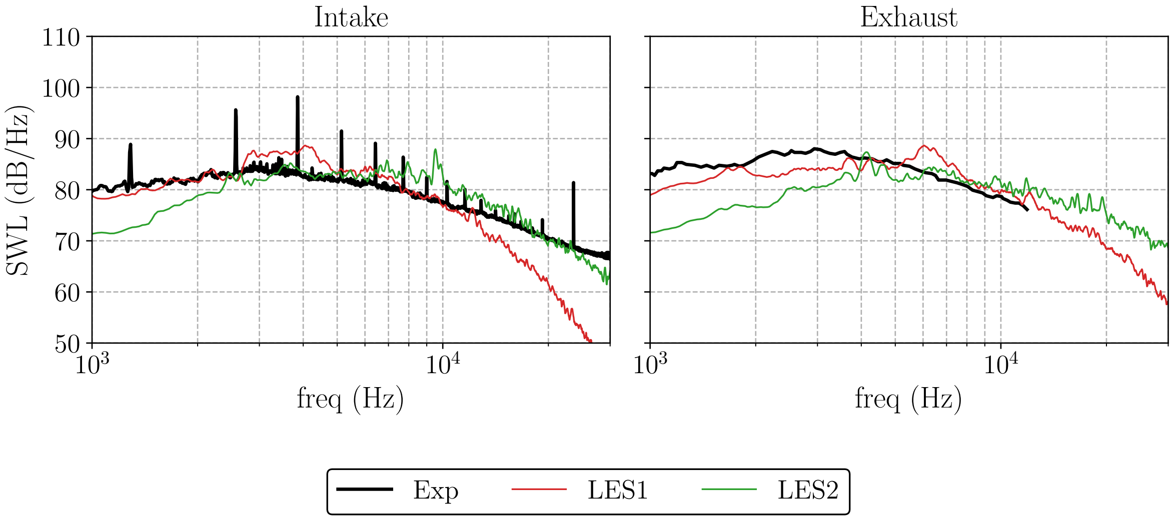

Figure 4.32: Upstream SWL (left) and downstream SWL (right) spectra obtained from Ffowcs Williams and Hawkings analogy (3 windows for both simulations).

Noise predictions using a hybrid numerical approach——————— Summary

Incident turbulent flow

- Radial coherence length scales similar for all velocity components and for both LES.
- On average Lr corresponds to 30-35% of the stator span.

Broadband noise sources

- Source localization:
  - Stator leading edge: significant pressure fluctuations due to the RSI mechanism.
  - Rear-part of the stator: pressure fluctuations of lower magnitude due to the flow separation and/or boundary layer transition.
  - Rotor: LE flow separation inducing intense wall pressure fluctuations over the whole blade chord.
- Vane response: radial coherence length scale similar to those of the incident flow confirming the assumption made in Posson's model.

Acoustic results

- Global overestimation of the noise observed when considering only the sources located on the OGV.
- Overestimation mainly attributed to the over-predicted RMS levels (especially for the LES1), and to the neglected duct-propagation effects.
- Highlighting of the dominant role of the stator rear boundary layer transition in the broadband noise production.
- Significant contribution of the rotor to the total radiated noise at low frequencies for the LES1, and at high frequencies for the LES2.

4.4 Conlusion

A comprehensive noise computation of the ACAT1 configuration at approach condition has been performed using two different hybrid noise computation methods. The first one is the CFD-informed analytical model approach. The impact of the chosen turbulent length scale estimate on the SWL has been assessed, showing discrepancies at low frequencies that are mainly attributed to the larger near casing TLS values obtained using Jurdic's estimate. This effect is however less important in the LES1 predictions because of the larger background and wake Λ_c values outside of the tip region, which have counterbalanced it. Both Hanson's and Posson's models underestimate the noise levels on a large part of the studied frequency range. This underestimation indicates the presence of additional noise sources in the experiment, which are not negligible with respect to the RSI mechanism.

A higher order hybrid approach, coupling LES with the Ffowcs Williams and Hawkings analogy, has then been applied to assess the noise radiated by the stator and rotor rows. The noise sources on the vane and blade surfaces have first been analyzed. The flow separations/boundary layer transitions occurring on the rotor and the stator, the resulting turbulent flow and its interaction with the rotor and stator trailing edges have come up as significant broadband noise sources since the wall pressure fluctuations they produce are almost of the same order of magnitude as those resulting from the RSI mechanism.

A global overestimation of the noise radiated by the OGV is observed, especially for the upstream predictions, which reveals low-frequency discrepancies with the experiment that can reach 12 dB and 8 dB for the LES1 and for the LES2, respectively. This overestimation is mainly attributed to the overestimated RMS levels (especially for the LES1), and to the fact that the FW-H analogy takes into account neither the duct propagation effect nor the shielding by the cascades. The noise resulting from the flow separations/boundary layer transitions on the stator vanes and on the rotor blades have also been assessed, showing that both mechanisms are part of the dominant noise sources for the ACAT1 fan stage at approach condition.

CHAPTER 5

Analytical model parametric study: application to the NASA SDT configuration

Introduction

This chapter presents a comparative study of four of the most advanced analytical models for broadband RSI noise predictions: Amiet's model [63, 138–140], Ventres's model [45], Hanson's model [162, 172] and Posson's model [12, 46, 48]. The main objective of this study is to assess the impact of the multiple assumptions made in the models and quantify their responsiveness to different input parameter modifications. This study has been performed on the Source Diagnostic Test (SDT) case, which is a 22-in fan rig that was experimentally assessed in the framework of the NASA advanced Subsonic Technology Noise Reduction Program.

Contents

5.1 Test case: the NASA SDT fan rig

This section presents the NASA Source Diagnostic Test case, which has become an AIAA benchmark for fan broadband noise predictions since 2015. The specific features of the configuration, as well as the RANS simulations from which the model input parameters have been extracted are described in detail.

5.1.1 Experimental set-up

In the framework of the NASA advanced Subsonic Technology Noise Reduction Program, a series of experiments were performed on the 22-in SDT fan rig of the NASA Glenn low-speed wind tunnel. One of the main objectives of this project was to identify and characterize the broadband noise sources in a modern high-bypass-ratio turbofan engine for different flight conditions: approach, cut-back and fly-over. The interaction noise was part of the main mechanisms that were studied during these experiments. Hot-wire and microphone measurements were performed upstream and downstream of the fan stage as well as in the inter-stage, providing both flow fields and acoustic power at these positions.

The SDT fan stage is representative of a 1/5th scale of a modern high bypass ratio turbofan engine. It consists of a 22-bladed rotor and variable number of OGV. Three different stage configurations have been tested: the baseline geometry composed of 54 vanes, the low-count geometry with 26 vanes, and the low-noise geometry composed of 26 swept vanes (see fig. 5.1). These three stators have the same solidity, resulting in an increased chord for the low-count and low-noise configurations. They all display a constant chord along the span.

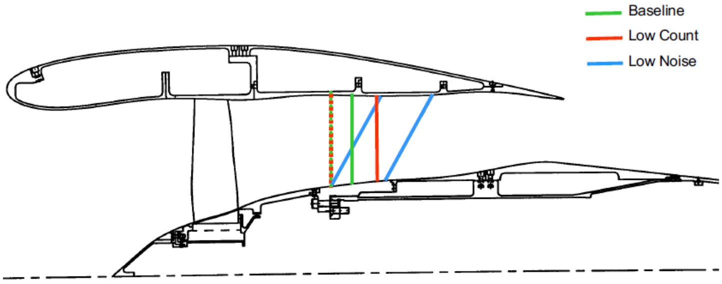

Figure 5.1: SDT stage configurations.

In the present study, the aforementioned models are only assessed at approach conditions on the baseline configuration, the main characteristics of which are listed in table 5.1:

R_H at OGV LE [m]	R_T at OGV LE [m]	Ω [rpm]	Vane chord [m]
0.1397	0.2794	7808	0.040

Table 5.1: Main parameters of the SDT baseline configuration.

The description of the test campaign as well as the main aerodynamic and acoustic experimental results can be found in [32–37].

5.1.2 CFD computations

In the present study, the input parameters of the models are retrieved from two different RANS simulations. The first one is a 3D viscous mixing-plane simulation performed by Nallasamy and Envia in 2005 [13] using the code APNASA. A modified k-ϵ turbulence model [216] was used to account for the effect of turbulence. The mesh is composed of about one million cells: 407 cells in the streamwise direction, and 51 cells in both azimuthal and radial directions.
The second was performed by Leonard *et al.* in 2016 [43] as part of a comprehensive numerical study on the SDT configuration, involving both RANS simulation and LES. The simulation was performed using the ANSYS CFX v15.0 solver with a mixing-plane approach at the rotor-stator interface. In this case the $k-\omega$ SST model was used to simulate the turbulent behavior of the

flow. The mesh is a hybrid unstructured grid composed of prism cells on walls, to accurately resolve the boundary layer, and of tetrahedral cells in the rest of the domain. It is composed of 75 million cells in total. The dimensionless wall-normal distance y^+ of the first cell was maintained under 50.

All the following acoustic predictions are performed using data retrieved from Leonard *et al.*'s RANS simulation, except in section 5.2.2.1 in which predictions relying on both simulations are explicitly compared, and in appendix E in which Nallasamy and Envia's RANS data are used to check the convergence of Ventres' cascade response.

Figure 5.2 displays the radial evolution at the stator leading edge of the main model input parameters: the absolute Mach number (fig. 5.2a), the axial Mach number (fig. 5.2b), the turbulence intensity (TI) in the background flow (fig. 5.2c) and in the wake (fig. 5.2d), as well as the turbulence length scale (fig. 5.2e). The most substantial disparities can be observed for the turbulence intensity, in both the background flow and the wake. The integral length scale also displays small discrepancies, especially close to the casing, which may have an impact on the noise predictions.

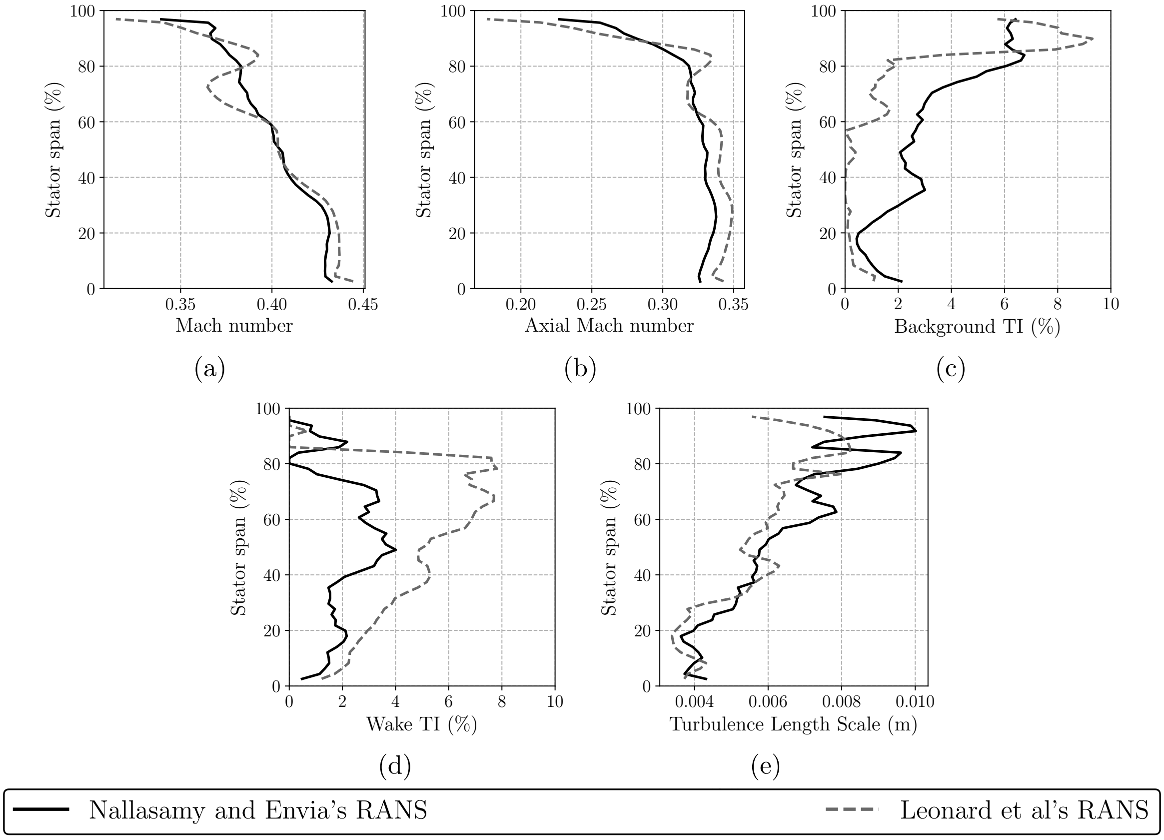

(a) (b) (c)

(d) (e)

Figure 5.2: Comparison of the model input parameter extractions performed on two different RANS simulations.

5.2 Sensitivity study

This section is dedicated to the parametric study of the models introduced in section 1.4.4.1. It aims at determining if some assumptions made in the development of the models are responsible for a lack of representativeness of the configuration. The objective of this study is also to highlight and characterize the impact of variations in the input parameters on the broadband noise predictions.

In the following section, Ventres' model implementation is based on the original model of Ventres *et al.* [45] extended with additional developments from Nallasamy and Envia [13] relatively to the turbulence spectrum, which enables to consider both the background and wake components of the impinging flow. The latter feature is implemented by default in the models of Posson [12, 46, 48], Hanson [162, 172] and Amiet [63, 138–140]. If not clearly mentioned, the turbulence state of the incident flow is modeled using the Liepmann isotropic spectrum.

5.2.1 Geometry definition

In the case of a fan stage, thin and moderately cambered profiles, with small angles of attack and small impinging perturbations are studied. These parameters ensure that the unsteady loading is hardly depending on geometric parameters [217] and, consequently, that the zero thickness flat plate approximation is a fairly justified assumption. The OGVs also display a substantial number of vanes with a significant overlapping. This implies that the response of the vane depends on its surrounding and therefore that the cascade effect cannot be neglected (as seen in section 5.2.3). One parameter that significantly determines the cascade effect is the stagger angle of the vanes [72]. Hence, the stagger angle of the equivalent flat plate geometry must be chosen in order to faithfully transpose the actual vane behavior. The first intuitive choice is to set the stagger angle with respect to the chord line (noted χ_{geo} in fig. 5.3).

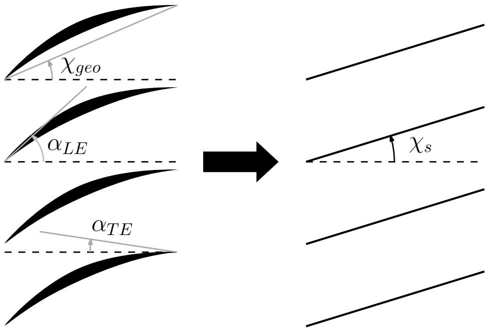

Figure 5.3: Equivalent flat plate geometry.

Grace *et al.* [55, 156] for instance suggested another option to select the stagger angle, which takes the camber at the leading edge α_{LE} and at the trailing edge α_{TE} into account. This weighted stagger angle is computed using the following relationship:

$$\chi_s = A\,\alpha_{LE} + B\,\alpha_{TE}. \tag{5.1}$$

Figures 5.4 and 5.5 show the SWL obtained from Hanson's model and Posson's model, respectively. Two weighting configurations are compared against the geometry using χ_{geo}: $(A, B) = (0.5, 0.5)$ (noted $A50B50$) and $(A, B) = (0.9, 0.1)$ (noted $A90B10$).

For Hanson's model, the χ_{geo}-configuration gives the lowest noise levels both upstream and downstream of the stator. The highest noise levels, however, are obtained for the $A90B10$-configuration. The SWL of the $A50B50$-configuration lies in between the two others but is closer to the χ_{geo}-configuration, especially for the exhaust prediction, for which the levels are almost identical, and at high frequency for the upstream prediction.
Downstream of the stator, a maximum gap of 2 dB is observed between the $A90B10$ and the χ_{geo} configurations. The $A50B50$-configuration gives quite similar results as the χ_{geo} configuration on

the studied range of frequency. The gap between the $A90B10$ -configuration and the two others progressively decreases until the curves are superimposed for frequencies higher than 14 kHz. The most noticeable changes are observed upstream of the stator where the gap between the configurations $A90B10$ and χ_{geo} can reach values up to 4.5 dB. From 1 kHz up to 8 kHz, this gap is of 3.8 dB on average and decreases progressively until it reaches a constant value of 1.3 dB. The noise levels obtained from the $A50B50$-configuration are between those of the two others, the gap with the χ_{geo}-configuration being smaller than with the $A90B10$ configuration. At very high frequency, the $A50B50$ and the χ_{geo} configurations give quite similar results. Even though the three curves are not overlaid at high frequency, as for the downstream predictions, the slopes of all spectra are almost identical, indicating a similar behavior.

The same comments can be made for the results obtained with Posson's model. Indeed, they display the same trends relatively to the stagger angle variation except at very high frequency for which the curves are not overlaid.

Posson *et al.* [218] also studied the impact of the modification of the stagger angle at constant solidity for an unwrapped vane cascade subject to particular harmonic gusts. Posson observed that an increase in the stagger angle induces a decrease in the downstream SWL, especially at low frequencies. The upstream SWL, however, is weakly impacted by such a modification since only a slight increase in the SWL can be observed when the stagger angle is increased. This is also consistent with the results from Blandeau *et al.* [219] and Gea-Aguilera *et al.* [60]. As it can be seen from the present study, this behavior is partially recovered but with discrepancies that are significantly larger than those observed by Posson. Considering a complete 3D vane row and integrating turbulence over a broad range of wavenumbers seems to intensify the impact of such modifications. As a consequence, the behavior of such models on a real geometry cannot be thoroughly assessed or anticipated only by studying particular harmonic gusts on an unwrapped vane row. This might be due to the fact that increasing the stagger angle exposes an increasing part of the suction side leading edge to the open flow : the waves are more easily refracted back into the inter-stage and less prone to downstream radiation across the cascade. According to diffraction theory, for low frequencies, that is, large wave numbers, this trend is even more pronounced and explains the results observed both at the intake and at the exhaust. It should however be kept in mind, that the rotor also filters the sound waves from the OGV, which is not taken into account in the present models.

Given that the RSI mechanism is mainly a leading edge phenomenon, the A90B10 configuration has been selected as the default stagger angle for the following sections, even though it does not produce the results which are the closest to the experimental data.

5.2.2 Impinging flow definition

5.2.2.1 Sensitivity to modifications of the mean flow characteristics

The mean flow parameter computation through RANS simulations is a determinant step. In particular, the structure of the rotor wakes is remarkably sensitive to the mesh refinements on the rotor blades, to the mesh refinements in the wake, and to the chosen turbulence model. Indeed, wall refinements as well as the turbulence model have a major impact on the simulation of flow separations that govern the structure of the wake downstream of the trailing edge. A very fine mesh is also required in the wake in order to correctly transport it down to the mixing plane and to get a good estimate of the turbulence intensity and integral length scale within it. Too coarse a mesh would diffuse the wake and dampen the turbulence intensity. Figures 5.6 and 5.7 show the noise predictions obtained with Hanson's and Posson's models, respectively, using the two different RANS inputs presented in section 5.1.2.

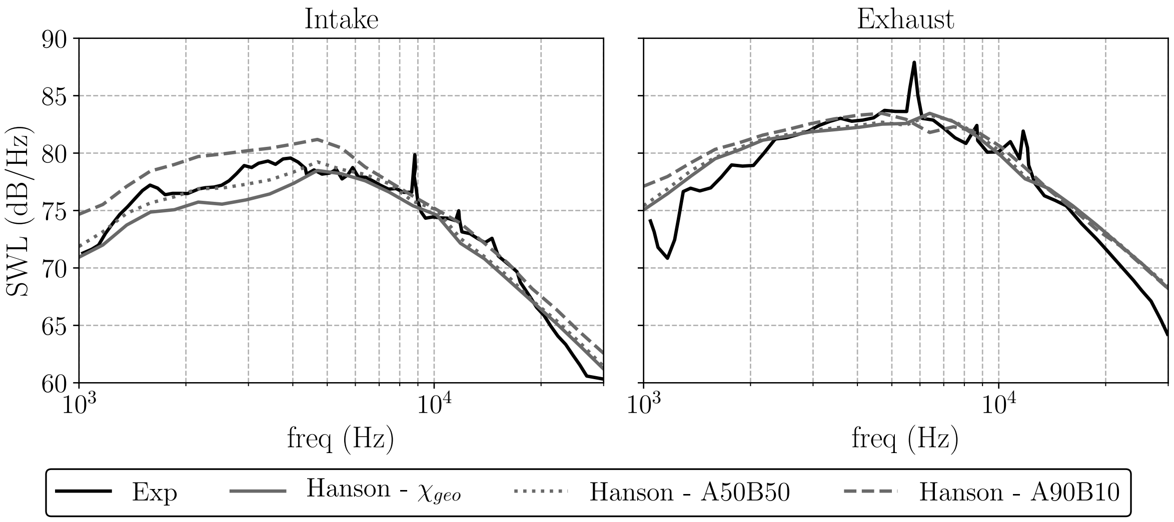

Figure 5.4: Stagger angle effect, Hanson model.

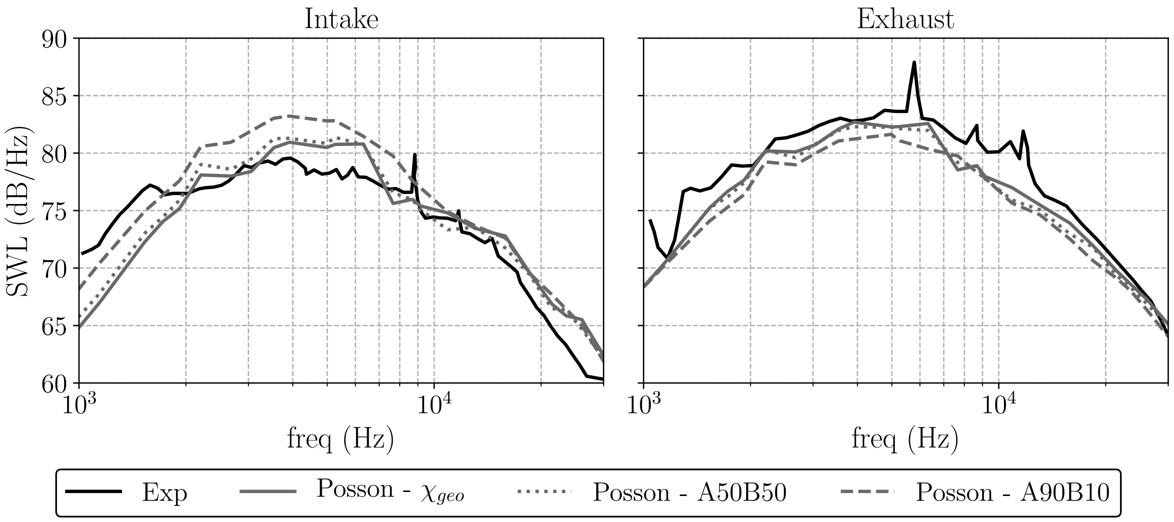

Figure 5.5: Stagger angle effect, Posson's model.

As it can be seen, the use of different data sets as input parameters for the models (see section 5.1.2) has a significant effect on the noise predictions, regarding both the absolute noise levels and the shape of the spectra. The higher wake turbulence intensity from Leonard *et al.*'s RANS simulation [43] is responsible for an increase in the predicted noise at medium frequencies of 2 to 3 dB for both Hanson's (fig. 5.6) and Posson's (fig. 5.7) models, whether it is for the upstream or the downstream noise. A slight increase in the noise at high frequencies can be observed for the predictions using Hanson's model. Additionally, the smaller integral length scale near the casing in Leonard *et al.*'s RANS (section 4.2.2.2) seems to be responsible for a decrease in the predicted noise at low frequencies. Indeed, as pointed out in chapter 4, larger turbulent structures near the casing (shown in section 4.2.2.2) lead to an increase in the noise at low frequencies which is consistent with an increased noise when using Nallasamy and Envia's data set.

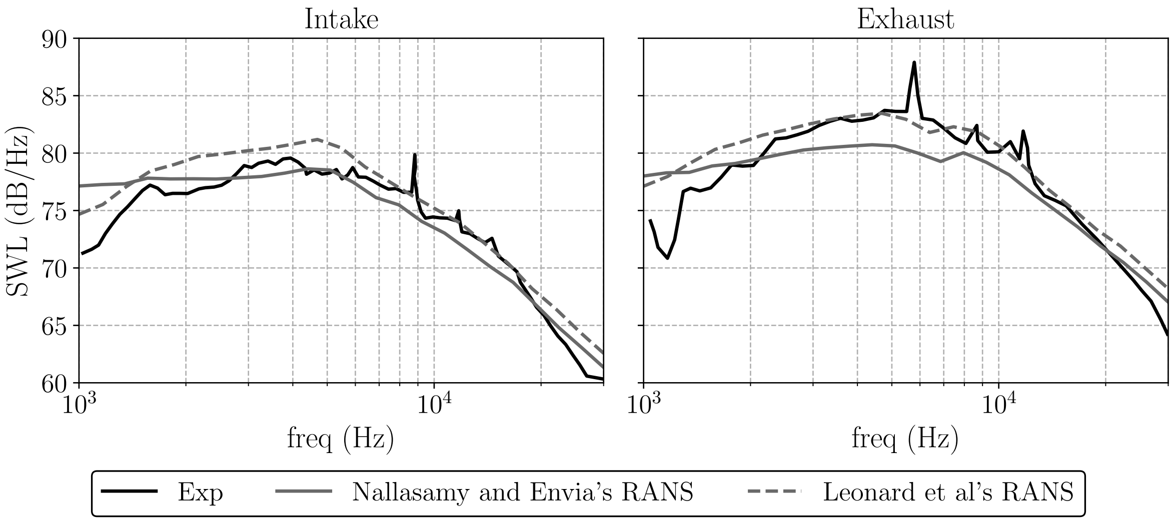

Figure 5.6: Mean flow variation effect, Hanson's model.

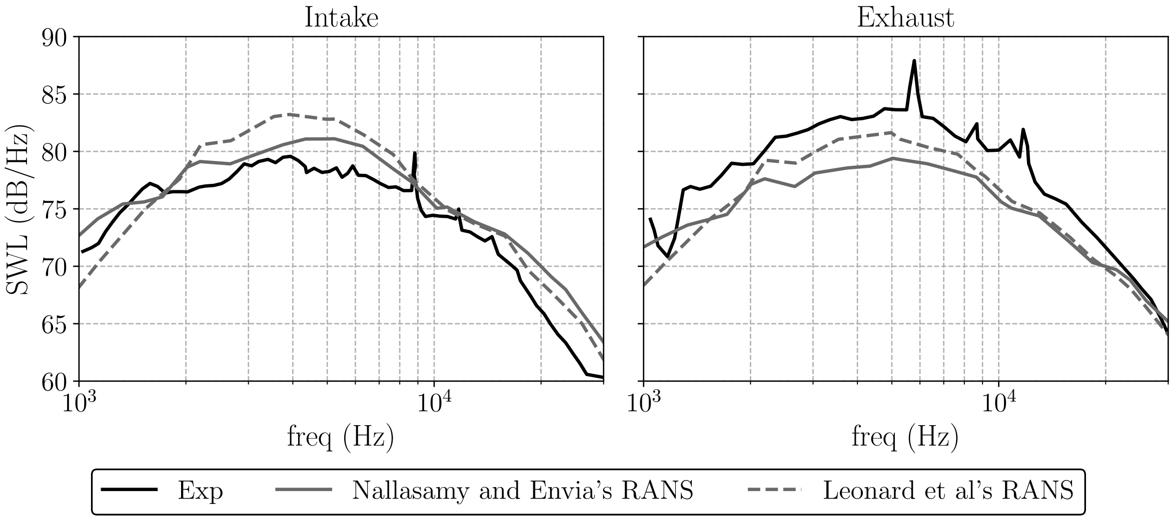

Figure 5.7: Mean flow variation effect, Posson's model.

5.2.2.2 Difference between 2D and 3D models

As stated in section 1.4.4.1, analytical models using the cascade approach can be split into two categories: on the one hand, there are the 2D models, which consider a wave vector in the (x_c, y_c) plane in the cascade reference frame to model the impinging flow and the cascade response. On the other hand, there are the 3D models, which consider a third wave number component k_{zc} in the spanwise direction.

The aim of this section is to assess the impact of the spanwise wave number on the noise prediction. To do so, the 3D model of Posson [12, 46, 48] is compared to the 2D model of Ventres *et al.* [45]. In order to get reliable comparisons, two points need to be addressed.

Firstly, the kernel function in Ventres *et al.*'s model is computed using a semi-analytic method contrary to that of Posson's model that is obtained analytically. As a consequence, the convergence of Ventres' cascade response needs to be ensured before any comparison with the 3D model of Posson. To this aim, the 2D cascade response of Posson has been implemented in the model of Ventres, while keeping the other characteristics of the code such as the 2D anisotropic turbulent spectrum introduced by Nallasamy and Envia [13], and has been directly compared to the noise predictions obtained from Ventres' model. This convergence study is presented in detail in appendix E and shows almost identical results between Ventres' model with 500 chordwise discretization points and the 2D Posson model, which ensures reliable predictions using Ventres' model.

Secondly, Ventres's model was originally built using a 2D anisotropic turbulence spectrum (see section 5.2.2.3 for more details). As highlighted by Atassi and Logue [220] [221], Posson *et al.* [46], Grace *et al.* [55], and Gea-Aguilera *et al.* [222], the turbulence spectrum has a substantial impact on the acoustic power prediction. As a consequence, it is of paramount importance that the two models make use of the same turbulence spectrum. For consistency with the Liepman model used in the 3D Posson model, the 2D version of the same spectrum has been implemented in Ventres' model. Following the methodology of Ventres *et al.* [45], the integration of the 3D Liepmann spectrum (see appendix G.1) must be done over the radial wave number and the strip width Δr, with $\mathbf{k} = (k_{xc}, k_{yc}, k_{zc})$:

$$\int_{-\infty}^{+\infty} \int_{-\infty}^{+\infty} \Phi_{ww}^{L}(\mathrm{k}) \mathrm{e}^{\mathrm{i} k_{zc} \Delta r} \mathrm{d}k_{zc} \mathrm{d}\Delta r. \tag{5.2}$$

Since the variables k_{zc} and Δr are independent, and $\Phi_{ww}^{L}(\mathrm{k})$ does not depend on Δr, the integral defined in eq. (5.2) can be rewritten in the following form:

$$\int_{-\infty}^{+\infty} \Phi_{ww}^{L}(\mathrm{k}) \int_{-\infty}^{+\infty} \mathrm{e}^{\mathrm{i} k_{z} \Delta r} \mathrm{d}\Delta r \mathrm{d}k_{zc} = 2\pi \Phi_{ww}^{L} \left(k_{xc}, k_{yc}, 0\right), \tag{5.3}$$

considering the definition of the delta function:

$$\int_{-\infty}^{+\infty} \mathrm{e}^{\mathrm{i} k_{zc} \Delta r} \mathrm{d}\Delta r = 2\pi \delta \left(k_{zc}\right). \tag{5.4}$$

Eventually, the Gaussian turbulence spectrum of Nallasamy and Envia [13] is replaced by the spectrum defined in eq. (5.3), which consists in the 3D Liepmann spectrum for which the radial wave number k_{zc} has been set to zero. The background and wake turbulence decomposition proposed by Nallasamy and Envia is then applied using this 2D Liepmann spectrum. The comparison between the 2D and 3D models using the Liepmann isotropic turbulence spectrum is shown in fig. 5.8.

Upstream of the stator, the prediction obtained with the model of Posson tends to slightly underestimate the acoustic power below 2 kHz and overestimate it by 2 to 4 dB between 2 kHz and 8 kHz. Above 8 kHz, the prediction recovers quite faithfully the acoustic power from the experiment. However, downstream of the stator, Posson's model underestimates the acoustic power on the entire range of studied frequencies by 2 to 4 dB with respect to the experiment. Regarding the 2D models of Ventres and Posson, a significant underestimation of 10 to 18 dB can be observed for both upstream and downstream predictions. The overall shape of the predictions, however, is similar to what is observed experimentally and with the model of Posson. Similar results have been presented by Grace *et al.* [55, 157], showing important discrepancies when using isotropic turbulence models such as the Liepmann or a Gaussian spectrum. This analysis shows that using a 2D homogeneous and isotropic turbulence spectrum with a 2D cascade response does not lead to reliable acoustic power predictions. For 2D models, the anisotropic model of Nallasamy and Envia, as shown in section 5.2.2.3, gives more satisfactory results. Nevertheless, only 3D models give results that are really consistent with experimental data, confirming that both 3D flow description and cascade response are compulsory to carry out analytically based

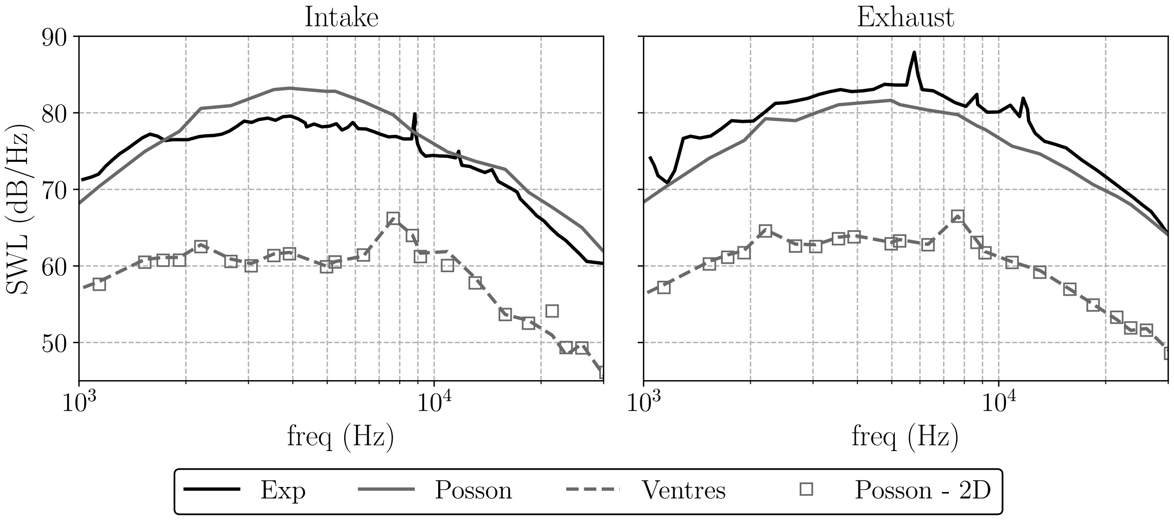

Figure 5.8: Comparison of the SWL of 2D and 3D models with Liepmann's spectrum (2D or 3D).

acoustic predictions. These predictions might be improved if anisotropy could be taken into account, as wake flows are likely to carry structures that are stretched in the local streamwise direction. However, since classical RANS models are intrinsically isotropic, taking into account anisotropic effects requires additional modeling efforts.

5.2.2.3 Modeling of turbulence

The description of the turbulent impinging flow can be addressed with stochastic variables to model the power spectral density. This eventually leads to compute the upwash velocity cross correlation function, which can be expressed as a function of the turbulent spectrum (see eq. (5.5)):

$$\langle \bar{w}(\vec{x_1}, r)\bar{w}(\vec{x_2}, r)^* \rangle = \iiint_{\mathbb{R}^3} \Phi_{ww}(\vec{K}, r) e^{i\vec{K}*\vec{\Delta x}} d\vec{K} \tag{5.5}$$

with $\vec{\Delta x} = \vec{x_2} - \vec{x_1}$, $\vec{K}$ the wave number vector and Φ_{ww} the upwash turbulent spectrum. Several spectra are used to model this term. They can be divided into two categories:

- The isotropic models: these models depend only on one integral length scale and the turbulence intensity. The Liepmann and von Karman spectra are usually the spectra of reference.
- The anisotropic models: they depend on multiple integral length scales and on the turbulence intensity. These spectra are used to model more realistically the turbulence for flows exhibiting some anisotropy. To this end, Kerschen and Gliebe [223] developed an axisymmetric turbulence spectrum to model more realistically the turbulence in turbomachinery. In the original version of the model of Ventres [45], the spectrum is approximated as a product of three Gaussian functions depending on three different coordinates and length scales. This model was specifically designed for the model of Ventres and is naturally anisotropic by construction.

The theoretical background of all these turbulence models are briefly recalled in appendix G. As mentioned before, these models directly depend on the integral length scale that is retrieved from the RANS simulations. Yet, it has been shown by Atassi *et al.* [220], Posson *et al.* [46], Leonard *et al.* [43], and Gea-Aguilera *et al.* [222] that variations of the integral length scale estimate have a substantial impact on the predicted noise, which implies that the choice of turbulence model itself is not inconsequential and may induce significant discrepancies in the noise predictions [204].

5.2.2.3.1 Isotropic models The turbulence near the stator leading edge is usually considered as isotropic since the anisotropy generated at the rotor trailing edge tends to rapidly decay through the inter-stage [44]. The most popular isotropic turbulence models are Liepmann's spectrum, von Karman's spectrum and Gaussian isotropic models. Previous studies by Atassi *et al.* [220] have identified the impact of using these three different models with their code BB3D. Posson *et al.* [46] also studied the discrepancies in predictions using both Liepmann's and Gaussian spectra. Both authors carried out this analysis on the low-count SDT configuration. This section extends their work, examining the disparities obtained when using Liepmann's and von Karman's spectra for both Hanson's and Posson's models.

Figure 5.9 shows the SWL predicted by Hanson's model using both isotropic turbulence models. Similar comments to those of Atassi *et al.* [220] can be made about the disparities between the two predictions. For the lowest studied frequency, a maximum gap of 2 dB can be observed. However, for frequencies above 2 kHz, the two SWL unexpectedly almost overlay. Indeed, the main difference between von Karman's and Liepmann's spectra is that the associated energy models were constructed to reproduce the inertial range energy decay of $k^{-5/3}$ for the former and of k^{-2} for the latter. However, this difference in their construction only has a very limited impact on the SWL.

Similar observations can be made when using Posson's model as shown in fig. 5.10. In this specific case, the disparities are slightly larger: for the lowest frequencies, the gap between the predictions using the two different turbulence models can be 1 dB higher than when using Hanson's model. For medium to high frequencies, a constant gap of around 1 dB can be observed between the two turbulence models for both upstream and downstream predictions. At low frequencies, the frequency range over which the predictions with the two turbulence models do not overlay is similar for the two acoustic models.

For both acoustic models, the Liepmann spectrum recovers the overall shape of the SWL better than von Karman's.

5.2.2.3.2 Anisotropic models As already mentioned, the flow close to the rotor trailing edge of a fan stage can be significantly anisotropic within the wake. Nevertheless, this anisotropy significantly decreases through the inter-stage [35, 44], leading to a quasi-isotropic flow at the stator leading edge of current engine architectures.

However, future engine architectures will display shortened nacelles, which will substantially decrease the spacing between the rotor and the stator, questioning the common assumption of isotropic turbulence near the stator leading edge. Thus, it is of great interest to assess the impact of the flow anisotropy on the predicted noise. To do so, several anisotropic models have been developed. Two of them are analyzed in the present work: the anisotropic spectrum of Nallasamy and Envia [13], which is based on previous work by Ventres, and the axisymmetric spectrum of Kerschen and Gliebe [223], based on the earlier works by Batchelor [224] and Chandrasekhar [225, 226]. The spectrum equations for both models are briefly recalled in appendix G.2.

Figure 5.11 compares the predictions obtained using the model of Ventres with two different turbulence models: the 2D Liepmann spectrum presented in section 5.2.2.2, and Nallasamy and Envia's anisotropic spectrum [13]. At high frequency, the noise levels obtained from the model

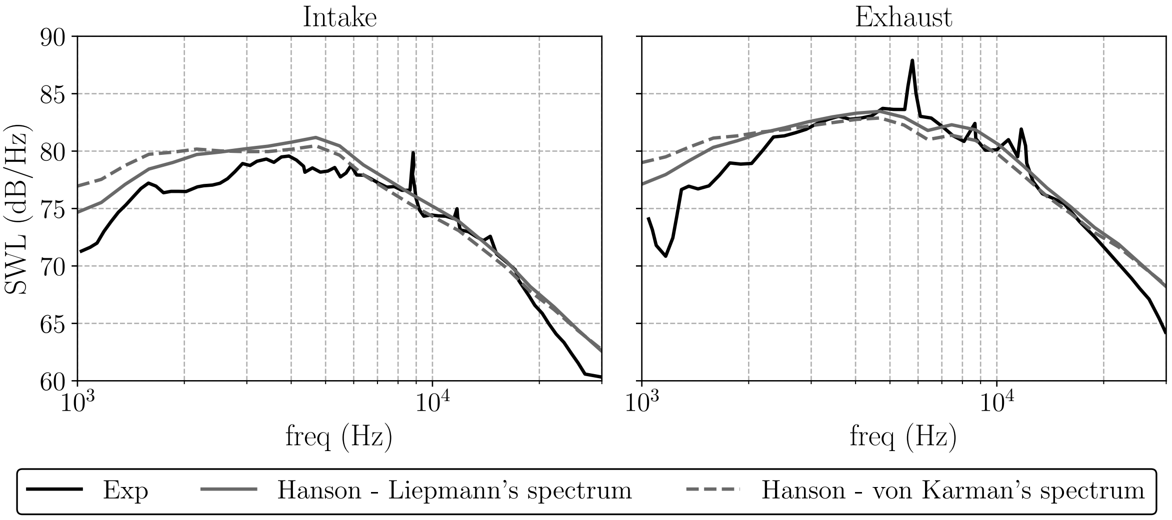

Figure 5.9: Predictions using Hanson's model with both Liepmann's and von Karman's spectra.

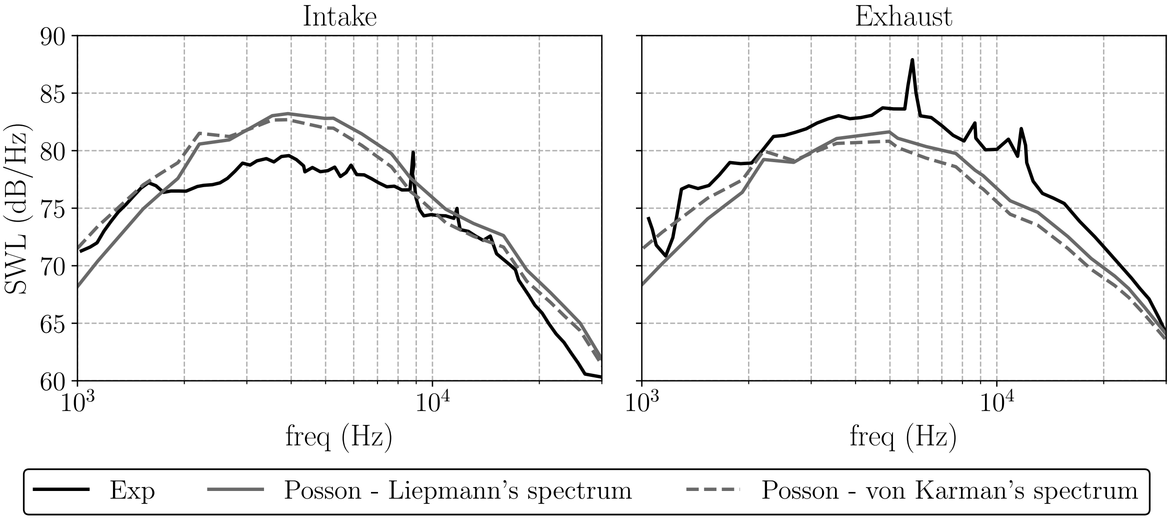

Figure 5.10: Predictions using Posson's model with both Liepmann's and von Karman's spectra.

of Ventres using Nallasamy and Envia's spectrum are comparable to the SWL provided by the 3D model of Posson with Liepmann's spectrum (see fig. 5.10). For low to medium frequencies, however, this model significantly under-predicts the noise, with a gap that can reach almost 7 dB with respect to the experimental data. Regarding the predictions obtained with the 2D Liepmann spectrum, the overall shape of the SWL is similar to the one obtained with Nallasamy and Envia's spectrum. Nevertheless, significant discrepancies ranging from 10 dB to 15 dB can be observed between the SWL obtained with the two turbulence models. This confirms that a 2D cascade response used in conjunction with a 2D isotropic turbulence model cannot provide reliable SWL predictions for this test case. The model of Nallasamy and Envia provides better results with the 2D cascade response. Still, the use of 3D models seems to be unavoidable to get predictions that are reasonably close to the experimental data.

Figures 5.12 and 5.13 show the predictions obtained with the 3D model of Posson using the axisymmetric model of Kerschen and Gliebe. The SWL are plotted for different values of l_a/l_t,

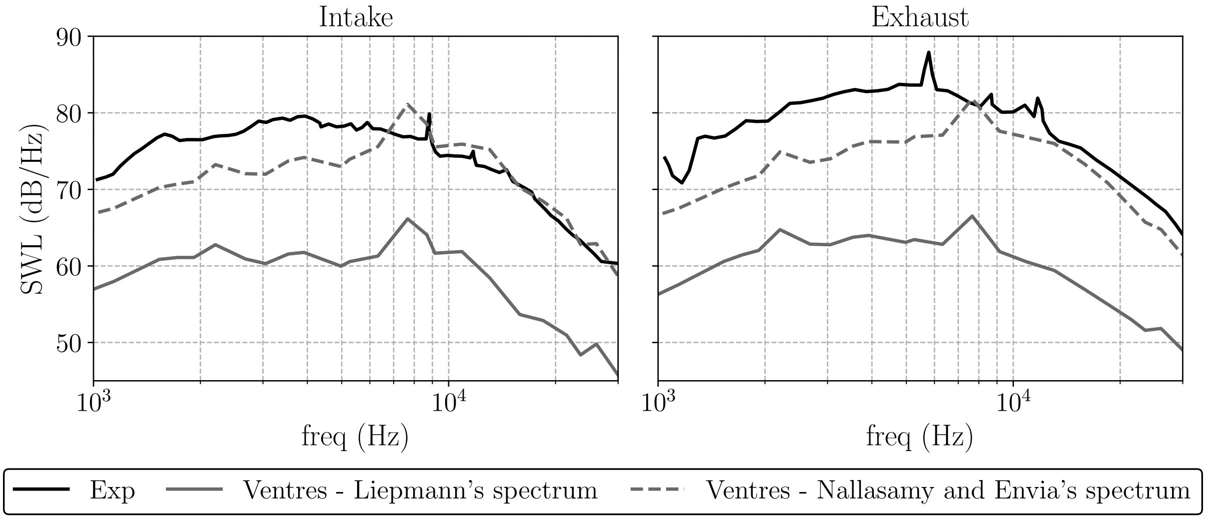

Figure 5.11: Predictions using Ventres's model with both Liepmann's and Nallasamy and Envia's spectra.

where l_a and l_t are the integral length scales in the direction of this axis of symmetry and in the transverse direction respectively. A preliminary study performed by Posson *et al.* [46] focusing on the case $l_a/l_t = 2$ gave a first overview of the impact of anisotropy onto the predicted noise. The present study focuses on ratios closer to 1, with values ranging from 0.7 to 1.5, in order to assess the impact of anisotropy for more realistic cases. The specific case $l_a/l_t = 1$ actually corresponds to Liepmann's spectrum. The most realistic cases are those for which $l_a/l_t > 1$, since the axial integral length scale tends to be larger than the transverse one. Predictions for $l_a/l_t < 1$ have been included for the sake of completeness. The objective of this study is more to quantify the impact of the anisotropy with respect to the isotropic case ($l_a/l_t = 1$), rather than to identify the ratio that gives results closest to the experimental data. As it can be seen from fig. 5.12, a ratio of $l_a/l_t = 0.9$ increases the noise by 0.5 dB at low frequencies, by 1.5 dB at medium frequencies, and by 2.5 dB at high frequencies with respect to the isotropic case ($l_a/l_t = 1$). This trend is the same for each 0.1 step down to $l_a/l_t = 0.7$, reaching a maximum gap of 1.5 dB at low frequencies, of 4.5 dB at mid frequencies and of 7.5 dB at high frequencies with respect to the isotropic case. For $l_a/l_t > 1$, the trends are relatively similar: from $l_a/l_t = 1$, each increase of 0.1 in the ratio induces a decrease in the noise of 0.5 dB at low frequencies, of 1.5 dB at mid frequencies and of 2.5 dB at high frequencies. This behavior is consistent with what Gea-Aguilera *et al.* [222] observed in their study on the broadband noise produced by the interaction of anisotropic turbulence with an isolated flat plate, using Kerschen and Gliebe's spectrum along with Amiet's model.

This study shows how sensitive these models are towards the flow anisotropy. A slight deviation from the isotropic case can lead to substantial modifications in the predicted noise, indicating that the anisotropy of the flow must be accurately measured and assessed in order to ensure reliable analytical noise predictions.

5.2.3 Computation of the acoustic sources: cascade effect

Previous studies by Cheong *et al.* [146], Jenkis *et al.* [227], Blandeau *et al.* [219] and Gea-Aguilera *et al.* [60] have shown that the cascade effect on the SWL becomes negligible at high frequencies. These studies were carried out using 2D approaches for both cascade and isolated-airfoil models,

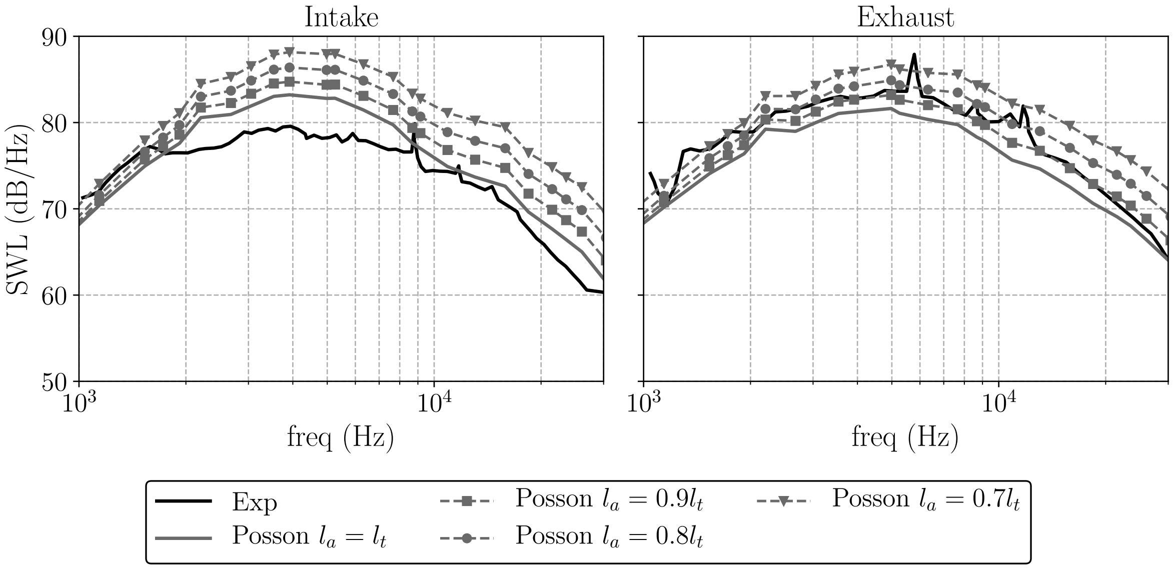

Figure 5.12: Predictions using Posson's model with Kerschen and Gliebe's spectrum ($l_a/l_t < 1$).

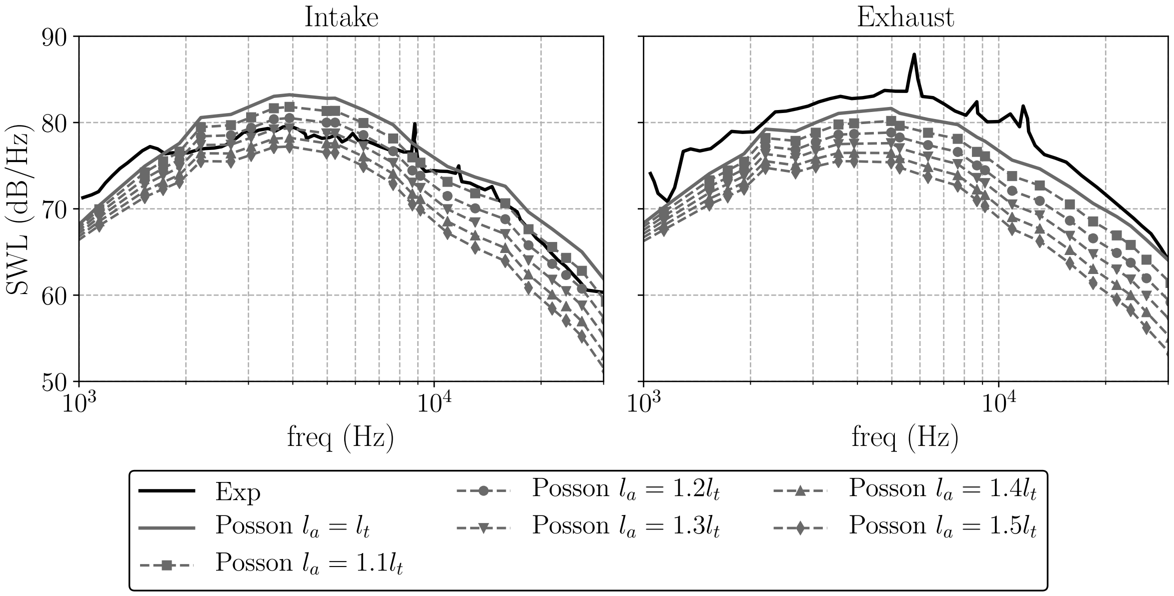

Figure 5.13: Predictions using the Posson's model with Kerschen and Gliebe's spectrum ($l_a/l_t > 1$).

on a single radial position and considering a free-field propagation. Posson *et al.* [12] also carried out a study on the cascade effect by comparing the unsteady loading obtained from the 3D Posson model with an isolated airfoil response. Posson *et al.* [12] pointed out that for a blade overlap close to zero, with small to moderate solidity, the cascade response gets closer to the response of an isolated airfoil. Some significant disparities however appear for high-solidity configurations. Grace [169] obtained similar results on the SDT configuration using a 3D approach similar to that of Posson. Grace showed that the vane responses provided by the single airfoil and the cascade methods do not agree for high-solidity configurations, even at high frequency. Grace also showed that these vane response disparities lead to a significant underestimation of the radiated noise when using a single airfoil-based approach. Both Posson *et al.*'s [12] and Grace's [169] 3D studies seem to contradict the results obtained in a 2D context.

This section further investigates this question by presenting an assessment of the impact of the cascade effect on the sound power. More precisely, the objective of this part is to determine if the single airfoil and the cascade responses lead to similar acoustic power spectra for 3D analytical models, especially at high frequencies.

In the 3D Posson model, the computed cascade response is actually the pressure jump $\Delta\hat{P}_0$ through the vanes. As proposed by Grace [169], a direct way to neglect the cascade effect is to replace this response with a 3D isolated profile response such as the one of Amiet's model [63, 138–140]. The present implementation considers a wake to wake correlation for the impinging turbulence statistics, which is consistent with the azimuthal periodicity of the configuration. This approach can be compared to the one adopted by de Gouville [31], in the context of incident turbulence noise, and by Joseph and Parry [228] for the noise resulting from the interaction of a boundary layer with a stator. Moreover, the present Amiet-based response includes the effect of sub-critical gusts since they have a significant impact at low and moderate frequencies as observed by Moreau *et al.* [139]. Since the integration of the pressure jump of Amiet's response is performed numerically, a convergence study has been carried out to guarantee the convergence of the presented results in terms of the number of points to discretize the chord.

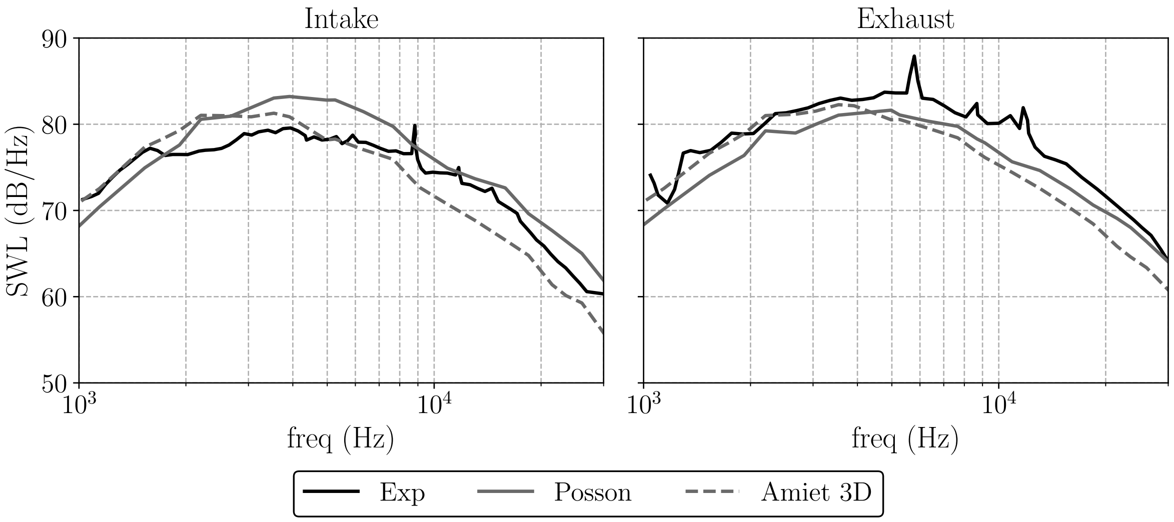

Figure 5.14: Cascade effect, baseline configuration.

Figure 5.14 shows the acoustic power radiated upstream and downstream of the SDT baseline configuration stage obtained following two approaches: the 3D Posson model either including the cascade response or considering a 3D Amiet independent response for each vane of the row as explained above. Since only the vane response is modified, the noise propagation step takes the duct walls into account for both computations. The upstream prediction displays the major discrepancies between the two models. Below 2 kHz, a gap of 2 dB can be observed between the predictions. Above 2 kHz, the two predictions significantly differ by a gap ranging from 3 to 5 dB. For the downstream SWL, a gap of 2 dB can be observed on almost all the studied frequency range.

This first study tends to confirm that, even at high frequencies, the cascade effect has a significant impact on the predicted acoustic power when using 3D analytical models. The relatively high solidity of the chosen configuration may be partly responsible for such important disparities between the two models. In order to confirm this hypothesis, a second test case, based on the baseline configuration, has been defined by dividing the number of vanes by 2 while keeping the same vane geometry and input parameters. This results in a reduced configuration with 27 vanes and halved solidity and vane overlap. Figure 5.15 shows the results obtained for this configuration. As expected, the experimental SWL, which were obtained with the full vane row (54 vanes), do not match the 27-vane predictions. For both upstream and downstream predictions, the gap between the two models has been radically reduced. For the upstream prediction, the two predictions overlay for low frequencies and a maximum gap of 2 dB is observed for medium and high frequencies. The downstream predictions are almost identical.

This confirms that, even at high frequencies the cascade effect cannot be neglected in realistic turbofan geometries, and that its impact on the predicted noise is even more significant for configurations with high solidity and vane overlap. Thus, this analysis extends the conclusions drawn by Posson *et al.* [12] about the unsteady loading to the resulting acoustic power spectrum, and simultaneously confirms Grace's [169] results. The results of this study are not consistent with what has been observed in most of the literature so far [60, 146, 219, 227]. However, the differences are most likely attributed to the fact that in the present study, 3D models with an in-duct acoustic analogy have been used whereas the other studies used 2D models with a free-field analogy.

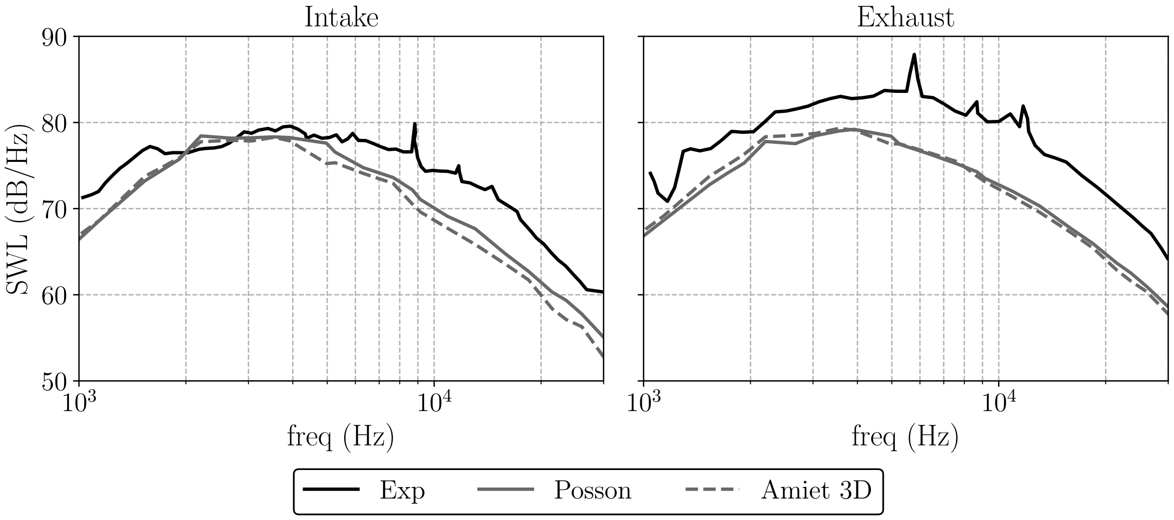

Figure 5.15: Cascade effect, baseline configuration with 27 vanes. The experimental results are obtained with 54 vanes.

5.2.4 Influence of the propagation type: free-field or duct propagation

The radiation part of these models is a determinant step in the prediction of the broadband interaction noise. Two main acoustic analogies are used: in Hanson's model, the propagation is performed within each strip accounting for mean axial flow whereas the models of Posson and Ventres resort to the in-duct analogy with a mean axial flow developed by Goldstein [132]. The latter analogy is described in section 1.4.3.2.

This section addresses the impact of the chosen propagation method on the broadband noise prediction. Considering only homogeneous turbulence, through the use of the Liepmann spectrum, the main differentiating parameter between the models of Hanson and Posson is the acoustic analogy that is used for the radiation step since they both make use of Glegg's cascade response.

Figure 5.16 shows the upstream and downstream SWL obtained from Hanson's and Posson's models. At low frequencies, for both the upstream and downstream predictions, the model of Hanson tends to overestimate the radiated noise contrary to the model of Posson. This is due to the fact that in the annular duct analogy, the duct cut-off effect is accounted for, leading to a reduced noise radiation especially at low frequencies. Upstream of the stator, the two models give relatively similar noise predictions at high frequencies. However, at medium frequencies, the model of Posson tends to overestimate the noise. The downstream predictions display significant differences between the two models. For Posson's model, a constant gap of at least 3.4 dB is observed for the entire range of studied frequencies. Hanson's model, however, gives satisfactory results, especially for frequencies between 3 kHz and 20 kHz for which it faithfully recovers the experimental acoustic noise levels. Outside of this range, the model of Hanson overestimates the SWL especially at low frequencies, as with the upstream prediction. This phenomenon is significant in the case of the SDT configuration in which the hub to tip ratio is $\sigma = \frac{R_{Hub}}{R_{Tip}} = 0.5$. In future UHBR engine architectures, this ratio should decrease in conjunction with an increase in the bypass ratio, resulting in a reduction of the cut-off effect of the duct geometry. Regarding the overall shape of the spectra, Hanson's model seems to better recover the shape of the upstream experimental spectrum, whereas Posson's model downstream prediction is closer to the experimental spectrum shape in the downstream direction.

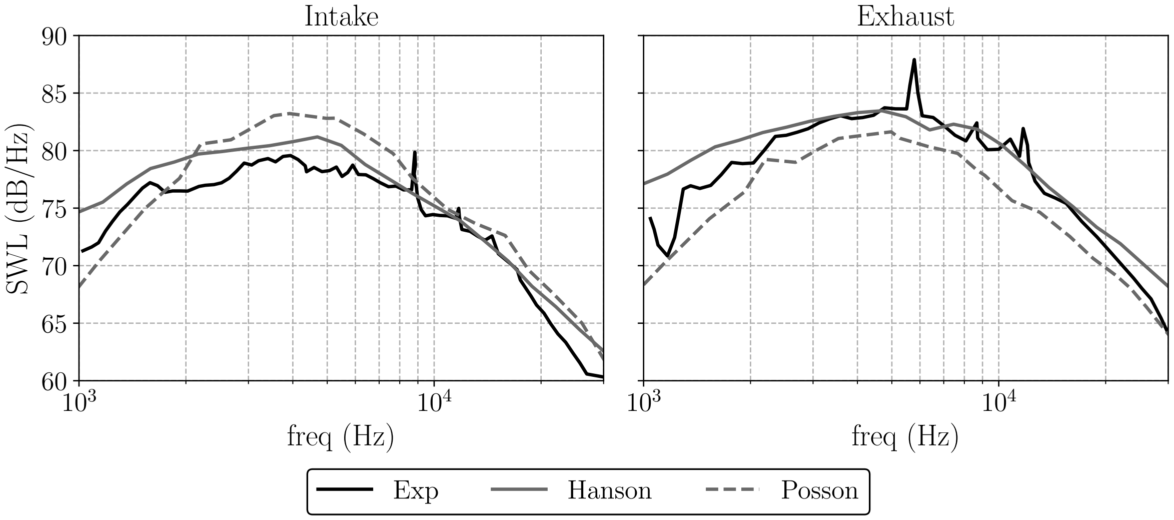

Figure 5.16: Propagation effect.

5.3 Conclusion

A comprehensive noise computation of the SDT baseline configuration, at approach condition has been performed using RANS-informed analytical models. Three of the most advanced analytical models taking the cascade effect into account have been tested in order to identify the impact of the assumptions made in the models on the noise predictions. The models have shown to be significantly dependent on the chosen stagger angle to model the equivalent flat plate geometry for the model. Substantial disparities have been observed especially in the upstream SWL whereas the impact on the downstream predictions is limited. The modeling of the impinging flow has then been investigated, showing great dependency on the accuracy of the RANS simulation from which the input parameters are extracted. Modeling the impinging flow and the cascade response in 3D has been shown to be compulsory to correctly recover the noise levels without relying on anisotropic turbulence models, which are not representative of the real flow in the SDT case. A limited difference between the noise predictions when using Liepmann's and von Karman's isotropic spectra has been observed. However, using the axisymmetric turbulence model of Kerschen and Gliebe has shown that the tested models are very sensitive to anisotropy and that it must be carefully configured to ensure reliable predictions. The present work has also confirmed that, for modern fan-OGV stages, isolated airfoil responses cannot faithfully predict the radiated noise since the cascade effect is too significant for the studied range of cascade solidity values. Finally, the type of acoustic analogy used to propagate the sound has shown to be a determinant choice in building the models. It has a substantial impact on both the shape and the absolute noise levels.

Conclusions and perspectives

Conclusions from a methodological point of view

Simulation approach

Two simulation approaches were compared: a wall-resolved RANS simulation, and two wall-modeled LES with different levels of mesh refinement (LES1 and LES2). Given the uncertainty of the measurements, all the simulations were in good agreement with the experimental data. They were all able to recover accurately each velocity component profile but displayed discrepancies in the turbulence levels. The RANS predicted RMS levels close to the experimental ones but could not precisely recover the RMS azimuthal velocity profiles, especially near the casing. The LES1 remarkably improved the shape of the RMS profiles but displayed a significant overestimation of the turbulence levels. Despite slight discrepancies in the performance parameters, the LES2 provided the most accurate results and precisely captured both the velocity and the RMS profiles for each velocity component. These differences between the simulations were attributed to the simulation method itself, as the laminar-turbulent transition could be captured by the LES while no transition model was used for the RANS. Both LES seemed to be able to capture flow features that the RANS could not totally predict, such as the complex interaction of the rotor leading edge flow separation with the LE radial vortex. The observed disparities were also related to the mesh refinement since more intense flow separations occurred in the LES1 because of the coarser near wall mesh. The significant flow pattern modifications, and the substantial improvement induced by the LES2 mesh refinement showed that, despite the use of a wall law, the wall-modeled LES approach still required a fine mesh close to the wall to provide accurate results. Indeed, in spite of the fact that the LES1 met the lower limit of the wall mesh requirements for wall-modeled LES, it appeared to be only slightly more accurate than the much less expensive RANS simulation on some key aspects of the flow, such as the prediction of the TKE levels. Nevertheless, it gave access to precious unsteady and turbulence data that could not be obtained by any lower order methods, which is still a determinant asset of the LES approach even with a medium sized mesh.

The RANS approach has a remarkable cost/accuracy ratio but is limited by the important embedded modeling, which prevents from accurately predicting key flow features, especially those related to the flow unsteadiness and its stochastic behavior. The WMLES fixes this issue and makes it possible to gather valuable information about the flow turbulence such as velocity spectra, pressure fluctuations and correlation length scales. This gave a better insight into the RSI mechanism but also enabled to identify other broadband noise sources. The additional cost was however substantial as a significantly refined mesh was required to exploit the full potential of the WMLES approach. The limit of this method might have been reached with the LES2 since a finer mesh might be out of the domain of applicability of wall laws and lead to erroneous results.

RANS-informed analytical predictions

The reliability of the RANS-informed analytical predictions appeared to depend on many parameters. The accuracy of the RANS simulation from which the input parameters are extracted was found to be closely related to the accuracy of the analytical noise predictions. In particular, the refinement of the mesh, as well as the chosen turbulence model had a significant impact on the noise predictions. These parameters completely determined the turbulent variables that were used to model the impinging flow, and induced noise estimate disparities of several decibels. In particular, the predictions proved to be relatively sensitive to the integral length scale estimate, which relied on both the accuracy of the simulation, and on the chosen estimation to compute it. A comparison with LES-informed analytical predictions showed that the choice of the RANS TLS estimate was not as obvious as for the LES, which made it possible to compute a much more accurate TLS estimate using the velocity cross-correlation. The right estimate to choose seemed to be case dependent, and had to be chosen wisely to reproduce the real behavior of the flow. The sensitivity study, which compared Amiet's, Ventres', Hanson's and Posson's models, revealed that modeling the impinging flow and the cascade response in 3D was compulsory to correctly recover the noise levels without relying on unrealistic anisotropic turbulence models. It was shown that the use of the latter must be restricted to cases with accurate data about the flow anisotropy since the models displayed a significant sensitivity to anisotropic turbulence spectra. The limits of the isolated blade response assumption were shown with the SDT configuration, which displayed an intense cascade effect even at high frequencies. Finally, the in-duct propagation with a mean axial flow had a significant effect on the noise estimates and better captured the overall noise spectrum shape with respect to the free-field propagation with a mean axial flow. Other propagation effects such as the rotor shielding, the presence of a swirled flow in the inter-stage, or the variation of the duct cross-section were not taken into account and may have an impact on the noise predictions.

Despite many constraining assumptions, the RANS-informed analytical method proved to give fairly reliable broadband RSI noise estimates. When choosing the best suited TLS estimate, it was able to provide upstream SWL levels comparable to those of the LES2 FW-H predictions considering only the front part of the OGV, while the downstream SWL was slightly overestimated. As a consequence, when the RSI mechanism is the only dominant noise source, such a method is expected to be reasonably accurate in predicting the total noise. When other dominant sources are present, it can only provide a good estimate of the RSI noise since the other sources are not modeled. This approach remains the best choice to carry out parametric studies as most of its computational cost comes from the RANS approach itself, which is the most widespread and affordable simulation approach to this day.

Hybrid numerical noise predictions

The accuracy of the hybrid numerical noise predictions proved to be directly dependent on the accuracy of each individual step composing this approach, the first one being the prediction of the noise sources using an LES, and the second one the propagation of the resulting sound using the Ffowcs Williams and Hawkings analogy. The predictions showed a global overestimation of the noise levels, especially when using the LES1 data while the discrepancies were significantly reduced with the LES2. Indeed, the coarser LES1 mesh resulted in amplified noise sources, both on the stator and on the rotor, and in the development of additional noise sources such as the stator mid-chord radial vortex, which was most likely the consequence of an under-resolved near-wall mesh. A remarkable improvement of the predicted noise levels was achieved when using the LES2, thanks to the more accurate description of the noise sources provided by its refined mesh. Still, a slight overestimation remained. This overestimation was mainly attributed to the free-field nature of the FW-H analogy, which totally neglects the duct propagation effects. As emphasized by other studies, resorting to Goldstein's analogy for ducted flows would substantially reduce this overestimation and lead to more realistic SWL. Furthermore, similarly to the analytical models, the rotor shielding effect as well as the swirled flow in the inter-stage were neglected, which also had an impact on the noise predictions.

The limited modeling involved in this approach, whether related to the turbulence or the stage geometry itself, considerably increased the accuracy of the numerical predictions with respect to the analytical approach. For instance, the numerical predictions took into account the real shape of the blades and vanes, which is currently not achieved by analytical models since they usually model them as infinite flat plates. It also relied directly on the unsteady data to collect information about the turbulence, which notably reduced the important uncertainty observed in the RANS when computing the TLS. The numerical approach also made it possible to assess the relative contribution of the RSI mechanism with respect to other dominant noise sources. Indeed, contrary to the analytical approach, it is not restricted to the RSI mechanism since all the sources located on the extracted surfaces are taken into account. For configurations in which the RSI mechanism is not the only dominant broadband noise source, it is thus compulsory to resort to this kind of methods to identify the different noise sources and precisely estimate the total noise.

Even though the computational cost of the propagation step is relatively reasonable (∼1 day), the substantial cost of the LES prevents this method from being used systematically for performing noise estimates, limiting its use to advanced acoustic studies. Indeed, the LES1 and the LES2 required 1 million and 4 million CPU-hours, respectively, while the RANS only required 2300 CPU-hours. Nevertheless, this approach should become more widespread in a near future since the present study revealed that relying exclusively on analytical approaches may lead to a significant underestimation of the total noise in some configurations.

Conclusions from a physical point of view

The comprehensive aerodynamic analysis conducted on the ACAT1 configuration made it possible to identify and better understand the complex flow features that characterize the flow within a fan stage at approach condition. A global pronounced radial flow was observed on both the fan blade and the stator vane surfaces. Intense 3D flow features were identified, in particular at the rotor leading edge where a radial vortical structure extending over more than 70% of the rotor span developed. It consisted of a leading-edge vortex, the streamlines of which originated from the lower part of the leading edge and traveled up to the rotor tip where they fed the tip clearance flow. This particular region also induced both a boundary layer separation and a transition, which took part in the dynamic production of large turbulent structures with intense TKE levels that grazed along the rotor suction side down to the trailing edge. This mechanism appeared to directly influence the pattern of the flow impinging onto the stator vanes by modifying the wake shape and by increasing its turbulence level, which most likely contributed to the increase in the RSI noise. Despite this interaction, the wake turbulence was almost isotropic, confirming the common hypothesis made in the analytical models. The radial coherence length scale of each velocity component of this incident flow was found to be of the same order of magnitude as that of the vane response, confirming the hypothesis made in Posson's model.

An in depth analysis of the boundary layer structure and of the wall pressure fluctuations revealed the presence of several noise sources on both the rotor and the stator surfaces:

- The RSI noise sources located at the stator leading edge.
- The sources induced by the intense boundary layer transition at the stator mid-chord.
- The sources related to the intense flow separation/boundary layer transition induced by the rotor LE radial vortex.

These sources displayed intense fluctuations over a large frequency range, especially between 1 kHz and 10 kHz. The rotor LE and stator rear part sources appeared to be of the same order of magnitude as the RSI sources, which indicated potential additional non-negligible sources in the fan stage. This was confirmed by the numerical noise predictions, which were performed for each of these sources separately. The noise caused by the rotor LE and stator rear part sources notably appeared to contribute to the total noise to the same extent as the RSI mechanism. This proved that in some configurations at approach conditions, the RSI mechanism should not be the only dominant noise mechanism to be considered.

Perspectives

The present study showed the capability of two hybrid methods to provide reliable broadband noise predictions when dealing with a full fan-OGV stage. It also made it possible to identify some of their main drawbacks and weaknesses, which paved the way to future improvements and developments.

Regarding the RANS informed analytical predictions, a first way to increase its accuracy could be to resort to a URANS simulation instead of the classic steady RANS approach. Indeed, the use of a URANS simulation would remove the uncertainty induced by the extrapolation process, which is required to obtain the wake information near the stator leading edge when using a RANS. This would only moderately increase the computational cost of this approach, since the reasonably extended convergence and acquisition times are the only additional cost that would be observed. Another way to increase the reliability of this approach is to resort to less stringent assumptions when building the analytical models, whether they are related to the cascade response or to the sound propagation. For instance, the classic infinite flat plate assumption could be discarded in favor of a model formulation that takes into account the camber and the thickness of the blades and vanes to obtain a more realistic modeling of the fan-OGV geometry. Furthermore, Goldstein's analogy already accounts for the duct propagation effects, but only considers a mean axial flow while a swirled flow would be more realistic in the inter-stage region. It also considers an infinite duct of constant section, while a duct with a slowly varying cross-section would be more appropriate. The mode matching technique could even make it possible to consider stronger duct section variations. Accounting for the rotor shielding effect and the multiple reflections between the rotor and the stator could also enhance the model accuracy. Finally, in order to get closer to real configurations, the reflections and refractions occurring at the duct exits as well as the free-field propagation outside of the nacelle could also be taken into account. The computational costs and the complexity induced by adding these features in the models must however be balanced with the gain of accuracy they induce so that this approach remains affordable and fast.

The capacity of the WMLES-FWH approach to provide accurate broadband noise predictions was demonstrated. Still, there is room for improvements on several aspects of this approach. A direct way to increase the accuracy of this approach would be to improve the prediction of the broadband noise sources themselves. However, the WMLES performed in this study showed a great sensitivity to the wall mesh refinement, even though the LES1 mesh met the mesh requirements for WMLES. This led to a refined LES2 mesh, which significantly improved the simulation results but also almost reached the lower limit of applicability of wall laws. As a consequence, an even finer mesh would require a wall-resolved simulation, which is still very challenging in terms of computational resources for a full fan-OGV stage. Nevertheless, less costly options remain available. Using Goldstein's analogy instead of Ffowcs Williams and Hawkings' would, for instance, provide more realistic noise predictions as the duct cut-off effect would be taken into account. Other propagation features such as the rotor shielding effect, the variation of the duct cross-section or the inter-stage swirled flow would however still be neglected. One option to take them into account would be to use a direct numerical noise prediction approach, which resolves the acoustic near-field up to the computational domain limits. All the propagation effects would thus be accounted for and the acoustic far-field could then be computed by extracting the acoustic field from porous surfaces at the inlet and outlets, and further propagate it using an adapted acoustic analogy. This option would increase the computational cost of the predictions since higher-order numerical schemes would have to be used to correctly propagate the sound waves. Such an approach would require an additional treatment to separate the hydrodynamic from the acoustic fluctuations downstream of the OGV, and would also question the use of periodic boundary conditions as the modal content of the acoustic field would inevitably be modified.

Besides the preceding suggested improvements, it would also be of great interest to study in more detail the properties of the turbulent flow observed in the fan-OGV stage. For example, the frozen turbulence hypothesis could be checked by computing the turbulence length scale from spatial correlations and confront it to the one obtained from the temporal correlations. The degree of anisotropy of the turbulent structures along the inter-stage could also be analyzed to quantify to which extent it could impact the RSI mechanism in future UHBR engines. Such studies would greatly enhance the overall knowledge about the turbulence properties of the flow within a fan-OGV stage, and could eventually lead to a better understanding of the induced broadband noise sources.

APPENDIX A

Duct acoustics: eigenfunctions and Green's function for the propagation of acoustic waves within a rigid annular duct with a uniform axial flow.

This section presents in details the fundamental features related to the propagation of acoustic waves in a rigid annular duct with an axial mean flow. Firstly, the complete derivation of the duct modes presented in section 1.4.2.1 is detailed. Secondly, the Green's function for an annular duct with a uniform axial flow presented in section 1.4.3.2.2 is derived.

For this entire section, let us consider an annular duct of axis x, with R_{hub} its inner radius and R_{casing} its outer radius. Any point inside the duct can be described in the cylindrical coordinate system so that $\mathbf{x_d} = (x, r, \theta)$ where r and θ are the radial and circumferential coordinates respectively.

A.1 Duct modes

A.1.1 Helmholtz equation

The pressure field in a hard-walled annular duct in the presence of an axial mean flow $\mathbf{U} = (U, 0, 0)$ follows the convected wave equation:

$$\left[\Delta - \frac{1}{c_0^2}\frac{D^2}{Dt^2}\right] \quad p\left(\mathbf{x}_d, t\right) = 0, \tag{A.1}$$

where c_0 is the speed of sound of the medium, $\frac{D}{Dt} = \frac{\partial}{\partial t} + U\frac{\partial}{\partial x}$ and the Laplacian operator in cylindrical coordinate is:

$$\Delta = \frac{\partial^2}{\partial x^2} + \frac{\partial^2}{\partial r^2} + \frac{\partial}{r\partial r} + \frac{\partial^2}{r^2\partial\theta^2}. \tag{A.2}$$

Additionally, a slip boundary condition is considered at the center (hub) and outer (casing) surfaces of the duct:

$$\frac{\partial}{\partial r}p\left(\mathbf{x}_d, t\right) = 0 \text{ for } r = R_{hub} \text{ and } r = R_{casing}. \tag{A.3}$$

Equation (A.1) can then be rewritten as follows:

$$\left[\beta^2\frac{\partial^2}{\partial x^2}+\frac{\partial^2}{\partial r^2}+\frac{\partial}{r\partial r}+\frac{\partial^2}{r^2\partial\theta^2}-\frac{2M}{c_0}\frac{\partial^2}{\partial x\partial t}-\frac{1}{c_0^2}\frac{\partial^2}{\partial t^2}\right]p(\mathbf{x}_d,t)=0, \tag{A.4}$$

where $M=U/c_0$ and $\beta^2=1-M^2$. Let us note $\hat{p}$ the Fourier transform of the pressure p defined as follows:

$$\widehat{p}\left(\mathbf{x}_d,\omega\right)=\frac{1}{2\pi}\int_{-\infty}^{\infty}p\left(\mathbf{x}_d,t\right)\mathrm{e}^{\mathrm{i}\omega\mathrm{t}}dt. \tag{A.5}$$

Applying the Fourier transform to eq. (A.4) leads to the so-called convected Helmholtz equation:

$$\left[\beta^2\frac{\partial^2}{\partial x^2}+\frac{\partial^2}{\partial r^2}+\frac{\partial}{r\partial r}+\frac{\partial^2}{r^2\partial\theta^2}+2iMk_0\frac{\partial}{\partial x}+k_0^2\right]\widehat{p}\left(\mathbf{x}_d,\omega\right)=0, \tag{A.6}$$

where $k_0=\omega/c_0$ is the acoustic wave-number. Equation (A.6) along with the boundary conditions from eq. (A.3) can be solved using the separation of variables:

$$\widehat{p}\left(\mathbf{x},\omega\right)=g\left(x,\omega\right)\Psi\left(r,\theta\right). \tag{A.7}$$

Injecting this relationship into eq. (A.6) yields:

$$\frac{1}{g\left(x,\omega\right)}\left[\beta^2\frac{\partial^2}{\partial x^2}+2iMk_0\frac{\partial}{\partial x}+k_0^2\right]g\left(x,\omega\right)=-\frac{1}{\Psi\left(r,\theta\right)}\left[\frac{\partial^2}{\partial r^2}+\frac{\partial}{r\partial r}+\frac{\partial^2}{r^2\partial\theta^2}\right]\Psi\left(r,\theta\right). \tag{A.8}$$

The left-hand terms only depend on (x,ω) whereas the right-hand terms depend on (r,θ). Since these four variables are independent from each other and that both equation sides are equal whatever their values, they must be both equal to a constant χ_1^2, which gives:

$$\left[\frac{\partial^2}{\partial r^2}+\frac{\partial}{r\partial r}+\frac{\partial^2}{r^2\partial\theta^2}\right]\Psi\left(r,\theta\right)+\chi_1^2\Psi\left(r,\theta\right)=0 \tag{A.9}$$

$$\left[\beta^2\frac{\partial^2}{\partial x^2}+2iMk_0\frac{\partial}{\partial x}+\left(k_0^2-\chi_1^2\right)\right]g\left(x\right)=0 \tag{A.10}$$

with the boundary conditions:

$$\frac{\partial}{\partial r}\Psi\left(r,\theta\right)=0 \quad \text{for} \quad r=R_{hub} \quad \text{and} \quad r=R_{casing}, \quad \forall\theta. \tag{A.11}$$

A.1.2 Derivation of the duct eigenfunctions

The first solving step is to determine the transverse function Ψ. Ψ needs to be 2π-periodic along θ, which means it can be decomposed into Fourier series as follows:

$$\Psi\left(r,\theta\right)=\sum_{m\in\mathbb{Z}}E_m(r)e^{im\theta}. \tag{A.12}$$

This means that for a fixed value of m, the radial function $E_m(r)$ needs to satisfy the following equation:

$$\left[\frac{\partial^2}{\partial r^2}+\frac{\partial}{r\partial r}+\left(\chi_1^2-\frac{m^2}{r^2}\right)\right]E_m(r)=0. \tag{A.13}$$

Equation (A.13) is a Bessel equations, the solution of which can be written as a linear combination of Bessel functions of first and second kind:

$$E_m(r) = A_m J_m(\chi_1 r) + B_m Y_m(\chi_1 r)\,. \tag{A.14}$$

The value of χ_1 is imposed by the boundary conditions at the hub and the casing of the duct, which can be rewritten as follows:

$$\frac{\partial}{\partial r} E_m(r) = 0 \quad \text{for} \quad r = R_{hub} \quad \text{and} \quad r = R_{casing}, \quad \forall\theta, \tag{A.15}$$

which implies:

$$\begin{vmatrix} J'_m(\chi_1 R_{hub}) & Y'_m(\chi_1 R_{hub}) \\ J'_m(\chi_1 R_{casing}) & Y'_m(\chi_1 R_{casing}) \end{vmatrix} = 0 \tag{A.16}$$

For each value of m, it can be shown that there is an infinite number of countable solutions to this equation. These solutions are noted $\chi_{m,\mu}$ with $(m,\mu) \in \mathbb{Z} \times \mathbb{N}$ and are referred to as the duct eigenvalues. Injecting this in eq. (A.14) yields:

$$E_{m,\mu}(r) = A_{m,\mu} J_m(\chi_{m,\mu} r) + B_{m,\mu} Y_m(\chi_{m,\mu} r) \tag{A.17}$$

In the latter relationship, m corresponds to the number of angular lobes whereas μ corresponds to the number of "nodes" or zeros of $E_{m,\mu}(r)$ in the radial direction. Injecting the radial function into eq. (A.12) eventually gives the so-called duct eigenfunctions $\Psi_{m,\mu}$:

$$\Psi(r,\theta) = \sum_{m\in\mathbb{Z}} \sum_{\mu\in\mathbb{N}} E_{m,\mu}(r) \mathrm{e}^{im\theta} = \sum_{m\in\mathbb{Z}} \sum_{\mu\in\mathbb{N}} \Psi_{m,\mu}(r,\theta) \tag{A.18}$$

As shown by the Sturm Liouville theory, these eigenfunctions are orthogonal for the following dot product:

$$\langle \Phi, \Psi \rangle = \int_0^{2\pi} \int_{R_{hub}}^{R_{casing}} \Phi(r,\theta)\, \Psi^*(r,\theta)\, r dr d\theta, \tag{A.19}$$

which implies:

$$\int_0^{2\pi} \int_{R_{hub}}^{R_{casing}} \Psi_{m,\mu}(r,\theta)\, \Psi^*_{m',\mu'}(r,\theta)\, r dr d\theta = \Gamma_{m,\mu} \delta_{mm'} \delta_{\mu\mu'}, \tag{A.20}$$

where δ_{ij} is the Kronecker symbol and $\Gamma_{m,\mu}$ is the squared norm of $\Psi_{m,\mu}$:

$$\Gamma_{m,\mu} = \int_0^{2\pi} \int_{R_{hub}}^{R_{casing}} |\Psi_{m,\mu}(r,\theta)|^2 r dr d\theta \tag{A.21}$$

A.1.3 Complete pressure field

The acoustic pressure $\widehat{p}$ can now be expressed using the eigenfunctions:

$$\widehat{p}(x,r,\theta,\omega) = \sum_{m\in\mathbb{Z}} \sum_{\mu\in\mathbb{N}} g_{m,\mu}(x,\omega)\, \Psi_{m,\mu}(r,\theta)\,. \tag{A.22}$$

The expression of $g_{m,\mu}$ can be derived by injecting eq. (A.22) into eq. (A.10). Using eq. (A.9) and the orthogonality properties of the eigenfunctions eventually shows that $g_{m,\mu}$ is the solution of eq. (A.10) with $\chi_1 = \chi_{m,\mu}$. This homogeneous second order differential equation with constant coefficients then admits solutions of the form:

$$g_{m,\mu}(x,\omega) = \mathcal{P}^{\pm}_{m,\mu}(\omega)\mathrm{e}^{ik^{\pm}_{x,m\mu}x}, \tag{A.23}$$

where $k^{\pm}_{x,m\mu}$ are the two solutions of the characteristic equation:

$$-\beta^2 k^{\pm 2}_{x,m\mu} - 2Mk_0 k^{\pm}_{x,m\mu} + k_0^2 - \chi^2_{m,\mu} = 0, \tag{A.24}$$

The reduced discriminant of this equation is expressed as:

$$\kappa^2_{m,\mu} = k_0^2 - \beta^2\chi^2_{m,\mu}, \tag{A.25}$$

which leads to the following expression for $k^{\pm}_{x,m\mu}$:

$$k^{\pm}_{x,m\mu} = \frac{-Mk_0 \mp \kappa_{m,\mu}}{\beta^2}. \tag{A.26}$$

$k^{\pm}_{x,m\mu}$ are the axial wave numbers of order (m,μ) that propagate upstream of the duct $(+)$ and downstream of the duct $(-)$ respectively. Depending on the sign of $\kappa^2_{m,\mu}$, $k^{\pm}_{x,m\mu}$ can be either real or complex, which will determine if the mode (m,μ) will be cut-on or cut-off. See section 1.4.2.2 for more details. Finally, the acoustic pressure field within the duct can be deduced by performing an inverse Fourier transform in time, which gives:

$$p(x,r,\theta,\omega) = \int_{-\infty}^{+\infty} \sum_{m\in\mathbb{Z}} \sum_{\mu\in\mathbb{N}} \mathcal{P}^{\pm}_{m,\mu}(\omega)\mathrm{e}^{ik^{\pm}_{x,m\mu}x}\Psi_{m,\mu}(r,\theta)\,e^{-i\omega t}d\omega. \tag{A.27}$$

A.2 Green's function for an infinite annular duct with a uniform axial flow

A.2.1 Inhomogeneous Helmholtz equation

Goldstein's acoustic analogy relies on the use of the Green's function for an infinite annular duct with a uniform axial flow, which is denoted G_{duct} in section 1.4.3.2. If $\mathbf{y} = (y, r_y, \theta_y)$ and τ denote the position and the emission time of the source, and $\mathbf{x} = (x, r_x, \theta_x)$ and t the position and the reception time of the observer, then $G_{duct}(\mathbf{x}, t|\mathbf{y}, \tau)$ satisfies:

$$\left[\Delta_y - \frac{1}{c_0^2}\frac{D^2}{Dt^2}\right] \quad G_{duct}(\mathbf{x}, t|\mathbf{y}, \tau) = -\delta(\mathbf{x}-\mathbf{y})\delta(t-\tau), \tag{A.28}$$

with the boundary conditions:

$$\frac{\partial G_{duct}}{\partial r} = 0, \quad \text{for } r = R_{hub} \text{ and } r = R_{casing}. \tag{A.29}$$

.

Δ_y is the Laplacian operator for the $\mathbf{y}$ coordinate. The Green's function $G_{duct}(\mathbf{x}, t|\mathbf{y}, \tau)$ depends on t and τ only in their combination $t' = \tau - t$ and is therefore written $G_{duct}(\mathbf{x}|\mathbf{y}, t')$. Its t'-Fourier transform can then be defined as:

$$\widehat{G}_{duct}(\mathbf{x}|\mathbf{y}, \omega) = \frac{1}{2\pi}\int_{-\infty}^{\infty} G_{duct}(\mathbf{x}|\mathbf{y}, t')\mathrm{e}^{\mathrm{i}\omega \mathrm{t}'}dt' \tag{A.30}$$

By performing a Fourier transform in time of the previous equations, $\widehat{G}_{duct}(\mathbf{x}|\mathbf{y},\omega)$ is eventually the solution of the inhomogeneous Helmholtz equation with an impulse source:

$$\left[\beta^2\frac{\partial^2}{\partial y^2}+\frac{\partial^2}{\partial r_y^2}+\frac{\partial}{r_y\partial r_y}+\frac{\partial^2}{r_y^2\partial\theta_y^2}+2iMk_0\frac{\partial}{\partial y}+k_0^2\right]\widehat{G}_{duct}(\mathbf{x}|\mathbf{y},\omega)=-\frac{\delta(\mathbf{x}-\mathbf{y})}{2\pi}, \qquad (A.31)$$

with the same boundary conditions as previously.

A.2.2 Equation solving

Similarly to what was performed for the duct modes, the separation of variables is used:

$$\widehat{G}_{duct}\left(\mathbf{x}|\mathbf{y},\omega\right)=g\left(\mathbf{x}|y,\omega\right)\Psi\left(r_y,\theta_y\right). \qquad (A.32)$$

Injecting this expression into the Helmholtz equation shows that Ψ is the solution of a Bessel equation. Once again, it can be shown that:

$$\Psi\left(r_y,\theta_y\right)=\sum_{m\in\mathbb{Z}}\sum_{\mu\in\mathbb{N}}E_{m,\mu}(r_y)\mathrm{e}^{im\theta_y}=\sum_{m\in\mathbb{Z}}\sum_{\mu\in\mathbb{N}}\Psi_{m,\mu}\left(r_y,\theta_y\right) \qquad (A.33)$$

The Green's function can then be decomposed on the base formed by the previously derived duct eigenfunctions:

$$\widehat{G}_{duct}\left(\mathbf{x}|\mathbf{y},\omega\right)=\sum_{m\in\mathbb{Z}}\sum_{\mu\in\mathbb{N}}g_{m,\mu}\left(\mathbf{x}|y,\omega\right)\Psi_{m,\mu}\left(r_y,\theta_y\right) \qquad (A.34)$$

Injecting this expression and taking into account that $\Psi_{m,\mu}$ is the solution of eq. (A.9) with $\chi_1=\chi_{m,\mu}$ eventually yields:

$$\sum_{m\in\mathbb{Z}}\sum_{\mu\in\mathbb{N}}\Psi_{m,\mu}\left(r_y,\theta_y\right)\left[\beta^2\frac{\partial^2}{\partial y^2}+2iMk_0\frac{\partial}{\partial y}+\left(k_0^2-\chi_{m,\mu}^2\right)\right]g_{m,\mu}\left(\mathbf{x}|y,\omega\right)=-\frac{\delta\left(\mathbf{x}-\mathbf{y}\right)}{2\pi} \qquad (A.35)$$

Multiplying this equation by $\Psi^*_{m,\mu}$, integrating over the duct section and using the property of orthogonality of the duct modes induce:

$$\left[\beta^2\frac{\partial^2}{\partial y^2}+2iMk_0\frac{\partial}{\partial y}+\left(k_0^2-\chi_{m,\mu}^2\right)\right]g_{m,\mu}\left(\mathbf{x}|y,\omega\right)=-\frac{\Psi^*_{m,\mu}\left(r_x,\theta_x\right)\delta\left(x-y\right)}{2\pi\Gamma_{m,\mu}} \qquad (A.36)$$

As the system is invariant to translation, $g_{m,\mu}\left(\mathbf{x}|y,\omega\right)$ can be expressed as a function of $e=x-y$ and is written $g_{m,\mu}\left(r_x,\theta_x|e,\omega\right)$. Injecting this into the previous equation leads to:

$$\left[\beta^2\frac{\partial^2}{\partial y^2}+2iMk_0\frac{\partial}{\partial y}+\left(k_0^2-\chi_{m,\mu}^2\right)\right]g_{m,\mu}\left(r_x,\theta_x|e,\omega\right)=-\frac{\Psi^*_{m,\mu}\left(r_x,\theta_x\right)\delta\left(e\right)}{2\pi\Gamma_{m,\mu}} \qquad (A.37)$$

The e-Fourier transform can be defined as:

$$\widehat{g}_{m,\mu}\left(r_x,\theta_x|k_x,\omega\right)=\frac{1}{2\pi}\int_{-\infty}^{\infty}g_{m,\mu}\left(r_x,\theta_x|e,\omega\right)\mathrm{e}^{\mathrm{ik_xe}}de. \qquad (A.38)$$

Applying it to eq. (A.37) yields:

$$\widehat{g}_{m,\mu}\left(r_x,\theta_x|k_x,\omega\right) = -\frac{\Psi^*_{m,\mu}\left(r_x,\theta_x\right)}{4\pi^2\Gamma_{m,\mu}\left[\beta^2\frac{\partial^2}{\partial y^2} + 2iMk_0\frac{\partial}{\partial y} + \left(k_0^2 - \chi^2_{m,\mu}\right)\right]}, \tag{A.39}$$

which can be rewritten as:

$$\widehat{g}_{m,\mu}\left(r_x,\theta_x|k_x,\omega\right) = -\frac{\Psi^*_{m,\mu}\left(r_x,\theta_x\right)}{8\pi^2\Gamma_{m,\mu}\kappa,\mu}\left[\frac{1}{k_x - k^+_{x,m\mu}} + \frac{1}{k_x - k^-_{x,m\mu}}\right], \tag{A.40}$$

where $k^{\pm}_{x,m\mu}$ is defined by eq. (A.26).
Applying the inverse e-Fourier transform in conjunction with the residue theorem then yields:

$$g_{m,\mu}\left(r_x,\theta_x|e,\omega\right) = -\frac{i\Psi^*_{m,\mu}\left(r_x,\theta_x\right)}{4\pi\Gamma_{m,\mu}\kappa,\mu} \times \begin{cases} \mathrm{e}^{ik^+_{x,m\mu}e} & e<0 \\ \mathrm{e}^{ik^-_{x,m\mu}e} & e>0 \end{cases} \tag{A.41}$$

The final expression of the Green's function G_{duct} can then be obtained by successively combining eqs. (A.33), (A.34) and (A.41), by reminding that $t' = t-\tau$ and that $e = x-y$, and by performing an inverse time Fourier transform:

$$G_{duct}\left(\mathbf{x},t|\mathbf{y},\tau\right) = \frac{i}{4\pi}\sum_{m=-\infty}^{+\infty}\sum_{\mu=0}^{+\infty}\frac{\Psi_{m,\mu}(r,\theta)\Psi^*_{m,\mu}\left(r_y,\theta_y\right)}{\Gamma_{m,\mu}} \times \int_{-\infty}^{+\infty}\frac{e^{-i\omega(t-\tau)+ik^{\pm}_{x,m\mu}(x-y)}}{\kappa_{m,\mu}}d\omega \tag{A.42}$$

APPENDIX B

Assessment of the impact of the OGV rescaling

In order to reduce the computational cost of the LES, the number of vanes has been reduced from 44 to 40, which made it possible to simulate a 1 rotor blade-2 stator vane configuration instead of a 5-11 configuration. This section is dedicated to the assessment of the impact of the OGV rescaling on the performance parameters, the pressure distribution on the vane, and on the RSI broadband noise.

B.1 Performance parameters

In both the baseline and the rescaled RANS simulations, the mass-flow rates are prescribed at the outlets, which implies that they match the bypass and the core experimental mass-flow rates. Tables B.1-B.3 show the fan pressure ratio, the stage pressure ratio and the stage isentropic efficiency, respectively. As expected, the OGV rescaling has a negligible impact on the performance parameters.

	Fan pressure ratio		
	Bypass	Core	Total
Baseline	1.106	1.098	1.105
Rescaled	1.105	1.097	1.104

Table B.1: Fan pressure ratios obtained from the RANS simulations at approach condition.

	Fan-OGV stage pressure ratio
Baseline	1.101
Rescaled	1.101

Table B.2: Fan-OGV stage pressure ratio obtained from the RANS simulations at approach condition.

	Fan-OGV stage isentropic efficiency (%)
Baseline	88.1
Rescaled	88.2

Table B.3: Fan-OGV stage isentropic efficiency obtained from the RANS simulations at approach condition.

B.2 Pressure coefficient

Figure B.1 shows the pressure coefficient C_p on the stator vane surface, for different radial positions. Negligible discrepancies can be observed at 95% stator span, close to the leading edge. On the rest of the surface, the C_p profiles on the baseline and on the rescaled geometries are almost identical.

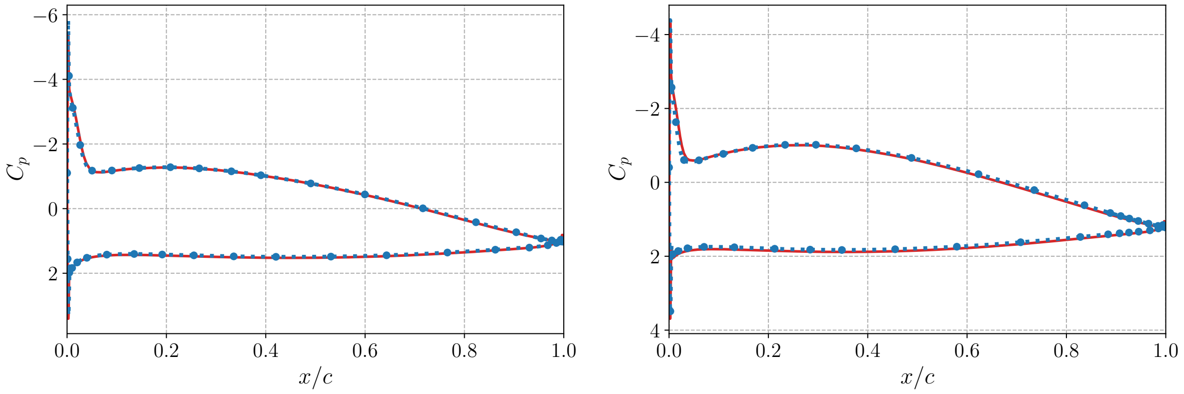

(a) 25% stator span.

(b) 50% stator span.

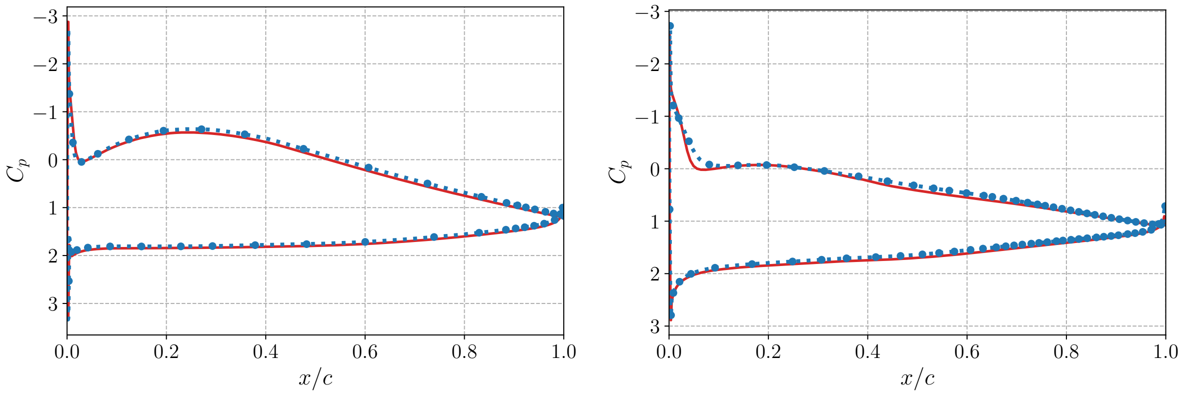

(c) 75% stator span.

(d) 95% stator span.

Figure B.1: Pressure coefficient on the stator vane surface at different stator radial positions.

B.2.1 Flow separations

Figure B.2 shows the mean friction coefficient C_f along with the streaklines on the vane suction side of both the baseline and the rescaled geometries. The zones where a flow separation occurs are almost identical from one simulation to the other.

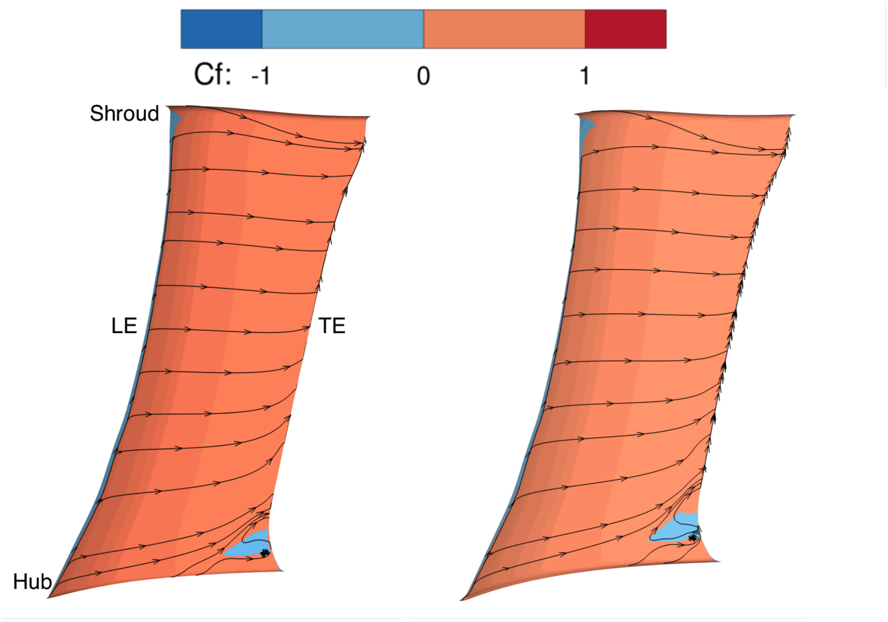

(a) Baseline.
(b) Rescaled.

Figure B.2: Mean friction coefficient and streaklines on the vane suction side.

B.2.2 RSI broadband noise predictions

In order to check the impact of the rescaling process on the radiated broadband RSI noise, predictions using both geometries have been performed using Hanson's model. Figure B.3 shows that the noise predictions using both geometries perfectly overlay over the entire studied frequency range, confirming that the rescaling process has only a negligible impact on the broadband RSI noise.

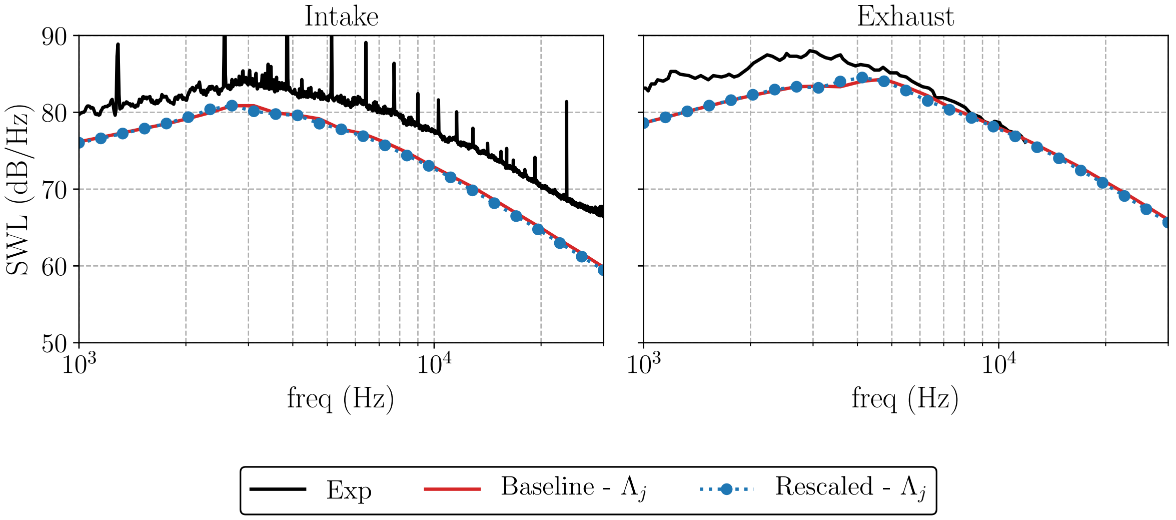

Figure B.3: Comparison of the broadband RSI noise radiated by both the baseline and the rescaled geometries. Predictions performed using Hanson's model.

APPENDIX C

LES statistics convergence

The plots to monitor the statistical convergence of both LES using Mockett *et al.*'s method are all gathered in this section.

C.1 LES1

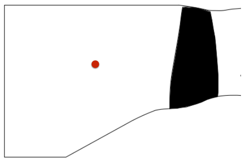

Probe 1.

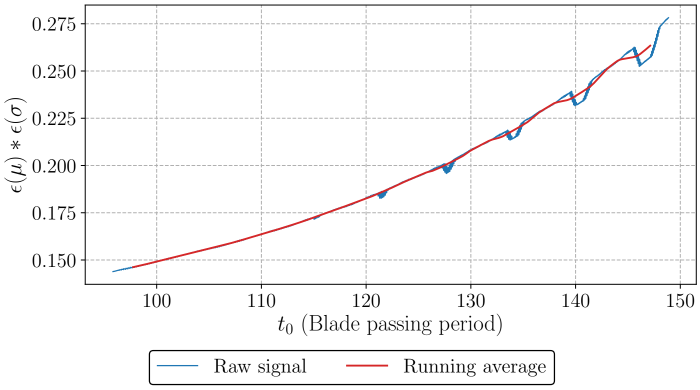

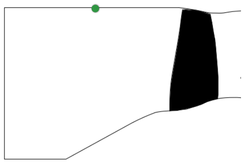

Probe 2.

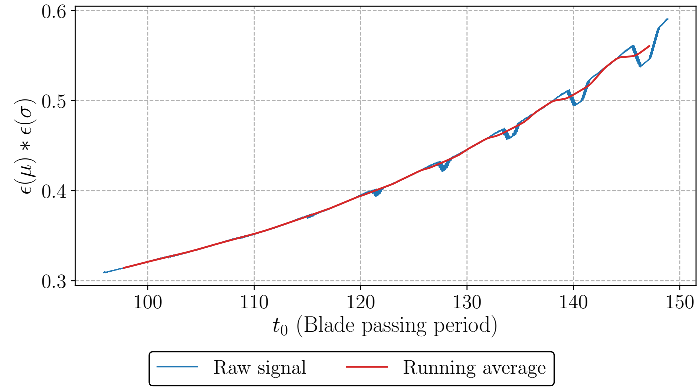

Figure C.1: Evolution of the product of the mean and standard deviation of the probe pressure signals following Mockett's methodology.

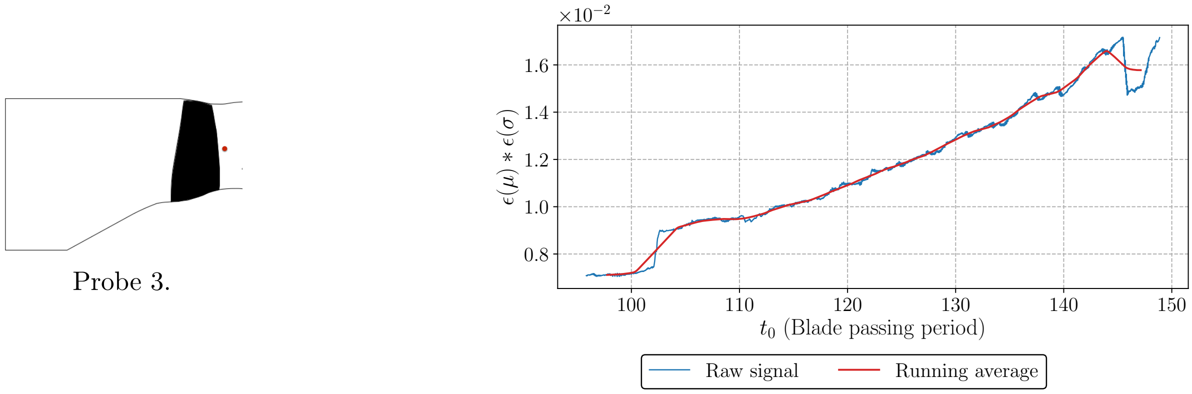

Probe 3.

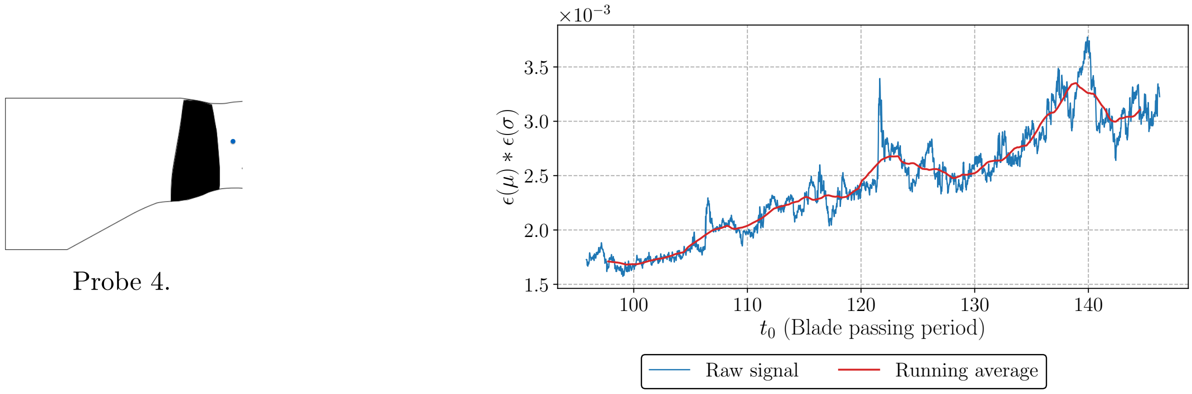

Probe 4.

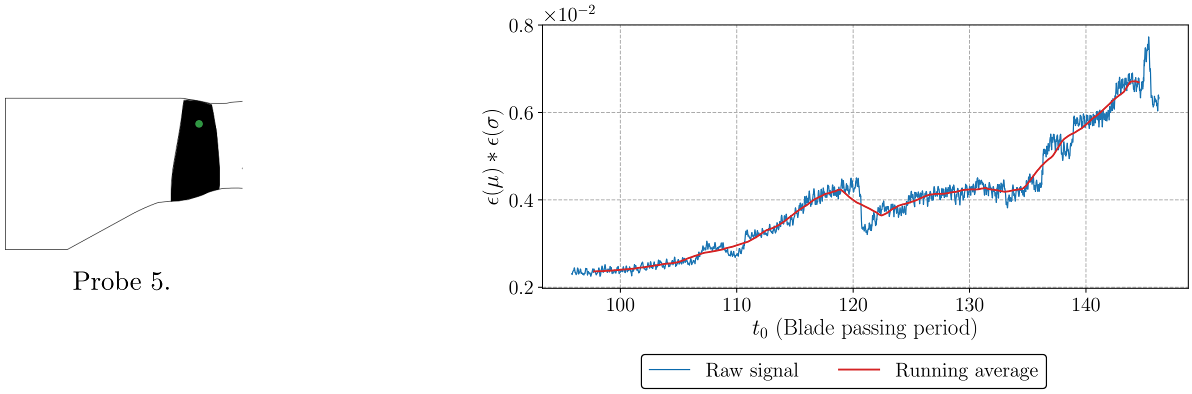

Probe 5.

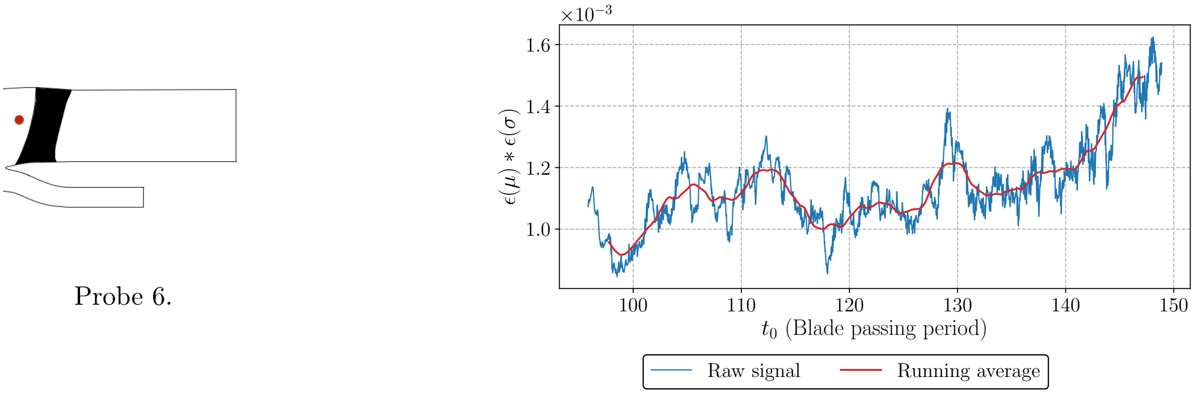

Probe 6.

Figure C.1: Evolution of the product of the mean and standard deviation of the probe pressure signals following Mockett's methodology.

C.2 LES2

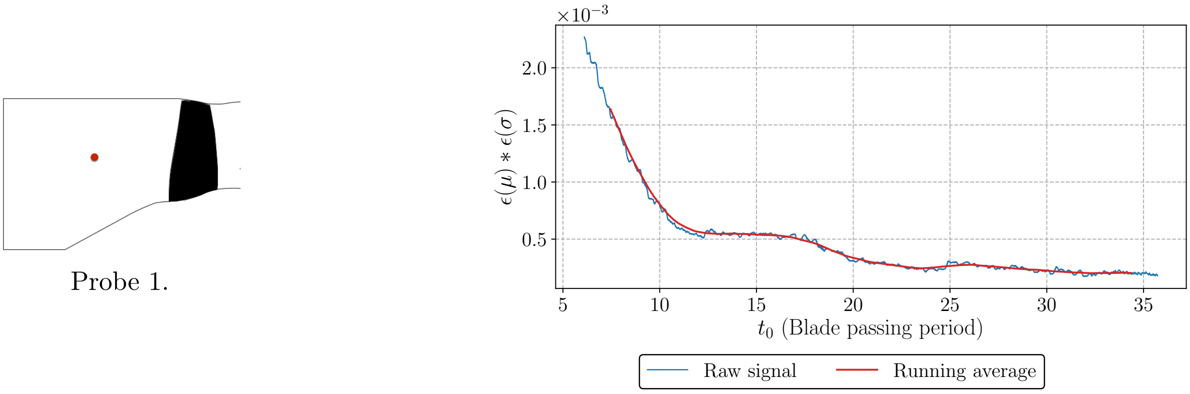

Probe 1.

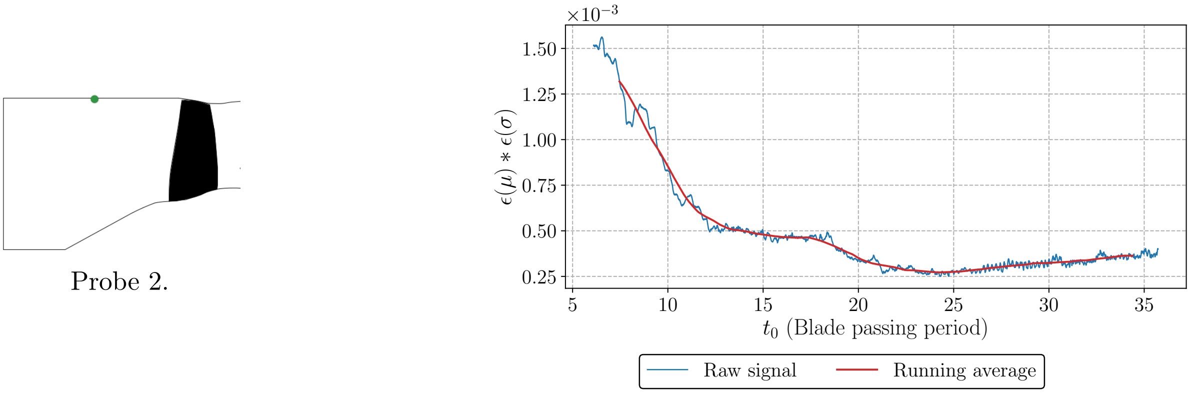

Probe 2.

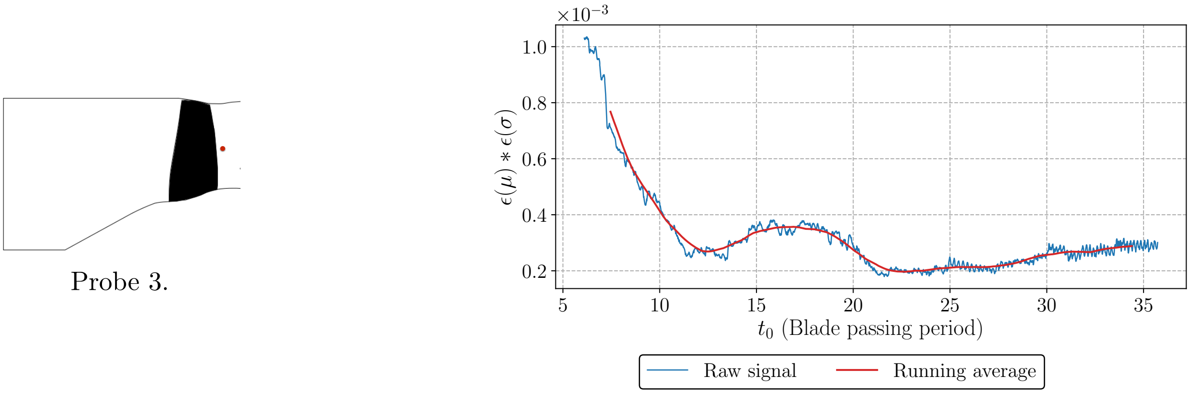

Probe 3.

Figure C.2: Evolution of the product of the mean and standard deviation of the probe pressure signals following Mockett's methodology.

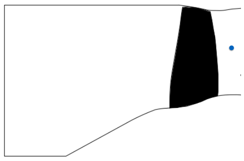

Probe 4.

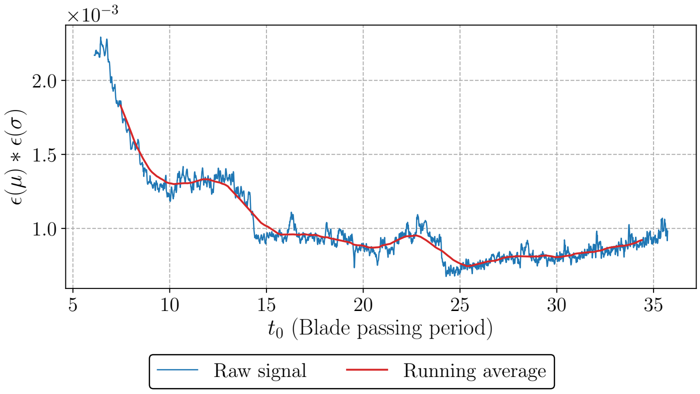

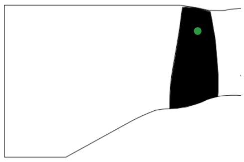

Probe 5.

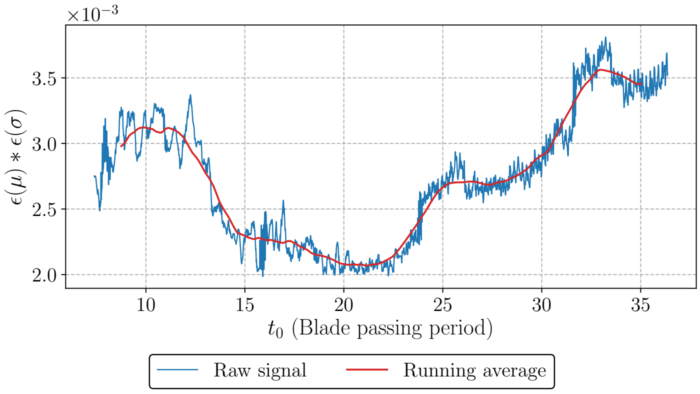

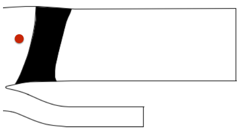

Probe 6.

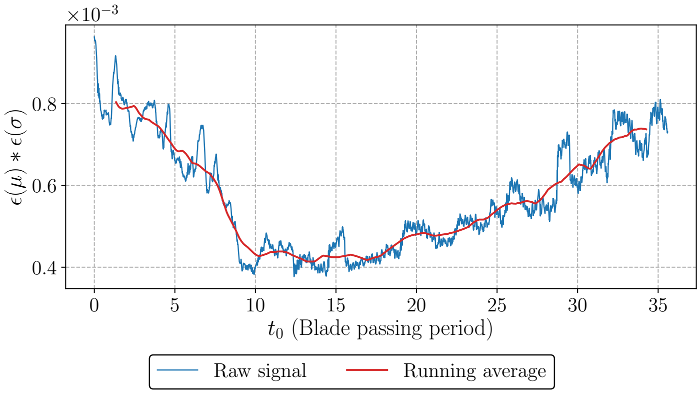

Figure C.2: Evolution of the product of the mean and standard deviation of the probe pressure signals following Mockett's methodology.

APPENDIX D

Boundary layer thickness

This section presents the process that has been used to estimate the boundary layer thickness in chapter 3.

D.1 Boundary layer thickness estimation methods

In the context of external flows, the determination of the outer edge of the boundary layer is usually achieved using techniques that start in the inviscid and undisturbed flow, and progressively approach the viscous layer based on a suitable criterion. Such an approach is however not well suited for turbomachine flows as the flow out of the boundary layer is usually significantly disturbed and can exhibit velocity profile inversions. To tackle this issue, several boundary layer thickness estimation processes based on criteria starting from the wall have been developed. The following sections present the three techniques that have been used in the present study.

D.1.1 Method based on the velocity gradient

Boundary layers are characterized by strong normal variations of the streamwise velocity profile, which can be both axial and radial or either one, while it remains almost constant outside of it. Methods based on the variations of the velocity profile have thus been developed to estimate the boundary layer thickness. Starting from the wall surface, let us consider two consecutive velocity profile points N and N-1, N-1 being closer to the wall. For these two points, if the following conditions are fulfilled:

$$| \left[\frac{\mathrm{d}u}{\mathrm{d}y}\right]_N | < \alpha \text{ and } \left| \left[\frac{\mathrm{d}u}{\mathrm{d}y}\right]_N - \left[\frac{\mathrm{d}u}{\mathrm{d}y}\right]_{N-1} \right| < \beta, \tag{D.1}$$

where α and β are user-defined constants, then the current point N is considered as the edge of the boundary layer. In the present case, $\alpha = 0.01$ and $\beta = 0.0001$.

D.1.2 Stock-Haase method

As suggested by Stock and Haase [229], the boundary layer thickness can be estimated using the diagnostic function:

$$F = y^a \left[\frac{\partial u}{\partial y}\right]^b, \tag{D.2}$$

resulting in the boundary layer thickness:

$$\delta = \epsilon y_{max} \tag{D.3}$$

where y_{max} is the wall distance for which $F = F_{max}$. The a, b, and ϵ constants for a turbulent boundary layer are then evaluated from Coles [230] velocity profiles such that:

$$\begin{aligned} F_{\text{turb}} &= y\left[\tfrac{\text{d}u}{\text{d}y}\right] \quad (a = b = 1) \\ \delta_{\text{turb}} &= 1.936 y_{\text{max}} \quad (\varepsilon = 1.936) \end{aligned} \tag{D.4}$$

D.1.3 Method based the on relative difference between the isentropic Mach number and the real Mach number

The isentropic Mach number M_{is} corresponds to the Mach number that would be observed without any losses in the flow, including those induced by the frictions on the walls, and is defined as follows:

$$M_{is} = \sqrt{\left(\left(\frac{p_0^{\text{freestream}}}{p}\right)^{\frac{\gamma-1}{\gamma}} - 1\right) \cdot \frac{2}{\gamma - 1}}. \tag{D.5}$$

Given that the flow outside of the boundary layer is assumed to be isentropic, the Mach number M profile in the boundary layer is expected to match the isentropic Mach number at the edge of the boundary layer, which corresponds to the point verifying:

$$\frac{|M_{is} - M|}{M_{is}} < K_{Mis}, \tag{D.6}$$

where $K_{Mis} = 0.01$ in the present case.

D.2 Computation of the boundary layer thickness

In order to compute the boundary layer thickness, the flow variables of interest are interpolated on the wall normal lines originating from each point of the considered surface. The three above methods are applied to estimate the boundary layer thickness and to obtain a mean thickness value δ_{num} that corresponds to an averaged value of the three estimates.

In the process of computing these boundary layer thicknesses, the momentum boundary layer thickness θ and the displacement thickness δ_d are also computed. Combining these variables, one can obtain another estimate of the boundary layer thickness:

$$\delta_g = \delta^I \left(\frac{\theta^I}{\delta_d^{*I}} H_1 + 1\right) \tag{D.7}$$

where the superscript I means that the incompressible formula is used, and H_1 is the mass flow shape factor computed with a correlation of Green [231]. The final value of the boundary layer thickness is the mean value of δ_{num} and δ_g.

APPENDIX E

Convergence study of the model of Ventres

This section is dedicated to the assessment of the number of points required to guarantee that Ventres' cascade response is converged. Figure E.1 shows the evolution of the SWL predicted by Ventres' model for various number of chordwise discretization points, using the RANS data from Nallasamy and Envia [13]. The increase in the number of points only affects the SWL at high frequencies for which only slight modifications can be observed. The 500-point discretization is the highest level of refinement that could be reached on the cluster used for the computation.

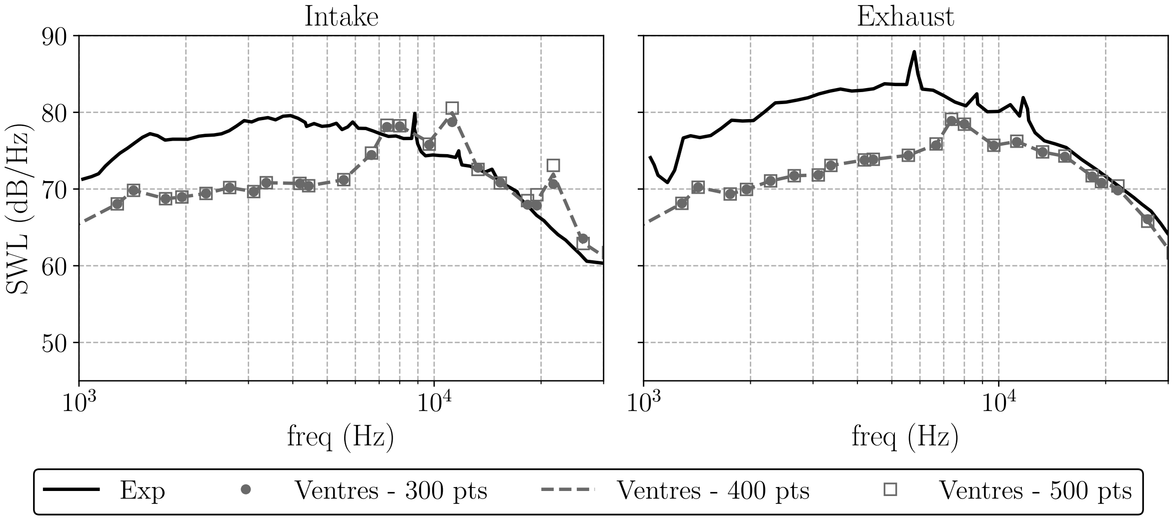

Figure E.1: Comparison of the SWL of the original Ventres model for different number of discretization points using the anisotropic spectrum of Nallasamy and Envia [13].

Figure E.2 shows the comparison between the most refined prediction using Ventres' model and the 2D model of Posson presented in section 5.2.2.2. The results from Nallasamy and Envia [13] are also plotted on the same figure. Even though they used an approach based on Ventres' model, the code has been significantly updated and is now called RSI (Rotor-Stator Interaction). The latest implementation of the code, however, is not available for our study. The discrepancies between their results and the Ventres implementation used in the present article illustrate the successive upgrades of the code. Indeed, in fig. E.2, it should be noted that the downstream and upstream predictions obtained with the 2D Posson model and the original model of Ventres are almost identical, ensuring the convergence of the original Ventres response. For the upstream SWL, however, a difference for a frequency at around 11 kHz can observed. This disparity may be due to the lack of discretization points required to compute the Ventres cascade response. However this isolated difference does not put the convergence of the cascade response into question since the predictions obtained from the two models overlay on the rest of the studied frequency range. The Ventres model cascade response is then considered reliable for this configuration when using 500 points.

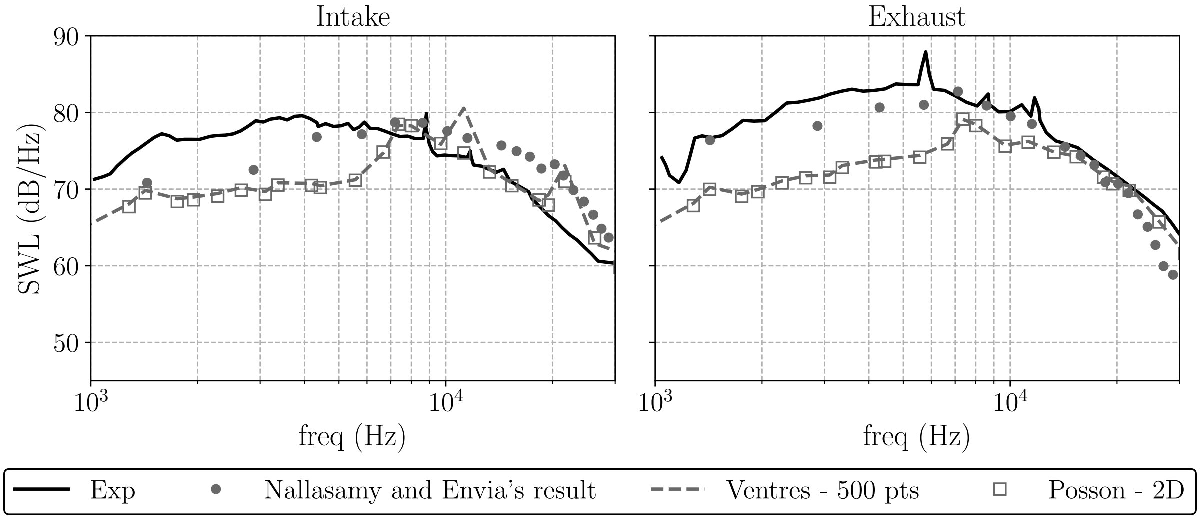

Figure E.2: Comparison of the SWL of the original Ventres model and the Ventres model with the 2D Posson response using the anisotropic spectrum of Nallasamy and Envia [13].

APPENDIX F

Wake model

As mentioned in section 5.2, the models used in the present work have been extended with additional developments from Nallasamy and Envia [13] which allow to separate the background flow from the wake flow in the model. This Section briefly presents the methodology developed by Nallasamy and Envia in [13].

Let us consider a radial slice as presented in fig. 1.10. Let $w(\vec{X}, r, t)$ denote the fluctuating component of the rotor wake velocity normal to the stator chord (*i.e.* the upwash) and $\left\langle w\left(\vec{X}, r_1, t\right) w^*\left(\vec{Y}, r_2, \tau\right)\right\rangle$ its correlation function in the rotating frame of reference. By performing a Fourier transform on this correlation function, we obtain the wavenumber frequency spectrum of the upwash velocity:

$$\left\langle \tilde{w}\left(\vec{k}, r_1, \omega\right) \tilde{w}^*\left(\vec{K}, r_2, v\right)\right\rangle = \int\int\int\int\int\int \left\langle w\left(\vec{X}, r_1, t\right) w^*\left(\vec{Y}, r_2, \tau\right)\right\rangle \mathrm{e}^{-\mathrm{i}(\vec{K}-\vec{k})\cdot\vec{D}} \times \mathrm{e}^{-\mathrm{i}\vec{k}\cdot\vec{X}+\mathrm{i}\vec{K}\cdot\vec{Y}+\mathrm{i}(\omega+(\Omega r_1 t)k_2)t-\mathrm{i}(v+(\Omega r_2 \tau)K_2)\tau}\mathrm{d}\vec{X}\mathrm{d}\vec{Y}\mathrm{d}t\mathrm{d}\tau, \tag{F.1}$$

where $\vec{D}$ is the distance between the reference rotor blade and the reference stator vane, and Ω is the rotor rotational speed.

Assuming that the turbulence is stationary, frozen and isotropic, the correlation of the upwash velocity can be approximated by the following relationship:

$$\left\langle w\left(\vec{X}, r_1, t\right) w^*\left(\vec{Y}, r_2, \tau\right)\right\rangle \approx \left\langle w\left(\vec{X}-\vec{W}t, r_1\right) w^*\left(\vec{Y}-\vec{W}\tau, r_2\right)\right\rangle, \tag{F.2}$$

with $W = \Omega\overline{r}$ and $\overline{r} = (r_2 + r_1)/2$. Nallasamy and Envia then proposed to use the following equation to model the upwash velocity:

$$w(\vec{X}-\vec{W}t, r) = F(\vec{X}\cdot\hat{n}, r)g(\vec{X}-\vec{W}t, r) \tag{F.3}$$

with $\hat{n}$ the stator chord normal vector and F the azimutal distribution of the rms turbulence intensity. Assuming a small turbulence radial length scale, F and g are defined in order to have:

$$\begin{aligned}&\left\langle w\left(\vec{X}-\vec{W}t,r_1\right)w^*\left(\vec{Y}-\vec{W}\tau,r_2\right)\right\rangle = F(\vec{X}\cdot\hat{n},\overline{r})F^*(\vec{Y}\cdot\hat{n},\overline{r})\Phi(\vec{X}-\vec{Y}-\vec{W}(t-\tau),\Delta r)\\&\Phi(\vec{X}-\vec{Y}-\vec{W}(t-\tau),\Delta r) = \left\langle g\left(\vec{X}-\vec{W}t,r_1\right)g^*\left(\vec{Y}-\vec{W}\tau,r_2\right)\right\rangle\end{aligned}, \tag{F.4}$$

with $\Delta r = r_2 - r_1$ and Φ the normalized correlation (i.e. $\Phi(0,\overline{r}) \equiv 1$). Nallasamy and Envia then assumed that F could be described with a Gaussian function complying with the periodicity requirements imposed by the configuration, leading to the following form:

$$F(\vec{X}\cdot\hat{n},\overline{r}) = u'_b + \frac{N_B L_w u'_w}{2\pi\overline{r}}\sum_{m=-\infty}^{\infty} e^{\frac{-1}{4\pi}\left(\frac{mN_B L_w}{\overline{r}}\right)^2} e^{\left(\frac{imN_B}{\overline{r}\cos\chi}\vec{X}\cdot\hat{n}b\right)} \tag{F.5}$$

with u'_b and u'_w the background and wake turbulence intensities respectively, N_B the number of rotor blades, L_w the width of the Gaussian function and χ the stagger angle of the rotor blade. Φ is given by the following equation:

$$\Phi(\vec{X},\Delta r) = \frac{1}{2\pi\overline{r}}\sum_{s=-\infty}^{\infty}\phi\left(X_1,\Delta r\right)\mathrm{e}^{\mathrm{i}sX_2/\overline{r}}, \tag{F.6}$$

ensuring the periodicity imposed by the configuration.

Noting $\vec{U} = \vec{W} - (\Omega\overline{r})\vec{y_d}$, substituting eqs. (F.5) and (F.6) in eq. (F.1), and after some algebra, the wavenumber frequency spectrum of the upwash velocity can be written as follows:

$$\begin{aligned}\left\langle\tilde{w}(\vec{k},\overline{r},\omega)\tilde{w}^*(\vec{K},\overline{r},v)\right\rangle = &\underbrace{\left\langle\tilde{w}(\vec{k},\overline{r},\omega)\tilde{w}^*(\vec{K},\overline{r},v)\right\rangle_1}_{\text{wake turbulence auto-correlation}}\\&+\underbrace{\left\langle\tilde{w}(\vec{k},\overline{r},\omega)\tilde{w}^*(\vec{K},\overline{r},v)\right\rangle_2}_{\text{wake/background turbulence cross-correlation}}\\&+\underbrace{\left\langle\tilde{w}(\vec{k},\overline{r},\omega)\tilde{w}^*(\vec{K},\overline{r},v)\right\rangle_3}_{\text{background turbulence auto-correlation}}\end{aligned}, \tag{F.7}$$

with:

$$\begin{aligned}\left\langle\tilde{w}(\vec{k},\overline{r},\omega)\tilde{w}^*(\vec{K},\overline{r},v)\right\rangle_1 = &\frac{(2\pi)^2\left(N_B L_w u'_w\right)^2}{\overline{r}^3}\delta(\omega-\vec{k}\cdot\vec{U})\\&\times\sum_{m=-\infty}^{\infty}\sum_{\ell=-\infty}^{\infty}\sum_{s=-\infty}^{\infty}\mathrm{e}^{-\frac{1}{4\pi}\left(\frac{mN_B L_w}{\overline{r}}\right)^2}\mathrm{e}^{-\frac{1}{4\pi}\left(\frac{\ell N_B L_W}{\overline{r}}\right)^2}\\&\times\mathrm{e}^{\mathrm{i}\left(\frac{(m-\ell)N_B}{\overline{r}\cos\chi}\right)\vec{D}\cdot\hat{n}}\tilde{\phi}\left(\vec{k}-\frac{mN_B}{\overline{r}\cos\chi}n_1,\Delta r\right)\delta\left((\vec{K}-\vec{k})+\frac{(m-\ell)N_B}{\overline{r}\cos\chi}\hat{n}\right)\\&\times\delta\left(k_2-\frac{(mN_B+s)}{\overline{r}}\right)\delta\left(v-\omega-\Omega(m-\ell)N_B\right),\end{aligned} \tag{F.8}$$

$$
\begin{aligned}
\left\langle \tilde{w}(\vec{k},\overline{r},\omega)\tilde{w}^*(\vec{K},\overline{r},v)\right\rangle_2 = {} & \frac{(2\pi)^3 N_B L_w u'_b u'_w}{\overline{r}^2}\delta(\omega-\vec{k}\cdot\vec{U})\sum_{m=-\infty}^{\infty}\sum_{s=-\infty}^{\infty}\mathrm{e}^{-\frac{1}{4\pi}\left(\frac{mN_B L_w}{r}\right)^2} \\
& \times\left\{\mathrm{e}^{\mathrm{i}\left(\frac{mN_B}{\overline{r}\cos x}\right)\vec{D}\cdot\hat{n}}\tilde{\phi}\left(\vec{k}-\frac{mN_B}{\overline{r}\cos\chi}n_1,\Delta r\right)\delta\left((\vec{K}-\vec{k})+\frac{mN_B}{\overline{r}\cos\chi}\hat{n}\right)\right. \\
& \times\delta\left(k_2-\frac{(mN_B+s)}{\overline{r}}\right)+\mathrm{e}^{-\mathrm{i}\left(\frac{mN_B}{\overline{r}\cos\chi}\right)\vec{D}\cdot\hat{n}}\tilde{\phi}(\vec{k},\overline{r}) \\
& \left.\times\delta\left((\vec{K}-\vec{k})-\frac{mN_B}{\overline{r}\cos\chi}\hat{n}\right)\delta\left(k_2-\frac{s}{\overline{r}}\right)\right\}\delta\left(v-\omega-\Omega mN_B\right),
\end{aligned}
\tag{F.9}
$$

and

$$
\begin{aligned}
\left\langle \tilde{w}(\vec{k},\overline{r},\omega)\tilde{w}^*(\vec{K},\overline{r},v)\right\rangle_3 = {} & \frac{(2\pi)^4 u'^2_b}{\overline{r}}\delta(\omega-\vec{k}\cdot\vec{U}) \\
& \times\sum_{s=-\infty}^{\infty}\tilde{\phi}(\vec{k},\Delta r)\delta(\vec{K}-\vec{k})\delta\left(k_2-\frac{s}{\overline{r}}\right)\delta(v-\omega)
\end{aligned}
\tag{F.10}
$$

$\tilde{\phi}$ being the Fourier transform of ϕ.

APPENDIX G

Turbulence models

As mentioned in section 5.2.2.3, the use of turbulence models is compulsory to compute the upwash velocity cross-correlation function. This section presents the different models used in the present work.

G.1 Isotropic turbulence models

G.1.1 Liepmann's turbulence model

Locally isotropic homogeneous turbulence can be modeled using Liepmann's spectrum. A convenient way to compute the upwash turbulence spectrum Φ_{ww} is to express it in the cascade reference frame as detailed in [46]. In this reference frame, the upwash turbulence spectrum divided by the turbulence intensity is:

$$\Phi_{ww} = \Phi_{2,2} = \Phi_{ww}^{\mathrm{Liep}}\left(\mathbf{k}_c\right) = \frac{2\Lambda^5}{\pi^2}\frac{k_{x_c}^2 + k_{z_c}^2}{(1+\Lambda^2 k_s^2)^3} \tag{G.1}$$

where $k_s^2 = k_{x_c}^2 + k_{y_c}^2 + k_{z_c}^2$.

G.1.2 von Karman's turbulence model

Similarly, von Karman's spectrum for the upwash velocity in the cascade reference frame, as detailed in [218], is:

$$\Phi_{ww}^{VK}\left(\mathbf{k}_c\right) = \frac{55\Gamma(5/6)}{36\pi^{3/2}\Gamma(1/3)k_e^3}\frac{k_{x_c}^2 + k_{z_c}^2}{\left[1+\left(\frac{k_s}{k_e}\right)^2\right]^{17/6}} \tag{G.2}$$

where $k_e = \frac{\sqrt{\pi}\Gamma(5/6)}{\Lambda\Gamma(1/3)}$ and $\Gamma()$ is the Gamma function.

G.2 Anisotropic turbulence models

G.2.1 Axisymmetric turbulence model

The axisymmetric model used in the present work has been developed by Kerschen and Gliebe [223]. The following equation defines the three-dimensional cross-spectrum of the i and j components of the turbulence velocity in Cartesian coordinates:

$$\Phi_{ij}(\mathbf{k}) = \left[k^2\delta_{i,j} - k_ik_j\right]F + \left[\left(k^2 - (\mathbf{k}\cdot\lambda)^2\right)\delta_{i,j} - k_ik_j - k^2\lambda_i\lambda_j + \mathbf{k}\cdot\lambda\left(\lambda_ik_j + \lambda_jk_i\right)\right]G \quad \text{(G.3)}$$

where

$$F = \frac{F_0}{\left(1 + l_a^2k_a^2 + l_t^2k_t^2\right)^3}, \quad F_0 = \frac{2u_a^2l_al_t^4}{\pi^2}, \quad G = BF \quad \text{and} \quad B = \frac{2u_t^2}{u_a^2} - \frac{l_t^2}{l_a^2} - 1. \quad \text{(G.4)}$$

λ is a unit vector in the direction of the symmetry axis. k_a is the wavenumber in the direction of the symmetry whereas k_{ty} and k_{tz} are the wavenumbers in the transverse directions which define the magnitude of the transverse wavenumber $k_t = \sqrt{k_{ty}^2 + k_{tz}^2}$. u_a and u_t correspond to the root mean square values of the velocity fluctuations along the axis of symmetry and in the transverse direction respectively. The integral lengthscales l_a and l_t are correspondingly defined along the axis of symmetry and in the transverse direction. These variables must comply with the following constraint:

$$2\frac{u_t^2}{u_a^2} \geq \frac{l_t^2}{l_a^2}.$$

Equation (G.3) corresponds to the spectrum in Cartesian coordinates and cannot be directly used to compute the upwash velocity cross-correlation. To do so, a change of reference frame from the duct reference frame to the cascade reference frame needs to be performed. This is out of the scope of this article but a detailed calculation of the equation of the upwash cross-correlation (recalled in eq. (G.5)) has been performed by Posson *et al.* [46].

$$\Phi_{ww}\left(\mathbf{k}_c\right) = \left[k_{x_c}^2 + k_{z_c}^2 + B\left(\tilde{\mathrm{Q}}_{31}k_{x_c} - \tilde{\mathrm{Q}}_{11}k_{z_c}\right)^2\right]F, \quad \text{(G.5)}$$

where $\tilde{\mathbf{Q}}$ is the transformation matrix from the duct reference frame to the cascade reference frame.

G.2.2 Ventres' turbulence model

In the original implementation of Ventres' model, the turbulence spectrum only takes the background turbulence into account. It has then been enhanced by Nallasamy and Envia by splitting the impinging flow into a background and a wake contribution.

In this section, the original spectrum of Ventres is briefly presented to emphasize its inherent anisotropic construction. The original spectrum defines the velocity cross-correlation as a product of three Gaussian correlation functions, each of them depending only on one coordinate in the duct reference frame:

$$\phi\left(x_c, y_c, \Delta r\right) = \phi_{xc}\left(x_c/\Lambda_{xc}\right)\phi_{yc}\left(y_c/\Lambda_{yc}\right)\phi_r\left(\Delta r/\Lambda_r\right), \quad \text{(G.6)}$$

where Λ_i is the integral length scale in each direction. As pointed out by Grace *et al.* [55], eq. (G.6) defines an anisotropic turbulence because of its multiplying form. The correlation functions ϕ being Gaussian functions, the turbulence spectral density which corresponds to the double Fourier transform of eq. (G.6) in the (x_c, y_c) plan, is defined as:

$$\phi_{ww}(\mathbf{k_c}, \Delta r) = \Lambda_{xc}\Lambda_{yc}\hat{\phi}_{xc}\left(k_{xc}\Lambda_{xc}\right)\hat{\phi}_{yc}\left(k_{yc}\Lambda_{yc}\right)\phi_r\left(\Delta r/\Lambda_r\right), \tag{G.7}$$

where $\mathbf{k_c} = (k_{xc}, k_{yc}, 0)$ is the wave number in the (x_c, y_c) plane. This model also assumes that the radial integral length scale is small, leading to:

$$\int_{-L_r}^{+L_r} \phi_r\left(\Delta r/\Lambda_r\right) \mathrm{d}\Delta r \approx \int_{-\infty}^{+\infty} \phi_r\left(\Delta r/\Lambda_r\right) \mathrm{d}\Delta r = \Lambda_r \tag{G.8}$$

where $L_r = l_r/2$ and l_r is the radial correlation length.

The spectrum defined by eqs. (G.7) and (G.8) does not depend on the radial wave number, which confirms it is a 2D model. The enhancements added by Nallasamy and Envia, which are included in the implementation used in the present work, are detailed in [13].

Bibliography

[1] T. Nodé-Langlois, "Aeroengine-airframe aeroacoustic integration and installation effects," *VKI Lecture Series*, 2014.

[2] https://www.geaviation.com/commercial/engines/ge9x-commercial-aircraft-engine.

[3] M. J. Smith, *Aircraft noise.* No. 3, Cambridge University Press, 2004.

[4] J. Huber and S. Illa, "Jet noise assessment and sensitivity at aircraft level," in *13th AIAA/CEAS Aeroacoustics Conference (28th AIAA Aeroacoustics Conference)*, p. 3728, 2007.

[5] H. H. Hubbard, "Aeroacoustics of flight vehicles: Theory and practice. volume 1. noise sources, chapitre 3 : Turbomachinery noise," Tech. Rep. WRDC-TR-90-3052, NASA Langley Research Center, 1991.

[6] M. Leitner, M. Zippel, and S. Staudacher, *Interaction of Tip Leakage Flow with Incoming Flow in a Compressor Cascade Exceeding the Stability Limit.* Deutsche Gesellschaft für Luft-und Raumfahrt-Lilienthal-Oberth eV, 2017.

[7] C. Hirsch, *Numerical computation of internal and external flows: The fundamentals of computational fluid dynamics.* Elsevier, 2007.

[8] P. Tucker, "Computation of unsteady turbomachinery flows: Part 2—LES and hybrids," *Progress in Aerospace Sciences*, vol. 47, no. 7, pp. 546–569, 2011.

[9] P. Sagaut, *Large eddy simulation for incompressible flows: an introduction.* Springer Science & Business Media, 2006.

[10] M. Daroukh, *Effects of distortion on modern turbofan tonal noise.* PhD thesis, 2017.

[11] J. De Laborderie, *Approches analytiques et numériques pour la prédiction du bruit tonal et large bande de soufflantes de turboréacteurs.* PhD thesis, 2013.

[12] H. Posson, M. Roger, and S. Moreau, "On a uniformly valid analytical rectilinear cascade response function," *Journal of Fluid Mechanics*, vol. 663, pp. 22–52, 2010.

[13] M. Nallasamy and E. Envia, "Computation of rotor wake turbulence noise," *Journal of Sound and Vibration*, vol. 282, no. 3-5, pp. 649–678, 2005.

[14] U. Piomelli, “Large eddy simulations in 2030 and beyond,” *Philosophical Transactions of the Royal Society A: Mathematical, Physical and Engineering Sciences*, vol. 372, no. 2022, 2014.

[15] C. Wagner, T. Hüttl, and P. Sagaut, “Large-eddy simulation for acoustics,” *Large-Eddy Simulation for Acoustics*, vol. 9780521871, pp. 1–441, 2007.

[16] M. J. Lighthill, “On sound generated aerodynamically i. general theory,” *Proceedings of the Royal Society of London. Series A. Mathematical and Physical Sciences*, vol. 211, no. 1107, pp. 564–587, 1952.

[17] M. J. Lighthill, “On sound generated aerodynamically ii. turbulence as a source of sound,” *Proceedings of the Royal Society of London. Series A. Mathematical and Physical Sciences*, vol. 222, no. 1148, pp. 1–32, 1954.

[18] N. Facts, “Making future commercial aircraft quieter,” *NASA Lewis Research Center, FS-1997-07*, vol. 3, 1999.

[19] E. Envia, A. G. Wilson, and D. L. Huff, “Fan noise: a challenge to CAA,” *International Journal of Computational Fluid Dynamics*, vol. 18, no. 6, pp. 471–480, 2004.

[20] N. Peake and A. B. Parry, “Modern challenges facing turbomachinery aeroacoustics,” *Annual Review of Fluid Mechanics*, vol. 44, pp. 227–248, 2012.

[21] S. L. Dixon and C. Hall, *Fluid Mechanics and thermodynamics of turbomachinery*. Butterworth-Heinemann, 2013.

[22] J. E. Ffowcs Williams and D. L. Hawkings, “Sound generation by turbulence and surfaces in arbitrary motion,” *Philosophical Transactions of the Royal Society of London. Series A, Mathematical and Physical Sciences*, vol. 264, no. 1151, pp. 321–342, 1969.

[23] R. K. Amiet, “Noise due to turbulent flow past a trailing edge,” *Journal of Sound and Vibration*, vol. 47, no. 3, pp. 387–393, 1976.

[24] J. F. Williams and L. Hall, “Aerodynamic sound generation by turbulent flow in the vicinity of a scattering half plane,” *Journal of Fluid Mechanics*, vol. 40, no. 4, pp. 657–670, 1970.

[25] M. S. Howe, “A review of the theory of trailing edge noise,” *Journal of Sound and Vibration*, vol. 61, no. 3, pp. 437–465, 1978.

[26] M. Roger and S. Moreau, “Back-scattering correction and further extensions of amiet’s trailing-edge noise model. part 1: theory,” *Journal of Sound and Vibration*, vol. 286, no. 3, pp. 477–506, 2005.

[27] S. Moreau and M. Roger, “Back-scattering correction and further extensions of amiet’s trailing-edge noise model. part ii: Application,” *Journal of Sound and Vibration*, vol. 323, no. 1-2, pp. 397–425, 2009.

[28] M. Roger and S. Moreau, “Extensions and limitations of analytical airfoil broadband noise models,” *International Journal of Aeroacoustics*, vol. 9, no. 3, pp. 273–305, 2010.

[29] S. Moreau and M. Roger, “Competing broadband noise mechanisms in low-speed axial fans,” *AIAA journal*, vol. 45, no. 1, pp. 48–57, 2007.

[30] B. Greschner, J. Grilliat, M. C. Jacob, and F. Thiele, “Measurements and wall modeled les simulation of trailing edge noise caused by a turbulent boundary layer,” *International Journal of Aeroacoustics*, vol. 9, no. 3, pp. 329–355, 2010.

[31] B. de Gouville, “Calcul du bruit á large bande d’un rotor caréné dûa la turbulence incidente,” *These de doctorat, Ecole Centrale de Lyon*, 1998.

[32] E. Envia, “Fan noise source diagnostics test-vane unsteady pressure results,” in *8th AIAA/CEAS Aeroacoustics Conference & Exhibit*, no. 2002-2430, (Breckenridge, Colorado), 2002.

[33] C. Hughes, “Aerodynamic performance of scale-model turbofan outlet guide vanes designed for low noise,” in *40th AIAA Aerospace Sciences Meeting & Exhibit*, no. 2002-0374, (Reno, NV, U.S.A.), 2002.

[34] C. Hughes, R. Jeracki, R. Woodward, and C. Miller, “Fan noise source diagnostic test-rotor alone aerodynamic performance results,” in *8th AIAA/CEAS Aeroacoustics Conference & Exhibit*, no. 2002-2426, (Breckenridge, Colorado), 2002.

[35] G. Podboy, M. Krupar, S. Helland, and C. Hughes, “Steady and unsteady flow field measurements within a NASA 22 inch fan model,” in *40th AIAA Aerospace Sciences Meeting & Exhibit*, no. 2002-1033, (Reno, NV, U.S.A.), 2002.

[36] G. Podboy, M. Krupar, C. Hughes, and R. Woodward, “Fan noise source diagnostic test-LDV measured flow field results,” in *8th AIAA/CEAS Aeroacoustics Conference & Exhibit*, no. 2002-2431, (Breckenridge, Colorado), 2002.

[37] R. Woodward, C. Hughes, R. Jeracki, and C. Miller, “Fan noise source diagnostic test–far-field acoustic results,” in *8th AIAA/CEAS Aeroacoustics Conference & Exhibit*, no. 2002-2427, (Breckenridge, Colorado), 2002.

[38] R. K. Meyer, S. Hakansson, W. Hage, and L. Enghardt, “Instantaneous flow field measurements in the interstage section between a fan and the outlet guiding vanes at different axial positions,” in *13 th European Conference on Turbomachinery Fluid dynamics & Thermodynamics*, 2019.

[39] M. Behn and U. Tapken, “Investigation of sound generation and transmission effects through the ACAT1 fan stage using compressed sensing-based mode analysis,” in *25th AIAA/CEAS Aeroacoustics Conference*, no. 2019-2502, (Delft, The Netherlands), 2019.

[40] U. Tapken, M. Behn, M. Spitalny, and B. Pardowitz, “Radial mode breakdown of the ACAT1 fan broadband noise generation in the bypass duct using a sparse sensor array,” in *25th AIAA/CEAS Aeroacoustics Conference*, no. 2019-2525, (Delft, The Netherlands), 2019.

[41] H. Brouwer and P. Sijtsma, “Phased array beamforming to identify broadband noise sources in the interstage section of a turbofan engine,” in *25th AIAA/CEAS Aeroacoustics Conference*, no. 2019-2669, (Delft, The Netherlands), 2019.

[42] M. Michard, M. Jacob, and N. Grosjean, “An experimental characterization of the flow past an airfoil in the wake of a circular rod,” in *ASME 2002 Joint US-European Fluids Engineering Division Conference*, pp. 1143–1149, American Society of Mechanical Engineers Digital Collection, 2002.

[43] T. Leonard, M. Sanjose, S. Moreau, and F. Duchaine, “Large Eddy Simulation of a scale-model turbofan for fan noise source diagnostic,” No. 2016-3000, (Lyon, France), 2016.

[44] C. Pérez Arroyo, T. Leonard, M. Sanjosé, S. Moreau, and F. Duchaine, “Large eddy simulation of a scale-model turbofan for fan noise source diagnostic,” *Journal of Sound and Vibration*, vol. 445, pp. 64–76, 2019.

[45] C. Ventres, M. Theobald, and W. Mark, “Turbofan noise generation. volume 1: Analysis,” Tech. Rep. NASA-CR-167952, NASA, 1982.

[46] H. Posson, S. Moreau, and M. Roger, “Broadband noise prediction of fan outlet guide vane using a cascade response function,” *Journal of Sound and Vibration*, vol. 330, no. 25, pp. 6153–6183, 2011.

[47] B. François, S. Bouley, M. Roger, and S. Moreau, “Analytical models based on a mode-matching technique for turbulence impingement noise on axial-flow outlet guide vanes,” in *22nd AIAA/CEAS Aeroacoustics Conference*, no. 2016-2947, (Lyon, France), 2016.

[48] H. Posson, S. Moreau, and M. Roger, “On the use of a uniformly valid analytical cascade response function for fan broadband noise predictions,” *Journal of Sound and Vibration*, vol. 329, no. 18, pp. 3721–3743, 2010.

[49] D. B. Hanson, “Theory for broadband noise of rotor and stator cascades with inhomogeneous inflow turbulence including effects of lean and sweep,” Tech. Rep. CR-2001-210762, NASA, 2001.

[50] D. Lewis, S. Moreau, and M. C. Jacob, “On the use of RANS-informed analytical models to perform broadband rotor-stator interaction noise predictions,” in *25th AIAA/CEAS Aeroacoustics Conference*, no. 2019-2667, (Delft, The Netherlands), 2019.

[51] A. Cader, C. Polacsek, T. Le Garrec, R. Barrier, F. Benjamin, and M. C. Jacob, “Numerical prediction of rotor-stator interaction noise using 3D CAA with synthetic turbulence injection,” in *2018 AIAA/CEAS Aeroacoustics Conference*, (Reston, Virginia), pp. 1–17, American Institute of Aeronautics and Astronautics, jun 2018.

[52] G. Reboul, A. Cader, C. Polacsek, T. Le Garrec, R. Barrier, and N. Ben Nasr, “CAA prediction of rotor-stator interaction using synthetic turbulence: application to a low-noise serrated ogv,” in *23rd AIAA/CEAS Aeroacoustics Conference*, p. 3714, 2017.

[53] C. A. Kissner, S. Guérin, and M. Behn, “Assessment of a 2D synthetic turbulence method for predicting the ACAT1 fan’s broadband noise,” in *25th AIAA/CEAS Aeroacoustics Conference*, no. 2019-2501, (Delft, The Netherlands), 2019.

[54] S. Guerin, C. A. Kissner, B. Kajasa, R. Jaron, M. Behn, B. Pardowitz, U. Tapken, S. Hakansson, R. Meyer, and L. Enghardt, “Noise prediction of the ACAT1 fan with a rans-informed analytical method: success and challenge,” in *25th AIAA/CEAS Aeroacoustics Conference*, no. 2019-2500, (Delft, The Netherlands), 2019.

[55] S. Grace, A. Wixom, J. Winkler, D. Sondak, and M. Logue, “Fan broadband interaction noise modeling,” in *18th AIAA/CEAS Aeroacoustics Conference (33rd AIAA Aeroacoustics Conference)*, no. 2012-2269, (Colorado Springs, CO), 2012.

[56] S. Grace, I. Gonzalez-Martino, and D. Casalino, “Analysis of fan-stage gap-flow data to inform simulation of fan broadband noise,” *Philosophical Transactions of the Royal Society A*, vol. 377, no. 2159, p. 20190080, 2019.

[57] C. Polacsek, V. Clair, T. Le Garrec, G. Reboul, and M. C. Jacob, "Numerical predictions of turbulence/cascade-interaction noise using computational aeroacoustics with a stochastic model," *AIAA Journal*, vol. 53, no. 12, pp. 3551–3566, 2015.

[58] S. Peth, J. H. Seo, Y. J. Moon, M. C. Jacob, and F. Thiele, "Computation of aerodynamic noise for rod wake-airfoil interactions," in *Parallel computational fluid dynamics: parallel computing and its applications, edited by Kwon,J. H., Ecer, A., Periaux, J., Satofuka, N., Fox, P., Elsevier, Amsterdam, The Netherlands*, 2006.

[59] M. Jacob, M. Ciardi, L. Gamet, B. Greschner, Y. Moon, and I. Vallet, "Assessment of cfd broadband noise predictions on a rod-airfoil benchmark computation," in *14th AIAA/CEAS Aeroacoustics Conference (29th AIAA Aeroacoustics Conference)*, p. 2899, 2008.

[60] F. Gea-Aguilera, J. Gill, and X. Zhang, "On the effects of fan wake modelling and vane design on cascade noise," *Journal of Sound and Vibration*, vol. 459, p. 114859, 2019.

[61] F. Gea-Aguilera, *Aerodynamic and aeroacoustic modelling of engine fan broadband noise*. PhD thesis, University of Southampton, 2017.

[62] D. B. Hanson, "Spectrum of rotor noise caused by atmospheric turbulence," *The Journal of the Acoustical Society of America*, vol. 56, no. 1, pp. 110–126, 1974.

[63] R. Paterson and R. Amiet, "Acoustic radiation and surface pressure characteristics of an airfoil due to incident turbulence," in *3rd Aeroacoustics Conference*, (East Hartford, Connecticut), p. 571, 1976.

[64] D. B. Stephens and S. C. Morris, "Sound generation by a rotor interacting with a casing turbulent boundary layer," *AIAA journal*, vol. 47, no. 11, pp. 2698–2708, 2009.

[65] M. C. Jacob, J. Grilliat, R. Camussi, and G. C. Gennaro, "Aeroacoustic investigation of a single airfoil tip leakage flow," *International Journal of Aeroacoustics*, vol. 9, no. 3, pp. 253–272, 2010.

[66] R. Camussi, J. Grilliat, G. Caputi-Gennaro, and M. C. Jacob, "Experimental study of a tip leakage flow: wavelet analysis of pressure fluctuations," *Journal of Fluid Mechanics*, vol. 660, pp. 87–113, 2010.

[67] M. C. Jacob, E. Jondeau, and B. Li, "Time-resolved PIV measurements of a tip leakage flow," *International Journal of Aeroacoustics*, vol. 15, no. 6-7, pp. 662–685, 2016.

[68] J. Grilliat, M. Jacob, E. Jondeau, M. Roger, and R. Camussi, "Broadband noise prediction models and measurements of tip leakage flows," in *14th AIAA/CEAS Aeroacoustics Conference (29th AIAA Aeroacoustics Conference)*, p. 2845, 2008.

[69] A. Cahuzac, J. Boudet, M. Jacob, and P. Kausche, "Large-eddy simulation of a rotor tip-clearance flow," in *17th AIAA/CEAS Aeroacoustics Conference (32nd AIAA Aeroacoustics Conference)*, p. 2947, 2011.

[70] S. Magne, S. Moreau, and A. Berry, "Subharmonic tonal noise from backflow vortices radiated by a low-speed ring fan in uniform inlet flow," *The Journal of the Acoustical Society of America*, vol. 137, no. 1, pp. 228–237, 2015.

[71] S. Moreau and M. Sanjose, "Sub-harmonic broadband humps and tip noise in low-speed ring fans," *The Journal of the Acoustical Society of America*, vol. 139, no. 1, pp. 118–127, 2016.

[72] J. de Laborderie, V. Blandeau, T. Node-Langlois, and S. Moreau, "Extension of a fan tonal noise cascade model for camber effects," *AIAA Journal*, vol. 53, no. 4, pp. 863–876, 2014.

[73] I. Gonzalez-Martino and D. Casalino, "Fan Tonal and Broadband Noise Simulations at Transonic Operating Conditions Using Lattice-Boltzmann Methods," in *2018 AIAA/CEAS Aeroacoustics Conference*, (Reston, Virginia), American Institute of Aeronautics and Astronautics, jun 2018.

[74] J. de Laborderie and S. Moreau, "Prediction of tonal ducted fan noise," *Journal of Sound and Vibration*, vol. 372, pp. 105–132, 2016.

[75] S. Grace, D. Sondak, W. Eversman, and M. Cannamela, "Hybrid prediction of fan tonal noise," in *14th AIAA/CEAS Aeroacoustics Conference (29th AIAA Aeroacoustics Conference)*, p. 2992, 2008.

[76] M. Sanjose, M. Daroukh, W. Magnet, J. De Laborderie, S. Moreau, and A. Mann, "Tonal fan noise prediction and validation on the ANCF configuration," in *Proceedings of the Fan 2015 Conference*, 2015.

[77] H. Atassi and M. Logue, "Modeling tonal and broadband interaction noise," *Procedia Engineering*, vol. 6, pp. 214–223, 2010.

[78] M. Pestana, A. Pereira, E. Salze, J. Thisse, M. Sanjosé, E. Jondeau, P. Souchotte, M. Roger, S. Moreau, J. Regnard, *et al.*, "Aeroacoustics of an axial ducted low mach-number stage: numerical and experimental investigation," in *23rd AIAA/CEAS Aeroacoustics Conference*, p. 3215, 2017.

[79] M. Sanjosé, S. Moreau, M. Pestana, and M. Roger, "Effect of weak outlet-guide-vane heterogeneity on rotor–stator tonal noise," *AIAA Journal*, pp. 3440–3457, 2017.

[80] R. Jaron, A. Moreau, and S. Guérin, "Rans-informed fan noise prediction: separation and extrapolation of rotor wake and potential field," p. 2946, 2014.

[81] M. Daroukh, S. Moreau, N. Gourdain, J.-F. Boussuge, and C. Sensiau, "Effect of distortion on turbofan tonal noise at cutback with hybrid methods," *International Journal of Turbomachinery, Propulsion and Power*, vol. 2, no. 3, p. 16, 2017.

[82] M. Daroukh, S. Moreau, N. Gourdain, J.-F. Boussuge, and C. Sensiau, "Tonal noise prediction of a modern turbofan engine with large upstream and downstream distortion," *Journal of Turbomachinery*, vol. 141, no. 2, 2019.

[83] M. Daroukh, N. Gourdain, S. Moreau, J.-F. Boussuge, and C. Sensiau, "Impact of inlet distortion on fan tonal noise," in *12th European Conference on Turbomachinery Fluid Dynamics and Thermodynamics*, 2017.

[84] R. Parker, "Paper 1: relation between blade row spacing and potential flow interaction effects in turbomachines," in *Proceedings of the Institution of Mechanical Engineers, Conference Proceedings*, vol. 184, pp. 1–8, Sage Publications Sage UK: London, England, 1969.

[85] M. Pestana, M. Sanjosé, S. Moreau, M. Roger, and M. Gruber, "Assessment of the impact of a heterogeneous stator on the noise of an axial-flow low mach-number stage," in *25th AIAA/CEAS Aeroacoustics Conference*, p. 2589, 2019.

[86] S. B. Pope, *Turbulent Flows.* 2001.

[87] H. Choi and P. Moin, "Grid-point requirements for large eddy simulation: Chapman's estimates revisited," *Physics of fluids*, vol. 24, no. 1, p. 011702, 2012.

[88] J. Kim, P. Moin, and R. Moser, "Turbulence statistics in fully developed channel flow at low reynolds number," *Journal of Fluid Mechanics*, vol. 177, pp. 133–166, 1987.

[89] X. Wu and P. A. Durbin, "Evidence of longitudinal vortices evolved from distorted wakes in a turbine passage," *Journal of Fluid Mechanics*, vol. 446, pp. 199–228, 2001.

[90] V. Michelassi, J. Wissink, and W. Rodi, "Analysis of DNS and LES of flow in a low pressure turbine cascade with incoming wakes and comparison with experiments," *Flow, turbulence and combustion*, vol. 69, no. 3-4, pp. 295–329, 2002.

[91] J. G. Wissink and W. Rodi, "Direct numerical simulation of flow and heat transfer in a turbine cascade with incoming wakes," *Journal of Fluid Mechanics*, vol. 569, pp. 209–247, 2006.

[92] V. Michelassi, L.-W. Chen, R. Pichler, and R. D. Sandberg, "Compressible direct numerical simulation of low-pressure turbines—Part II: Effect of inflow disturbances," *Journal of Turbomachinery*, vol. 137, no. 7, 2015.

[93] R. D. Sandberg, V. Michelassi, R. Pichler, L. Chen, and R. Johnstone, "Compressible direct numerical simulation of low-pressure turbines—Part I: Methodology," *Journal of Turbomachinery*, vol. 137, no. 5, 2015.

[94] G. Wang, S. Moreau, F. Duchaine, J. De Laborderie, and L. Gicquel, "LES investigation of aerodynamics performance in an axial compressor stage," in *22nd Annual Conference of the CFD Society of Canada, Toronto, Canada, June*, 2014.

[95] G. Wang, S. Moreau, F. Duchaine, N. Gourdain, and L. Gicquel, "Large eddy simulations of the MT1 high-pressure turbine using TurboAVBP," in *Proceeding of 21st Annual Conference of the CFD Society of Canada, Sherbrooke, Quebec, Canada*, pp. 70–106, 2013.

[96] G. Wang, M. Sanjose, S. Moreau, D. Papadogiannis, F. Duchaine, and L. Gicquel, "Noise mechanisms in a transonic high-pressure turbine stage," *International Journal of Aeroacoustics*, vol. 15, no. 1-2, pp. 144–161, 2016.

[97] G. Wang, F. Duchaine, D. Papadogiannis, I. Duran, S. Moreau, and L. Y. Gicquel, "An overset grid method for large eddy simulation of turbomachinery stages," *Journal of Computational Physics*, vol. 274, pp. 333–355, 2014.

[98] P. Kholodov, C. Pérez Arroyo, M. Sanjosé, and S. Moreau, "Fan broadband noise computation at transonic regime," in *25th AIAA/CEAS Aeroacoustics Conference*, p. 2714, 2019.

[99] N. Odier, F. Duchaine, L. Gicquel, G. Staffelbach, A. Thacker, N. García Rosa, G. Dufour, and J.-D. Muller, "Evaluation of integral turbulence scale through the fan stage of a turbofan using hot wire anemometry and large eddy simulation," in *ASME Turbo Expo 2018: Turbomachinery Technical Conference and Exposition*, American Society of Mechanical Engineers Digital Collection, 2018.

[100] P. R. Spalart, "Comments on the feasibility of LES for wings, and on a hybrid rans/les approach," in *Proceedings of first AFOSR international conference on DNS/LES*, Greyden Press, 1997.

[101] P. R. Spalart, S. Deck, M. L. Shur, K. D. Squires, M. K. Strelets, and A. Travin, “A new version of detached-eddy simulation, resistant to ambiguous grid densities,” *Theoretical and computational fluid dynamics*, vol. 20, no. 3, p. 181, 2006.

[102] V. Bonneau, C. Polacsek, L. Castillon, J. Marty, Y. Gervais, and S. Moreau, “Turbofan broadband noise predictions using a 3-D ZDES rotor blade approach,” in *22nd AIAA/CEAS Aeroacoustics Conference*, 2016.

[103] B. Mohammadi and O. Pironneau, “Analysis of the k-epsilon turbulence model,” 1993.

[104] F. Menter, “Improved two-equation k–ω turbulence models for aerodynamic flows,” Tech. Rep. TM-103975, NASA, Ames, CA, 1992.

[105] B. Smith, “The k-kl turbulence model and wall layer model for compressible flows,” in *21st Fluid dynamics, plasma dynamics and lasers conference*, p. 1483, 1990.

[106] P. Spalart and S. Allmaras, “A one-equation turbulence model for aerodynamic flows,” in *30th aerospace sciences meeting and exhibit*, p. 439, 1992.

[107] N. Gourdain, “Prediction of the unsteady turbulent flow in an axial compressor stage. Part 1: Comparison of unsteady RANS and LES with experiments,” *Computers & Fluids*, vol. 106, pp. 119–129, 2015.

[108] N. Gourdain, “Prediction of the unsteady turbulent flow in an axial compressor stage. Part 2: Analysis of unsteady RANS and LES data,” *Computers & Fluids*, vol. 106, pp. 67–78, 2015.

[109] N. Gourdain and F. Leboeuf, “Unsteady simulation of an axial compressor stage with casing and blade passive treatments,” *Journal of turbomachinery*, vol. 131, no. 2, 2009.

[110] N. Gourdain, S. Burguburu, F. Leboeuf, and G. J. Michon, “Simulation of rotating stall in a whole stage of an axial compressor,” *Computers & Fluids*, vol. 39, no. 9, pp. 1644–1655, 2010.

[111] N. Odier, F. Duchaine, L. Gicquel, G. Dufour, and N. García Rosa, “Comparison of LES and RANS Predictions With Experimental Results of the Fan of a Turbofan,” *12th European Conference on Turbomachinery Fluid Dynamics & Thermodynamics*, 2017.

[112] J. Boudet, J. Caro, L. Shao, and E. Lévêque, “Numerical studies towards practical large-eddy simulation,” *Journal of Thermal Science*, vol. 16, no. 4, pp. 328–336, 2007.

[113] J. Smagorinsky, “General circulation experiments with the primitive equations: I. the basic experiment,” *Monthly weather review*, vol. 91, no. 3, pp. 99–164, 1963.

[114] C. Bailly and G. Comte-Bellot, “Turbulence, springer,” 2004.

[115] H. Fujiwara, P. R. Voke, and C. Arakawa, “Large-eddy simulation of TL10 LP turbine blade row,” in *Engineering Turbulence Modelling and Experiments 5*, pp. 751–758, Elsevier, 2002.

[116] E. R. Van Driest, “On turbulent flow near a wall,” *Journal of the aeronautical sciences*, vol. 23, no. 11, pp. 1007–1011, 1956.

[117] E. Lévêque, F. Toschi, L. Shao, and J.-P. Bertoglio, “Shear-improved smagorinsky model for large-eddy simulation of wall-bounded turbulent flows,” *Journal of Fluid Mechanics*, vol. 570, pp. 491–502, 2007.

[118] J. Boudet, J. Caro, and M. Jacob, "Large-eddy simulation of a low-speed tip-clearance flow," in *9th European Conference on Turbomachinery Fluid Dynamics and Thermodynamics (ETC9), Istanbul, Turkey, March*, pp. 21–25, 2011.

[119] M. C. Jacob, J. Boudet, D. Casalino, and M. Michard, "A rod-airfoil experiment as a benchmark for broadband noise modeling," *Theoretical and Computational Fluid Dynamics*, vol. 19, no. 3, pp. 171–196, 2005.

[120] M. Germano, U. Piomelli, P. Moin, and W. H. Cabot, "A dynamic subgrid-scale eddy viscosity model," *Physics of Fluids A: Fluid Dynamics*, vol. 3, no. 7, pp. 1760–1765, 1991.

[121] J. C. R. Hunt, A. A. Wray, and P. Moin, "Eddies, streams, and convergence zones in turbulent flows," *Center for Turbulence Research, Proceedings of the Summer Program report CTR-S88*, pp. 193–208, 1988.

[122] A. Wray and J. Hunt, "Algorithms for classification of turbulent structures," *Topological Fluid Mechanics*, pp. 95–104, 1990.

[123] F. Nicoud and F. Ducros, "Subgrid-scale stress modelling based on the square of the velocity gradient tensor," *Flow, Turbulence and Combustion*, vol. 62, no. 3, pp. 183–200, 1999.

[124] F. Nicoud, H. B. Toda, O. Cabrit, S. Bose, and J. Lee, "Using singular values to build a subgrid-scale model for large eddy simulations," *Physics of Fluids*, vol. 23, no. 8, p. 085106, 2011.

[125] K. B. Kontos, R. E. Kraft, and P. R. Gliebe, "Improved NASA-ANOPP Noise Prediction Computer Code for Advanced Subsonic Propulsion Systems," Tech. Rep. NASA-CR-195480, NASA, 1996.

[126] L. Lopes and C. Burley, "Design of the next generation aircraft noise prediction program: ANOPP2," in *17th AIAA/CEAS Aeroacoustics Conference (32nd AIAA Aeroacoustics Conference)*, (Portland, Oregon), p. 2854, 2011.

[127] S. A. Glegg, "The response of a swept blade row to a three-dimensional gust," *Journal of Sound and Vibration*, vol. 227, no. 1, pp. 29–64, 1999.

[128] M. Wang, J. B. Freund, and S. K. Lele, "Computational prediction of flow-generated sound," *Annu. Rev. Fluid Mech.*, vol. 38, pp. 483–512, 2006.

[129] M. Roger, "Fundamentals of aero-acoustics, part i," *Lecture Series*, vol. 4, 1996.

[130] B.-T. Chu and L. S. Kovásznay, "Non-linear interactions in a viscous heat-conducting compressible gas," *Journal of Fluid Mechanics*, vol. 3, no. 5, pp. 494–514, 1958.

[131] M. Wang and P. Moin, "Computation of trailing-edge flow and noise using large-eddy simulation," *AIAA journal*, vol. 38, no. 12, pp. 2201–2209, 2000.

[132] M. E. Goldstein, "Aeroacoustics," *New York, McGraw-Hill International Book Co., 1976. 305 p.*, 1976.

[133] N. Curle, "The influence of solid boundaries upon aerodynamic sound," *Proceedings of the Royal Society of London. Series A. Mathematical and Physical Sciences*, vol. 231, no. 1187, pp. 505–514, 1955.

[134] S. Glegg and W. Devenport, *Aeroacoustics of low Mach number flows: fundamentals, analysis, and measurement.* Academic Press, 2017.

[135] S. Moreau and M. Roger, "Advanced noise modeling for future propulsion systems," *International Journal of Aeroacoustics*, vol. 17, no. 6-8, pp. 576–599, 2018.

[136] S. Moreau, "Turbomachinery noise predictions: present and future," in *Acoustics*, vol. 1, pp. 92–116, Multidisciplinary Digital Publishing Institute, 2019.

[137] W. R. Sears, "Some aspects of non-stationary airfoil theory and its practical application," *Journal of the Aeronautical Sciences*, vol. 8, no. 3, pp. 104–108, 1941.

[138] R. K. Amiet, "Acoustic radiation from an airfoil in a turbulent stream," *Journal of Sound and Vibration*, vol. 41, no. 4, pp. 407–420, 1975.

[139] S. Moreau, M. Roger, and V. Jurdic, "Effect of angle of attack and airfoil shape on turbulence-interaction noise," in *11th AIAA/CEAS aeroacoustics conference*, (Monterey, California), p. 2973, 2005.

[140] M. Roger, S. Moreau, and A. Guedel, "Broadband fan noise prediction using single-airfoil theory.," *Noise control engineering journal*, vol. 54, no. 1, 2006.

[141] M. R. Myers and E. J. Kerschen, "Influence of camber on sound generation by airfoils interacting with high-frequency gusts," *Journal of Fluid Mechanics*, vol. 353, pp. 221–259, 1997.

[142] I. Evers and N. Peake, "Noise generation by high-frequency gusts interacting with an airfoil in transonic flow," *Journal of Fluid Mechanics*, vol. 411, pp. 91–130, 2000.

[143] S. Kaji and T. Okazaki, "Generation of sound by rotor-stator interaction," *Journal of Sound and Vibration*, vol. 13, no. 3, pp. 281–307, 1970.

[144] M. F. Platzer and F. O. Carta, *AGARD Manual on Aeroelasticity in Axial-Flow Turbomachines. Volume 1. Unsteady Turbomachinery Aerodynamics, Chapter 3.* 1987.

[145] S. N. Smith, "Discrete frequency sound generation in axial flow turbomachines," Tech. Rep. 3709, Procurement executive ministry of defence aeronautical research council reports and memoranda, University of Cambridge, 1971.

[146] C. Cheong, P. Joseph, and S. Lee, "High frequency formulation for the acoustic power spectrum due to cascade-turbulence interaction," *The Journal of the Acoustical Society of America*, vol. 119, no. 1, pp. 108–122, 2006.

[147] V. Jurdic, A. Moreau, P. Joseph, L. Enghardt, and J. Coupland, "A comparison between measured and predicted fan broadband noise due to rotor-stator interaction," in *13th AIAA/CEAS Aeroacoustics Conference (28th AIAA Aeroacoustics Conference)*, no. 2007-3692, (Rome, Italy), 2007.

[148] A. Lloyd and N. Peake, "Rotor-stator broadband noise prediction," in *14th AIAA/CEAS Aeroacoustics Conference (29th AIAA Aeroacoustics Conference)*, no. 2008-2840, (Vancouver, British Columbia, Canada), 2008.

[149] H. Atassi and G. Hamad, "Sound generated in a cascade by three-dimensional disturbances convected in a subsonic flow," in *7th Aeroacoustics Conference*, no. 1981-2046, (Palo Alto,CA,U.S.A.), 1981.

[150] M. Namba, "Three-dimensional analysis of blade force and sound generation for an annular cascade in distorted flows," *Journal of Sound and Vibration*, vol. 50, no. 4, pp. 479–508, 1977.

[151] M. F. Platzer and F. O. Carta, *AGARD Manual on Aeroelasticity in Axial-Flow Turbomachines. Volume 1. Unsteady Turbomachinery Aerodynamics, Chapter 4.* 1987.

[152] H. Kodama and M. Namba, "Unsteady Lifting Surface Theory for a Rotating Cascade of Swept Blades," *Journal of Turbomachinery*, vol. 112, no. 3, pp. 411–417, 1990.

[153] J. Schulten, "Sound generated by rotor wakes interacting with a leaned vane stator," *AIAA Journal*, vol. 20, no. 10, pp. 1352–1358, 1982.

[154] J. B. H. M. Schulten, "Vane sweep effects on rotor/stator interaction noise," *AIAA journal*, vol. 35, no. 6, pp. 945–951, 1997.

[155] H. D. Meyer and E. Envia, "Aeroacoustic analysis of turbofan noise generation," Tech. Rep. NASA-CR-4715, NASA, 1996.

[156] J. Maunus, S. Grace, and D. Sondak, "Effect of CFD wake prediction in a hybrid simulation of fan broadband interaction noise," in *17th AIAA/CEAS Aeroacoustics Conference (32nd AIAA Aeroacoustics Conference)*, p. 2875, 2011.

[157] S. M. Grace and G. Forsyth, "Prediction of broadband fan exit guide vane response," in *19th AIAA/CEAS Aeroacoustics Conference*, no. 2013-2153, (Berlin, Germany), 2013.

[158] S. M. Grace and M. M. Logue, "Comparison of two low-order models for the prediction of fan broadband noise," *Journal of Sound and Vibration*, vol. 431, pp. 304–327, 2018.

[159] R. Mani and G. Horvay, "Sound transmission through blade," *Journal of Sound and Vibration*, vol. 12, no. 1, pp. 59–83, 1970.

[160] W. Koch, "On the transmission of sound waves through a blade row," *Journal of Sound and Vibration*, vol. 18, no. 1, pp. 111–128, 1971.

[161] N. Peake, "The interaction between a high-frequency gust and a blade row," *Journal of Fluid Mechanics*, vol. 241, pp. 261–289, 1992.

[162] D. Hanson and K. Horan, "Turbulence/cascade interaction-spectra of inflow, cascade response, and noise," in *4th AIAA/CEAS Aeroacoustics Conference*, no. 98-2319, (Toulouse,France), 1998.

[163] V. Masson, H. Posson, M. Sanjose, T. Léonard, S. Moreau, and M. Roger, "Fan-OGV interaction broadband noise prediction in a rigid annular duct with swirling and sheared mean flow," in *22nd AIAA/CEAS Aeroacoustics Conference*, no. 2016-2944, (Lyon, France), 2016.

[164] H. Posson and N. Peake, "The acoustic analogy in an annular duct with swirling mean flow," *Journal of Fluid Mechanics*, vol. 726, pp. 439–475, 2013.

[165] J. Mathews and N. Peake, "The acoustic Green's function for swirling flow in a lined duct," *Journal of Sound and Vibration*, vol. 395, pp. 294–316, 2017.

[166] P. J. Baddoo and L. J. Ayton, "An analytic solution for gust-cascade interaction noise including effects of realistic aerofoil geometry: Inter-blade region," in *2018 AIAA/CEAS Aeroacoustics Conference*, no. 2018-2957, (Atlanta, Georgia), 2018.

[167] S. Bouley, B. François, M. Roger, and S. Moreau, “On a mode-matching technique for sound generation and transmission in a linear cascade of outlet guide vanes,” in *21st AIAA/CEAS Aeroacoustics Conference*, no. 2015-2825, (Dallas, TX), 2015.

[168] L. Girier, M. Roger, H. Bériot, A. Lafitte, and H. Posson, “A two-dimensional model of sound transmission through curved and staggered OGV: Effect of inter-vane channel mode transitions,” in *25th AIAA/CEAS Aeroacoustics Conference*, (Delft, The Netherlands), pp. 2019–2690, 2019.

[169] S. M. Grace, “Influence of model parameters and the vane response method on a low-order prediction of fan broadband noise,” *International Journal of Aeroacoustics*, vol. 15, no. 1-2, pp. 131–143, 2016.

[170] C. M. Bender and S. A. Orszag, *Advanced mathematical methods for scientists and engineers I: Asymptotic methods and perturbation theory.* Springer Science & Business Media, 2013.

[171] S. J. Majumdar and N. Peake, “Three-dimensional effects in cascade-gust interaction,” *Wave motion*, vol. 23, no. 4, pp. 321–337, 1996.

[172] D. Hanson, “Influence of lean and sweep on noise of cascades with turbulent inflow,” in *5th AIAA/CEAS Aeroacoustics Conference and Exhibit*, no. 99-1863, (Bellevue,WA,U.S.A.), 1999.

[173] H. Wu, M. Sanjose, S. Moreau, and R. D. Sandberg, “Direct numerical simulation of the self-noise radiated by the installed controlled-diffusion airfoil at transitional reynolds number,” in *2018 AIAA/CEAS Aeroacoustics Conference*, p. 3797, 2018.

[174] M. Sanjosé, S. Moreau, F. Perot, and M.-S. Kim, “Direct self-noise simulation of the installed controlled diffusion airfoil,” in *17th AIAA/CEAS Aeroacoustics Conference (32nd AIAA Aeroacoustics Conference)*, p. 2716, 2011.

[175] D. Crighton, “Computational aeroacoustics for low mach number flows,” in *Computational aeroacoustics*, pp. 50–68, Springer, 1993.

[176] F. Farassat and M. Myers, “Extension of Kirchhoff’s formula to radiation from moving surfaces,” *Journal of Sound and Vibration*, vol. 123, no. 3, pp. 451–460, 1988.

[177] J. B. Freund, S. K. Lele, and P. Moin, “Calculation of the radiated sound field using an open Kirchhoff surface,” *AIAA journal*, vol. 34, no. 5, pp. 909–916, 1996.

[178] A. S. Lyrintzis, “Surface integral methods in computational aeroacoustics—from the CFD near-field to the (acoustic) far-field,” *International journal of aeroacoustics*, vol. 2, no. 2, pp. 95–128, 2003.

[179] K. S. Brentner and F. Farassat, “An analytical comparison of the acoustic analogy and Kirchhoff formulation for moving surfaces,” 1997.

[180] B. A. Singer and Y. Guo, “Development of computational aeroacoustics tools for airframe noise calculations,” *International Journal of Computational Fluid Dynamics*, vol. 18, no. 6, pp. 455–469, 2004.

[181] J. E. F. Williams and D. L. Hawkings, “Sound Generation by Turbulence and Surfaces in Arbitrary Motion,” *Philosophical Transactions of the Royal Society A: Mathematical, Physical and Engineering Sciences*, vol. 264, no. 1151, pp. 321–342, 1969.

[182] C. A. Kissner and S. Guérin, “Influence of wake and background turbulence on predicted fan broadband noise,” *AIAA Journal*, vol. 58, no. 2, pp. 659–672, 2020.

[183] C. Bailly and D. Juve, “A stochastic approach to compute subsonic noise using linearized euler’s equations,” in *5th AIAA/CEAS aeroacoustics conference and exhibit*, no. 99-1872, (Bellevue,WA,U.S.A.), 1999.

[184] C. Bailly and D. Juve, “Numerical Solution of Acoustic Propagation Problems Using Linearized Euler Equations,” *AIAA Journal*, vol. 38, no. 1, pp. 22–29, 2000.

[185] F. Gea-Aguilera, J. Gill, and X. Zhang, “Synthetic turbulence methods for computational aeroacoustic simulations of leading edge noise,” *Computers & Fluids*, vol. 157, pp. 240–252, 2017.

[186] C. Polacsek, A. Cader, M. Buszyk, R. Barrier, F. Gea-Aguilera, and H. Posson, “Aeroacoustic design and broadband noise predictions of a fan stage with serrated outlet guide vanes,” *Physics of Fluids*, vol. 32, no. 10, p. 107107, 2020.

[187] C. Paruchuri and P. Vellanki, “Bayesian optimisation for low-noise aerofoil design with aerodynamic constraints,” *International Journal of Aeroacoustics*, pp. 2–27, 2020.

[188] D. Mueller, H.-J. Schulz, G. Zitouni, and W. Baumann, “Europe’s largest aero acoustic test facility for aero engine fans-the development and operation of the anecom aerotest anechoic chamber,” in *11th AIAA/CEAS Aeroacoustics Conference*, no. 2005-3050, 2005.

[189] F. R. Menter, “Two-equation eddy-viscosity turbulence models for engineering applications,” *AIAA journal*, vol. 32, no. 8, pp. 1598–1605, 1994.

[190] D. C. Wilcox, “Reassessment of the scale-determining equation for advanced turbulence models,” *AIAA journal*, vol. 26, no. 11, pp. 1299–1310, 1988.

[191] M. M. Rai and N. K. Madavan, “Multi-Airfoil Navier–Stokes Simulations of Turbine Rotor–Stator Interaction,” *Journal of Turbomachinery*, vol. 112, no. 3, p. 377, 1990.

[192] T. Schönfeld and M. Rudgyard, “Steady and Unsteady Flow Simulations Using the Hybrid Flow Solver AVBP,” *AIAA Journal*, vol. 37, no. 11, pp. 1378–1385, 1999.

[193] P. D. Lax and B. Wendroff, “Difference schemes for hyperbolic equations with high order of accuracy,” *Communications on Pure and Applied Mathematics*, vol. 17, pp. 381–398, aug 1964.

[194] T. Poinsot and S. Lele, “Boundary conditions for direct simulations of compressible viscous flows,” *Journal of Computational Physics*, vol. 101, pp. 104–129, jul 1992.

[195] N. Odier, M. Sanjosé, L. Gicquel, T. Poinsot, S. Moreau, and F. Duchaine, “A characteristic inlet boundary condition for compressible, turbulent, multispecies turbomachinery flows,” *Computers & Fluids*, vol. 178, pp. 41–55, 2019.

[196] E. Nicoud, O. Colin, C. Angelberger, F. Nicollet, and C. Krüger, “A no-slip implementation of a wall law boundary condition in a cell-vertex code for les of internal aerodynamics on unstructured meshes,” in *Conference LES4ICE, IFP Energies nouvelles, Rueil-Malmaison*, 2016.

[197] P. Schmitt, T. POINSOT, B. Schuermans, and K. Geigle, “Large-eddy simulation and experimental study of heat transfer, nitric oxide emissions and combustion instability in a swirled turbulent high-pressure burner,” *Journal of Fluid Mechanics*, vol. 570, pp. 17–46, 2007.

[198] C. Mockett, T. Knacke, and F. Thiele, “Detection of Initial Transient and Estimation of Statistical Error in Time-Resolved Turbulent Flow Data,” *8th International ERCOFTAC Symposium on Engineering Turbulence Modelling and Measurements*, no. June, 2010.

[199] J. S. Bendat and A. G. Piersol, *Random data: analysis and measurement procedures*, vol. 729. John Wiley & Sons, 2011.

[200] C. Pérez Arroyo, T. Leonard, M. Sanjosé, S. Moreau, and F. Duchaine, “Large eddy simulation of a rotor stage for fan noise source diagnostic,” in *Proceedings of the Global Power and Propulsion Forum, Montreal, QC, Canada*, pp. 7–9, 2018.

[201] M. Deuse and R. D. Sandberg, “Different noise generation mechanisms of a controlled diffusion aerofoil and their dependence on mach number,” *Journal of Sound and Vibration*, p. 115317, 2020.

[202] J. Boudet, J. Caro, B. Li, E. Jondeau, and M. C. Jacob, “Zonal large-eddy simulation of a tip leakage flow,” *International Journal of Aeroacoustics*, vol. 15, no. 6-7, pp. 646–661, 2016.

[203] F. Perot, S. Moreau, M.-S. Kim, M. Henner, and D. Neal, “Direct aeroacoustics predictions of a low speed axial fan,” in *16th AIAA/CEAS aeroacoustics conference*, p. 3887, 2010.

[204] C. Kissner, S. Guérin, P. Seeler, M. Billson, C. Paruchuri, P. Carrasco Laraña, H. de Laborderie, B. François, K. Lefarth, D. Lewis, G. Montero Villar, and T. Nodé-Langlois, “ACAT1 benchmark of RANS-informed analytical methods for fan broadband noise prediction: Part I - Influence of the RANS simulation,” in *Acoustics*, Multidisciplinary Digital Publishing Institute, 2020.

[205] B. François, R. Barrier, and C. Polacsek, “Zonal detached eddy simulation of the fan-ogv stage of a modern turbofan engine,” in *ASME Turbo Expo 2020: Turbine Technical Conference and Exposition*, American Society of Mechanical Engineers Digital Collection, 2020.

[206] C. Polacsek, M. Daroukh, B. François, and R. Barrier, “Turbofan broadband noise predictions based on a zdes calculation of a fan-ogv stage,” in *9th Forum Acusticum*, 2020.

[207] V. Jurdic, P. Joseph, and J. Antoni, “Investigation of Rotor Wake Turbulence Through Cyclostationary Spectral Analysis,” *AIAA Journal*, vol. 47, no. 9, pp. 2022–2030, 2009.

[208] R. Jaron, A. Moreau, and S. Guerin, “Extrapolation of RANS flow data for improved analytical fan tone prediction,” in *21st AIAA/CEAS Aeroacoustics Conference*, no. June, (Reston, Virginia), pp. 1–19, American Institute of Aeronautics and Astronautics, jun 2015.

[209] J. Grilliat, M. Jacob, R. Camussi, and G. Caputi-Gennaro, “Tip leakage experiment-part one: Aerodynamic and acoustic measurements,” in *13th AIAA/CEAS Aeroacoustics Conference (28th AIAA Aeroacoustics Conference)*, p. 3684, 2007.

[210] S. Guérin, C. Kissner, P. Seeler, R. A. Blazquez Navarro, P. Carrasco Laraña, H. de Laborderie, D. Lewis, C. Paruchuri, and C. Polacsek, "ACAT1 benchmark of RANS-informed analytical methods for fan broadband noise prediction: Part II - influence of the acoustic models," in *Acoustics*, Multidisciplinary Digital Publishing Institute, 2020.

[211] H. Posson and S. Moreau, "Effect of Rotor Shielding on Fan-Outlet Guide Vanes Broadband Noise Prediction," *AIAA Journal*, vol. 51, no. 7, pp. 1576–1592, 2013.

[212] J. de Laborderie, S. Moreau, and A. Berry, "Compressor stage broadband noise prediction using a large-eddy simulation and comparisons with a cascade response model," in *19th aiaa/ceas aeroacoustics conference*, p. 2042, 2013.

[213] A. Fosso Pouangué, M. Sanjosé, S. Moreau, G. Daviller, and H. Deniau, "Subsonic jet noise simulations using both structured and unstructured grids," *AIAA Journal*, vol. 53, no. 1, pp. 55–69, 2015.

[214] D. Casalino, "An advanced time approach for acoustic analogy predictions," *Journal of Sound and Vibration*, vol. 261, no. 4, pp. 583–612, 2003.

[215] A. Najafi-Yazdi, G. A. Brès, and L. Mongeau, "An acoustic analogy formulation for moving sources in uniformly moving media," *Proceedings of the Royal Society A: Mathematical, Physical and Engineering Sciences*, vol. 467, no. 2125, pp. 144–165, 2011.

[216] T.-H. Shih, W. W. Liou, A. Shabbir, Z. Yang, and J. Zhu, "A new k-ϵ eddy viscosity model for high reynolds number turbulent flows," *Computers & Fluids*, vol. 24, no. 3, pp. 227–238, 1995.

[217] T. von Kármán, "Airfoil theory for non-uniform motion," *Journal of the Aeronautical Sciences*, vol. 5, no. 10, pp. 379–390, 1938.

[218] H. Posson, *Fonctions de réponse de grille d'aubes et effet d'écran pour le bruit à large bande des soufflantes.* PhD thesis, École Centrale de Lyon, 2008.

[219] V. P. Blandeau, P. F. Joseph, G. Jenkins, and C. J. Powles, "Comparison of sound power radiation from isolated airfoils and cascades in a turbulent flow," *The Journal of the Acoustical Society of America*, vol. 129, no. 6, pp. 3521–3530, 2011.

[220] H. Atassi and M. Logue, "Effect of turbulence structure on broadband fan noise," in *14th AIAA/CEAS Aeroacoustics Conference (29th AIAA Aeroacoustics Conference)*, no. 2008-2842, (Vancouver, British Columbia, Canada), 2008.

[221] H. Atassi and M. Logue, "Fan broadband noise in anisotropic turbulence," in *15th AIAA/CEAS Aeroacoustics Conference (30th AIAA Aeroacoustics Conference)*, no. 2009-3148, (Miami, Florida), 2009.

[222] F. Gea Aguilera, J. R. Gill, X. Zhang, X. Chen, and T. Nodé-Langlois, "Leading edge noise predictions using anisotropic synthetic turbulence," in *22nd AIAA/CEAS Aeroacoustics Conference*, no. 2016-2840, 2016.

[223] E. J. Kerschen and P. Gliebe, "Noise caused by the interaction of a rotor with anisotropic turbulence," *AIAA Journal*, vol. 19, no. 6, pp. 717–723, 1981.

[224] G. Batchelor, "The theory of axisymmetric turbulence," *Proceedings of the Royal Society of London. Series A. Mathematical and Physical Sciences*, vol. 186, no. 1007, pp. 480–502, 1946.

[225] S. Chandrasekhar, "The theory of axisymmetric turbulence," *Philosophical Transactions of the Royal Society of London. Series A, Mathematical and Physical Sciences*, vol. 242, no. 855, pp. 557–577, 1950.

[226] S. Chandrasekhar, "The decay of axisymmetric turbulence," *Proceedings of the Royal Society of London. Series A. Mathematical and Physical Sciences*, vol. 203, no. 1074, pp. 358–364, 1950.

[227] G. Jenkins, C. Powles, V. Blandeau, and P. Joseph, "Low and high frequency models for the prediction of noise due to cascade-turbulence interaction," in *17th AIAA/CEAS Aeroacoustics Conference (32nd AIAA Aeroacoustics Conference)*, no. 2011-2826, (Portland, Oregon), 2011.

[228] P. Joseph and A. Parry, "Rotor/wall boundary-layer interaction broadband noise in turbofan engines," in *7th AIAA/CEAS Aeroacoustics Conference and Exhibit*, no. 2001-2244, (Maastricht, Netherlands), 2001.

[229] H. W. Stock and W. Haase, "Feasibility study of e transition prediction in navier-stokes methods for airfoils," *AIAA journal*, vol. 37, no. 10, pp. 1187–1196, 1999.

[230] D. Coles, "The law of the wake in the turbulent boundary layer," *Journal of Fluid Mechanics*, vol. 1, no. 2, pp. 191–226, 1956.

[231] J. Green, D. Weeks, and J. Brooman, "Prediction of turbulent boundary layers and wakes in compressible flow by a lag-entrainment method," Tech. Rep. 3791, Procurement executive ministry of defence aeronautical research council reports and memoranda, 1973.

dernière page de la thèse

AUTORISATION DE SOUTENANCE

Vu les dispositions de l'arrêté du 25 mai 2016,

Vu la demande des directeurs de thèse

Messieurs M. JACOB et S. MOREAU

et les rapports de

Mme P. CINNELLA
Professeure - Laboratoire de Dynamique des Fluides - ENSAM - 151 bd de l'Hôpital
75013 Paris

et de

M. F. DUCHAINE
Docteur HDR - Centre Européen de Recherche et de Formation Avancée en Calcul Scientique
42 avenue Gaspard Coriolis - 31057 Toulouse cedex 01

Monsieur LEWIS Danny

est autorisé à soutenir une thèse pour l'obtention du grade de **DOCTEUR**

Ecole doctorale MECANIQUE, ENERGETIQUE, GENIE CIVIL ET ACOUSTIQUE

Fait à Ecully, le 12 novembre 2020

P/Le directeur de l'E.C.L.
Le directeur des Etudes

Grégory VIAL
Directeur des études
École Centrale de Lyon

Grégory VIAL